UC Berkeley
UC Berkeley Electronic Theses and Dissertations

Title
Mechanistic Insights into Metal-Catalyzed Hydrogenations and the Role of Metal Oxide Co-catalysts

Permalink
https://escholarship.org/uc/item/9j25x833

Author
Fischer, Ari

Publication Date
2021

Peer reviewed|Thesis/dissertation

eScholarship.org Powered by the California Digital Library
University of California

Mechanistic Insights into Metal-Catalyzed Hydrogenations and the Role of Metal Oxide Co-catalysts

by

Ari Fischer

A dissertation submitted in partial satisfaction of the

requirements for the degree of

Doctor of Philosophy

in

Chemical Engineering

in the

Graduate Division

of the

University of California, Berkeley

Committee in charge:

Professor Enrique Iglesia, Chair
Professor Jeffrey R. Long
Professor T. Don Tilley

Fall 2021

Mechanistic Insights into Metal-Catalyzed Hydrogenations and the Role of Metal Oxide Co-catalysts

© 2021

by

Ari Fischer

Abstract

Mechanistic Insights into Metal-Catalyzed Hydrogenations and the Role of Metal Oxide Co-catalysts

by

Ari Fischer

Doctor of Philosophy in Chemical Engineering

University of California, Berkeley

Professor Enrique Iglesia, Chair

The mechanistic origins of bifunctional synergies between metal nanoclusters and insulating oxide materials, present as a support or volumetric diluent, for catalytic hydrogenation reactions remains controversial despite decades of research. These bifunctional routes are often attributed to reaction pathways mediated by hydrogen spillover whereby H atoms migrate from metal surfaces, where they form from dissociated H_2, to oxide surfaces and react with unsaturated molecules; however, such routes are unlikely to occur with insulating oxides which do not interact favorably with H atoms except at crystallographic defects. Herein, alternative explanations for such effects are investigated by exploring the mechanistic underpinnings of toluene hydrogenation on Pt surfaces and extending these insights to bifunctional reactions with γ-Al_2O_3 as a co-catalyst as an example of such phenomena.

Turnover rates of methylcyclohexane formation from toluene and H_2 reactants were measured on SiO_2-supported Pt nanoparticles (3.6 mean Pt diameter) across a wide range of temperatures (333-533 K) and reactant pressures (20-80 kPa H_2, 0.3-3 kPa toluene). Gaseous pressures of 1-methylcyclohexene and 4-methylcyclohexene intermediates are also reported. These methylcyclohexene species form as reactive intermediates during kinetically-relevant toluene hydrogenation routes; their gas-phase concentrations reflect the pseudo-steady state balance of their rates of formation (from toluene-H_2 reactants) and consumption (by reaction with H_2 to form methylcyclohexane) at lower temperatures (393-493 K), and their approach to thermodynamic equilibrium with toluene and H_2 reactants at higher temperatures (493-533 K). These insights are leveraged to reduce the mechanistic complexity of toluene hydrogenation into two half reactions allowing for the kinetically-relevant steps and most abundant surface intermediates to be identified through kinetic modeling coupled with density functional theory calculations that probe binding energies and geometries of surface intermediates. Methylcyclohexane formation is shown to be kinetically limited primarily by the addition of the second H atom to toluene at low temperatures (333-493 K) and by the addition of the second H atom to methylcyclohexene intermediates at higher temperatures (493-533 K). These kinetic interpretations along with density functional theory calculations also show that the Pt surfaces are saturated with molecularly bound forms of toluene at all temperatures considered. Such a shift in the kinetically relevant steps towards later H additions along the toluene hydrogenation reaction coordinate as the temperature increases occurs because each H-addition step incurs a large entropic

penalty due to the loss of highly entropic translation degrees of freedom of H_2 molecules. The toluene-derived intermediates that participate in these later H-addition reactions are formed exothermically from stoichiometric amounts of toluene and H_2, resulting in a negative apparent activation enthalpy when their hydrogenation becomes rate limiting. These behaviors account for the decrease in methylcyclohexane formation rates with increasing temperature that was observed at higher temperatures (>453 K).

The ubiquitous presence of gaseous methylcyclohexene intermediates during toluene-H_2 reactions on Pt surfaces informs plausible bifunctional reactions on Pt/SiO_2+γ-Al_2O_3 mixtures. Two novel mechanistic interpretations are proposed and compared to relevant experimental and theoretical observations. One route involves the formation of partially hydrogenated toluene-derived intermediates (TH_n*) from toluene-H_2 reactions on Pt surfaces. These species can desorb and hydrogenate at nearby γ-Al_2O_3 surfaces, without requiring atomic contact between Pt and γ-Al_2O_3, thus circumventing the monofunctional bottlenecks at Pt surfaces and increasing methylcyclohexane formation rates. Another route involves the formation of TH_n* species that undergo slow H-addition reactions to form methylcyclohexane, but which compete effectively for binding sites on crowded Pt surfaces with the predominant reactive intermediates involved in monofunctional routes. These stranded, less reactive TH_n* species can desorb to give very low equilibrium concentrations of their gaseous analogs; their migration to and hydrogenation at γ-Al_2O_3 surfaces present beyond atomic distances leads to their scavenging from the fluid phase, thus decreasing their equilibrium surface coverages and increasing the binding spaces available for the competitive reactions of intermediates that mediate monofunctional hydrogenation turnovers at Pt surfaces.

Toluene hydrogenation was carried out over Pt/SiO_2+γ-Al_2O_3 mixtures with varying separation between the Pt/SiO_2 and γ-Al_2O_3 domains (via variation in the aggregate domain size of the respective catalytic components contained in physical mixtures). Methylcyclohexane formation rates were largest for Pt/SiO_2+γ-Al_2O_3 mixtures with the smallest separation (and therefore greatest site proximity) and decreased asymptotically towards the rate observed on Al_2O_3-free Pt/SiO_2 as the domain sizes of the respective components increased. Such trends resemble characteristic features of bifunctional reactions mediated by mobile and highly reactive gaseous intermediates. 1,3-Cyclohexadiene and 4-methylcyclohexene reactions with H_2 were carried out over Pt-free γ-Al_2O_3 surfaces (30-300 Pa hydrocarbon, 0-90 kPa H_2, 393 K). These unsaturated molecules are shown to hydrogenate predominantly via reaction with molecular H_2 at rates that are catalytically significant in the context of Al_2O_3-catalyzed rates in bifunctional Pt/SiO_2+γ-Al_2O_3 mixtures necessary to account for rate enhancements. Reaction-transport modelling based on the proposed bifunctional mechanisms and measured reactivity trends for independent Pt/SiO_2 and γ-Al_2O_3 functions show that bifunctional synergies are best attributed to γ-Al_2O_3-mediated scavenging of methylcyclohexadiene inhibitors at low temperatures (393 K), prevalent only on Pt/SiO_2 catalysts with small Pt clusters (0.7 nm mean diameter). At higher temperatures (493-533 K), in which methylcyclohexene hydrogenation becomes rate-limiting on Pt surfaces, an additive methylcyclohexene hydrogenation route at nearby γ-Al_2O_3 is likely to become more prevalent.

These results thus provide novel mechanistic interpretations of bifunctional hydrogenation catalyzed by Pt/SiO_2+γ-Al_2O_3 mixtures involving mobile, highly reactive gaseous molecular shuttles rather than H-atom spillover. Insights gained from this work advance the understanding of bifunctional synergies between metals and their nearby supports or diluent materials in composite catalytic materials.

Table of Contents

Chapter 1: Introduction to Mechanistic Insights into Metal-Catalyzed Hydrogenations and the Role of Metal Oxide Co-catalysts 1

References 4

Chapter 2: Mechanistic Interpretations of Pt-catalyzed Toluene Hydrogenation: Unravelling the Effects of Saturation Coverages, Adsorption Site-ensemble Requirements, and the Emission of Reactive Gaseous Alkene Intermediates. 7

2.1. Introduction 8

2.2. Methods and materials 9
2.2.1. Catalyst synthesis and characterization. 9
2.2.2. Catalytic rate measurements. 10
2.2.3. Computational methods. 11

2.3. Results and discussion 12
2.3.1. The effects of temperature, hydrogen pressure, and toluene pressure on methylcyclohexane formation turnover rates and pressures of prevalent methylcyclohexene intermediates. 12
2.3.2. Elementary steps for toluene and methylcyclohexene hydrogenation and their consequences for prevalent methylcyclohexene pressures. 14
2.3.3. Thermodynamics and relative coverages of bound intermediates during toluene hydrogenation on Pt. 18
2.3.4. Kinetically-relevant steps for toluene hydrogenation at low temperatures (333-393 K) and the chemical significance of the relevant kinetic and thermodynamic parameters for methylcyclohexane formation. 20
2.3.5. Kinetically-relevant steps, chemical significance of the relevant kinetic and thermodynamic parameters, and origins of the negative temperature dependence for toluene hydrogenation at high temperatures (493-533 K). 27

2.4. Conclusions 33

2.5. Acknowledgements 33

2.6. Figures, tables, and schemes 34

2.7 References 52

2.8 Supporting information 56
2.8.1. Hydrogen adsorption isotherms on Pt/SiO_2 and estimation of Pt particle dispersions. 56
2.8.2. Depiction of Pt(111) surface and adsorption sites. 57
2.8.3. Statistical mechanics methods for calculating thermodynamic properties of species formed during toluene-H_2 reactions on Pt/SiO_2 from density functional theory calculations. 57

2.8.4. Derivation of the relationship between methylcyclohexene isomer pressures and toluene conversion during toluene-H_2 reactions on Pt surfaces. 59
2.8.5. Multisite Langmuir adsorption model for site occupancy on toluene covered Pt surfaces. 60

Chapter 3: Proximity Effects, Mechanistic Insights, and the Nature of Molecular Shuttles in Catalytic Hydrogenations Involving Bifunctional Cascades 64

3.1. Introduction 65

3.2. Materials and methods 68
3.2.1. Catalyst synthesis and characterization. 68
3.2.2. Catalytic rate measurements. 68
3.2.3. Calculations of diffusion and mass transfer coefficients. 70
3.2.4. Computational methods. 70

3.3. Results and discussion 71
3.3.1. Effects of Pt/SiO_2 dilution with SiO_2 or Al_2O_3 on methylcyclohexane formation rates from toluene-H_2 reactants. 71
3.3.2. The effects of propanoic acid on methylcyclohexane formation rates during toluene-H_2 reactions on Pt/SiO_2 and intimate Pt/SiO_2-Al_2O_3 mixtures. 73
3.3.3. 1,3-Cyclohexadiene and 4-methylcyclohexene reactions with H_2 on Pt-free Al_2O_3 surfaces. 73
3.3.4. The role of additive/stochiometric toluene hydrogenation routes via molecular shuttles in Pt/SiO_2 and Al_2O_3 mixtures. 74
3.3.5. The role of inhibitor-scavenging routes via molecular shuttles in Pt/SiO_2 and Al_2O_3 mixtures and supporting evidence from reaction-transport models. 77
3.3.6. The relevance of methylcyclohexene isomers as reactive intermediates in prevalent inhibitor-scavenging routes. 82
3.3.7. The relevance of methylcyclohexadiene isomers as reactive intermediates in prevalent inhibitor-scavenging routes. 83
3.3.8. Chemical significance of kinetic parameters that govern reactivity in methylcyclohexadiene-mediated inhibitor-scavenging routes. 86
3.3.9. The effects of Pt nanoparticle size on the prevalence of Al_2O_3-dilution induced methylcyclohexane formation rate enhancements on Pt/SiO_2. 89

3.4. Conclusions 90

3.5. Acknowledgements 91

3.6. Figures, tables, and schemes 92

3.7. References 113

3.8. Supporting information 118
3.8.1. Hydrogen chemisorption isotherms and estimation of Pt particle dispersions 118
3.8.2. N_2 adsorption isotherms, surface areas, and pore volumes for SiO_2 and Al_2O_3. 119

3.8.3. Time on stream data for 1,3-cyclohexadiene and 4-methylcyclohexene reactions with H_2 on Al_2O_3. 121
3.8.4. Complete set of toluene-derived intermediates. 124
3.8.5. Expanded reaction-transport model describing methylcyclohexane formation via inhibitor-scavenging routes. 125
3.8.6. Derivation of enhancement factors for intimate Pt/SiO_2 and Al_2O_3 mixtures for inhibitor-scavenging routes at pseudo-steady state. 128

Appendices 130

A.1. Density functional theory-derived optimized geometries of molecules bound to Pt(111) surfaces. 130

A.2. Density functional theory-derived vibrational frequencies of molecules bound to Pt(111) surfaces. 136

A.3. Density functional theory-derived optimized geometries of gas-phase molecules. 139

A.4. Density functional theory-derived vibrational frequencies of gas-phase molecules. 141

A.5. Molecular geometries of gas-phase molecules optimized using coupled cluster singles and doubles (CCSD) theory. 143

A.6. Vibrational frequencies of gas-phase molecules using the complete basis set (CBS-QB3) method. 146

Acknowledgements

I would like to extend my deepest gratitude to Professor Enrique Iglesia, my dissertation advisor, for fostering intellectual curiosity and inspiring passion for fundamental science. His mentorship has played a pivotal role in my development as a scientist and scholar, which I will cherish for the rest of my life.

The completion of my dissertation would not have been possible without the comradery, collaboration, and mentorship of my lab mates in the Laboratory for the Science and Applications of Catalysis (LSAC), most notably Dr. Haefa Mansour, Dr. Samuel Leung, Dr. Shashikant Kadam, Dr. Gina Noh, Dr. Stephanie Kwon, Dr. Junnan Shangguan. It was a pleasure to work with such a bright, positive, and inspiring community.

I am grateful to Professor Kranthi Mandadapu, Dr. Marjorie Went, and Dr. Alexandra Landry Herrmann, whom I had the pleasure of working with as a Graduate Student Instructor, for exemplifying dedication to teaching and undergraduate education.

I am also grateful to Carlet Altamirano and Sigrid Allen for their compassionate support during my educational process.

I also acknowledge the financial support from the National Science Foundation Graduate Research Fellowships Program, Chevron Corporation, and Chevron Graduate Research Fellowship, and computational support from the Extreme Science and Engineering Discovery Environment (XSEDE) and the National Energy Research Scientific Computing Center (NERSC).

I am thankful to Dr. Edwin Yik, Dr. Prashant Deshlahra, Dr. Xueyi Zhang, and Dr. Zhijie Wu for helping to establish the foundations for much of the work that appears in this dissertation. I thank Nancy Ye for contributions to this work through her role as an undergraduate researcher.

Finally, I acknowledge my friends and family who have encouraged and supported me along my journey. This work would not have been possible without my parents, Helaine and Harold, and siblings, Zachary and Jordan, whose love and support have given me strength and courage.

CHAPTER ONE

Introduction to Mechanistic Insights into Metal-Catalyzed Hydrogenations and the Role of Metal Oxide Co-catalysts

In the seminal work of Khoobiar [1], WO_3 was shown to reduce to tungsten bronze in the presence of H_2 when mixed physically with Al_2O_3-supported Pt nanoclusters, despite no evidence of such reduction on Pt-free WO_3. Benson et al. [2] elucidated the mechanistic underpinnings of such processes, showing that H atoms bound to Pt nanoclusters within atomic distances of WO_3 surfaces donate their valence electrons to the conduction band of the WO_3 to form proton-electron pairs that can migrate across WO_3 surfaces. Rates of WO_3 reduction were later shown to increase in the presence of H_2O and other oxygenates with large proton affinities which stabilize the H^+ species thus lowering the barrier for migration of Pt-bound H atoms to the WO_3 surfaces [3]. Mechanisms inspired by such H-atom migration from metal surfaces (where they form from H_2 dissociation) to oxide surfaces (where they react with a substrate), commonly referred to as hydrogen spillover (H-spillover), have been proposed to account for selective acetylene hydrogenation to ethylene on Cu supported single-atom Pd catalysts [4], increased CO hydrogenation turnover rates to methanol on Cu nanoparticles when ZrO_2 is used as a support compared with SiO_2 [5], and increased monoarene [6] and alkene hydrogenation [7] turnover rates on metal oxide-supported Pt nanoclusters when they are mixed physically with γ-Al_2O_3.

Among these mechanistic proposals, the catalytic consequences of H-spillover from Pt nanoclusters to γ-Al_2O_3 surfaces (or other insulating oxides) present as a support or diluent is especially controversial [8,9]. γ-Al_2O_3 is an insulating material that, unlike WO_3, lacks reducible metal cations to react with the valence electrons of Pt-bound H atoms to form stable H^+-e^- pairs necessary for H migration [10]. H atoms can only bind to γ-Al_2O_3 surfaces at crystallographic defects, such as coordinatively unsaturated Al^{3+} centers [11,12], which may not be abundant enough to provide sufficient connectivity for H migration. In order to be of catalytic significance, H atoms must migrate from the Pt to the γ-Al_2O_3 and diffuse across its surface at rates that are commensurate with increased hydrogenation rates [8]. Surface diffusion, in general, requires that adsorbates translate from one binding site to another, overcoming significant activation barriers to form transition states between local energy minima in the process. Coordinatively unsaturated Al^{3+} centers form at 0.5 sites nm^{-2} [13] on γ-Al_2O_3, which corresponds to an average distance of 1.4 nm between such sites, provided that they are evenly distributed; the surface between such defects is terminated with coordinatively saturated Al-O-Al and Al-OH groups which interact only weakly with diffusing H atoms [12]. Thus, a large activation barrier is incurred as strong Al^{3+} and H interactions are broken without significant compensation by interactions with Al-O-Al and Al-OH. These limitations have been born out experimentally using nano-fabrication techniques to synthesize TiO_2 (a semi-conductive material) and γ-Al_2O_3 (an insulating material) surfaces as supports for Pt and Fe_2O_3 nanoclusters separated by nanometer length scales [11]. Exposure to H_2 led to significant reduction of the Fe_2O_3 particles when TiO_2 was used as the support irrespective of the Pt-Fe_2O_3 separation, but a much lower extent of Fe_2O_3 reduction was observed with the γ-Al_2O_3 support and decreased monotonically with increasing separation distances [11]. Activation barriers (calculated using density functional theory) for translation between coordinatively unsaturated Al^{3+} centers was calculated to be 1.15-1.63 eV (depending on the H_2O coverage at the Al_2O_3 surface), which was similar to the desorption barrier for these same bound H atoms [11], revealing that H atoms desorb to form H-radicals just as easily as they diffuse across the surface.

Alternate explanations that do not involve H-spillover have been proposed to account for the promotional effects of γ-Al_2O_3 for metal-catalyzed hydrogenation reactions. Higher ethylene hydrogenation rates were reported for Pt/SiO_2 diluted with γ-Al_2O_3 compared with SiO_2; these rate differences were attributed to the poisoning of the Pt by carbonaceous impurities introduced into the reactor by the SiO_2 diluent, but absent on γ-Al_2O_3 surfaces [14]. These rate differences disappeared upon brief treatment in oxygen at 493 K, a finding attributed to the removal of such impurities by oxidation [14]. Higher rates for benzene hydrogenation [6] on Pt/γ-Al_2O_3 and for toluene hydrogenation on Pt/SiO_2 (as shown in **Chapter 3**) when mixed with γ-Al_2O_3 persisted, however, even after such treatments in O_2, suggesting that the effects of any such impurities cannot account for the γ-Al_2O_3-induced rate enhancements in these monoarene hydrogenation reactions. Hydrogen spillover has been shown to occur from Pt particles to carbon supports [15,16], suggesting that carbonaceous deposits consisting of unsaturated organic residues may form on Al_2O_3 surfaces, thus potentially acting as conducting bridges for hydrogen spillover from Pt nanoparticles to unsaturated molecules bound at γ-Al_2O_3 surfaces or at such organic debris [9].

In light of the uncertainties surrounding the catalytic importance of H-spillover for increased reactivity for metals mixed with insulating oxides, this dissertation investigates alternative bifunctional mechanisms that are mediated by organic species serving as molecular shuttles, instead of H atoms directly, as pathways for the hydrogenation of unsaturated molecules. These mechanisms involve the formation of reactive intermediates by reactions of the hydrocarbon and H_2 at the metal surface to form gaseous intermediates that then diffuse to and react at the oxide support or diluent surfaces in advantageous reactions. Such bifunctional reaction schemes have been well established in catalytic processes such as dehydro-isomerization, hydrogenolysis, and aromatization of alkylcycloalkanes [17]. In such processes, the two catalytic functions are kinetically coupled via gaseous intermediates that diffuse through barrierless Knudsen or molecular diffusion instead of slow, activated diffusion across catalyst surfaces. Toluene hydrogenation on Pt/SiO_2 mixed physically with γ-Al_2O_3 is examined in **Chapter 3** as an example of bifunctional synergies during metal-catalyzed monoarene hydrogenations (and hydrogenations of unsaturated hydrocarbons, more generally). The mechanistic origins of several characteristic features of monoarene hydrogenation reactions on metal surfaces remain controversial, however, impeding mechanistic interpretations of bifunctional processes. To identify plausible bifunctional routes involving toluene-derived molecular shuttles during toluene-H_2 reactions on Pt/SiO_2+γ-Al_2O_3 mixtures, the mechanistic underpinnings of toluene hydrogenation on γ-Al_2O_3-free Pt surfaces during these reactions is first elucidated (**Chapter 2**).

Monoarenes, such as benzene and toluene, are hydrogenated by six successive H-addition steps between bound arenes and H atoms (formed from H_2 dissociation) forming partially hydrogenated surface intermediates with a range of H content in the process [18–20]. The kinetically-relevant steps among these sequential H additions and the most abundant surface intermediates (MASI) remain controversial because several competing mechanistic interpretations are able to account for reactivity trends [19,20]. Such complexities manifest in unique kinetic trends for monoarene hydrogenations including rates that reach a maximum value as a function of temperature (which cannot be attributed to thermodynamic equilibrium between toluene, H_2, and methylcyclohexane) and rate dependences on H_2 and toluene pressures that increase monotonically with temperature.

Unsaturated hydrocarbons form strong covalent bonds with transition metal surfaces, and in the presence of H_2, moreover, undergo H-addition and H-abstraction reactions and rearrangements on the surface to reach their kinetic or thermodynamic endpoints. Ultimately, such strong interactions lead to metal surfaces that become saturated at high coverages with hydrocarbon moieties, as is evident from surface science investigations [21,22] and from ubiquitous zero-order reaction kinetics for hydrocarbon conversions [20]. Aromatic rings can, moreover, be hydrogenated via several parallel sequences of H-addition steps that differ in the relative C atom positions of the added H atoms that contribute to overall hydrogenation rates to varying extents. The multiplicity of surface species among this hydrocarbon pool presents a formidable challenge in identifying which species cover the metal surfaces and impede active sites from forming transition states that mediate rate-limiting elementary steps. Interactions between unsaturated hydrocarbons and metal surfaces decrease with increasing surface coverage because electron donation from the hydrocarbon to the metal changes the metal's electron density and thus the strength of the metal-adsorbate interactions [23]. As a result, high hydrocarbon coverage on metal surfaces attenuates the binding energies of individual intermediates rendering their desorption comparable to their forward rates of reaction with H atoms. Indeed, gaseous methylcyclohexene intermediates are formed from toluene-H_2 reactions on Pt surfaces at pressures that reflect quasi-equilibrium with their surface counterparts (as shown in **Chapter 2**). Their pressures reflect a balance at pseudo-steady state between the rates that they are formed from toluene and H_2, and consumed by reaction with H_2, providing valuable insight into which H-addition step(s) along the sequence of steps that govern toluene hydrogenation are rate limiting. This novel insight is leveraged in **Chapter 2** to reduce the mechanistic complexity of toluene hydrogenation into two simpler half reactions to an extent where the kinetically-relevant steps and MASI can be identified through kinetics-based reaction modeling coupled with density functional theory calculations to probe binding energies and geometries of surface intermediates. In doing so, the mechanistic origins of controversial kinetic behaviors of monoarene hydrogenation reactions are elucidated.

Ubiquitous gaseous methylcyclohexene intermediates formed during toluene-H_2 reactions on Pt surfaces may react further at γ-Al_2O_3 surfaces present within diffusion distances in Pt/SiO_2+ γ-Al_2O_3 physical mixtures. Gaseous methylcyclohexadiene intermediates may also form from desorption of their Pt-bound counterparts (at concentrations below the limits of detection due to their low thermodynamic stability) and react in advantageous reaction at proximate γ-Al_2O_3 surfaces. Such toluene-derived gaseous intermediates unlock additional mechanistic avenues for bifunctional metal-metal oxide mixtures, explored in detail in **Chapter 3**.

Rates of toluene hydrogenation reactions are reported for physical Pt/SiO_2+γ-Al_2O_3 mixtures where the two components are geometrically segregated into distinct domains (**Chapter 3**). Such segregation requires that intermediates generated at the Pt function must diffuse across distances on the order of 10-100 μm to reach sites at the γ-Al_2O_3 function to carry out a catalytic turnover. The data reported in this study demonstrate that rates decrease as the domain size of the two components increase (along with the intermediates' diffusion path), a strong indication that bifunctional routes mediated by gaseous intermediates are of catalytic importance [17].

Surfaces of γ-Al_2O_3 catalyze reactions including alcohol dehydration, skeletal isomerization of alkenes, and H_2-D_2 exchange [13]. Recent studies have also reported that γ-Al_2O_3 surfaces can heterolytically cleave H-H and C-H bonds [12]. Reactions of cyclohexenes and

cyclohexadienes with H_2 are investigated on Pt-free γ-Al_2O_3 surfaces to elucidate reaction pathways that partially hydrogenated toluene-derived intermediates undergo that may be of catalytic importance for bifunctional Pt/SiO_2+γ-Al_2O_3 catalytic mixtures (**Chapter 3**). Appreciable hydrogenation rates of these unsaturated molecules via reaction with H_2 are reported (but not for toluene hydrogenation); while these rates are relatively slow compared to metal-catalyzed rates for alkene hydrogenation reactions at similar conditions, they become significant at the temperatures in which toluene hydrogenation (a slower reaction than alkene and alkadiene hydrogenations) are carried out (**Chapter 3**).

Considering these demonstrations of γ-Al_2O_3-catalyzed C=C bonds hydrogenations, two novel bifunctional reaction schemes are proposed to account for the methylcyclohexane formation rate enhancements conferred by γ-Al_2O_3 in Pt/SiO_2+γ-Al_2O_3 physical mixtures. One route involves the formation of partially hydrogenated toluene-derived surface intermediates (TH_n*) at the Pt surface from reactions between toluene and H_2. These TH_n* species desorb to form their gaseous counterparts that can diffuse to and hydrogenate at nearby γ-Al_2O_3 surfaces, without requiring Pt-γ-Al_2O_3 atomic contact, thus providing an additive TH_n(g) hydrogenation route that bypassing rate-limiting steps at the Pt surfaces. Another route involves the formation of TH_n* species from toluene-H_2 reactants at Pt surfaces that react slowly in subsequent H-addition steps to form methylcyclohexane, but which form at significant coverages on crowded surfaces and inhibit the formation of other, more reactive toluene-derived intermediates. These stranded, less reactive TH_n* species can desorb to form their gaseous counterparts at low equilibrium concentrations which diffuse to and react at nearby γ-Al_2O_3 surfaces thus decreasing their concentrations in the fluid phase and their equilibrium surface coverages at the Pt. Such TH_n* scavenging increases the number of binding sites available for the competitive reactions of intermediates that mediate predominant toluene hydrogenation routes at Pt nanocluster surfaces, thus increasing methylcyclohexane formation turnover rates (**Chapter 3**).

Predicted kinetic trends in reactant pressures and catalyst domain sizes from mechanism-based reaction-transport models developed from these proposed mechanisms are compared with observed behaviors for Pt/SiO_2+γ-Al_2O_3 mixtures to investigate their catalytic importance (**Chapter 3**). Comparisons between kinetic and thermodynamic parameters derived from these modeling efforts and relevant experimental and theoretical benchmarks are drawn to assess their chemical significance and lend credence to the mechanistic conclusions from which they derive. Ultimately, the data and analysis reported in this dissertation provide a mechanistic picture consistent with experimental observations pertaining to γ-Al_2O_3-promoted Pt hydrogenation reactions with general insights that are likely relevant for metal-characterized reactions that occur under conditions with high metal coverages and mobile gaseous intermediates. These mechanistic considerations enable future catalytic design that leverages these bifunctional pathways mediated by molecular shuttles.

References

[1] S. Khoobiar, Particle to particle migration of hydrogen atoms on platinum-alumina catalysts from particle to neighboring particles, J. Phys. Chem. 68 (1964) 411–412.

[2] J.E. Benson, H.W. Kohn, M. Boudart, On the reduction of tungsten trioxide accelerated by platinum and water, 5 (1966) 307–313.

[3] R.B. Levy, M. Boudart, The kinetics and mechanism of spillover, J. Catal. 32 (1974) 304–314.

[4] G. Kyriakou, M.B. Boucher, A.D. Jewell, E.A. Lewis, T.J. Lawton, A.E. Baber, H.L. Tierney, M. Flytzani-Stephanopoulos, E.C.H. Sykes, Isolated Metal Atom Geometries as a Strategy for Selective Heterogeneous Hydrogenations, Science. 335 (2012) 1209–1212. https://doi.org/10.1126/science.1215864.
[5] K.D. Jung, A.T. Bell, Role of hydrogen spillover in methanol synthesis over Cu/ZrO_2, J. Catal. 193 (2000) 207–223. https://doi.org/10.1006/jcat.2000.2881.
[6] S. Cęckiewicz, B. Delmon, Cooperative action of $Pt/\gamma\text{-}Al_2O_3$ catalyst and $\gamma\text{-}Al_2O_3$ diluent in the hydrogenation of benzene, J. Catal. 108 (1987) 294–303. https://doi.org/10.1016/0021-9517(87)90179-5.
[7] J.H. Sinfelt, P.J. Lucchesi, Kinetic evidence for the migration of reactive intermediates in surface catalysis, J. Am. Chem. Soc. 85 (1963) 3365–3367. https://doi.org/10.1021/ja00904a012.
[8] M. Xiong, Z. Gao, Y. Qin, Spillover in heterogeneous catalysis: New insights and opportunities, ACS Catal. 11 (2021) 3159–3172. https://doi.org/10.1021/acscatal.0c05567.
[9] R. Prins, Hydrogen spillover. Facts and fiction, Chem. Rev. 112 (2012) 2714–2738. https://doi.org/10.1021/cr200346z.
[10] R. Prins, V.K. Palfi, M. Reiher, Hydrogen spillover to nonreducible supports, J. Phys. Chem. C. 116 (2012) 14274–14283. https://doi.org/10.1021/jp212274y.
[11] W. Karim, C. Spreafico, A. Kleibert, J. Gobrecht, J. Vandevondele, Y. Ekinci, J.A. Van Bokhoven, Catalyst support effects on hydrogen spillover, Nature. 541 (2017) 68–71. https://doi.org/10.1038/nature20782.
[12] R. Wischert, P. Laurent, C. Coperet, F. Delbecq, P. Sautet, γ-Alumina: The essential and unexpected role of water for the structure, stability, and reactivity of “defect” sites, J. Am. Chem. Soc. 134 (2012) 14430–14449. https://doi.org/10.1021/ja3042383.
[13] G. Busca, Structural, surface, and catalytic properties of aluminas, in: Adv. Catal., 1st ed., Elsevier Inc., 2014: pp. 319–404. https://doi.org/10.1016/B978-0-12-800127-1.00003-5.
[14] J.C. Schlatter, M. Boudart, Hydrogenation of ethylene on supported platinum, J. Catal. 24 (1972) 482–492. https://doi.org/10.1039/tf9625801761.
[15] M. Boudart, A.W. Aldag, M.A. Vannice, On the slow uptake of hydrogen by platinized carbon, J. Catal. 18 (1970) 46–51. https://doi.org/10.1016/0021-9517(70)90310-6.
[16] A.J. Robell, E. V Ballou, M. Boudart, Surface diffusion of hydrogen carbon, J. Phys. Chem. 68 (1964) 2748–2753.
[17] P.B. Weisz, Polyfunctional Heterogeneous Catalysis, in: Adv. Catal., 1962: pp. 137–190. https://doi.org/10.1016/S0360-0564(08)60287-4.
[18] S.D. Lin, M.A. Vannice, Hydrogenation of aromatic hydrocarbons over supported Pt catalysts: I. Benzene hydrogenation, J. Catal. 143 (1993) 539–553. https://doi.org/10.1006/jcat.1993.1297.
[19] A. Stanislaus, H.C. Barry, Aromatic hydrogenation catalysis: A review, Catal. Rev. Eng. 36 (1994) 75–123. https://doi.org/10.1080/01614949408013921.
[20] G.C. Bond, Metal-catalysed reactions of hydrocarbons, Springer, 2005. https://doi.org/10.1016/s1351-4180(06)71746-9.
[21] H. Ihm, H.M. Ajo, J.M. Gottfried, P. Bera, C.T. Campbell, Calorimetric measurement of the heat of adsorption of benzene on Pt(111), J. Phys. Chem. B. 108 (2004) 14627–14633. https://doi.org/10.1021/jp040159o.
[22] M. Yang, K.C. Chou, G.A. Somorjai, The structures and reactions of linear and cyclic C6 hydrocarbons adsorbed on the Pt(111) crystal surface studied by sum frequency generation

vibrational spectroscopy: Pressure, temperature, and H_2 coadsorption effects, J. Phys. Chem. B. 108 (2004) 14766–14779. https://doi.org/10.1021/jp048238n.
[23] T. Bligaard, J.K. Nørskov, B.I. Lundqvist, Understanding heterogeneous catalysis from the Fundamentals, in: Handb. Surf. Sci., 2008: pp. 269–340.

CHAPTER TWO

Mechanistic Interpretations of Pt-catalyzed Toluene Hydrogenation: Unravelling the Effects of Saturation Coverages, Adsorption Site-ensemble Requirements, and the Emission of Reactive Gaseous Alkene Intermediates.

Abstract

Kinetics-based modeling and density functional theory (DFT) calculations are combined here to examine toluene hydrogenation on SiO_2-supported Pt nanoclusters. Methylcyclohexane (MA) forms as the complete hydrogenation product while methylcyclohexene (ME) isomers form as partially hydrogenated intermediates; the kinetic trends of gaseous ME pressures are leveraged in order to separate toluene hydrogenation into two half reactions, thereby reducing the mechanistic complexity to an extent where identification of the kinetically-relevant steps and most abundant surface intermediate (MASI) becomes tenable. At high temperatures (493-533 K), pressures of ME intermediates approach gas-phase equilibrium values for their formation from toluene and two H_2, which indicates that MA formation turnover rates are limited predominantly by H_2 addition to ME (493-533 K). The exothermic nature of gas-phase ME formation from toluene and two H_2 results in decreasing ME pressures as temperature increases. ME pressures and MA formation rate dependences on H_2 and toluene pressures (493-533 K) reflect MA formation rates that are limited, in large part, by the addition of bound H atoms to co-adsorbed methylcyclohexyl intermediates (TH_5*). DFT-derived estimates of the Gibbs free energy to form molecularly bound toluene from toluene(g) on Pt(111) are more negative than the DFT-derived free energies to form other toluene-derived surface species from stoichiometric amounts of gaseous toluene and H_2, indicating that toluene is the MASI during toluene-H_2 reactions (493-533 K). Kinetics-based mechanistic models formulated using multisite, multicomponent adsorption isotherms to describe the site occupancies of the various intermediates on the Pt surface reveal that the transition states for H-addition to prevalent TH_5* intermediates (6CH TS) occupy a two-fold smaller ensemble of adjacent Pt sites than bound toluene. The consequences of these site ensemble differences for measured activation enthalpies and entropies from kinetic models are elucidated. At low temperatures (333-393 K), prevalent ME pressures reflect the balance between their rates of formation from toluene-H_2 reactants and consumption by reactions with H_2 at pseudo-steady state. Measured ME pressure and MA formation rate dependences on H_2 and toluene pressures at 333-393 K, combined with DFT-derived free energies of surface species reveals that MA formation is limited by reactions between surface-bound mono-hydrogenated toluene moieties (TH_1*) and co-adsorbed H atoms on a toluene-saturated surface. MA formation turnover rates at these low temperatures increase exponentially with temperature, reflecting a positive enthalpy difference between the transition state that mediates H addition to TH_1* and the reactant state consisting of bound toluene and H_2(g). These findings elucidate the mechanistic origins of negative rate dependences on temperature and shifting rate dependences on reactant pressures, ubiquitous among monoarene hydrogenation reactions on metal surfaces. These findings are relevant to other hydrocarbon conversion processes characterized by high coverages and involving reactants and intermediates with different sizes and binding orientations.

2.1. Introduction

Monoarene hydrogenation is used to decrease the aromatic content in fuels [1] and is also an important step in bio-oil [2] and petroleum hydroprocessing [1]. Hydrogenating monoarene molecules to their saturated cycloalkane products is also a promising strategy for storing H_2 molecules as a liquid in the form of C-H bonds that can be released in a subsequent dehydrogenation process [3]. Arene hydrogenation is typically carried out via surface catalysis on supported transition metal nanoclusters [1] because aromatic rings interaction strongly with their surfaces and they easily dissociate H_2 into reactive H adatoms. Monoarenes, such as benzene and toluene, are hydrogenated by six successive H-addition steps forming partially hydrogenated surface intermediates with a range of H content in the process [1,4,5]. The kinetically-relevant steps among these sequential H additions and the most abundant surface intermediates (MASI) remain controversial because several competing mechanistic interpretations are able to account for reactivity trends [1,5].

Arene hydrogenation occurs on hydrocarbon-covered surfaces because arenes and their partially hydrogenated products form strong covalent bonds with metal surface atoms [5–9]. Benzene hydrogenation on Pt nanoclusters [1] occurs at rates that are independent of benzene pressure, consistent with saturation coverages of benzene-derived intermediates [4,10]. Dehydrogenated benzene derivatives [4,10], benzene [8], and mixtures of partially hydrogenated benzene-derived species with different H content [11] have all been proposed as MASI. Sum frequency generation (SFG) vibrational spectroscopy on Pt(111) revealed that surfaces became saturated with molecularly bound forms of benzene and H adatoms at typical hydrogenation conditions (1-2 kPa benzene, 2-20 kPa H_2, 310-440 K) instead of hydrogenated or dehydrogenated benzene-derived surface species [12]. The number of bound species at saturation coverage, from microcalorimetry on Pt(111), was greater for cyclohexene (0.24 monolayer, denoted ML, and defined as the number of adsorbed molecules per exposed Pt-atom; 300 K) [13] than for benzene (0.15 ML, 100 K) [14], consistent with a larger ensemble of adjacent Pt sites required to bind benzene than partially hydrogenated benzene derivatives. SFG vibrational spectroscopic studies showed that benzene [15–17], 1,3-cyclohexadiene, and 1,4-cyclohexadiene [18] bind on Pt (111) with the ring aligned parallel to the surface, while molecularly-bound cyclohexene binds perpendicular to the surface by forming two σ-bonds between two of its C atoms and the Pt surface [15,19]. Mechanisms for arene hydrogenation typically assume, however, that all intermediates bind to same sized site ensembles [4,11,20], despite of the differences between binding orientations of benzene and its partially hydrogenated counterparts evident from surface science studies.

Gaseous cyclohexene forms as an intermediate at low concentrations during benzene-H_2 reactions on Pt surfaces [11,20–22] because of its rapid sequential hydrogenation to cyclohexane. Bound cycloalkenes are reactive intermediates in kinetically-relevant steps for monoarene hydrogenation because aromatic rings are hydrogenated more rapidly through sequences of elementary steps where H atoms are added to unsaturated C atoms at positions vicinal to C atoms saturated in previous steps [23,24]. Comparing pressures of gaseous cyclohexene intermediates generated during monoarene-H_2 reactions to their equilibrium values reveals whether the first four H additions to the arene are irreversible and limit overall arene conversion rates or are quasi-equilibrated and rates become limited by the two H additions to the cyclohexene intermediate.

In this work, toluene reactants, that show similar reactivity trends as benzene [1,4,10,25], are used to assess the identity and kinetic relevance of elementary steps, the abundance and type of bound intermediates involved, and the size of the Pt ensembles required to bind them (0.3-3 kPa toluene, 20-80 kPa H_2, 333-533 K). The gas-phase approach to equilibrium for 1-methylcyclohexene (1ME) and 4-methylcyclohexene (4ME) formation from toluene and two H_2 shows that methylcyclohexene (ME) intermediates form irreversibly at low temperatures (333-453 K) but at near-equilibrium pressures at higher temperatures (493-533 K). These trends provide evidence for a shift in the kinetically-relevant steps for MA formation from one or more of the first four H additions to the final two H additions as the temperature increases. The dependences of prevalent ME pressures and MA formation turnover rates on H_2 and toluene pressures at the low temperatures (333-393 K) reveal that MA formation is limited by the addition of H atoms to mono-hydrogenated toluene (TH_1*) intermediates. At higher temperatures (493-533 K), on the other hand, the dependences of prevalent ME pressures and MA formation turnover rates on H_2 and toluene pressures reveal that MA formation is limited predominantly by H addition to bound methylcyclohexyl (TH_5*) intermediates. Moreover, the exothermic nature of gas phase ME formation from toluene and two H_2 results in decreasing ME pressures as temperature increases. Such a decrease in ME pressure manifests in decreases in the MA formation turnover rates with temperature (493-533 K). Density functional theory (DFT)-derived electronic energies combined with statistical thermodynamic formalisms are used to calculate the coverages of toluene-derived intermediates and to show the prevalence of molecularly-bound toluene as the MASI. Differences between the number of adjacent Pt sites that bind the toluene MASI and the kinetically-relevant transition states for MA formation are elucidated from the MA formation turnover rates and prevalent ME pressures dependences on toluene pressure using a kinetics-based mechanistic model derived using a multisite adsorption isotherm to describe site occupancy [26]. At low temperatures, the kinetically-relevant step consisting of H addition to TH_1* is mediated by a transition state that occupies an ensemble of vicinal Pt sites that is similar in size to that which bound toluene occupies. At high temperatures, on the other hand, the kinetically-relevant step that involving H addition to TH_5* is mediated by a transition state that occupies a two-fold smaller ensemble of vicinal Pt sites than that which bound toluene occupies. The consequences of such site requirements for the chemical interpretations of kinetic and thermodynamic parameters derived from kinetics-based modeling are explored. The combined theoretical and experimental evidence provide a mechanistic picture that is consistent with the shift from positive to negative MA formation turnover rate dependence on temperature (ubiquitous for metal-catalyzed monoarene hydrogenation reactions [5,27]), the changes to MA formation turnover rate dependences on toluene and H_2 pressures with temperature, and the differences between the numbers of site occupied by toluene and its partially hydrogenated derivatives.

2.2. Methods and materials

2.2.1. Catalyst synthesis and characterization.

Pt nanoclusters dispersed on SiO_2 (Pt/SiO_2) were prepared using electrostatic adsorption methods. SiO_2 (Cabot Cab-o-sil HS-5; washed with deionized (DI) H_2O (resistivity ≥ 17.6 ohm-cm), treated in ambient air at 373 K for 12 h, and treated in ambient air at 873 K (0.017 K s^{-1}) for 4 h) was added to a solution of $Pt(NH_3)_4(NO_3)_2$ (Sigma-Aldrich, 99.995%) and DI H_2O (4 cm^3 g^{-1} SiO_2) and then stirred magnetically for 4 h at ambient temperature. NH_4OH (Sigma-Aldrich, 28% NH_3 in H_2O, 99.99%) was added to the SiO_2, DI H_2O, and $Pt(NH_3)_4(NO_3)_2$ mixture in order to

maintain 7-8 pH. The solids were collected by filtration and rinsed with DI H_2O, then treated in (i) flowing dry air (Praxair, ultra-zero purity) at 1.7 $cm^3\ g^{-1}\ s^{-1}$ by increasing the temperature from ambient to 873 K at 0.017 $K\ s^{-1}$ and holding for 3 h, (ii) flowing He (Praxair, 99.999%) at 1.7 $cm^3\ g^{-1}\ s^{-1}$ by decreasing the temperature to 373 K at 0.083 $K\ s^{-1}$, (iii) flowing H_2 (Praxair, 99.999%) at 1.7 $cm^3\ g^{-1}\ s^{-1}$ by increasing the temperature from 373 to 773 K at 0.017 $K\ s^{-1}$ and holding for 2 h then decreasing the temperature at 0.083 $K\ s^{-1}$ to below 373 K, and (iv) flowing 2% O_2 with He bal. (Praxair) at 1.7 $cm^3\ g^{-1}\ s^{-1}$ for at least 1 h. The Pt content was determined by inductively-coupled plasma–atomic emission spectroscopy (ICP-AES; Galbraith Laboratories). Pt dispersions ($D = \frac{N_s}{N_T}$, where N_s is the total number of surface metal atoms and N_T is the total number of metal atoms) were measured by H_2 chemisorption uptakes as described in **Section 2.8.1**. The Pt content, dispersion, and treatment temperatures are reported in **Table 2.1**.

2.2.2. Catalytic rate measurements.

Products formed during toluene-H_2 reactions were measured on Pt/SiO_2 samples (0.005-0.01 g) using a fritted U-shaped quartz tube reactor (1.3 cm internal diameter). Catalyst powders were pressed into wafers then crushed and sieved to retain the target aggregate sizes (180-250 μm, Gilson sieves). These aggregates were mixed with quartz granules (Sigma-Aldrich, 180-250 μm; treated in ambient air at 973 K) to maintain a bed height of 3 cm. Hydrogenation rates were unaffected by changes in volumetric heat release rates (varied by changing the Pt/SiO_2 loading), thus confirming the absence of reaction-induced bed temperature gradients. The reactor was electrically heated (National Electric furnace), and the temperature was maintained constant with a Watlow controller. The bed temperature was measured by a thermocouple placed in a dimple at the center of the bed. Catalysts were treated in (i) flowing 10% O_2/He (Praxair) at 100-200 cm^3 g $Pt/SiO_2^{-1}\ s^{-1}$ by increasing the temperature from ambient to 573 K at 0.033 $K\ s^{-1}$ and holding for 1 h, (ii) flowing He (Praxair, 99.999%) at 100-200 cm^3 g $Pt/SiO_2^{-1}\ s^{-1}$ by holding at 573 K for 0.25 h, and (iii) flowing H_2 (Praxair, 99.999%) at 100-200 cm^3 g $Pt/SiO_2^{-1}\ s^{-1}$ by holding at 573 K for 1 h before decreasing the temperature to the reaction temperature in flowing H_2. The O_2/He, He, and H_2 were purified by passing over moisture traps (Agilent BMT). Inlet molar rates were set using electronic Parker mass flow controllers. Liquid toluene (Sigma-Aldrich, 99.9%) was injected into flowing H_2 and He mixtures (100-200 cm^3 g $Pt/SiO_2^{-1}\ s^{-1}$) upstream of the reactor using a Parker Hamilton syringe pump. The effluent stream was analyzed online using gas chromatography (GC; Agilent 6890A) with flame ionization detection (FID) after separation using a capillary column (HP-1). Methylcyclohexane, 1-methylcyclohexene and 4-methylcyclohexene products were identified in the chromatographs by comparing their retention times to those of chemical standards. Process lines between the liquid injection port and the inlet of the GC instrument were held at 373-473 K to prevent reactant and product condensation; these heated lines contributed negligibly to measured rates.

MA formation turnover rates (mole methylcyclohexane g-atom surface Pt $(Pt_s)^{-1}\ s^{-1}$) were measured as functions of toluene pressure (0.3-2.1 kPa), hydrogen pressure (10-80 kPa), and temperature (333-533 K) by varying toluene and H_2 pressures at a constant temperature. MA formation turnover rate data were collected for each toluene pressure, H_2 pressure, and temperature for a duration of 1.5-2 ks. MA formation turnover rates were measured at 1.4 kPa toluene and 80 kPa H_2 every 5-8 ks; these MA formation turnover rates followed a first-order trend at 333-453 K given by:

$$r(t) = r_0 e^{-k_d t} \quad (2.1)$$

where $r(t)$ is the MA formation turnover rate at time t, r_0 is the MA formation turnover rate at zero time on stream, and k_d is the deactivation rate constant. Values of k_d at each temperature were determined by regressing the time-dependent MA formation turnover rate at 1.4 kPa toluene and 80 kPa H_2 to the functional form of **equation 2.1**. These k_d values were then used to calculate r_0 values from measured $r(t)$ for other toluene and H_2 pressures. Measured k_d values were smaller than 0.01 ks^{-1} in all experiments; these values correspond to mean-lives longer than 100 ks, making such corrections relatively minor. MA formation turnover rates at 493-533 K decreased asymptotically towards a value below one-half of the value after initial contact (following the pretreatment) during the first 50 ks, then stabilized with negligible k_d values. The extrapolated MA formation turnover rates at zero time on stream at 333-453 K and the stable values following the initial deactivation period at 493-533 K are reported.

2.2.3. Computational methods.

Density functional theory (DFT) calculations were used to assess the energies for bound toluene and its partially hydrogenated and dehydrogenated derivatives on model Pt(111) surfaces using periodic plane-wave DFT methods implemented in Vienne Ab-Initio Simulation Package (VASP) [28–31]. The projector augmented-wave (PAW) potentials [32,33] with a cutoff energy of 396 eV were used to generate the plane waves. The optPBE-vdW [34,35] version of the vdW-DF [36] functional was used as implemented in VASP to calculate the exchange correlation energy [37]; this functional was used because of its accurate calculation of adsorption energies for unsaturated hydrocarbons on Pt(111) surfaces [38]. An optimization of bulk Pt gave a lattice constant of 3.986 Å which was used to construct slabs with a 3x3 unit cell exposing the Pt(111) surface with four layers of Pt present in the z-coordinate and with a 10 Å vacuum space above and below the Pt atoms. The bottom two layers were kept at their bulk coordinates and the top two layers were relaxed to their energy minima during all geometry optimization calculations. Forces on the unconstrained atoms were <0.05 eV $Å^{-1}$ in all relaxed structures. The wavefunctions were converged to $<10^{-6}$ eV using an 8x8x1 gamma-centered k-point mesh to sample the Brillouin zone. Binding sites for hydrocarbons included atop, two-fold bridge, three-fold hcp hollow, and four-fold bridge (shown in **Scheme 2.S1**). Atomic coordinates of optimized geometries are reported in **Appendix A.1** (adsorbates) and **Appendix A.3** (gaseous molecules).

Zero-point energies (ZPE), enthalpies (*H*), entropies (*S*), and Gibbs free energies (*G*) to form toluene-derived surface intermediates on Pt surfaces were calculated from DFT-derived electronic energies and vibrational frequencies using standard statistical thermodynamics methods [39]. Reaction free energies to form toluene-derived surface intermediates with *n* H atoms added or removed ($\Delta G_{A*,tol}$) were determined from the free energy difference between the bound species (G_{A*}) and their precursors, toluene(g) (G_{tol}), *n*/2 H_2(g) (G_{H_2}), and the bare Pt slab (G_*):

$$\Delta G_{A*,tol} = G_{A*} - G_{tol} - \frac{n}{2} G_{H_2} - G_*. \quad (2.2)$$

Reaction free energies to form surface intermediates from a given methylcyclohexene isomer (*i*ME, where *i* denotes the position of the C atom with the methyl substituent) with *n* H atoms added or removed ($\Delta G_{A*,iME}$) were determined from the free energy difference between the bound species (G_{A*}) and their precursors, *i*ME(g) (G_{iME}), *n*/2 H_2(g) (G_{H_2}), and the bare Pt slab (G_*):

$$\Delta G_{A*,iME} = G_{A*} - G_{iME} - \frac{n}{2} G_{H_2} - G_*. \quad (2.3)$$

The free energy of a surface bound or gaseous species at a given temperature (T) is given from its enthalpy and entropy:

$$G = H - TS \quad (2.4)$$

The enthalpy was calculated from the electronic energy at 0 K (E), ZPE, and the translational, rotational, and vibrational enthalpies (H_{trans}, H_{rot}, and H_{vib}, respectively):

$$H = E_0 + ZPE + H_{trans} + H_{rot} + H_{vib} \quad (2.5)$$

The entropy was described by the sum of the translational, rotational, and vibrational entropies (S_{trans}, S_{rot}, and S_{vib}, respectively):

$$S = S_{trans} + S_{rot} + S_{vib} \quad (2.6)$$

Vibrational frequencies were used to calculate the ZPE, H_{vib}, and S_{vib} with the harmonic oscillator approximation (**Section 2.8.3**). Vibrational frequencies for optimized gaseous and adsorbed molecular structures (fixing the Pt atoms to their optimized coordinates) were calculated by diagonalizing the Hessian matrix, which was determined using a 0.015 Å displacement. The wavefunction was converged to $<10^{-4}$ eV and a 4x4x1 gamma-centered k-point mesh grid was used to sample the Brillouin zone. Translational enthalpies, rotational enthalpies, and entropies were calculated using standard statistical thermodynamics methods [39] as reported in **Section 2.8.3**. The calculated vibrational frequencies are reported in **Appendix A.2** (adsorbates) and **Appendix A.4** (gaseous molecules).

2.3. Results and discussion

2.3.1. The effects of temperature, hydrogen pressure, and toluene pressure on methylcyclohexane formation turnover rates and pressures of prevalent methylcyclohexene intermediates.

Figure 2.1 shows methylcyclohexane (MA) formation turnover rates (moles MA g-atoms surface Pt $(Pt_s)^{-1}$ s^{-1}) from toluene-H_2 reactants as a function of temperature on SiO_2-supported Pt nanoclusters (denoted Pt/SiO_2) with a mean nanocluster diameter of 3.6 nm (1.4 kPa toluene, 20-80 kPa H_2, 333-533 K). These MA formation turnover rates increased exponentially with temperature at low temperatures (333-393 K), reached a maximum value between 413-453 K, then decreased exponentially at higher temperatures (493-533 K). **Figure 2.2** shows MA formation turnover rates as a function of toluene and H_2 pressure (0.35-2.1 kPa toluene, 20-80 kPa H_2, 333-533 K). MA formation turnover rates followed a dependence on H_2 pressure between one-half and first order at low temperatures and became increasingly more sensitive to H_2 pressure as the temperature increased, ultimately exceeding a second-order trend at 493-533 K. Rates were insensitive to toluene pressure at low temperatures and then increased with increasing toluene pressure at higher temperatures (493-533 K).

MA formation from toluene-H_2 reactants consists of a sequence of six H-addition steps to saturate the aromatic ring, any of which may be kinetically relevant. The most abundant surface intermediates (MASI) must be discerned among the pool of toluene-derived surface species that form from toluene-H_2 reactants with differing H-content and points of C attachments to the surface. Such mechanistic complexities impose difficulties in understanding the temperature and reactant

pressure trends. Methylcyclohexene (ME) isomers form from toluene-H_2 reactants at pressures that reflect the ratio between the rate that the first four H atoms are added to toluene and the rate that the final two H atoms are added to the methylcyclohexene isomers to form MA. These ME isomers and their surface counterparts are kinetically-relevant intermediates during toluene hydrogenation because aromatic rings are hydrogenated more rapidly through sequences of elementary steps in which H atoms are added to unsaturated C atoms at positions vicinal to C atoms saturated in previous steps [23,24]. Investigating their trends with toluene and H_2 pressures allows MA formation rates to be separated into two half reactions thereby reducing the mechanistic complexity to the extent that kinetically-relevant steps and most abundant surface intermediate (MASI) can be identified.

Figure 2.3 shows 1ME and 4ME pressures as functions of toluene conversion at several temperatures (1.4 kPa toluene, 80 kPa H_2, 333-533 K). 3-Methylcyclohexene could not be separated from toluene with the chromatographic methods used (**Section 2.2.2**). These 1ME and 4ME pressures were insensitive to toluene conversion at all conditions. The approach to equilibrium for the formation of each ME isomer (*i*ME, where *i* denotes the position of the C atom with the methyl substituent) from toluene and two H_2 ($\eta_{iME,tol}$) and their consumption via reaction with H_2 to form MA ($\eta_{MA,iME}$), are:

$$\eta_{iME,tol} = \frac{[iME]}{[tol][H_2]^2} K_{iME,tol}^{-1} \tag{2.7}$$

and

$$\eta_{MA,iME} = \frac{[MA]}{[iME][H_2]} K_{MA,iME}^{-1} \tag{2.8}$$

where $[tol]$, $[iME]$, $[MA]$, and $[H_2]$ are the toluene, *i*ME, MA, and H_2 pressures, respectively, in bar; and $K_{iME,tol}$ and $K_{MA,iME}$ are the equilibrium constants for the *i*ME and MA formation reactions, respectively. **Figure 2.4** shows the temperature-dependent $\eta_{iME,tol}$ and $\eta_{MA,iME}$ values (1.4 kPa toluene, 80 kPa H_2, 393-533 K). The $\eta_{1ME,tol}$ and $\eta_{4ME,tol}$ values were of order 10^{-3} at 393 K, indicating that 1ME and 4ME were formed irreversibly from toluene-H_2 reactants. These values increase monotonically with temperature, eventually approaching values near unity at higher temperatures (493-533 K), consistent with their quasi-equilibrated formation from toluene-H_2 reactants. Their quasi-equilibrated formation at high temperatures accounts for the toluene-conversion insensitive $[iME]$ values (**Figure 2.3**) because $[iME]$ values are proportional to the toluene pressure at equilibrium, which does not change significantly at the differential conversions for which rate measurements were carried out. The $\eta_{MA,1ME}$ and $\eta_{MA,4ME}$ values also increased monotonically with temperature but remained below 10^{-2} at all temperatures, indicating that MA was formed irreversibly from ME-H_2 reactants.

The net formation turnover rate (r_{iME}) for each ME isomer (*i*ME) is given from difference between the rate that it is formed from toluene-H_2 reactants and consumed by reaction with H_2:

$$r_{iME} = \alpha_{tol \rightarrow iME}[tol] - \alpha_{iME \rightarrow MA}[iME] \tag{2.9}$$

where $\alpha_{tol \rightarrow iME}$ is the pseudo-first-order rate constant for *i*ME formation from toluene-H_2 reactants and $\alpha_{iME \rightarrow MA}$ is the pseudo-first-order rate constant for the *i*ME-H_2 reaction. The pseudo-steady state *i*ME pressure ($[iME]_{PSS}$) reflects the pressure at which the net *i*ME formation rate is

zero ($r_{iME} = 0$), corresponding to equality between the *i*ME formation and consumption rates ($\alpha_{tol \rightarrow iME}[tol] = \alpha_{iME \rightarrow MA}[iME]$). The *i*ME pressure can be expressed as a function of the fractional toluene conversion (X_{tol}; with corresponding derivation provided in **Section 2.8.4**):

$$[iME] = [iME]_{PSS} - [iME]_{PSS} \exp\left(\frac{\alpha_{iME \rightarrow MA}\, ln(1 - X_{tol})}{\sum_{j=1,3,4}\left(\alpha_{tol \rightarrow jME}\right)}\right) \quad (2.10)$$

1ME and 4ME pressures described by **equation 2.10** are consistent with the toluene-insensitivity of observed 1ME and 4ME pressures when the second term in **equation 2.10** is negligible and their values equal those at pseudo-steady state ($[iME] = [iME]_{PSS}$). Such toluene-conversion insensitive rates arise when the exponential term in **equation 2.10** becomes small, which indicates that the rate constant for *i*ME hydrogenation ($\alpha_{iME \rightarrow MA}$; in the numerator of the exponential (**eq 2.10**)) is much larger than the sum of the *i*ME formation rate constants (the summation term in the denominator of the exponential (**eq 2.10**)). The irreversible formation of 1ME and 4ME species at pressures that are insensitive to toluene conversion at low temperatures (393 K) is thus consistent with their formation at pseudo-steady state.

Figure 2.5 shows 1ME and 4ME pressures as functions of toluene and H_2 pressure (0.3-2 kPa toluene, 20-80 kPa H_2, 333-533 K). These 1ME and 4ME pressures were insensitive to H_2 pressure at 393-413 K and approached a second-order trend at 493-533 K. 1ME and 4ME pressures showed a sublinear dependence on toluene at 393 K and approached a linear dependence at 493-533 K. The second-order and first-order dependence of 1ME and 4ME pressure on H_2 and toluene pressure, respectively, follow the expected trends for an equilibrated mixture (as evident from **equation 2.7** with $\eta_{iME,tol}$=1), consistent with the $\eta_{1ME,tol}$ and $\eta_{4ME,tol}$ values that were near unity at 493-533 K (**Figure 2.4**). 1ME and 4ME pressures showed a nearly zero-order dependence on H_2 pressure and sublinear dependence on toluene pressure at 393 K, in contrast; such significant deviation from the trends expected for an equilibrated mixture provides additional evidence for their irreversible formation at pseudo-steady state rather than equilibrium. Kinetic trends for these ME pressures, taken together with measured MA formation turnover rates, are used next to assess which kinetically-relevant steps dictate MA formation and which species constitute the MASI for Pt-catalyzed toluene hydrogenation reactions.

2.3.2. Elementary steps for toluene and methylcyclohexene hydrogenation and their consequences for prevalent methylcyclohexene pressures.

Scheme 2.1 shows a sequence of elementary steps that account for measured MA formation turnover rates, and which are analogous to steps for alkene and other monoarene hydrogenation reactions on transition metal surfaces [1,40,41]. Two distinct sites are used to bind hydrocarbons (*) and H atoms (*S*) based on the precedent established for reactions on surfaces with high hydrocarbon coverages (i.e., alkane hydrogenolysis [42], alkene hydrogenation [43,44], and monoarene hydrogenation [25,45]). The *S*-sites correspond to interstices among the hydrocarbon adlayer that are sufficiently large in size to bind relatively small H atoms but not hydrocarbon molecules. Partial toluene hydrogenation forms cyclic hydrocarbon surface intermediates that differ in their numbers of C atoms that form σ- or π-bonds with surface Pt-atoms ([19,46]). Calorimetric studies on Pt(111) have revealed that fewer benzene molecules bind at saturation coverage (0.15 ML, 300 K [14]) than does cyclohexene (0.24 ML, 100 K [13]); these

studies indicate that toluene and its partially hydrogenated counterparts differ in the number of adjacent *-sites that bind them.

The relationship between reactant pressures and coverages of toluene-derived surface intermediates, which bind to different numbers of adjacent *-sites depending on their number of C contacts to the surface, are described in subsequent mechanistic models using a multisite, multicomponent adsorption isotherm (adapted from the work of Nitta et al. [26] and explained in detail in **Section 2.8.5**). The mechanistic conclusions reached later in **Sections 2.3.4** and **2.3.5** reveal that toluene-H_2 reactions occur on Pt surfaces that are saturated with toluene at the conditions of this study (20-80 kPa H_2, 0.3-2 kPa toluene, 333-533 K); as a result, coverage dependent changes to the potential energy for interactions between a toluene-derived adsorbate (*A*) and the surface due to changes to the electron density of the metal [47] need not be accounted for. In addition, *A* species bind amidst a saturated toluene monolayer; as a result, only the pair-wise interactions between species A_i and neighboring toluene adsorbates are significant and energetic contributions from A_i-A_j are negligible. The multisite, multicomponent isotherm for the adsorption of species *A* on a toluene-saturated surface (derived in detail in **Section 2.8.5)** is thus given as:

$$\ln(\gamma_A K_{A*} p_A) = \ln \theta_{A*} - \gamma_A \ln(1 - \theta_{tol}^{sat}), \tag{2.11}$$

with

$$K_{A*} = \frac{j_{A*}}{j_{A(g)}} \frac{\Lambda}{kT} \exp\left(\frac{-\epsilon_{A*}^{sat} + \gamma_A \theta_{tol}^{sat} u_{A*}^{sat}}{kT}\right), \tag{2.12}$$

where γ_A is the number of adjacent *-sites that bind species *A*, p_A is the partial pressure of species *A*, θ_{A*} is the coverages of species *A* at *-sites, θ_{tol}^{sat} is the number of toluene molecules bound per exposed Pt site at saturation coverage, u_{A*}^{sat} is the potential energy for the interactions between adsorbate *A* and the saturated toluene monolayer, *k* is Boltzmann's constant, j_{A*} is the internal and vibrational partition function of the adsorbed molecule *A*, $j_{A(g)}$ is the internal and vibration partitional function of the gaseous molecule *A*, Λ is the deBroglie wavelength, and ϵ_{A*}^{sat} is the potential energy for *A* interactions with the Pt surface at *-sites. The functional form of **equation 2.11** resembles a multisite, multicomponent Langmuir isotherm because non-idealities arising from adsorbate-adsorbate interactions and ϵ_{A*}^{sat} values are constants at saturation coverages.

Scheme 2.1 shows elementary steps involving molecular toluene adsorption at γ_{tol} adjacent *-sites (T*; **Scheme 2.1, step 1**), H_2 dissociation to form H adatoms at vicinal *S*-sites (H-*S*) (**Scheme 2.1, step 2**), toluene hydrogenation via sequential H-addition steps to form partially hydrogenated toluene-derived bound intermediates with *n* added H atoms (TH_n*, where $1 \leq n \leq 5$) and $\gamma_{\Delta nCH}$ number of vicinal *-site vacancies (**Scheme 2.1, steps 3-7**), MA(g) formation via H addition to TH_5* (**Scheme 2.1, step 8**), and TH_4* desorption to form ME(g) (**Scheme 2.1, step 9**). D_2 and benzene react to form deuterobenzenes much faster than deuterocyclohexanes on Pt surfaces [48,49] suggesting that toluene binding and H_2 dissociation steps are quasi-equilibrated, thus leaving one or more of the H-addition steps (**Scheme 2.1, steps 3-8**) as the only plausible kinetically-relevant steps. Next, a kinetic model based on the elementary steps in **Scheme 2.1** is developed in an effort to identify the kinetically-relevant elementary steps and the nature and

coverage of prevalent MASI that best describe observed MA formation rate and ME pressure dependences on H_2 and toluene pressures.

Pseudo-steady state 1ME and 4ME pressures depended similarly on toluene and H_2 pressures (**Figure 2.5**) indicating that the methyl substitution of the C atoms forming the double bond did not affect the nature of the kinetically-relevant steps that governed *i*ME formation and consumption. Such similarity is consistent with the small difference between the free energies of formation between these isomers (8 kJ mol^{-1} at 393 K; from ΔH [50] and ΔS [51] of isomerization) compared to the DFT-derived activation barriers typical of H-addition steps that mediate aromatic ring hydrogenation, which are on the order of 60-80 kJ mol^{-1} [23]. The similar nature of the kinetically-relevant steps for the formation and consumption of the 1ME and 4ME suggests, more generally, that surface coverages of prevalent TH_n* intermediates that differ in the position of the C atom with the methyl substituent (*i*TH_n*, where *i* denotes the position of the C atom with the methyl substituent) vary with toluene and H_2 pressures in a manner that is independent of the location of the methyl group because they too are likely formed and consumed in elementary steps with similar kinetic relevance. The combined ME pressure, denoted [ME], and the combined coverages of *i*TH_n* with the same H-content, denoted $\theta_{TH_{n^*}}$, are defined as:

$$[ME] = \sum_{i=1,3,4} [iME] \tag{2.13}$$

and

$$\theta_{TH_{n^*}} = \sum_{i} \theta_{iTH_{n^*}}, \tag{2.14}$$

where $\theta_{iTH_{n^*}}$ is the *i*TH_n* coverage at *-sites.

Measured MA pressures were far from thermodynamic equilibrium with gaseous 1ME, 4ME, and H_2 at 393-533 K (**Figure 2.4**) indicating that ME species were hydrogenated irreversibly; therefore, at least one of the two H-addition steps required to form MA from ME and H_2 (**Scheme 2.1, steps 7-8**) were irreversible. The difference between the forward rate of H addition to an ensemble of TH_n* intermediates ($\vec{r}_{CH,n+1}$) and H abstraction from an ensemble of TH_{n+1}* intermediates ($\overleftarrow{r}_{CH,n+1}$) gives the net rate of TH_n* conversion ($r_{CH,n+1}$):

$$r_{CH,n+1} = \vec{r}_{CH,n+1} - \overleftarrow{r}_{CH,n+1} \tag{2.15}$$

The forward rate ($\vec{r}_{CH,n+1}$) is proportional to the coverage of TH_n* and H-*S* reactants and the reverse rate ($\overleftarrow{r}_{CH,n+1}$) is proportional to the coverage of TH_{n+1}* and vacant *S*-sites:

$$r_{CH,n+1} = k_{CH,n+1}\theta_{H,S}\theta_{TH_{n^*}} - k_{-CH,n+1}\theta_S\theta_{TH_{n+1^*}}\theta_*^{\Delta\gamma_{CH,n+1}} \tag{2.16}$$

where $k_{CH,n+1}$ is the forward rate constant for the reaction between TH_n* and H-*S* form TH_{n+1}*, θ_S is the coverage of vacant *S*-sites, $k_{-CH,n+1}$ is the rate constant for H abstraction from TH_{n+1}* to form TH_n* and H-*S*, θ_* is the coverage of vacant *-sites, and $\Delta\gamma_{CH,n+1}$ is the difference between the number of adjacent *-sites that are occupied by TH_{n+1}* and TH_n*. The functional form of **equation 2.16** is restated assuming that H_2 dissociation at *S*-sites is quasi-equilibrated ($\theta_{H,S} = K_{H,S}[H_2]^{\frac{1}{2}}\theta_S$):

$$r_{CH,n+1} = k_{CH,n+1}K_{H,S}[H_2]^{\frac{1}{2}}\theta_S\theta_{TH_{n^*}} - k_{-CH,n+1}\theta_S\theta_{TH_{n+1^*}}\theta_*^{\Delta\gamma_{CH,n+1}} \quad (2.17)$$

where $K_{H,S}$ is the equilibrium constant for one-half H_2 dissociation on one *S*-site. The ME hydrogenation rate (r_{ME}) is derived from the fifth (**Scheme 2.1, step 7**) and sixth (**Scheme 2.1, step 8**) H-addition rates given by **equation 2.17** (evaluated for *n*=4 and *n*=5, respectively), assuming that ME isomers bind to *-sites in quasi-equilibrium to form $\theta_{TH_{4^*}}$, $\theta_{TH_{5^*}}$ forms at pseudo-steady state, and TH_4* and TH_5* occupy similar ensembles of *-sites ($\gamma_{TH_4} = \gamma_{TH_5}$):

$$r_{ME} = \frac{k_{CH,6}K_{CH,5}K_{ME*}K_{H,S}^2[H_2]\theta_S\theta_*^{\gamma_{ME}}}{1 + \frac{k_{CH,6}}{k_{-CH,5}}K_{H,S}[H_2]^{\frac{1}{2}}}[ME] \quad (2.18)$$

where $K_{CH,5}$ is the equilibrium constant for the reaction between TH_5* and H-*S* ($K_{CH,5} = k_{CH,5}/k_{-CH,5}$; **Scheme 2.1, step 7**), γ_{ME} is the number of adjacent *-sites that are occupied by TH_4*, and K_{ME*} is the equilibrium constant for ME adsorption at ensembles of γ_{ME} vicinal *-sites (**Scheme 2.1, step 9**). The $k_{CH,6}$, $K_{CH,5}$, $k_{-CH,5}$, K_{ME}, and γ_{ME} terms represent averages associated with the values for *i*TH_5, *i*TH_4, or *i*ME isomers weighted by their relative abundances.

ME hydrogenation turnover rates described by **equation 2.18** depend on H_2 pressure arising from the combination of H_2-pressure dependent terms, *S*-site vacancy coverage, *-site vacancy coverage, and the ME pressure. The observed MA formation turnover rates (r_{MA}) must be equal to the ME hydrogenation turnover rates ($r_{ME} = r_{MA}$) during toluene-H_2 reactions to maintain steady-state, suggesting that the MA formation rate dependence on H_2 and toluene pressures can shed light on the contributions from each of the conflated terms in **equation 2.18**. Substituting r_{ME} with r_{MA} and dividing both sides of **equation 2.18** by [*i*ME] (to give the rate to *i*ME ratio, denoted ψ_{iME}) isolates the group of terms on the right-hand side of **equation 2.18** excluding [ME], which consists of kinetic and thermodynamic constants, H_2 pressures, and *S*- and *-site vacancy coverages:

$$\psi_{iME} = \frac{k_{CH,6}K_{CH,5}K_{ME*}K_{H,S}^2[H_2]\theta_S\theta_*^{\gamma_{ME}}}{\zeta_{iME}\left(1 + \frac{k_{CH,6}K_{H,S}[H_2]^{\frac{1}{2}}}{k_{CH,-5}}\right)}, \quad (2.19)$$

with

$$\psi_{iME} = \frac{r_{MA}}{[iME]}, \quad (2.20)$$

$$\zeta_{iME} = \frac{[iME]}{[ME]}, \quad (2.21)$$

where ζ_{iME} term denotes the fraction of *i*ME among ME isomers.

Figure 2.6 shows ψ_{1ME} and ψ_{4ME} values as a function of H_2 pressure (1.4 kPa toluene, 20-80 kPa H_2, 393-533 K). These measured ψ_{1ME} and ψ_{4ME} values showed between a one-half and first-order dependence on H_2 pressure at 393 K and approached a first-order dependence at 493-533 K. These observed H_2-pressure dependences reflect the $[H_2]$ term in the numerator combined

with the dependences of θ_S (numerator), $\theta_*^{\gamma_{ME}}$ (numerator), and the term enclosed in parentheses in the denominator of **equation 2.19**. The values of θ_S are determined from the balance law describing the conservation of occupied and unoccupied *S*-sites given by:

$$1 = \theta_S + K_{H,S}[H_2]^{\frac{1}{2}}\theta_S. \quad (2.22)$$

The θ_S values depend on H_2 pressure ranging from negative one-half order, corresponding to saturation coverages of *S*-sites with H adatoms, to zero order, corresponding to negligible coverage of *S*-sites with H adatoms. The θ_* values are determined from the balance law describing the conservation of occupied and unoccupied *-sites which, assuming an ensemble of toluene-derived surface species with an average number of *y* H atoms added or removed, is given:

$$1 = \theta_* + K_{MASI}[tol][H_2]^{\frac{y}{2}}\theta_*^{\gamma_{MASI}}. \quad (2.23)$$

where K_{MASI} represents the average equilibrium constant to form the prevalent MASI from toluene and *y*/2 H_2, and γ_{MASI} is the average number of adjacent *-sites that bind the prevalent MASI. These θ_* values vary with H_2 pressure resulting from the solution to the polynomial equation (**eq 2.23**) depending on the values of *y* and γ_{MASI}. At 393 K, the observed ψ_{1ME} and ψ_{4ME} values followed a dependence on H_2 pressure that was below first order, indicating that the first-order dependence on H_2 pressure in the numerator of **equation 2.19** is partially canceled by either a significant H_2 dependence of the term enclosed in the parentheses in the denominator, significant H-*S* coverages, or the presence of toluene-derived surface species at coverages that are positively correlated with H_2 pressures. The first-order ψ_{1ME} and ψ_{4ME} dependences on H_2 pressure observed at 493-533 K, on the other hand, indicate that the combined θ_S and $\theta_*^{\gamma_{ME}}$ dependences on H_2 pressure cancel with that of the term enclosed in the parentheses in **equation 2.19**. To distinguish further between these conflated factors that contribute to the observed H_2 dependences, the nature and coverage of the *-site MASI are examined using DFT and statistical thermodynamics to determine their contributions to observed kinetic trends.

2.3.3. Thermodynamics and relative coverages of bound intermediates during toluene hydrogenation on Pt.

Reactions of toluene-H_2 mixtures occur on Pt surfaces at high coverages of toluene-derived species because alkenes and arenes form strong covalent bonds with Pt surface atoms [5,6]. These species bind at the same *-sites that stabilize the transition states that mediate kinetically-relevant H-addition steps. Toluene derived species form with different H contents via incomplete hydrogenation or dehydrogenation of toluene co-reactants. H-rich species formed from toluene and H_2 via quasi-equilibrated steps are present at surface coverages that are proportional to H_2 pressure raised to the power of one-half the number of added H atoms. H-deficient species, in contrast, liberate stoichiometric amounts of H_2(g) from cleaved C-H bonds and form at coverages that are inversely proportional to H_2 pressure raised to the power of one-half the number of removed H atoms. The Gibbs free energies of formation (**eq 2.2**) of these bound species are determined from DFT-derived electronic energies and statistical thermodynamics methods to estimate their relative coverages (**Section 2.8.2**) and to determine the dependence of vacant *-site coverages on H_2 pressure and consequences for toluene conversion turnover rates and prevalent ME pressures.

Table 2.2 shows DFT-derived electronic energies at 0 K, enthalpies, entropies, and free energies for the formation of plausible MASI including T*, iTH$_n$* species, and methylenebenzene from stoichiometric amounts of toluene(g) and H_2(g) (as described by **equations 2.2-2.6**) at 1/9 ML coverage. These enthalpies and entropies were evaluated at 393 K unless specified otherwise. The optimized geometries of adsorbates are shown in **Scheme 2.2** and **Scheme 2.3**. iTH$_n$* for each n value denotes a mixture of surface species that differ in the positions of the C atoms with added H atoms relative to toluene. The iTH$_n$* species with $2 \leq n \leq 5$ examined here include those formed via a sequence of elementary steps where H atoms are added to C atoms at positions that are adjacent to C atoms saturated in previous steps, which follows the sequence of elementary steps expected to contribute predominantly to MA formation. The methyl group for iTH$_n$* species with $1 \leq n \leq 5$ is positioned at C atoms that reflect the species that form from the adsorption and reaction of 1-methyl-1,3-cyclohexadiene, 1-methylcyclohexene, and 4-methylcyclohexene. Bound 1-methyl-1,4-cyclohexadiene was also considered because reported energies for bound 1,4-cyclohexadiene formation from gaseous benzene(g) and H_2(g) are more negative than that of 1,3-cyclohexadiene on Pt(111) [38,46] thus rendering its high coverage plausible despite not being expected to react along predominant MA formation reaction pathways. The adsorbate binding sites reflect the methylated counterparts of the most stable structures that have been reported for benzene hydrogenation reactions on Pt(111) surfaces [38,46]. The molecular orientations for prevalent TH$_2$*, TH$_3$*, and TH$_5$* species reflect those proposed for their C6 counterparts from sum frequency generation vibrational spectroscopy [19]. **Figure 2.7** shows these enthalpies, entropies, and free energies for species with different numbers of H atoms added to or removed from toluene molecules.

Toluene was bound at bridge sites (toluene-bri) and three-fold hcp hollow sites (toluene-hcp) with calculated enthalpies of formation from toluene(g) of -134 and -86.4 kJ mol^{-1}, respectively. H addition to T* occurred endothermically to form 1-methyl-6-hydrobenzene-hcp and 2-methyl-6-hydrobenzene-bri with enthalpies of formation from toluene(g) and ½ H_2(g) of -96 and -121 kJ mol^{-1}, respectively. The second H-atom addition formed 1-methyl-5,6-dihydrobenzene-bri and 1-methyl-5,6-dihydrobenzene-hcp with enthalpies of formation from toluene(g) and H_2(g) of -93.1 and -146 kJ mol^{-1}, respectively. 1-Methyl-3,6-dihydrobenzene-bri, formed from T* via H addition at the 3 and 6 C positions, showed a more negative change in enthalpy from the same reactants (-184 kJ mol^{-1}, 393 K) than the 1-methyl-5,6-dihydrobenzene counterparts. Three H-atom additions to adjacent C atoms of T* formed 2-methyl-4,5,6-trihydrobenzene-hcp and 5-methyl-4,5,6-trihydrobenzene-hcp with enthalpies of formation from toluene(g) and 3/2 H_2(g) of -158 and -159 kJ mol^{-1}, respectively. The bound 1-methylcyclohexene and 4-methylcyclohexene molecules formed two C-Pt bonds at vicinal Pt atoms (denoted 1-methylcyclohexene-bri and 4-methylcyclohexene-bri, respectively) with enthalpies of formation from toluene and 2 H_2(g) of -156 and -160 kJ mol^{-1}, respectively. H addition to these methylcyclohexene intermediates formed 1-methylcyclohexyl and 4-methylcyclohexyl with a single C-Pt bond at the atop position (denoted 1-methylcyclohexyl-atop and 4-methylcyclohexyl-atop, respectively) with enthalpies of formation from toluene and 5/2 H_2(g) of -175 and -181 kJ mol^{-1}, respectively. The iTH$_3$*, iTH$_4$*, and iTH$_5$* species along with 1-methyl-3,6-dihydrobenzene-bri and 1-methyl-5,6-dihydrobenzene-hcp form from toluene(g) and H_2(g) and the bare Pt with more negative enthalpies than toluene-bri (the most stable adsorbed state of toluene); these values reflect a significant enthalpic driving force towards Pt surface coverage by partially hydrogenated toluene-derived species in favor of T*.

The enthalpic driving force that favors high coverages of partially hydrogenated toluene-derived species on Pt surfaces from the gaseous reactants is offset, for the most part, by an entropic penalty to form C-H bonds from stoichiometric amounts of H_2(g). The entropies to form bound species from stoichiometric amounts of toluene and H_2 reactants decreased linearly with the number of H atoms added with a slope of -73 J K^{-1} g-atom H^{-1} (**Figure 2.7**). The entropies of formation of gaseous methylcyclohexadiene isomers, ME isomers, and MA from H_2-toluene reactants [51] showed a similar linear decrease with the number of H atoms added with a slope of -66 J K^{-1} g-atom H^{-1} (**Figure 2.7**). The similar slopes indicate that a similar decrease in entropy occurs whether H_2(g) reacts with gaseous or bound hydrocarbon species. Such decreases in entropy resulting from H_2(g) consumption are accounted for by the loss of H_2(g) translational entropy (64 J K^{-1} g-atom H^{-1}, 393 K, **equation 2.S76**), by in large, because H_2(g) translational degrees of freedom are converted to lower entropy vibrational and rotational modes in the hydrocarbon moiety.

The free energies to form toluene-derived surface species from toluene(g), H_2(g) and the bare surface were determined from the corresponding changes in enthalpies and entropies (**eq 2.4**). Toluene-bri showed a free energy of formation of -57 and -38 kJ mol^{-1} at 393 K and 493 K, respectively. 1-Methyl-3,6-dihydrotoluene-bri showed a negative free energy of formation (-24 kJ mol^{-1}) that was 16 kJ mol^{-1} less negative than that of toluene-bri at 493 K and therefore unlikely to form at significant surface coverages. At 393 K, however, 1-methyl-3,6-dihydrotoluene-bri formed with a free energy of -56 kJ mol^{-1} that was comparable to that of toluene-bri; therefore, it would coexist at comparable coverages with toluene-bri at equilibrium. All other partially hydrogenated toluene-derived species had less negative (or even positive) free energies of formation and thus would not compete with toluene-bri.

The cleavage of a benzyl C-H bond from toluene-bri formed methylenebenzene-bri and ½ H_2(g) in an endothermic step with an entropy gain caused by the evolution of H_2(g). Methylenebenzene-bri and ½ H_2(g) formed from toluene(g) with an enthalpy of -69.3 kJ mol^{-1}, which is 65 kJ mol^{-1} less negative than the formation enthalpy for toluene-bri (-134 kJ mol^{-1}) from the same reactants. Methylenebenzene-bri and ½ H_2(g) formed from toluene(g) with an entropy change of -143 J mol^{-1} K^{-1}, which was 51 J mol^{-1} K^{-1} less negative than the entropy change to form toluene-bri from toluene(g) because of the translational entropy gained from the evolved ½ H_2(g). These enthalpies and entropies combined to give a free energy to form methylenebenzene-bri and ½ H_2(g) from toluene(g) that is less negative than that of toluene-bri (333-533 K), indicating a thermodynamic preference for high toluene-bri covered surfaces in favor of methylenebenzene-bri (at H_2 pressures above $1x10^{-13}$ and $1x10^{-6}$ kPa at 333 and 533 K, respectively).

2.3.4. Kinetically-relevant steps for toluene hydrogenation at low temperatures (333-393 K) and the chemical significance of the relevant kinetic and thermodynamic parameters for methylcyclohexane formation.

1ME and 4ME formed irreversibly from toluene and H_2 at 393 K which renders one or more of the first four H-addition steps to toluene (**Scheme 2.1, steps 3-6**) kinetically relevant and irreversible. MA formation turnover rates must therefore be equal to the forward rate of H addition to the first group of TH_n* intermediates that react irreversibly, denoted TH_x*, given by the first term in **equation 2.17**:

$$\vec{r}_{CH,x+1} = k_{CH,x+1} K_{H,S} [H_2]^{\frac{1}{2}} \theta_S \theta_{TH_{x^*}} \quad (2.24)$$

where $k_{CH,x+1}$ is the first-order rate constant for the reaction between TH_x* and H-*S* and $\theta_{TH_{x^*}}$ is the coverage of TH_x* at *-sites.

MA formation turnover rates at 333-393 K showed a dependence on H_2 pressure between one-half-order and first-order (**Figure 2.2**) which exceeds that of the expected half-order H_2 pressure dependence in **equation 2.24**; this indicates that the values of the *S*-site vacancy (θ_S) and TH_x* coverage terms ($\theta_{TH_{x^*}}$) combine to give a positive dependence on H_2 pressure between zero and one-half order. The θ_S values (**eq 2.22**) do not have positive dependences on H_2 pressure; as a result, the larger than one-half order H_2 dependence of MA formation turnover rates must arise instead from a $\theta_{TH_{x^*}}$ term that increases with increasing H_2 pressure. TH_x* forms from a series of H additions to bound toluene (**Scheme 2.1, steps 3-6**) and forms at coverages that depend on H_2 pressure related to the number of added H atoms and the reversibility of the H-addition steps. If the H-addition steps that form TH_x* are in quasi-equilibrium with bound toluene and H_2(g), **equation 2.24** becomes:

$$\vec{r}_{CH,x+1} = \frac{k_{TH_{x+1},tol} K_{tol*} [H_2]^{\frac{x+1}{2}} [tol]}{\left(1 + K_{H,S} [H_2]^{\frac{1}{2}}\right)} \theta_*^{\gamma_{tol}} \quad (2.25)$$

with

$$k_{TH_{x+1},tol} = k_{CH,x+1} \prod_{i=1}^{x} \left(K_{CH,i}\right) K_{H,S}^{x+1} \quad (2.26)$$

The functional form of **equation 2.25** is thus proportional to the (x+1)/2 H_2 pressure in the numerator and to any H_2 pressure dependences arising from the $\theta_*^{\gamma_{tol}}$ term in the numerator. The $\theta_*^{\gamma_{tol}}$ term reflects the coverage of γ_{tol} numbers of adjacent *-sites, which can be determined from the balance law describing the conservation of occupied and unoccupied *-sites at the Pt surface during reaction (**eq 2.23**)**.** MA formation turnover rates at 333-393 K were insensitive to toluene pressure; as a result, a toluene-derived species must be present as the MASI so as to cancel the toluene pressure terms in the numerator arising from the kinetically-relevant H-addition transition states. The DFT-based modeling reported in **Section 2.3.3** revealed that among plausible toluene-derived surface species, toluene-bri and 1-methyl-3,6-dihydrobenzene-bri formed with the most negative free energies relative to stoichiometric amounts of toluene(g), H_2(g), and the bare Pt(111) slab. These data indicate that bound forms of toluene and 1-methyl-3,6-dihydrobenzene are likely the most prevalent surface species. The balance on occupied and unoccupied surface sites including these bound species and *-site vacancies is restated (from **eq 2.23**), assuming that toluene and 1-methyl-3,6-dihydrobenzene occupy the same number of adjacent Pt-sites ($\theta_*^{\gamma_{tol}}$), as:

$$1 = \theta_* + K_{tol*}[tol]\theta_*^{\gamma_{tol}} + K_{1M36DHB*}[H_2][tol]\theta_*^{\gamma_{tol}}, \quad (2.27)$$

where $K_{1M36DHB}$ denotes the equilibrium constant to form bound 1-methyl-3,6-dihydrobenzene from gaseous toluene and H_2 molecules.

The effects of H_2 pressure on measured MA formation rates indicate a kinetic order of 0.5-1, which is consistent with MA formation rates limited by an irreversible TH_3*+H-*S* reaction (**Scheme 2.1, step 6**; **equation 2.25** with *x*=3) occurring on a surface predominantly covered by 1-methyl-3,6-dihydrobenzene (**equation 2.27**; with only the third term in the right-hand side being prevalent):

$$\vec{r}_{CH,4} = \frac{k_{TH_4,tol} K_{tol*} [H_2]}{K_{1M36DHB*} \left(1 + K_{H,S} [H_2]^{\frac{1}{2}}\right)} \tag{2.28}$$

The rates of C-H cleavage from TH_4* ($\overleftarrow{r}_{CH4}$; **Scheme 2.1, step 6**) must be small for the TH_3*+H-*S* reaction (**Scheme 2.1, step 6**) to be kinetically relevant and for ME intermediates to form irreversibly. The $\overleftarrow{r}_{CH4}$ value is described by the second term on the left-hand side of **equation 2.17**:

$$\overleftarrow{r}_{CH4} = k_{-CH,4} \theta_S \theta_{TH_4*} \theta_*^{\Delta\gamma_{CH,4}}. \tag{2.29}$$

The functional form of **equation 2.29** is restated by substituting the θ_S term with its value from **equation 2.22** and assuming that ME adsorption is quasi-equilibrated:

$$\overleftarrow{r}_{CH4} = \frac{k_{-CH,4} K_{ME*} [ME] \theta_*^{\gamma_{ME}+\Delta\gamma_{CH,4}}}{\left(1 + K_{H,S} [H_2]^{\frac{1}{2}}\right)}. \tag{2.30}$$

The functional form of **equation 2.30** is restated further by assuming that the sum of γ_{ME} and $\Delta\gamma_{CH,4}$, which constitutes the number of adjacent *-sites that are occupied by the TH_3* intermediates formed by H abstraction from TH_4*, is equal to γ_{tol} and by substituting the resulting $\theta_*^{\gamma_{tol}}$ term with its value from **equation 2.27** for a 1M13CHD-covered surface (with only the third term in the right-hand side being prevalent):

$$\overleftarrow{r}_{CH4} = \frac{k_{-CH,4} K_{ME*} [ME]}{K_{1M36DHB*} [H_2][tol] \left(1 + K_{H,S} [H_2]^{\frac{1}{2}}\right)}. \tag{2.31}$$

These $\vec{r}_{CH,4}$ and $\overleftarrow{r}_{CH4}$ values can be related to one another at a hypothetical thermodynamic equilibrium between gaseous toluene, H_2, and ME. Equilibrated ME formation from toluene and H_2 reactants indicate that the net rates of the elementary steps that mediate ME formation (**Scheme 2.1, step 1-6, 9**) are zero. The $\vec{r}_{CH,4}$ (**eq 2.28)** and $\overleftarrow{r}_{CH4}$ (**eq 2.30**) values evaluated at equilibrium pressures of ME ($[ME]_{eq} = [1ME]_{eq} + [3ME]_{eq} + [4ME]_{eq}$), H_2 ($[H_2]_{eq}$), and toluene ($[tol]_{eq}$) are equal as a consequence, giving the following relation:

$$\vec{r}_{CH,4} = \frac{k_{-CH,4} K_{ME*} K_{tol \rightarrow ME} [H_2]_{eq}}{K_{1M36DHB*} \left(1 + K_{H,S} [H_2]_{eq}^{\frac{1}{2}}\right)}, \tag{2.32}$$

where $K_{ME,tol}$ is the equilibrium constant for gaseous ME formation from toluene and 2 H_2.

The left-hand side of **equation 2.32** ($\vec{r}_{CH,4}$) is equal to the measured MA formation turnover rate because ME forms irreversibly from toluene-H_2 reactants. Evaluation of the terms on the right-hand side of the equation based on theoretical and experimental values can determine whether

TH_3*+H-*S* limited MA formation is consistent with observed MA formation turnover rates. The $K_{tol\rightarrow ME}$ value is 0.68 bar^{-2} (393 K) based on reported enthalpies and entropies [51]. The K_{ME*} values were calculated to be 8.2 x10^6 and 2.4 x10^8 bar^{-1} for 1ME and 4ME adsorption, respectively from DFT-derived free energies of formation of surface bound 1-methylcyclohexene-bri from gaseous 1ME and H_2 and 4-methylcyclohexene-bri (**Scheme 2.3**) from gaseous 4ME and H_2, as reported in **Table 2.3**. The $K_{1M36DHB*}$ value was calculated to be 1.9 x10^7 bar^{-2} (393 K) based on the free energy of formation of 1-methyl-5,6-dihydrobenzene-hcp from gaseous toluene and H_2 (**Table 2.2**). The $K_{H,S}$ value (0.2±0.1 bar^{-1}) was determined by regressing the rate data in **Figure 2.2** at 393 K to the functional form of **equation 2.28**. The $k_{-CH,4}$ value was given by the reported DFT-derived rate constant to cleave a C-H bond from bound cyclohexene (5.1 x10^4 bar^{-1} s^{-1}; PW91 functional [20]). These DFT-derived kinetic and thermodynamic rate constants combined to give values to the right-hand side of **equation 2.32** of 1.0 x10^4 and 2.9 x10^5 mole MA g-atom Pt$_s^{-1}$ s^{-1} for 1ME and 4ME, respectively; these values are much larger than the measured MA formation turnover rates (0.14 mole MA g-atom Pt$_s^{-1}$ s^{-1}) indicating these measured these rates are not consistent with the kinetic model for MA formation limited TH_3*+H-*S* reactions occurring on a 1-methyl-3,6-dihydrobenzene-covered surface.

The effects of H_2 pressure on MA formation rates may reflect instead kinetically-relevant TH_1*+H-*S* reactions on toluene-covered surfaces. The forward rate of TH_1*+H-*S* reactions (**Scheme 2.1, step 4**) is given by the forward rate of reaction from **equation 2.25** (*x*=1) with the $\theta_*^{\gamma_{tol}}$ term substituted with the value from **equation 2.27** for a toluene covered surface (i.e. $1 = K_{tol*}[tol]\theta_*^{\gamma_{tol}}$):

$$\vec{r}_{CH,2} = \frac{k_{TH_2,tol}[H_2]}{1 + K_{H,S}[H_2]^{\frac{1}{2}}} \tag{2.33}$$

These steps limit not only MA formation but also ME formation and must occur irreversibly to account for the 1ME and 4ME intermediates formed at pressures well below their equilibrium limits; as a result, the $\vec{r}_{CH,2}$ values describe overall MA formation turnover rates. Such purported irreversibility of the TH_1*+H-*S* reaction requires that rates of C-H cleavage from TH_2* intermediates ($\overleftarrow{r}_{CH,2}$) be small in comparison. The $\overleftarrow{r}_{CH,2}$ value is described by the second term on the left-hand side of **equation 2.17** and by substituting the θ_S term with its value from **equation 2.22**:

$$\overleftarrow{r}_{CH,2} = \frac{k_{-CH,2}\theta_{TH_2*}\theta_*^{\Delta\gamma_{CH,2}}}{1 + K_{H,S}[H_2]^{\frac{1}{2}}}. \tag{2.34}$$

The relation between $\vec{r}_{CH,2}$ and $\overleftarrow{r}_{CH,2}$ at a hypothetical equilibrium between toluene, H_2, and ME can be leveraged to determine whether the kinetic and thermodynamic parameters in **equations 2.33** and **2.34** are reasonable. The $\vec{r}_{CH,2}$ and $\overleftarrow{r}_{CH,2}$ values are equal for an equilibrated mixture of toluene, H_2, and ME:

$$\vec{r}_{CH,2} = \frac{k_{-CH,2}\theta_{TH_2*}\theta_*^{\Delta\gamma_{CH,2}}}{1 + K_{H,S}[H_2]^{\frac{1}{2}}}. \quad (2.35)$$

For an equilibrated mixture of toluene, H_2, and ME, the elementary steps that catalyze the reaction must also be equilibrated; consequently, TH_2* coverages follow an equilibrium relationship with gaseous ME:

$$\theta_{TH_2*,eq} = \frac{K_{CH,3}K_{CH,4}K_{ME*}[ME]_{eq}\theta_*^{\gamma_{TH_2}}}{[H_2]_{eq}}. \quad (2.36)$$

Substituting the θ_{TH_2*} term in **equation 2.35** with its equilibrium value (**eq 2.36**) and substituting the resulting $\theta_*^{\gamma_{TH_2}+\Delta\gamma_{CH,2}}$ term with its value from **equation 2.27 (**assuming that $\gamma_{TH_2} + \Delta\gamma_{CH,2} = \gamma_{tol}$) for a toluene covered surface (i.e. $1 = K_{tol*}[tol]\theta_*^{\gamma_{tol}}$) gives:

$$\vec{r}_{CH,2} = \frac{k_{-CH,2}K_{CH,3}K_{CH,4}K_{ME*}K_{tol\rightarrow ME}[H_2]_{eq}}{K_{tol*}\left(1 + K_{H,S}[H_2]^{\frac{1}{2}}\right)}. \quad (2.37)$$

The left-hand side of **equation 2.37** ($\vec{r}_{CH,2}$) is equal to the measured MA formation turnover rate (0.14 mole MA g-atom Pt_s^{-1} s^{-1}) because ME forms irreversibly from toluene-H_2 reactants. Evaluation of the terms on the right-hand side of the equation based on theoretical and experimental values can determine whether TH_1*+H-*S* limited MA formation is consistent with observed MA formation turnover rates. The $K_{tol\rightarrow ME}$ value is 0.68 bar^{-2} (393 K) based on reported enthalpies and entropies [51]. The K_{ME*} values were calculated to be 8.2 x10^6 and 2.4 x10^8 bar^{-1} for 1ME and 4ME adsorption, respectively from DFT-derived free energies of formation of surface bound 1-methylcyclohexene-bri from gaseous 1ME and H_2 and 4-methylcyclohexene-bri (**Scheme 2.3**) from gaseous 4ME and H_2, as reported in **Table 2.3**. The K_{tol*} in the denominator of the right-hand side of **equation 2.37** was calculated to be 4.5 x10^7 bar^{-1} (393 K) based on DFT-derived enthalpies and entropies to form toluene-bri (the most stable toluene adsorbate species) from gaseous toluene at Pt(111) surfaces (**Table 2.2**). The $K_{CH,3}K_{CH,4}$ terms on the left-hand side of **equation 2.37** combine to describe the equilibrium constant for the formation of TH_4* from TH_2* and a gaseous H_2 molecule. The values of $K_{CH,3}K_{CH,4}$ were calculated from the change in free energy to form 4-methylcyclohexene-bri and 1-methylcyclohexene-bri, respectively, from 1-methyl-5,6-dihydrobenzene-hcp and gaseous H_2(g) (**Table 2.2**) to be 1.0 x10^{-5} bar^{-1} and 3.3 x10^{-5} bar^{-1}. The $k_{-CH,2}$ value was given by the reported DFT-derived rate constant to cleave a C-H bond from bound dihydrobenzene (1.4x10^6 bar^{-1} s^{-1}; PW91 functional [20]). These DFT-derived kinetic and thermodynamic parameters combined to give values of the right-hand side of **equation 2.37** (1.2 and 110 mole MA g-atom Pt_s^{-1} s^{-1} for 1ME and 4ME, respectively) that differed from the $\vec{r}_{CH,2}$ value (0.14 mole MA g-atom Pt_s^{-1} s^{-1}) by factors of 10 and 10^3 for 1ME and 4ME, respectively. The closer agreement between terms on the left and right-hand sides of **equation 2.37** than **equation 2.32** indicates that the measured MA formation turnover rate kinetic trends are best explained by MA formation limited by TH_1*-H-*S* reactions (**Scheme 2.1, step 4**) occurring on a toluene-covered surface. Such purported presence of bound forms of molecular toluene, rather than 1-methyl-3,6-dihydrotoluene, as the MASI is consistent with evidence for benzene-saturated

surfaces during benzene hydrogenation (rather than partially hydrogenated forms of benzene) on Pt(111) (1-2 kPa benzene, 2-20 kPa H_2, 310-440 K) studied using sum frequency generation vibrational spectroscopy [12].

The presence of ME intermediates at pseudo-steady state concentrations indicates that MA formation and ME hydrogenation turnover rates are equal; pseudo-steady state *i*ME pressures at 393 K ($[iME]_{PSS}^{393K}$) can therefore be obtained by equating **equations 2.18** and **2.33**, and substituting the resulting $[ME]$ term with its value from equation 2.21:

$$[iME]_{PSS}^{393K} = \frac{k_{iME,2CH}\zeta_{iME}\left(1+\frac{k_{CH,6}}{k_{-CH,5}}K_{H,S}[H_2]^{\frac{1}{2}}\right)}{\theta_*^{\gamma_{ME}}} \quad (2.38)$$

where

$$k_{iME,2CH} = \frac{k_{TH_2,tol}}{k_{CH,6}K_{CH,5}K_{ME*}K_{H,S}^2}. \quad (2.39)$$

The values of $\theta_*^{\gamma_{ME}}$ do not depend on H_2 pressure for conditions in which *-sites are covered with molecularly bound forms of toluene leaving the summation term in the parentheses of **equation 2.38** as the only origin of H_2-pressure dependence. Measured pseudo-steady state 1ME and 4ME pressures were independent of H_2 pressure at 393 K (**Figure 2.5**) indicating that the H_2-dependent term on right-hand side of **equation 2.38** is negligible ($1 \gg \frac{k_{CH,6}}{k_{-CH,5}}K_{H,S}[H_2]^{\frac{1}{2}}$), consistent with ME conversion limited by the second respective H-addition step.

The conclusion that MA formation is limited by TH_1*+H-*S* reactions (**Scheme 2.1, step 4**) enables rigorous assessment of the chemical significance of the kinetic and thermodynamic parameters that govern its rates. The $k_{TH_2,tol}$ term ($k_{CH,2}K_{CH,1}K_{H,S}^2$ from **equation 2.26** with an *x*=1) represents the equilibrium constants for the formation of TH_1*+H-*S* from bound toluene and one H_2(g) molecule ($K_{CH,1}K_{H,S}^2$) and the forward rate constant for the TH_1*+H-*S* reaction ($k_{CH,2}$). The $k_{TH_2,tol}$ term depends exponentially on the difference in free energy between the transition state for the TH_1*+H-*S* reaction (denoted 2CH TS, with free energy $G_{CH,2}^{\ddagger}$) and the reactant state consisting of adsorbed toluene (G_{tol*}) and one H_2(g) molecule (G_{H_2}), according to transition state theory formalisms [52,53]:

$$k_{2H,tol} = \frac{k_B T}{h}\exp\left(-\frac{\Delta G_{2H,tol}^{\ddagger}}{RT}\right). \quad (2.40)$$

with

$$\Delta G_{2H,tol}^{\ddagger} = G_{CH,2}^{\ddagger} - G_{tol*} - G_{H_2}. \quad (2.41)$$

The $K_{H,S}$ term reflects the free energy of formation of H-*S* ($G_{H,S}$) from ½ H_2(g) and a bare *S*-site (G_S):

$$K_{H,S} = \exp\left(-\frac{\Delta G_{H,S}}{RT}\right). \quad (2.42)$$

where $\Delta G_{H,S}$ is given by:

$$\Delta G_{H,S} = G_{H,S} - \frac{1}{2} G_{H_2} - G_s. \tag{2.43}$$

The enthalpy and entropy components of $\Delta G^{\ddagger}_{2H,tol}$ ($\Delta G^{\ddagger}_{2H,tol} = \Delta H^{\ddagger}_{2H,tol} - T\Delta H^{\ddagger}_{2H,tol}$) and $\Delta G_{H,S}$ ($\Delta G_{H,S} = \Delta H_{H,S} - T\Delta S_{H,S}$) were determined by regressing MA formation turnover rate values at 333-393 K, 0.35-2.1 kPa toluene, and 10-80 kPa H_2 to the functional form of **equation 2.33**; their values and uncertainties are reported in **Table 2.4**. **Figure 2.8** shows a logarithmic plot of parity for measured and predicted MA formation turnover rates at the same conditions to demonstrate the excellent agreement between the mechanism-based kinetic model and measured MA formation turnover rates.

The measured $\Delta H_{H,S}$ value was -26 ± 6 kJ g-atom H^{-1}; this negative value indicates an enthalpic driving force for H_2 dissociation at *S*-sites amongst a toluene adlayer. Heats of H_2 dissociative adsorption ($Q_{H_2} = -\Delta H_{H_2}$, where ΔH_{H_2} is the change in enthalpy upon dissociating H_2(g) into bound H atoms on Pt surfaces without co-adsorbed hydrocarbons) from H_2 uptakes (473-673 K) on supported Pt nanoparticles (1.6, 3.0, and 9.1 nm mean cluster diameters) lie between 24 and 28 kJ g-atom H^{-1} at 0.2 ML, 20-23 kJ g-atom H^{-1} at 0.5 ML, and approaches near zero values at 1.0 ML where Pt-H interactions are weakened by through surface repulsive interactions [54]. Calorimetric data on Pt filaments at 273 K give Q_{H_2} values of 50 kJ mol^{-1} extrapolated to 0 ML coverage, 40 kJ mol^{-1} at 0.6 ML coverage, and <30 kJ mol^{-1} at 0.8 ML [55]. The $Q_{H,S}$ ($-\Delta H_{H,S}$) values derived from measured rates and the functional form of **equation 2.33** (26 ± 6 kJ mol^{-1}) are similar to those measured on Pt surfaces at near-saturation H* coverages, indicating that the measured $\Delta H_{H,S}$ value is typical of H_2 adsorption processes and that the kinetics-based model gave chemically realistic values.

The measured $\Delta S_{H,S}$ value (-50 ± 30 J g-atom H^{-1} K^{-1}) indicates a loss of entropy upon dissociation of H_2 into two H-*S* species on a crowded Pt surface. The predominant contribution to the H_2(g) entropy ($S_{H_2(g)}$; 77 J g-atom H^{-1} K^{-1} at 1 bar and 393 K (**eq 2.S68**)) comes from the translational entropy of the H_2 molecule ($S_{H_2(g),trans}$; 64 kJ g-atom H^{-1} (**eq 2.S73**)). Upon H_2 dissociation, translational modes become hindered translations and vibrations for H-*S* species. The magnitude of these measured $\Delta S_{H,S}$ values are within a factor of 1.3 of $S_{H_2(g),trans}$, accounting for a significant loss in entropy as the H_2(g) translational degrees of freedom are converted to the H-*S* translational and vibrational degrees of freedom that have smaller entropies. Such a loss of entropy is consistent with reported entropies of H_2 adsorption on Pt surfaces [54], further demonstrating that the kinetics-based model gave reasonable values compared with relevant experimental benchmarks.

The measured $\Delta H^{\ddagger}_{2H,tol}$ value (+41 ± 5 kJ mol^{-1}) reflects the positive enthalpy change to form the transition state for the second H-addition step (2CH TS) from the T* and one H_2(g) molecule. This $\Delta H^{\ddagger}_{2H,tol}$ value can be expressed in terms of the enthalpic barrier to form the 2CH TS from TH_1* and H-*S* ($\Delta H^{\ddagger}_{CH,2}$), its immediate precursors, and the change in enthalpy to form TH_1* and H-*S* from T* and one H_2(g) molecule ($\Delta H_{TH_1*,tol*} + \Delta H_{H,S}$):

$$\Delta H^{\ddagger}_{2H,tol} = \Delta H^{\ddagger}_{CH,2} + \Delta H_{TH_1*,tol*} + \Delta H_{H,S} \tag{2.44}$$

with

$$\Delta H^{\ddagger}_{CH,2} = H^{\ddagger}_{CH,2} - H_{TH_{1},*} - H_{H,S} \quad (2.45)$$

and

$$\Delta H_{TH_{1}*,tol*} = H_{TH_{1}*} - H_{tol*} - \frac{1}{2}H_{H_2} \quad (2.46)$$

where $H_{TH_{1}*}$ is the TH_1* enthalpy. The equation for $\Delta H_{TH_{1}*,tol*}$ (**eq 2.46**) can be rewritten in terms of the enthalpies to form TH_1* ($\Delta H_{TH_{1},*}$) and bound toluene ($\Delta H_{tol,*}$) from toluene(g) and H_2(g):

$$\Delta H_{TH_{1}*,tol*} = \Delta H_{TH_{1}*} - \Delta H_{tol*} \quad (2.47)$$

with

$$\Delta H_{TH_{1}*} = H_{TH_{1}*} - H_{tol} - \frac{1}{2}H_{H_2} \quad (2.48)$$

and

$$\Delta H_{tol*} = H_{tol*} - H_{tol} \quad (2.49)$$

where H_{tol} is the toluene(g) enthalpy. ΔH_{tol*} is calculated from the DFT-derived enthalpy to form toluene-bri from toluene(g) (-134 kJ mol^{-1} at 393 K, **Table 2.2**) and $\Delta H_{TH_{1},*}$ is calculated from the DFT-derived enthalpy to form 1-methyl-6-hydrobenzene-hol (the most stable among TH_1* species considered in **Section 2.3.3**) from toluene(g) and ½ H_2(g) (-121 kJ mol^{-1} at 393 K, **Table 2.2**); these values give a $\Delta H_{TH_{1}*,tol*}$ value of +13 kJ mol^{-1}. $\Delta H^{\ddagger}_{CH,2}$ is for toluene hydrogenation is approximated by the reported DFT-derived enthalpy of formation of the transition state that mediates the reaction between H-*S* and bound monohydrobenzene to form bound dihydrobenzene on Pt(111) (64 kJ mol^{-1} at 393 K) from Sabbe et al. [20]. The DFT-derived $\Delta H_{TH_{1}*,tol*}$ value and the reported $\Delta H^{\ddagger}_{CH,2}$ value, taken together with the measured $\Delta H_{H,S}$ (-26 ± 6 kJ g-atom H^{-1}, **Table 2.4**), give a $\Delta H^{\ddagger}_{2H,tol}$ value of +51 ± 6 kJ mol^{-1}, which is similar in magnitude to measured $\Delta H^{\ddagger}_{2H,tol}$ values (+41 ± 5) which demonstrates good agreement between the measured enthalpies for the parameters in the mechanism-based kinetic model and the DFT-derived enthalpies for the chemical transformations that they represent.

The measured $\Delta S^{\ddagger}_{2H,tol}$ values (-150 ± 10 J mol^{-1} K^{-1}) indicate a significant decrease in entropy to form the transition states that mediates TH_1*+H-*S* reactions from T* and a gaseous H_2 molecule. This $\Delta S_{2H,tol}$ value is comparable to the change in entropy for the gas phase reaction to form 1-methyl-1,3-cyclohexadiene from toluene and H_2 based on reported experimental results (-118 J mol^{-1} K^{-1} [51]). These negative entropy changes are accounted for in large part by the loss of H_2(g) translational entropy (128 J mol$_{H2}^{-1}$ K^{-1}) as H_2(g) translational degrees of freedom are converted to lower entropy vibrational and rotational modes in the bound or gaseous hydrocarbon moieties.

2.3.5. Kinetically-relevant steps, chemical significance of the relevant kinetic and thermodynamic parameters, and origins of the negative temperature dependence for toluene hydrogenation at high temperatures (493-533 K).

The ratios of the MA formation turnover rate to 1ME pressure (ψ_{1ME}; **eq 2.16**) and to 4ME pressure (ψ_{4ME}; **eq 2.16**) increased linearly with H_2 pressure at 493-533 K (**Figure 2.6**). The ψ_{1ME}

and ψ_{4ME} values predicted by **equation 2.19** depend on H_2 pressure through the $[H_2]$ term in the numerator, θ_S (numerator), and $\theta_*^{\gamma_{ME}}$ (numerator), and the collection of terms enclosed in the parenthesis in the denominator. The DFT-derived free energy of formation of bound toluene from its gaseous form is at least 16 kJ mol^{-1} more negative than that of other toluene-derived bound species from stoichiometric amounts of gaseous toluene and H_2 on Pt(111) (493 K, **Table 2.2**, with 1-methyl-3,6-dihydrotoluene having the next lowest energy); thus, toluene is the most likely among plausible adsorbates to bind to *-sites at significant coverages. Toluene coverages do not depend on H_2 pressures, leading to θ_* values that are also independent of H_2 pressure for toluene-covered surfaces (**eq 2.27**). The magnitude of θ_S (**eq 2.22**) may depend on H_2 pressure, however, with such dependences ranging from $(H_2)^{-0.5}$ (for saturation H-*S* coverages) to zero order (at low H-*S* coverages). *S*-sites must be predominantly bare (at 493-533 K) for θ_S to retain a H_2 pressure dependence because significant H-*S* coverages would lead to the cancelation of the $[H_2]$ term in **equation 2.19** (numerator) to give ψ_{1ME} and ψ_{4ME} values that have a sublinear H_2 pressure dependence. The $k_{CH,6}K_{H,S}[H_2]^{\frac{1}{2}}/k_{CH,-5}$ term in **equation 2.19** must also be much smaller than unity ($1 \ll k_{CH,6}K_{H,S}[H_2]^{\frac{1}{2}}/k_{CH,-5}$) for the terms in the parenthesis in the denominator to be independent of H_2 pressure so as not to cancel with the H_2 pressure term in the numerator. Such $k_{CH,6}K_{H,S}[H_2]^{\frac{1}{2}}/k_{CH,-5}$ values reflect effective rate constants for H abstraction from TH_5* ($k_{CH,-5}$; **Scheme 2.1, step 7**) that are much larger than those of H addition to TH_5* ($k_{CH,6}K_{H,S}[H_2]^{\frac{1}{2}}$; **Scheme 2.1, step 8**), resulting in quasi-equilibrated TH_5* formation from ME(g) and ½ H_2(g). Measured ψ_{1ME} and ψ_{4ME} values can therefore be described by the following restated form of the **equation 2.19** with negligible H-*S* coverage and quasi-equilibrated TH_5* formation:

$$\psi_{iME,HT} = \frac{k_{CH,6}K_{CH,5}K_{ME*}K_{H,S}^2[H_2]\theta_*^{\gamma_{ME}}}{\zeta_{iME}} \tag{2.50}$$

where $\psi_{iME,HT}$ denotes the ψ_{iME} values at the conditions of high temperatures (493-533 K) with kinetic trends shown in **Figure 2.6**.

Figure 2.9 shows measured ψ_{1ME} and ψ_{4ME} values as a function of toluene pressure at 80 kPa H_2 and 493-533 K. These ψ_{1ME} and ψ_{4ME} values showed kinetic orders in toluene pressure between -1 and 0 (near one-half order) that were nearly independent of temperature. The ψ_{1ME} and ψ_{4ME} values predicted by the functional form of **equation 2.50** depend on toluene pressure arising from the $\theta_*^{\gamma_{ME}}$ term. The θ_* values are determined from the previously-defined balance law describing the conservation of occupied and unoccupied *-sites (**eq 2.27**; where the second term pertaining to the 1-methyl-3,6-dihydrobenzene coverage is negligible because it has a 16 kJ mol^{-1} (at 493 K) less negative free energy of formation than toluene (**Table 2.2**)). These θ_* values depend inversely on $[tol]^{\gamma_{tol}}$ for toluene-saturated surfaces and are independent of toluene pressure for essentially bare surfaces. Pt surfaces during reaction conditions may reflect the low coverage limit, (corresponding to a zero-order dependence), high toluene coverage limit (corresponding to a $[tol]^{-\gamma_{tol}}$ dependence), or fall somewhere in between. The measured ψ_{1ME} and ψ_{4ME} dependences on toluene pressure (near one-half order) are thus consistent with one of two plausible explanations: (i) bound toluene is the sole MASI and binds to an ensemble of adjacent *-sites (γ_{tol}) that is larger than that for the transition state that mediates the TH_5*+H-*S* reaction (6CH TS;

Scheme 2.1, step 9; γ_{ME}; $\gamma_{tol} > \gamma_{ME}$); or (ii) bound toluene and 6CH TS ($\gamma_{tol} = \gamma_{ME}$) occupy similar ensembles of adjacent *-sites, and both bound toluene and *-site vacancies constitute the MASI. The measured values of both ψ_{1ME} and ψ_{4ME} showed similar toluene pressure dependences at temperatures between 493 K to 533 K, indicating that $\theta_*^{\gamma_{ME}}$ must also be insensitive to temperature. For scenario (i), θ_* values are evaluated from **equation 2.27** for toluene-saturated surfaces to give $\theta_*^{\gamma_{ME}}$ values:

$$\theta_*^{\gamma_{ME}} = (K_{tol*}[tol])^{-\epsilon_{ME}}, \tag{2.51}$$

with

$$\epsilon_{ME} = \frac{\gamma_{ME}}{\gamma_{tol}}. \tag{2.52}$$

The $\theta_*^{\gamma_{ME}}$ values described by the functional form of **equation 2.51** are inversely proportional to toluene pressure raised to the ϵ_{ME} power which describes the smaller size of 6CH TS compared with the toluene MASI. This $[tol]^{-\epsilon_{ME}}$ dependence is unaffected by changes in temperature because only the $K_{tol*}^{-\epsilon_{ME}}$ term in **equation 2.51** has a temperature dependence. Scenario (ii), in contrast, is characterized by both θ_* and $K_{tol*}[tol]\theta_*^{\gamma_{tol}}$ terms in **equation 2.27** that are significant; in this case, K_{tol*} must be independent of temperature for $\theta_*^{\gamma_{ME}}$ values to be insensitive to temperature. The K_{tol*} values from DFT-derived toluene adsorption enthalpies and entropies ($K = \exp(-H/RT + S/R)$, **Table 2.2**) differed about 10-fold in this temperature range ($1.2\text{x}10^4$ bar^{-1} at 493 K; $1.0\text{x}10^3$ bar^{-1} at 533 K); it is thus unlikely that scenario (ii) retains the same toluene-pressure dependences across the temperature range. A toluene-saturated surface with ϵ_{ME} values smaller than unity (scenario (i)) represents, in turn, the explanation most consistent with the observed ψ_{1ME} and ψ_{4ME} trends.

The conclusion that TH_5* intermediates are formed in quasi-equilibrium with their respective *i*ME precursors and ½ H_2 (such that $k_{CH,6}K_{H,S}[H_2]^{\frac{1}{2}}/k_{CH,-5}$<<1) enables the following simplification of the functional form describing the combined ME hydrogenation rates (r_{ME}; **equation 2.15**):

$$r_{ME} = k_{CH,6}K_{CH,5}K_{ME*}K_{H,S}^2[H_2]\theta_S\theta_*^{\gamma_{ME}}[ME] \tag{2.53}$$

The functional form of **equation 2.53** is restated as a function the pressure of each *i*ME isomer by substituting the $[ME]$ term with its value from **equation 2.17**, and equating it to the methylcyclohexane formation rate (r_{MA}, because MA is the sole product of the ME hydrogenation reaction):

$$r_{MA} = \frac{k_{CH,6}K_{CH,5}K_{ME*}K_{H,S}^2[H_2]\theta_S\theta_*^{\gamma_{ME}}[iME]}{\zeta_{iME}} \tag{2.54}$$

The observation that Pt surfaces are saturated with toluene even at these higher temperatures allows for **equation 2.54** to be simplified further by substituting the $\theta_*^{\gamma_{ME}}$ term with its value from the solution of **equation 2.27** (with only the second term being significant):

$$r_{MA} = \frac{k_{MA,iME}[H_2]}{[tol]^{\epsilon_{ME}}}[iME] \tag{2.55}$$

with

$$k_{MA,iME} = \frac{k_{CH,6} K_{CH,5} K_{ME*} K_{H,S}^2}{\zeta_{iME} K_{tol*}^{\epsilon_{ME}}}. \quad (2.56)$$

The resulting functional form (**eq 2.56**) describes MA formation turnover rates as a function of toluene, H_2, and *i*ME pressures with only two relevant parameters ($k_{MA,iME}$ and ϵ_{ME}). The $k_{MA,iME}$ term consists of kinetic and thermodynamic parameters that describe the forward rate constant for TH_5*+H-*S* reactions ($k_{CH,6}$; **Scheme 2.1, step 8**), the desorption of ϵ_{ME} bound toluene molecules from the toluene adlayer ($K_{tol*}^{-\epsilon_{ME}}$) to form an ensemble of γ_{ME} adjacent *-sites, TH_5* and H-*S* formation from one ME(g) and one H_2(g) molecule at an ensemble of γ_{ME} adjacent *-sites (**Scheme 2.1, step 2,7,9**), and the ratio of the *i*ME to combined ME pressures (ζ_{iME}, **eq 2.21**). $k_{MA,iME}$ depends exponentially on the difference between the free energy of the prevalent transition states for the TH_5*+H-*S* reactions (denoted 6CH TS, with free energy $G_{CH,6}^{\ddagger}$) with ϵ_{ME} toluene(g) molecules ($\epsilon_{ME} G_{tol}$) and the free energy of the reactant state consisting of ϵ_{ME} adsorbed toluene molecules ($\epsilon_{ME} G_{tol*}$), one H_2(g) molecule (G_{H_2}), and one *i*ME(g) molecule (G_{iME}), according to transition state theory formalisms [52,53]:

$$k_{MA,iME} = \frac{k_B T}{h} \exp\left(-\frac{\Delta G_{MA,iME}}{RT} + ln\left(\frac{1}{\zeta_{iME}}\right)\right) \quad (2.57)$$

with

$$\Delta G_{MA,iME} = G_{CH,6}^{\ddagger} - G_{H_2} - G_{iME} - \epsilon_{ME}(G_{tol*} + G_{tol}) \quad (2.58)$$

ζ_{iME} values could not be measured directly because 3ME intermediates were not detectable. 3ME and 4ME both have double bonds at pairs of secondary C atoms whereas the double bond of 1ME forms at a secondary-tertiary C atom pair. The similar substitution of the C atoms that form the double bond in 3ME and 4ME is reflected in the small free energy change to form 3ME from 4ME (+2 kJ mol^{-1}, 493 K [51]) compared with the free energy change to form 3ME from 1ME (8 kJ mol^{-1}, 493 K [51]). Pseudo-steady state 3ME pressures were approximated by measured 4ME values (**Figure 2.5**), in light of their similar energetics and structures, to describe ζ_{iME} by the following restated form of **equation 2.21**:

$$\zeta_{iME} = \frac{[iME]}{2[4ME] + [1ME]}. \quad (2.59)$$

The enthalpy and entropy components of $\Delta G_{2H,iME}$ ($\Delta G_{2H,iME} = \Delta H_{2H,iME} - T\Delta S_{2H,iME}$) were determined by regressing the measured r_{MA}, $[iME]$, and ζ_{iME} values at 493-533 K (0.35-2.1 kPa toluene and 10-80 kPa H_2) to the functional form of **equation 2.55** with temperature-dependent $k_{MA,iME}$ values; their values and uncertainties are reported in **Table 2.4**. **Figure 2.10** shows a logarithmic plot of parity for measured and predicted $\psi_{iME,HT}$ values at the same conditions to demonstrate the excellent agreement between the mechanism-based kinetic model and measured $\psi_{iME,HT}$ values.

The measured ϵ_{ME} values were 0.54 ± 0.06 and 0.51 ± 0.06 for regression of ψ_{1ME}-ζ_{1ME} and ψ_{4ME}-ζ_{4ME} values to **equation 2.55**, respectively, corresponding to a nearly two-fold larger ensemble of adjacent *-sites required to bind toluene (γ_{tol}) than prevalent 6CH TS (γ_{ME}). Bound toluene was shown to form from toluene(g) with the most negative change in free energy at the

bridge position (**Table 2.2**) forming covalent bonds with four adjacent Pt-atoms and with the plane of the ring oriented in parallel with the surface (**Scheme 2.2**). Methylcyclohexyl species formed from toluene(g) and 5/2 H_2(g) were shown to bind at the atop position and in the chair conformation with the saturated C atoms of the ring extending upwards and perpendicular to the Pt surface (**Scheme 2.3**). Occupied surface areas for bound toluene-bri and 4-methylcyclohexyl-atop were calculated to be 0.414 and 0.301 nm^2, respectively, from the projection of the atomic volumes of C and H atoms (calculated from their van der Waals radii) at their optimized coordinates onto the plane of the Pt(111). The relatively larger van der Waals area for toluene-bri is directionally consistent with a larger γ_{tol} value than γ_{ME} reflected in measured ϵ_{ME} values that were less than one. The larger γ_{tol} value than γ_{ME} is also consistent with calorimetric studies that report that fewer benzene molecules bind to form a saturated monolayer (0.15 ML, 300 K [14]) than do cyclohexene (0.24 ML, 100 K [13]) on Pt(111) surfaces, indicating that benzene occupies a larger number adjacent Pt-atoms than cyclohexene on Pt surfaces with high hydrocarbon coverages.

The negative measured $\Delta H_{MA,1ME}$ and $\Delta H_{MA,4ME}$ values (-14 ± 4 kJ mol^{-1} and -29 ± 4 kJ mol^{-1}, respectively) reflect an enthalpic driving force to form the transition states, consisting of the prevalent 6CH TS and ϵ_{ME} toluene(g) molecules, from the reactant state, consisting of ϵ_{ME} bound toluene molecules, H_2(g), and 1ME(g) or 4ME(g), respectively. These measured enthalpy changes can be expressed in terms of the change in enthalpy to form the prevalent 6CH TS from TH_5* and H-*S* intermediates ($\Delta H^{\ddagger}_{CH,6}$); the change in enthalpy to form prevalent TH_5* intermediates from 1ME(g) or 4ME(g), ½ H_2(g), and an ensemble of γ_{ME} adjacent vacant *-sites ($\Delta H_{TH_5*,iME}$); $\Delta H_{H,S}$; and the change in enthalpy to desorb ϵ_{ME} bound toluene molecules from the toluene adlayer ($-\epsilon_{ME}\Delta H_{tol*}$):

$$\Delta H_{MA,iME} = \Delta H^{\ddagger}_{CH,6} + \Delta H_{TH_5*,iME} + \Delta H_{H,S} - \epsilon_{ME}\Delta H_{tol*} \tag{2.60}$$

with

$$\Delta H^{\ddagger}_{CH,6} = H^{\ddagger}_{CH,6} - H_{TH_5*} - H_{H,S} \tag{2.61}$$

and

$$\Delta H_{TH_5*,iME} = H_{TH_5*} - H_{iME} \tag{2.62}$$

where H_{TH_5*} is the TH_5* enthalpy and H_{iME} is the 1ME(g) or 4ME(g) enthalpy. **Table 2.3** reports DFT-derived electronic energies, enthalpies, entropies, and free energies to form surface-bound 1-methylcyclohexene-bri and 1-methylcyclohexyl-atop (**Scheme 2.3**) from 1ME(g) and H_2(g), and 4-methylcyclohexene-bri and 4-methylcyclohexyl-atop (**Scheme 2.3**) from 4ME(g) and H_2(g). DFT-derived enthalpies to form 1-methylcyclohexyl-atop from 1ME(g) and H_2(g), and 4-methylcyclohexyl-atop from 4ME(g) and H_2(g) were used to calculate $\Delta H_{TH_5*,1ME}$ (-130 kJ mol^{-1}) and $\Delta H_{TH_5*,4ME}$ (-143 kJ mol^{-1}) values, respectively. ΔH_{tol*} was calculated from the DFT-derived enthalpy to form toluene-bri from toluene(g) (-134 kJ mol^{-1}, **Table 2.2**). $\Delta H^{\ddagger}_{CH,6}$ is given by the reported DFT-derived change in enthalpy to form the transition state for the reaction between bound H and cyclohexyl to form bound cyclohexane on Pt (111) (78 kJ mol^{-1}, 493 K; PW91 functional) [20]. These DFT-derived $\Delta H_{TH_5*,iME}$ and $\Delta H_{tol,*}$ values along with the reported $\Delta H^{\ddagger}_{CH,6}$ combine with measured $\Delta H_{H,S}$ (-26 ± 6, **Table 2.4**) and ϵ_{ME} (0.54 and 0.51 for 1ME and

4ME, respectively; **Table 2.4**) to give $\Delta H_{MA,1ME}$ and $\Delta H_{MA,4ME}$ values of -6 kJ mol^{-1} and -23 kJ mol^{-1}, respectively. These calculated $\Delta H_{MA,1ME}$ and $\Delta H_{MA,4ME}$ values both differ by less than 8 kJ mol^{-1} in magnitude of their respective measured values (-14 ± 4 kJ mol^{-1} and -29 ± 4 kJ mol^{-1}, respectively) which demonstrates good agreement between the measured enthalpies for the parameters in the mechanism-based kinetic model and the DFT-derived enthalpies for the chemical transformations that they represent.

These negative measured $\Delta H_{MA,1ME}$ and $\Delta H_{MA,4ME}$ values moreover indicate that the combined positive changes in enthalpy to form prevalent 6CH TSs from TH_5* and H-*S* and to desorb ϵ_{ME} numbers of bound toluene molecules are smaller in magnitude than the negative change in enthalpy to form prevalent TH_5* intermediates and H-*S* from ME(g) and H_2(g). Such negative $\Delta H_{MA,1ME}$ and $\Delta H_{MA,4ME}$ values arise, despite the large positive $\Delta H^{\ddagger}_{CH,6}$ value, because prevalent TH_5* intermediates form from ME(g) and ½ H_2(g) with a negative change in enthalpy that is larger in magnitude than the change in enthalpy to desorb ϵ_{ME} bound toluene molecules. These negative measured $\Delta H_{MA,1ME}$ and $\Delta H_{MA,4ME}$ values combined with 1ME and 4ME pressures that decrease with increasing temperature (**Figure 2.5**) give rise to the negative dependence of MA formation turnover rates on temperature at high temperatures (493-533 K; **Figure 2.1**).

The large negative measured $\Delta S_{2H,1ME}$ and $\Delta S_{2H,4ME}$ values (-220 ± 10 and -240 ± 10 J mol^{-1} K, respectively) reflect the significant decrease in entropy to form prevalent 6CH TSs from H_2(g) and 1ME(g) or 4ME(g), respectively. These measured entropy changes can be expressed in terms of the change in entropy to form prevalent 6CH TSs from bound 1ME or 4ME and one H_2(g) molecule ($\Delta S^{\ddagger}_{CH,6;iME*}$); the change in entropy to form bound 1ME or 4ME from 1ME(g) or 4ME(g), respectively, and an ensemble of γ_{ME} adjacent vacant *-sites (ΔS_{iME*}); and the change in entropy to desorb ϵ_{ME} bound toluene molecules from the toluene adlayer ($-\epsilon_{ME}\Delta S_{tol*}$):

$$\Delta S_{MA,iME} = \Delta S^{\ddagger}_{CH,6;iME*} + \Delta S_{iME*} - \epsilon_{ME}\Delta S_{tol*} \tag{2.63}$$

with

$$\Delta S^{\ddagger}_{CH,6;iME*} = S^{\ddagger}_{CH,6} - S_{iME*} - S_{H_2} \tag{2.64}$$

$$\Delta S_{iME*} = S_{iME*} - S_{iME} \tag{2.65}$$

and

$$\Delta S_{tol*} = S_{tol*} - S_{tol} \tag{2.66}$$

where $S^{\ddagger}_{CH,6}$ is the entropy of the prevalent 6CH TSs, S_{iME*} is the entropy of 1ME(g) or 4ME(g), S_{H_2} is the entropy of gaseous H_2(g), S_{tol*} is the entropy of bound toluene, and S_{tol} is the entropy of toluene(g). The reported changes in entropy to form MA(g) from 1ME(g) and H_2(g) and from 4ME(g) and H_2(g) are -135 and -133 J mol^{-1} K, respectively, at 493 K [51] which are accounted for in large part by the loss of H_2(g) translational entropy (128 J mol^{-1} K^{-1}) as gaseous H_2 translational degrees of freedom are converted to lower entropy vibrational and rotational modes in the gaseous hydrocarbon. These same H_2(g) translational degrees of freedom are also lost upon gaseous H_2 reaction with ME-derived species at the surface to form prevalent 6CH TSs ($\Delta S^{\ddagger}_{CH,6;iME*}$), accounting for the majority of the measured $\Delta S_{MA,1ME}$ and $\Delta S_{MA,4ME}$ values. The measured $\Delta S_{MA,1ME}$ and $\Delta S_{MA,4ME}$ values are more negative than the H_2(g) translational entropy

loss (-128 J mol^{-1} K^{-1}) by -90 ± 10 and -110 ± 10 J mol^{-1} K, respectively; these excess negative $\Delta S_{MA,1ME}$ and $\Delta S_{MA,4ME}$ values arising from the difference between ΔS_{iME*} and $\epsilon_{ME}\Delta S_{tol*}$. DFT-derived values of ΔS_{iME*} (-212 J mol^{-1} K; **Table 2.3**) and ΔS_{tol*} (-194 J mol^{-1} K, **Table 2.2**) primarily reflect the loss of translational entropy as translational degrees of freedom in the gas phase are converted to vibrational and rotational modes at the surface. Toluene(g) and ME(g) translational entropies are similar because they depend predominantly on molecular masses (**eq 2.S73**), which only differs by a factor of 1.04 between the two molecules. The similar ΔS_{iME*} and ΔS_{tol*} values therefore result in a negative difference between the DFT-derived ΔS_{iME*} and $\epsilon_{ME}\Delta S_{tol*}$ values of -80. and -86 J mol^{-1} K for 1ME and 4ME, respectively, because measured ϵ_{ME} values are less than one. The negative entropy differences to displace bound toluene with ME(g) combined with the loss of H_2(g) translational entropy to form prevalent 6CH TSs thus account for the large negative measured $\Delta S_{MA,1ME}$ and $\Delta S_{MA,4ME}$ values.

2.4. Conclusions

The reaction kinetics and density functional theory (DFT)-based assessments of toluene-H_2 reactions on Pt/SiO_2 shown here elucidate the identity and kinetic relevance of elementary steps, the abundance and type of bound intermediates involved, and the consequences of size differences between the Pt ensembles are required to bind them. At low temperatures (333-393 K), gaseous 1ME and 4ME intermediates were formed at pressures that were a factor of 10^3 less than their thermodynamic equilibrium with toluene(g) and H_2(g) at 333-393 K and at pseudo-steady state. MA formation turnover rates were shown to be limited by reactions between monohydogenated toluene (TH_1*) and bound H atoms (H-*S*) and to occur on a toluene covered surface. The transition states for prevalent TH_1*+H-*S* reactions formed from bound toluene and H_2(g) with a measured change of enthalpy of 41 ± 5 kJ mol^{-1} and entropy of -150 ± 10 J mol^{-1} K^{-1}. At higher temperatures (493-533 K), 1ME and 4ME intermediates were formed at pressures that were within a factor of 10 of their equilibrium values with stoichiometric amounts of toluene(g) and H_2(g). At these temperatures, MA formation turnover rates became limited by ME hydrogenation rates. ME hydrogenation was shown to be limited by H addition to pentahydrogenated toluene (TH_5*) intermediates and to occur on a toluene covered surface. The TH_5*+H-*S* reactions were mediated by an ensemble of adjacent Pt sites that was a factor of two smaller than the ensemble that was occupied by the toluene most abundant surface intermediate. The transition states that mediated prevalent TH_5*+H-*S* reactions were formed from gaseous 1ME-H_2 and 4ME-H_2 precursors with measured enthalpy changes of -14 ± 4 kJ mol^{-1} and -29 ± 4 kJ mol^{-1}, respectively, and entropy changes of -220 ± 10 and -240 ± 10 J mol^{-1} K, respectively. These negative enthalpies combined with ME pressures that decreased with temperature accounted for the negative MA formation turnover rate dependence on temperature.

2.5. Acknowledgements

I would like to acknowledge financial support from the Chevron Corporation, Chevron UC Berkeley Graduate Research Fellowship, and the National Science Foundation Graduate Research Fellowship and computational resources supported by The Extreme Science and Engineering Discovery Environment (*XSEDE*) of the NSF and National Energy Research Scientific Computing Center of the DOE. I would also like to acknowledge Dr. Junnan Shangguan for helpful discussions revisions.

2.6. Figures, tables, and schemes

Figure 2.1: Methylcyclohexane (MA) formation turnover rates (moles MA g-atoms surface Pt $(Pt_s)^{-1}$ s^{-1}) on Pt/SiO_2 (3.6 nm mean nanocluster diameter) as a function of inverse temperature (1.4 kPa toluene, 333–533 K) at 20 kPa (■), 40 kPa (●), and 80 kPa (▲) H_2 on Pt/SiO_2 (3.6 nm average particle diameter). Solid curves indicate trends.

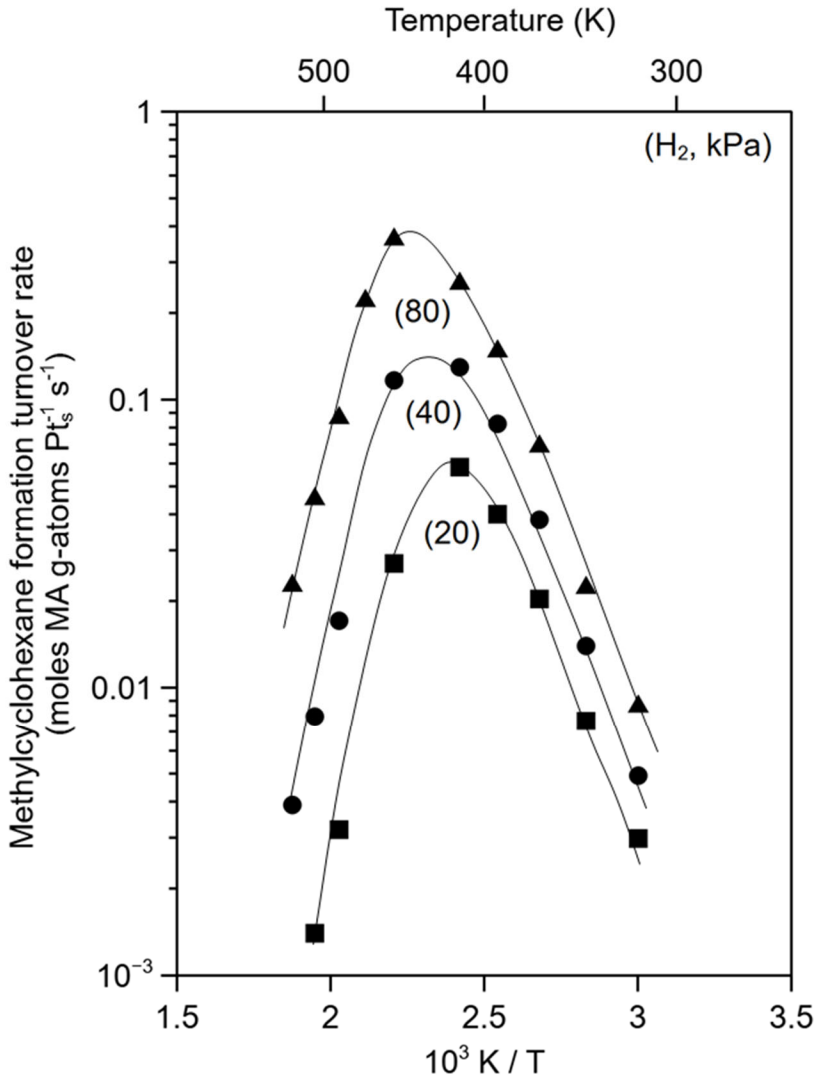

Figure 2.2: Methylcyclohexane (MA) formation turnover rates (moles MA g-atoms surface Pt $(Pt_s)^{-1}$ s^{-1}) on Pt/SiO_2 (3.6 nm mean nanocluster diameter) as a function of H_2 ((a); 1.4 kPa toluene) and toluene ((b); 80 kPa H_2) pressure at 333-533 K (333, ■; 353, ●; 373, ▲; 393, ◆; 413, ×; 493, △; 513, ○; 533, □) on Pt/SiO_2 (3.6 nm average particle diameter). Solid curves indicate trends.[a]

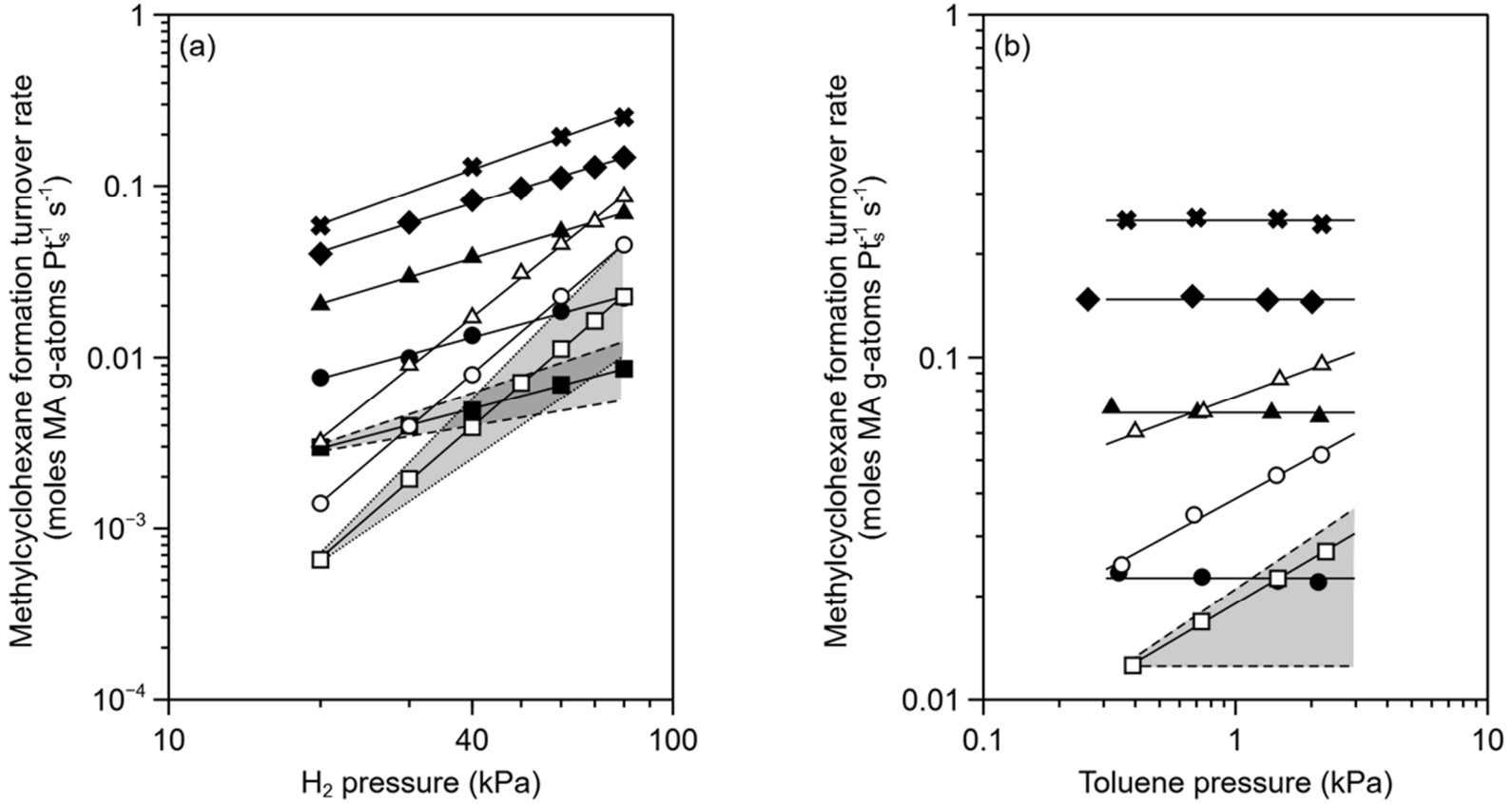

[a]The dashed lines at the lower and upper sides of the grey triangle enclosing the data measured at 333 K (■ symbols) in (a) illustrate the trends for one-half- and first-order H_2 pressure dependences, respectively; the dotted lines at the lower and upper sides of the grey triangle enclosing the data measured at 533 K (□ symbols) in (a) illustrate the trends for second- and third-order H_2 pressure dependences, respectively; and the dashed lines at the lower and upper sides of the grey triangle enclosing the data measured at 333 K (□ symbols) in (b) illustrate the trends for zero- and one-half-order toluene pressure dependences, respectively.

Figure 2.3: 1-Methylcyclohexene (1ME) (filled symbols) and 4-methylcyclohexene (4ME) (open symbols) pressures as a function of toluene conversion (1.4 kPa toluene, 80 kPa H_2) at 393 (●), 413 (■), 493 (▲), and 513 (♦) K during toluene-H_2 reaction on Pt/SiO_2 (3.6 nm average particle diameter). Toluene conversion was varied through changes in bed residence time (via changes in molar inlet rates or Pt/SiO_2 mass). Solid and dashed lines indicate trends for 1ME and 4ME, respectively.

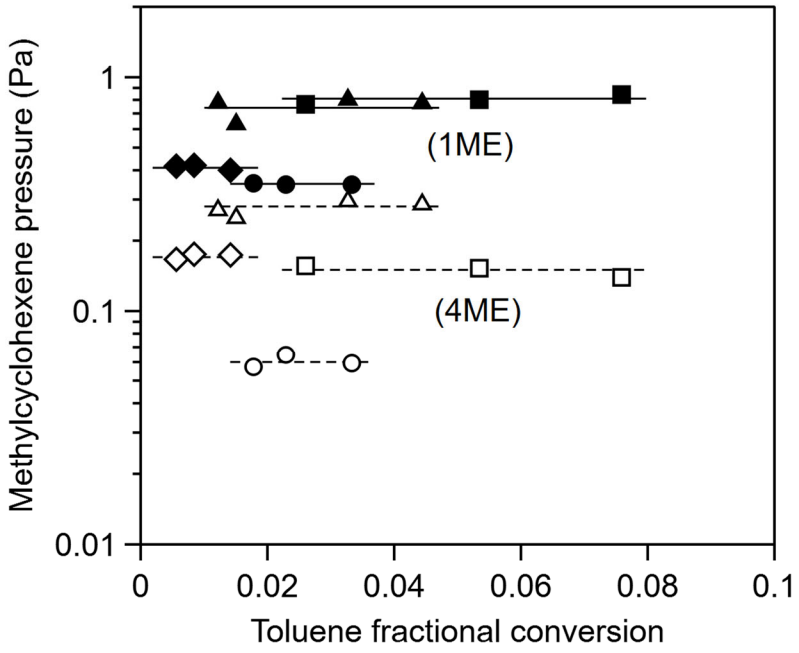

Figure 2.4: Approach to equilibrium parameter (η) for 1-methylcyclohexene (1ME) (●) and 4-methylcyclohexene (4ME) (▲) reactions with H_2 to form methylcyclohexane (MA) (**eq 2.8**) and toluene reaction with 2 H_2 to form 1ME (○) and 4ME (△) (**eq 2.7**) as a function of inverse temperature (1.4 kPa toluene, 80 kPa H_2, 393-533 K) during toluene-H_2 reactions on Pt/SiO_2 (3.6 nm average particle diameter). The solid and dashed error bars represent 95% confidence intervals for 1ME and 4ME, respectively, representing uncertainties in reported reaction enthalpies and entropies [51]. Solid curves are included to indicate trends.

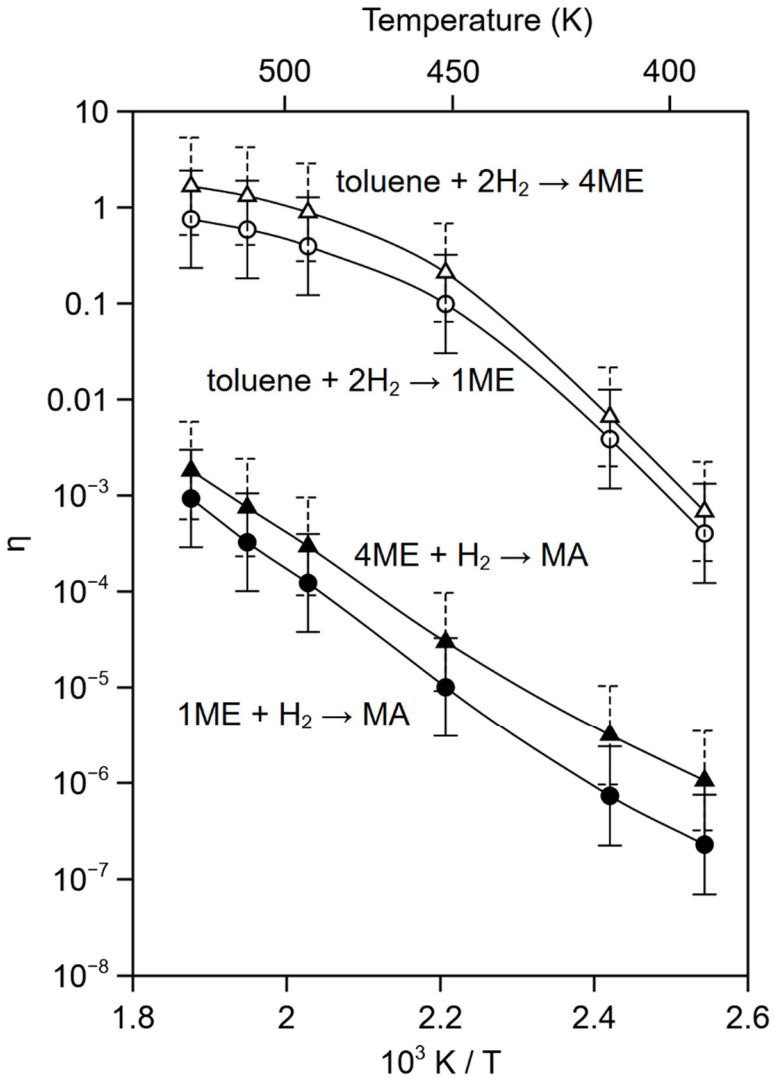

Figure 2.5: 1-Methylcyclohexene (1ME) (filled symbols) and 4-methylcyclohexene (4ME) (open symbols) pressures as a function of H_2 ((a); 1.4 kPa toluene) and toluene ((b); 80 kPa H_2) pressure at 393 (▲), 413 (♦), 493 (●), 533 (■) K during toluene-H_2 reactions on Pt/SiO_2 (3.6 nm average particle diameter). Solid and dashed lines indicate trends for 1ME and 4ME, respectively.

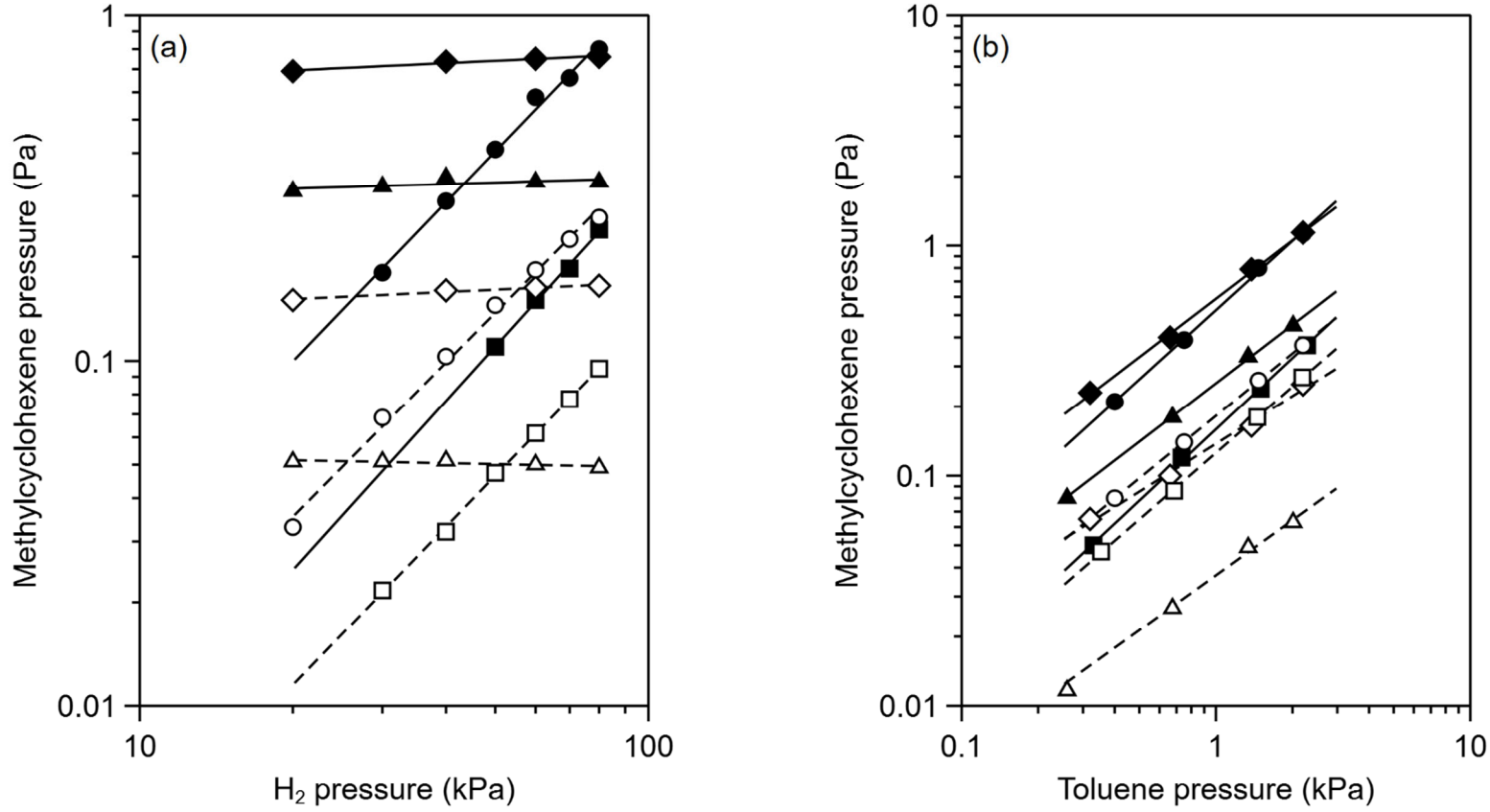

Figure 2.6: Ratio of methylcyclohexane (MA) formation turnover rates (r_{MA}) to 1-methylcyclohexene ((a); 1ME) or 4-methylcyclohexene ((b); 4ME) (b) pressure (denoted ψ_{1ME} or ψ_{4ME}, respectively; **eq 2.18**) as a function of H_2 pressure at 393 (■), 413 (♦), 493 (●), 533 (▲) K. Solid lines indicate trends and dashed lines at the lower and upper sides of the grey triangle enclosing each isotherm illustrate the trends for one-half- and first-order H_2-pressure dependences, respectively.

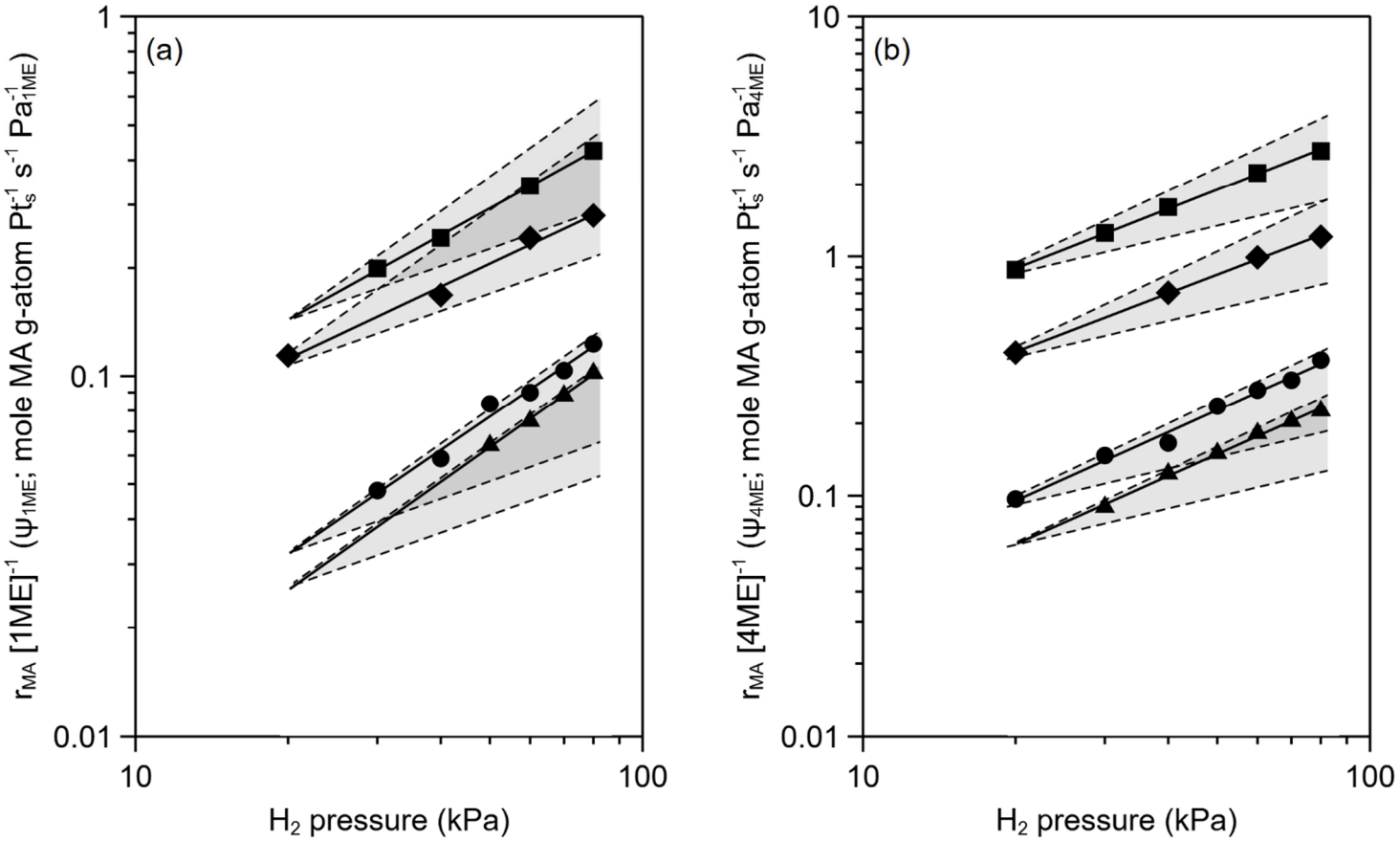

Figure 2.7: DFT-derived enthalpies ((a); 393 K), entropies ((b); ●, 393 K), and Gibbs free energies ((c); ●, 393 K; □, 493 K) for the formation of surface species (depicted in **Scheme 2.2** and **Scheme 2.3**) from gaseous toluene and H_2 at 0.11 ML coverage (**Table 2.2**) as a function of the number of H atoms added to or removed from toluene. Reported entropies to form gaseous toluene hydrogenation products from toluene(g) and H_2(g) [51] ((b); □, 393 K) as functions of the number of H atoms added to or removed from toluene. Dashed lines indicate linear trends. The slope for the entropies of formation of surface species is -73 J K^{-1} g-atom H^{-1} ((b); ●) and the slope for the entropies of formation of gaseous species is -66 J K^{-1} g-atom H^{-1} ((b); □).

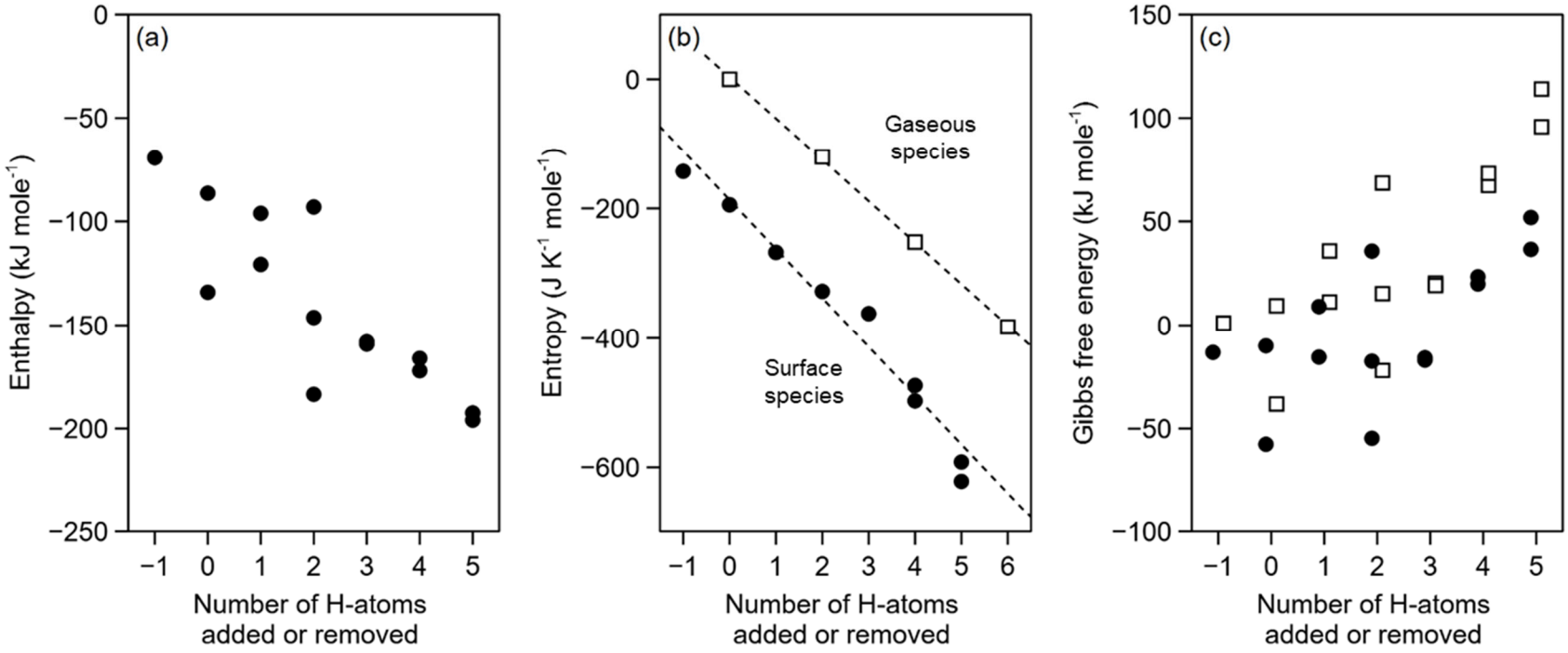

Figure 2.8: Logarithmic plot of parity for measured and predicted (**eq 2.33**) methylcyclohexane (MA) formation turnover rates (moles MA g-atoms surface Pt $(Pt_s)^{-1}$ s^{-1}) with temperature dependent parameters from **equations 2.40** and **2.42** with regressed values reported in **Table 2.4** at 333 (●), 353 (■), 373 (♦), and 393 (▲) K (20-80 kPa H_2, 0.3-3 kPa toluene) on Pt/SiO_2 (3.6 nm mean nanocluser diameter). Dashed line indicates parity.

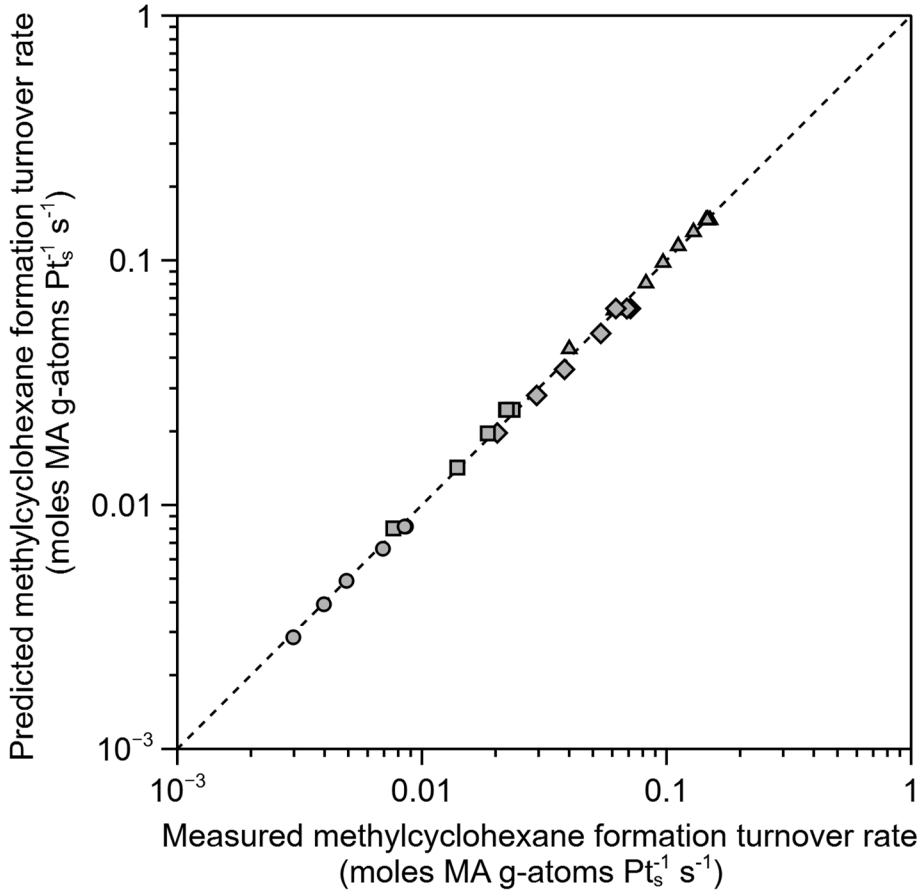

Figure 2.9: Ratio of methylcyclohexane (MA) formation turnover rates (r_{MA}) to 1-methylcyclohexene (1ME; filled symbols) or 4-methylcyclohexene (4ME; open symbols) pressure (denoted ψ_{1ME} or ψ_{4ME}, respectively (**eq 2.18**)) as a function of toluene pressure at 493 (●), 533 (▲) K. Solid lines indicate trends and dashed lines at the lower and upper sides of the grey triangle enclosing each isotherm illustrate the trends for zero- and negative-first-order toluene-pressure dependences, respectively.

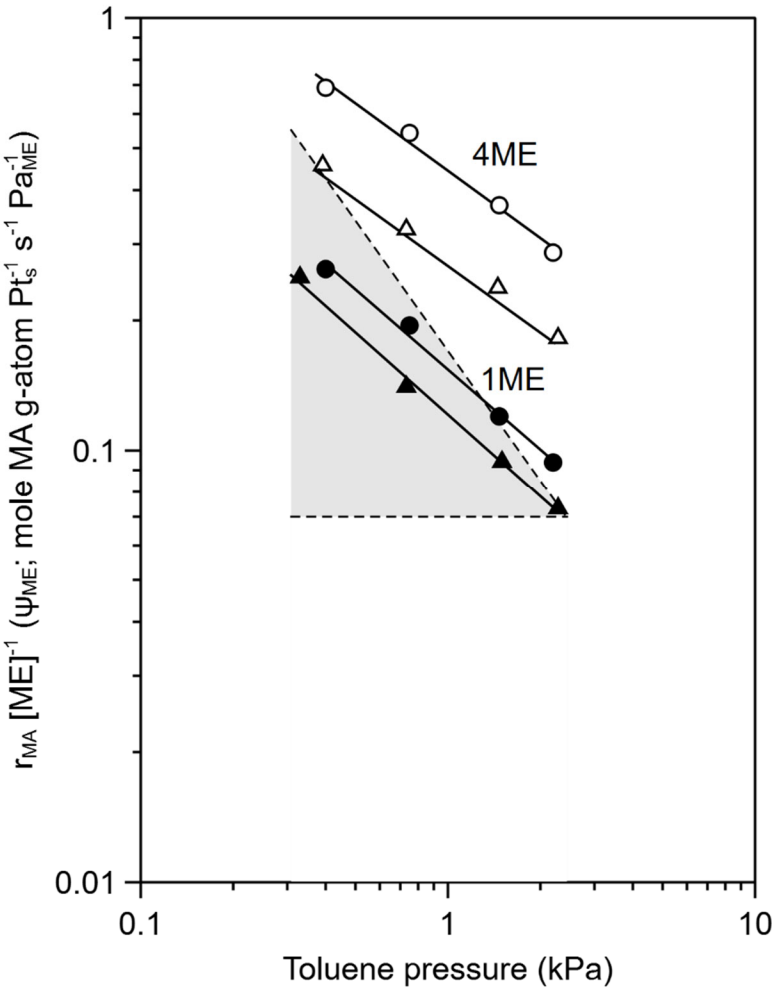

Figure 2.10: Logarithmic plot of parity for measured and predicted methylcyclohexane (MA) formation turnover rates (moles MA g-atoms surface Pt $(Pt_s)^{-1}$ s^{-1}) for rates predicted from **equation (**2.55) using observed 1ME (filled symbols) and 4ME (open symbols) pressures at 493 (●), 513 (▲), and 533 (◆) K (20-80 kPa H_2, 0.3-3 kPa toluene) with temperature dependent parameters from **equation 2.57** and with regressed values reported in **Table 2.4**. Dashed line indicates parity.

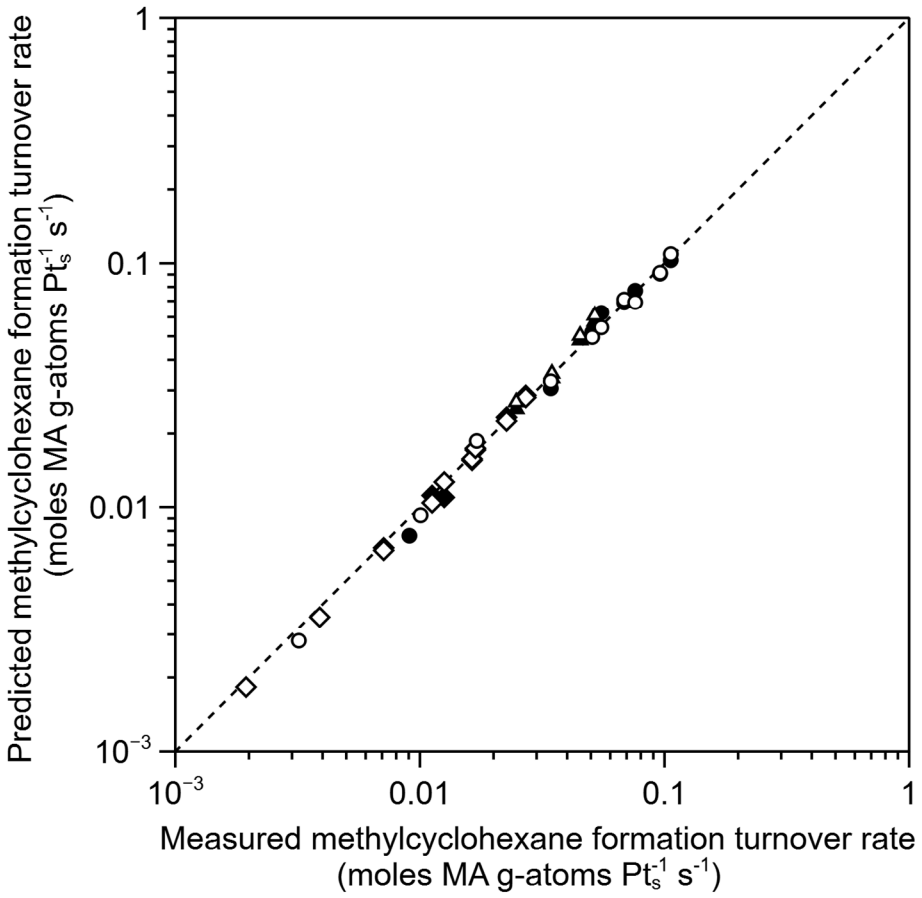

Table 2.1: Pt loading, Pt fractional dispersion (D), mean Pt cluster diameter (d_{Pt}), and temperatures for air and H_2 treatments during synthesis for the Pt/SiO_2 catalyst.

	Pt/SiO_2
Pt loading (wt.%)[a]	2.1
Pt fractional dispersion (D)[b]	0.30
Mean Pt cluster diameter, d_{Pt} [c] (nm)	3.6
Treatment temperature (K): air, [H_2]	873, [773]

[a] From inductively coupled plasma – atomic emission spectroscopy.

[b] Metal dispersion (D) from H_2 uptake data, defined as $D = N_H/N_B$, where N_H is the number of H bound by the Pt surface and N_B is the number of metal atoms in the bulk.

[c] Mean Pt cluster diameter from the Pt dispersion with the following relation: $d_{Pt} = 6\,v_{Pt}/(D\,a_{Pt})$ [56], where v_{Pt} is the atomic volume of a Pt-atom in metal (15.10 x 10^{-3} nm^3) and a_{Pt} is the occupied area of a Pt-atom on a bulk Pt(111) surface for an FCC lattice (6.7 x 10^{-2} nm^{-2} [57]), the lowest energy crystal facet.

Table 2.2: DFT-derived changes in electronic energy at 0 K (ΔE), enthalpy (ΔH), entropy (ΔS), and Gibbs free energy (ΔG) to form bound methylenebenzene, toluene, and partially-hydrogenated toluene-derivatives with *n* number of H atoms added from toluene(g) and *n*/2 H_2(g) at 0.11 ML coverage on Pt (111) (**eq 2.2**, **2.5**, and **2.6**). Optimized geometries for these bound species are depicted in **Scheme 2.2** and **Scheme 2.3**.

Hydrocarbon moiety	H atoms added	Binding site[a]	ΔE (kJ mol^{-1})	ΔH[b] (kJ mol^{-1})	ΔS[b] (J mol^{-1} K^{-1})	ΔG_{393K}[c] (kJ mol^{-1})	ΔG_{493K}[d] (kJ mol^{-1})
Methylenebenzene	-1	four-fold bridge	-90.2	-69.3	-143	-13	1
Toluene	0	four-fold bridge	-146	-134	-194	-57	-38
	0	hcp hollow	-98.7	-86.4[e]	-194[e]	-10.	9
2-Methyl-6-hydrobenzene	1	four-fold bridge	-119	-96.1	-268	9	35
1-Methyl-6-hydrobenzene	1	hcp hollow	-144	-121[e]	-268[e]	-15	11
1-Methyl-5,6-dihydrobenzene	2	four-fold bridge	-129	-93.1[e]	-328[e]	35	68
	2	hcp hollow	-182	-146	-328	-17	15
1-Methyl-3,6-dihydrobenzene	2	two-fold bridge	-219	-184	-323	-56	-24
2-Methyl-4,5,6-trihydrobenzene	3	hcp hollow	-204	-158	-362	-15	20
5-Methyl-4,5,6-trihydrobenzene	3	hcp hollow	-206	-159[e]	-362[e]	-17	19
1-Methylcyclohexene	4	two-fold bridge	-226	-156	-438	9	52
4-Methylcyclohexene	4	two-fold bridge	-230.	-160.	-438[e]	5	49
1-Methylcyclohexyl	5	atop	-250.	-175	-481	13	62
4-Methylcyclohexyl	5	atop	-256.	-181[e]	-481[e]	8	56

[a] Binding sites correspond to positions on the Pt(111) surface as depicted in **Scheme 2.S1**.

[b] ΔH and ΔS values are computed at 393 K using methods reported in **Section 2.8.2**.

[c] ΔG_{393K} values from ΔH and ΔS (**eq 2.4**) (393 K, 1 bar).

[d] ΔG_{493K} values from ΔH and ΔS (**eq 2.4**) (493 K, 1 bar).

[e] The vibrational frequencies used to calculate these ΔH and ΔS values were approximated by values calculated for the other isomers (i.e. toluene hcp hollow from toluene four-fold bridge, 1-methyl-6-hydrobenzene from 2-methyl-6-hydrobenzene, 1-methyl-5,6-dihydrobenzene bridge from 1-methyl-5,6-dihydrobenzene hcp hollow, 5-Methyl-4,5,6-trihydrobenzene from 2-methyl-4,5,6-trihydrobenzene, 4-methylcyclohexene from 1-methycyclohexene, and 4-methylcyclohexyl from 1-methylcyclohexyl).

Table 2.3: DFT-derived electronic energies at 0 K (ΔE), enthalpies (ΔH), entropies (ΔS), and Gibbs free energies (ΔG) to form bound 1-methylcyclohexene and 1-methylcyclohexyl or 4-methylcyclohexene and 4-methylcyclohexyl (**Scheme 2.3**) from 1ME(g) or 4ME(g), *n*/2 H_2(g) (where *n* is the number of H atoms added to 1ME(g) or 4ME(g) to form the bound species), and bare Pt at 0.11 ML coverage on Pt (111) (**eq 2.3-2.6**).

Hydrocarbon moiety	Temperature (K)	Binding site[a]	ΔE (kJ mol^{-1})	ΔH[b] (kJ mol^{-1})	ΔS[b] (J mol^{-1} K^{-1})	ΔG[c] (kJ mol^{-1})
1-Methylcyclo-hexene	393	two-fold bridge	-122	-118	-168	-52
	493	two-fold bridge	-122	-119	-170	-35
4-Methylcyclo-hexene[d]	393	two-fold bridge	-132	-129	-168	-63
	493	two-fold bridge	-132	-130	-170	-46
1-Methylcyclo-hexyl	493	atop	-146	-130.	-212	-26
4-Methylcyclo-hexyl[d]	493	atop	-159	-143	-212	-39

[a] Binding sites correspond to positions on the Pt(111) surface as depicted in **Scheme 2.S1**.
[b] ΔH and ΔS values are computed using methods reported in **Section 2.8.2**
[c] ΔG values from ΔH and ΔS (**eq 2.4**) (493 K, 1 bar).
[d] The ZPE and enthalpic contributions to ΔH and ΔS values for the 4-methylcyclohexene and 4-methylcyclohexyl structures were approximated by values calculated for the respective 1-methyl isomers.

Table 2.4: Enthalpies (ΔH), entropies (ΔS), and free energies (ΔG) for $k_{2H,tol}$ (**eq 2.40**) and $K_{H,S}$ (**eq 2.42**) determined by regressing methylcyclohexane (MA) formation turnover rate (moles MA g-atoms surface Pt $(Pt_s)^{-1}$ s^{-1}) data[a] to the functional form of **equation 2.33**. ΔH, ΔS, and ΔG values for $k_{2H,1ME}$ and $k_{2H,4ME}$ (**eq 2.57**) and ε values (**eq 2.52**) determined by regressing the MA formation turnover rate, 1ME or 4ME pressure, and ζ_{1ME} or ζ_{4ME} (**eq 2.59**) data[b] to the functional form of **equation 2.55**.[c]

Parameter	ΔH (kJ mol^{-1})	ΔS (J mol^{-1} K^{-1})	ΔG (kJ mol^{-1})[d]	ε
$k_{2H,tol}$	41 ± 5	-150 ± 10	100 ± 6[d]	
$K_{H,S}$	-26 ± 6	-50 ± 30	0 ± 20[d]	
$k_{2H,1ME}$	-14 ± 4	-220 ± 10	94 ± 6[e]	0.54 ± 0.04
$k_{2H,4ME}$	-29 ± 4	-240 ± 10	89 ± 6[e]	0.51 ± 0.06

[a] 333-393 K, 0.35-2.1 kPa toluene, 10-80 kPa H_2, on Pt/SiO_2 (3.6 nm mean cluster diameter).
[b] 493-533 K, 0.35-2.1 kPa toluene, 10-80 kPa H_2, on Pt/SiO_2 (3.6 nm mean cluster diameter).
[c] Uncertainties reflect 95% confidence intervals for regressed parameters.
[d] ΔG values from ΔH and ΔS (**eq 2.4**) (493 K, 1 bar).

Scheme 2.1. Proposed sequence of elementary steps for toluene hydrogenation on Pt surfaces as described in **Section 2.3.2**. T denotes toluene and TH_n denotes ensembles of partially hydrogenated toluene-derived species with the same number of added H atoms (where $1 \leq n \leq 6$). R-* denotes a hydrocarbon surface intermediate bound to *-sites and H-*S* denotes bound H atoms. K_x denotes equilibrium adsorption constants and k_x and k_{-x} denote the forward and reverse kinetic constants for the elementary steps. Single forward arrow denote irreversible steps, forward and backward arrows denote reversible steps, and circled forward and backward arrows denote quasi-equilibrated steps.

$$T + \gamma_{tol}^{*} \overset{K_{tol}}{\rightleftharpoons} T^{*} \quad (1.1)$$

$$H_2 + 2\,S \overset{K_{H2}}{\rightleftharpoons} 2\,H\text{-}S \quad (1.2)$$

$$T^{*} + H\text{-}S \underset{k_{-CH,1}}{\overset{k_{CH,1}}{\rightleftharpoons}} TH^{*} + \gamma_{\Delta CH,1}^{*} + S \quad (1.3)$$

$$TH^{*} + H\text{-}S \underset{k_{-CH,2}}{\overset{k_{CH,2}}{\rightleftharpoons}} TH_2^{*} + \gamma_{\Delta CH,2}^{*} + S \quad (1.4)$$

$$TH_2^{*} + H\text{-}S \underset{k_{-CH,3}}{\overset{k_{CH,3}}{\rightleftharpoons}} TH_3^{*} + \gamma_{\Delta CH,3}^{*} + S \quad (1.5)$$

$$TH_3^{*} + H\text{-}S \underset{k_{-CH,4}}{\overset{k_{CH,4}}{\rightleftharpoons}} TH_4^{*} + \gamma_{\Delta CH,4}^{*} + S \quad (1.6)$$

$$TH_4^{*} + H\text{-}S \underset{k_{-CH,5}}{\overset{k_{CH,5}}{\rightleftharpoons}} TH_5^{*} + \gamma_{\Delta CH,5}^{*} + S \quad (1.7)$$

$$TH_5^{*} + H\text{-}S \underset{k_{-CH,6}}{\overset{k_{CH,6}}{\rightleftharpoons}} TH_6 + \gamma_{\Delta CH,6}^{*} + S \quad (1.8)$$

$$TH_4^{*} \overset{K_{ME}}{\rightleftharpoons} TH_4 + \gamma_{ME}^{*} \quad (1.9)$$

Scheme 2.2. Top and side view of DFT-derived optimized geometries for methylenebenzene, toluene, hydrobenzene, and dihydrobenzene species on Pt(111) slab (3x3 unit cell with four Pt layers). The bottom three Pt layers are omitted for clarity.

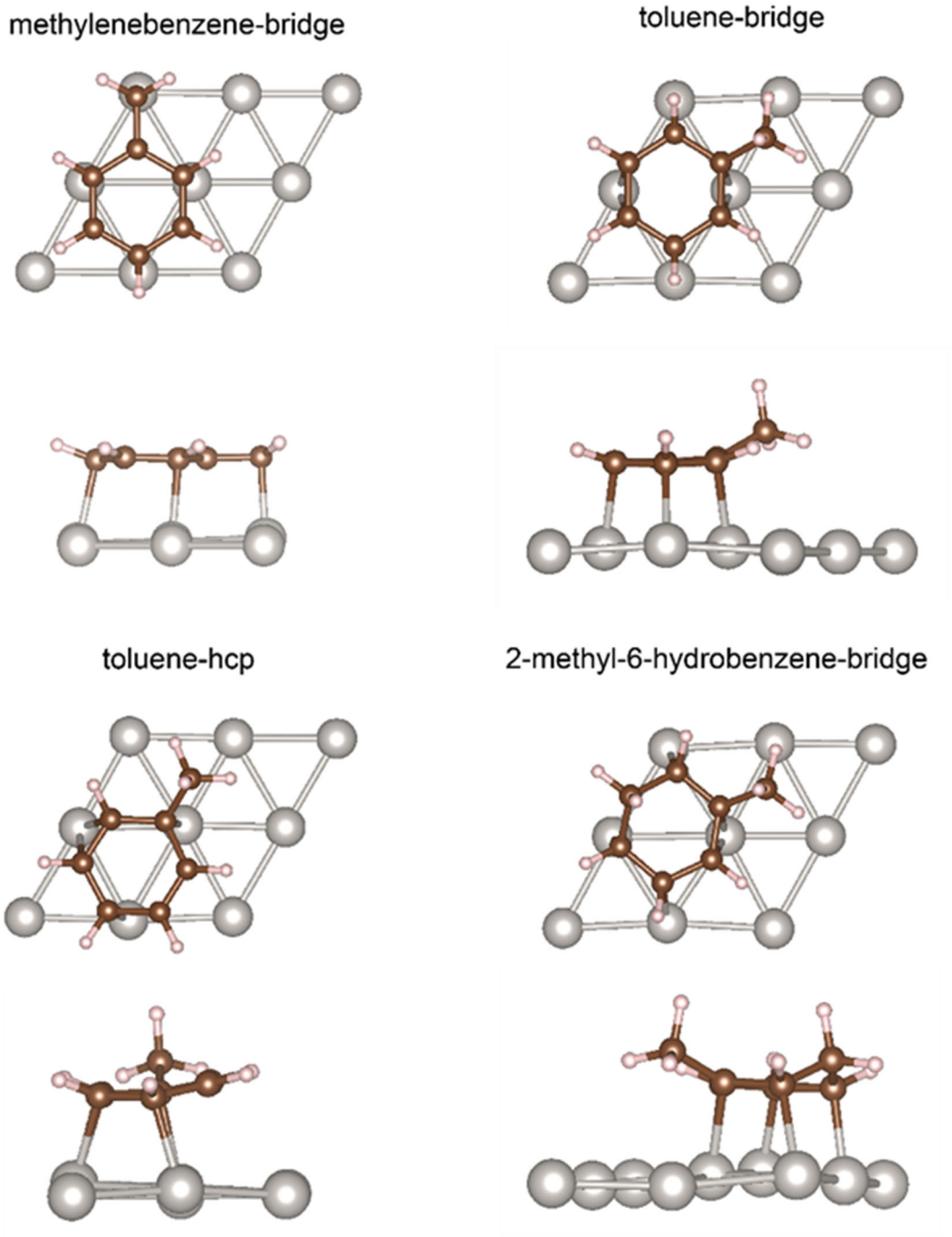

1-methyl-6-hydrobenzene-hcp

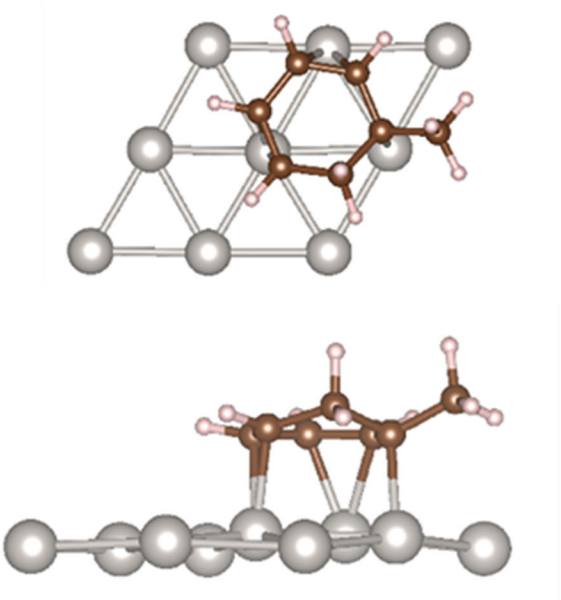

1-methyl-5,6-dihydrobenzene-bridge

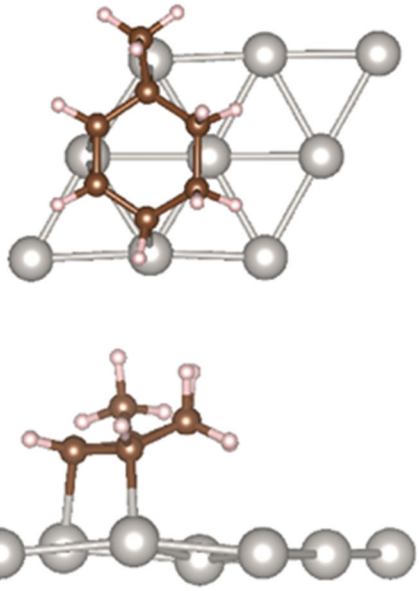

1-methyl-5,6-dihydrobenzene-hcp

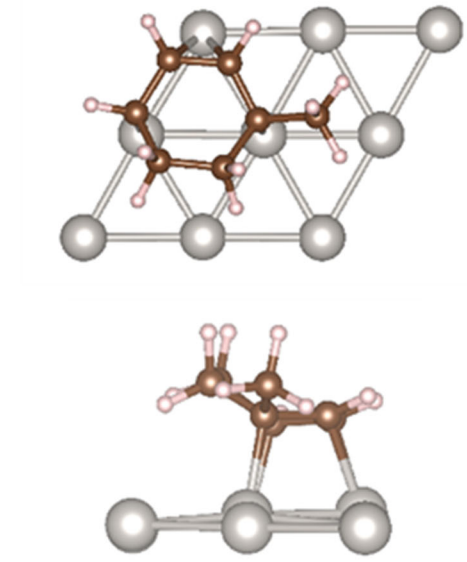

1-methyl-3,6-dihydrobenzene-bridge

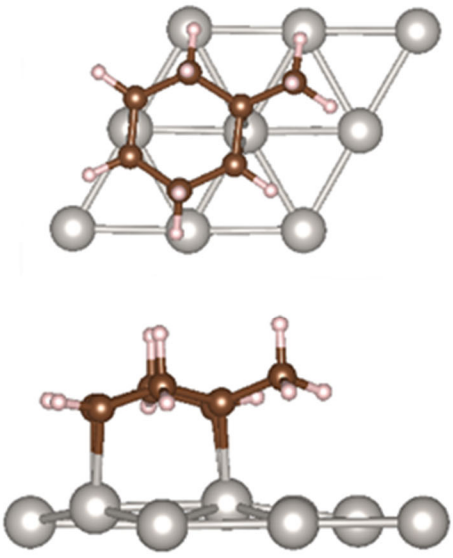

Scheme 2.3. Top and side view of DFT-derived optimized geometries for trihydrobenzene, methylcyclohexene, and methylcyclohexyl species on Pt(111) slab (3x3 unit cell with four Pt layers). The bottom three Pt layers are omitted for clarity.

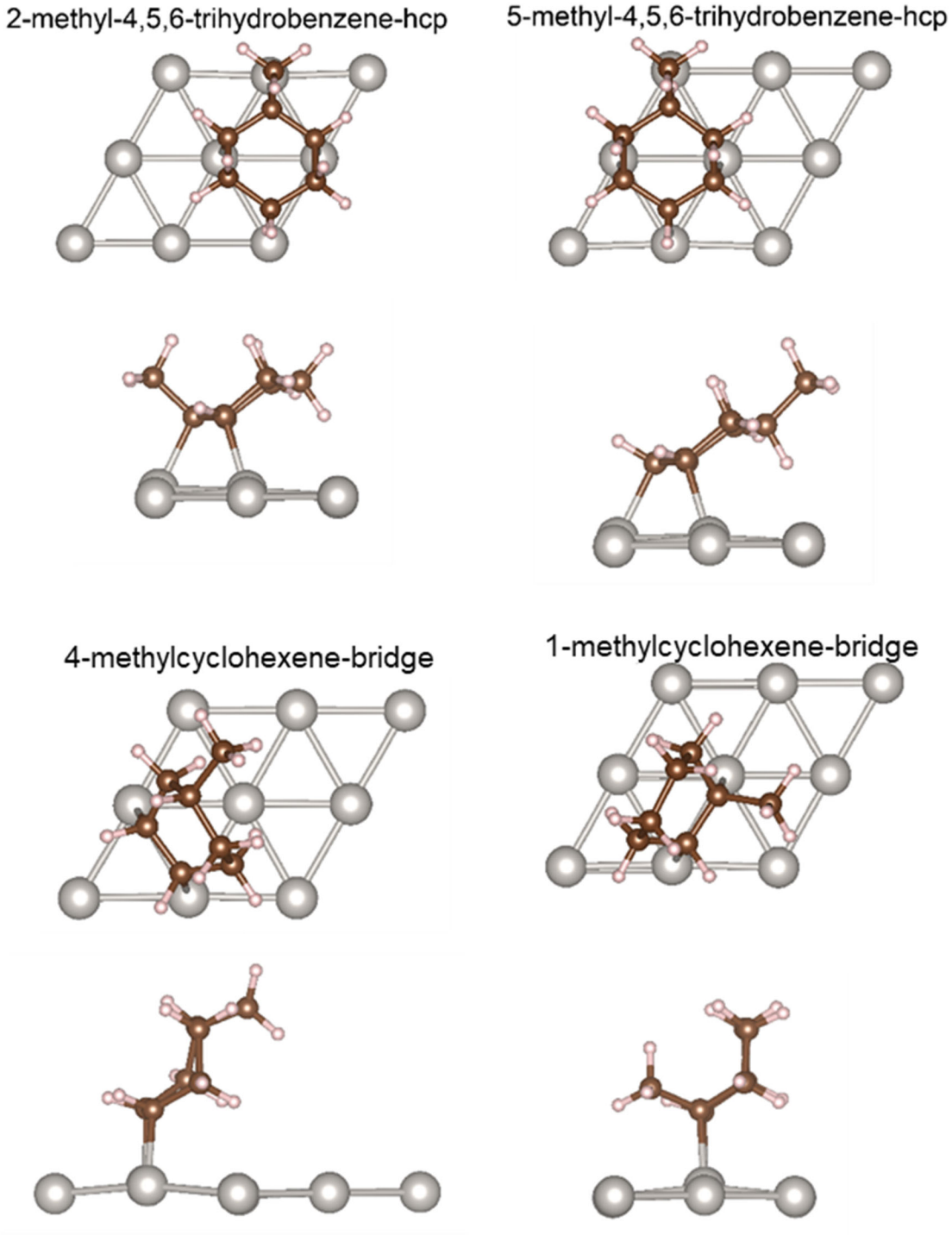

4-methylcyclohexyl-atop

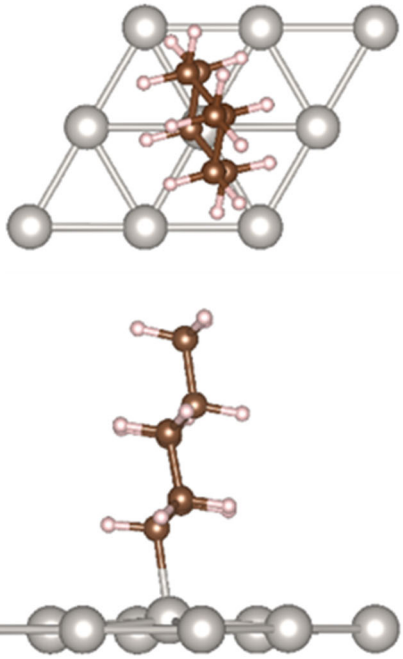

1-methylcyclohexyl-atop

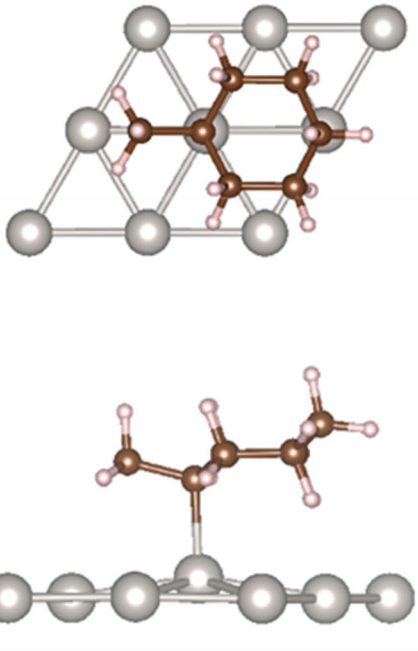

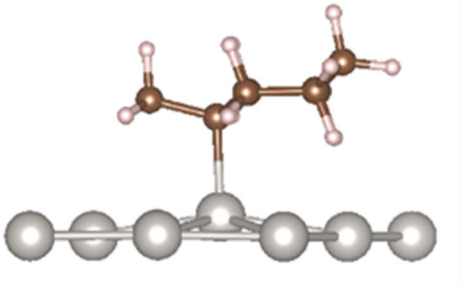

2.7 References

[1] A. Stanislaus, H.C. Barry, Aromatic hydrogenation catalysis: A review, Catal. Rev. Eng. 36 (1994) 75–123. https://doi.org/10.1080/01614949408013921.

[2] A.H. Zacher, M. V. Olarte, D.M. Santosa, D.C. Elliott, S.B. Jones, A review and perspective of recent bio-oil hydrotreating research, Green Chem. 16 (2014) 491–515. https://doi.org/10.1039/c3gc41382a.

[3] P.M. Modisha, C.N.M. Ouma, R. Garidzirai, P. Wasserscheid, D. Bessarabov, The prospect of hydrogen storage using liquid organic hydrogen carriers, Energy and Fuels. 33 (2019) 2778–2796. https://doi.org/10.1021/acs.energyfuels.9b00296.

[4] S.D. Lin, M.A. Vannice, Hydrogenation of aromatic hydrocarbons over supported Pt catalysts: I. Benzene hydrogenation, J. Catal. 143 (1993) 539–553. https://doi.org/10.1006/jcat.1993.1297.

[5] G.C. Bond, Metal-catalysed reactions of hydrocarbons, Springer, 2005. https://doi.org/10.1016/s1351-4180(06)71746-9.

[6] R.B. Moyes, P.B. Wells, The chemisorption of benzene, Adv. Catal. 23 (1973) 121–156. https://doi.org/10.1016/S0360-0564(08)60300-4.

[7] M. Saeys, M. Neurock, G.B. Marin, T. Hall, V. Charlottes, Density functional theory analysis of benzene (de)hydrogenation on Pt(111): Addition and removal of the first two H-atoms, J. Phys. Chem. B. 107 (2003) 3844–3855.

[8] M. Saeys, M.F. Reyniers, M. Neurock, G.B. Marin, Ab initio reaction path analysis of benzene hydrogenation to cyclohexane on Pt(111), J. Phys. Chem. B. 109 (2005) 2064–2073. https://doi.org/10.1021/jp049421j.

[9] M. Saeys, M.F. Reyniers, M. Neurock, G.B. Marin, Adsorption of cyclohexadiene, cyclohexene and cyclohexane on Pt(1 1 1), Surf. Sci. 600 (2006) 3121–3134. https://doi.org/10.1016/j.susc.2006.05.059.

[10] S.D. Lin, M.A. Vannice, Hydrogenation of aromatic hydrocarbons over supported Pt catalysts: II. Toluene hydrogenation, J. Catal. 143 (1993) 554–562. https://doi.org/10.1006/jcat.1993.1298.

[11] T. Bera, J.W. Thybaut, G.B. Marin, Single-Event microkinetics of aromatics hydrogenation on Pt/H-ZSM22, Ind. Eng. Chem. Res. 50 (2011) 12933–12945. https://doi.org/10.1021/ie200541q.

[12] K.M. Bratlie, L.D. Flores, G.A. Somorjai, In situ sum frequency generation vibrational spectroscopy observation of a reactive surface intermediate during high-pressure benzene hydrogenation, J. Phys. Chem. B. 110 (2006) 10051–10057. https://doi.org/10.1021/jp0612735.

[13] O. Lytken, W. Lew, J.J.W. Harris, E.K. Vestergaard, J.M. Gottfried, C.T. Campbell, Energetics of cyclohexene adsorption and reaction on Pt(111) by low-temperature microcalorimetry, J. Am. Chem. Soc. 130 (2008) 10247–10257. https://doi.org/10.1021/ja801856s.

[14] H. Ihm, H.M. Ajo, J.M. Gottfried, P. Bera, C.T. Campbell, Calorimetric measurement of the heat of adsorption of benzene on Pt(111), J. Phys. Chem. B. 108 (2004) 14627–14633. https://doi.org/10.1021/jp040159o.

[15] M. Montano, M. Salmeron, G.A. Somorjai, STM studies of cyclohexene hydrogenation/dehydrogenation and its poisoning by carbon monoxide on Pt(1 1 1), Surf. Sci. 600 (2006) 1809–1816. https://doi.org/10.1016/j.susc.2006.02.026.

[16] K.M. Bratlie, M.O. Montano, L.D. Flores, M. Paajanen, G.A. Somorjai, Sum frequency

generation vibrational spectroscopic and high-pressure scanning tunneling microscopic studies of benzene hydrogenation on Pt(111), J. Am. Chem. Soc. 128 (2006) 12810–12816. https://doi.org/10.1021/ja0626032.
[17] J.L. Gland, G.A. Somorjai, Low energy electron diffraction and work function studies of benzene, naphthalene and pyridine adsorbed on Pt(111) and Pt(100) single crystal surfaces, Surf. Sci. 38 (1973) 157–186. https://doi.org/10.1016/0039-6028(73)90281-1.
[18] X. Su, K.Y. Kung, J. Lahtinen, Y.R. Shen, G.A. Somorjai, 1,3- and 1,4-cyclohexadiene reaction intermediates in cyclohexene hydrogenation and dehydrogenation on Pt(111) crystal surface: A combined reaction kinetics and surface vibrational spectroscopy study using sum frequency generation, J. Mol. Catal. A Chem. 141 (1999) 9–19. https://doi.org/10.1016/S1381-1169(98)00245-3.
[19] M. Yang, K.C. Chou, G.A. Somorjai, The structures and reactions of linear and cyclic C6 hydrocarbons adsorbed on the Pt(111) crystal surface studied by sum frequency generation vibrational spectroscopy: Pressure, temperature, and H_2 coadsorption effects, J. Phys. Chem. B. 108 (2004) 14766–14779. https://doi.org/10.1021/jp048238n.
[20] M.K. Sabbe, G. Canduela-rodriguez, M. Reyniers, G.B. Marin, DFT-based modeling of benzene hydrogenation on Pt at industrially relevant coverage, J. Catal. 330 (2015) 406–422. https://doi.org/10.1016/j.jcat.2015.08.003.
[21] M.C. Schoenmaker-Stolk, J.W. Verwijs, J.A. Don, J.J.F. Scholten, The catalytic hydrogenation of benzene over supported metal catalysts: I. Gas-phase hydrogenation of benzene over ruthenium-on-silica, Appl. Catal. 29 (1987) 73–90. https://doi.org/https://doi.org/10.1016/S0166-9834(00)82608-1.
[22] P.J. Van Der Steen, J.J.F. Scholten, Selectivity to cyclohexene in the gas phase hydrogenation of benzene over ruthenium, as influenced by reaction modifiers: II. Catalytic hydrogenation of benzene to cyclohexene and cyclohexane, Appl. Catal. 58 (1990) 291–304. https://doi.org/https://doi.org/10.1016/S0166-9834(00)82297-6.
[23] M.K. Sabbe, G. Canduela-Rodriguez, M.F. Reyniers, G.B. Marin, DFT-based modeling of benzene hydrogenation on Pt at industrially relevant coverage, J. Catal. 330 (2015) 406–422. https://doi.org/10.1016/j.jcat.2015.08.003.
[24] M.K. Sabbe, G. Canduela-Rodriguez, J.F. Joly, M.F. Reyniers, G.B. Marin, Ab initio coverage-dependent microkinetic modeling of benzene hydrogenation on Pd(111), Catal. Sci. Technol. 7 (2017) 5267–5283. https://doi.org/10.1039/c7cy00962c.
[25] S.D. Lin, M.A. Vannice, Hydrogenation of aromatic hydrocarbons over supported pt catalysts: III. Reaction models for metal surfaces and acidic sites on oxide supports, J. Catal. 143 (1993) 563–572. https://doi.org/10.1006/jcat.1993.1299.
[26] T. Nitta, M. Kuro-Oka, T. Katayama, An adsorption isotherm of multi-site occupancy model for heterogeneous surface, J. Chem. Eng. Japan. 17 (1984) 45–52. https://doi.org/10.1252/jcej.17.45.
[27] M.A. Keane, P.M. Patterson, Compensation behaviour in the hydrogenation of benzene, toluene and o-xylene over Ni/SiO2. Determination of true activation energies, J. Chem. Soc., Faraday Trans. 92 (1996) 1413–1421. https://doi.org/10.1039/FT9969201413.
[28] G. Kresse, J. Hafner, Ab initio molecular dynamics for liquid metals, Phys. Rev. B. 47 (1993) 558–561. https://doi.org/10.1103/PhysRevB.47.558.
[29] G. Kresse, J. Hafner, Ab initio molecular-dynamics simulation of the liquid-metalamorphous- semiconductor transition in germanium, Phys. Rev. B. 49 (1994) 14251–14269. https://doi.org/10.1103/PhysRevB.49.14251.

[30] G. Kresse, J. Furthmüller, Efficient iterative schemes for ab initio total-energy calculations using a plane-wave basis set, Phys. Rev. B. 54 (1996) 169–186. https://doi.org/10.1021/acs.jpca.0c01375.
[31] G. Kresse, J. Furthmüller, Efficiency of ab-initio total energy calculations for metals and semiconductors using a plane-wave basis set, Comput. Mater. Sci. 6 (1996) 15–50. https://doi.org/10.1016/0927-0256(96)00008-0.
[32] D. Joubert, From ultrasoft pseudopotentials to the projector augmented-wave method, Phys. Rev. B - Condens. Matter Mater. Phys. 59 (1999) 1758–1775. https://doi.org/10.1103/PhysRevB.59.1758.
[33] P.E. Blöchl, Projector augmented-wave method, Phys. Rev. B. 50 (1994) 17953–17979. https://doi.org/10.1103/PhysRevB.50.17953.
[34] J. Carrasco, W. Liu, A. Michaelides, A. Tkatchenko, Insight into the description of van der Waals forces for benzene adsorption on transition metal (111) surfaces, J. Chem. Phys. 140 (2014). https://doi.org/10.1063/1.4866175.
[35] J. Klimeš, D.R. Bowler, A. Michaelides, Chemical accuracy for the van der Waals density functional, J. Phys. Condens. Matter. 22 (2010). https://doi.org/10.1088/0953-8984/22/2/022201.
[36] M. Dion, H. Rydberg, E. Schröder, D.C. Langreth, B.I. Lundqvist, Van der Waals density functional for general geometries, Phys. Rev. Lett. 92 (2004) 22–25. https://doi.org/10.1103/PhysRevLett.92.246401.
[37] G. Román-Pérez, J.M. Soler, Efficient implementation of a van der Waals density functional: Application to double-wall carbon nanotubes, Phys. Rev. Lett. 103 (2009) 1–4. https://doi.org/10.1103/PhysRevLett.103.096102.
[38] S. Gautier, S.N. Steinmann, C. Michel, P. Fleurat-Lessard, P. Sautet, Molecular adsorption at Pt(111). How accurate are DFT functionals?, Phys. Chem. Chem. Phys. 17 (2015) 28921–28930. https://doi.org/10.1039/c5cp04534g.
[39] D. McQuarrie, J. Simon, Molecular Thermodynamics, University Science Books, 1999.
[40] F. Zaera, The Surface Chemistry of Metal-Based Hydrogenation Catalysis, ACS Catal. 7 (2017) 4947–4967. https://doi.org/10.1021/acscatal.7b01368.
[41] G.C. Bond, P.B. Wells, The mechanism of the hydrogenation of unsaturated hydrocarbons on transition metal catalysts, in: Adv. Catal., 1965: pp. 91–226. https://doi.org/10.1016/S0360-0564(08)60554-4.
[42] M. Boudart, G. Djega-Mariadassou, Kinetics of Heterogeneous Catalytic Reactions, Princeton University Press, 1984.
[43] J.E. Rekoske, R.D. Cortright, S.A. Goddard, S.B. Sharma, J.A. Dumesic, Microkinetic analysis of diverse experimental data for ethylene hydrogenation on platinum, J. Phys. Chem. 96 (1992) 1880–1888. https://doi.org/10.1021/j100183a067.
[44] R.D. Cortright, S.A. Goddard, J.E. Rekoske, J.A. Dumesic, Kinetic study of ethylene hydrogenation, J. Catal. 127 (1991) 342–353. https://doi.org/10.1016/0021-9517(91)90230-2.
[45] L.P. Lindfors, T. Salmi, S. Smeds, Kinetics of toluene hydrogenation on a supported Ni catalyst, Chem. Eng. Sci. 48 (1993) 3813–3828. https://doi.org/10.1016/0009-2509(93)80224-E.
[46] C. Morin, D. Simon, P. Sautet, Intermediates in the hydrogenation of benzene to cyclohexene on Pt(111) and Pd(111): A comparison from DFT calculations, Surf. Sci. 600 (2006) 1339–1350. https://doi.org/10.1016/j.susc.2006.01.033.

[47] A. Clark, The theory of adsorption and catalysis, Academic Press, New York, 1970.
[48] C. Kemball, The catalytic exchange of hydrocarbons with deuterium, in: Adv. Catal., 1959: pp. 223–262. https://doi.org/10.1016/S0360-0564(08)60419-8.
[49] J.R. Anderson, C. Kemball, Catalytic exchange and deuteration of benzene over evaporated metallic films in a static system, in: Adv. Catal., 1957: pp. 51–64. https://doi.org/10.1016/S0360-0564(08)60153-4.
[50] I.A. Yursha, G.Y. Kabo, D.N. Andreevskii, Equilibriums and thermodynamics of the isomerization of methylcyclohexenes, Neftekhimiya. 14 (1974) 688–693.
[51] K. Kroenlein, C. Muzny, A. Kazakov, V. Diky, R. Chirico, J. Magee, I. Abdulagatov, M. Frenkel, NIST/TRC Web Thermo Tables (WTT) NIST Standard Reference Subscription Database 3 - Professional Edition Version 2, (2011).
[52] H. Eyring, The activated complex in chemical reactions, J. Chem. Phys. 3 (1935) 63–71. https://doi.org/10.1063/1.1749604.
[53] W.F.K. Wynne-Jones, H. Eyeing, The absolute rate of reactions in condensed phases, J. Chem. Phys. 3 (1935) 492–502. https://doi.org/10.1063/1.1749713.
[54] M. García-Diéguez, D.D. Hibbitts, E. Iglesia, Hydrogen chemisorption isotherms on platinum particles at catalytic temperatures: Langmuir and two-dimensional gas models revisited, J. Phys. Chem. C. 123 (2019) 8447–8462. https://doi.org/10.1021/acs.jpcc.8b10877.
[55] P.R. Norton, P.J. Richards, The heat of adsorption of hydrogen on platinum, Surf. Sci. 44 (1974) 129–140.
[56] G. Ertl, K. Helmut, F. Schüth, J. Weitkamp, Handbook of Heterogeneous Catalysis, 2nd edition, Wiley-VCH, 2008.
[57] W.P. Davey, Precision Measurements of the Lattice Constants of Twelve Common Metals, Phys. Rev. 25 (1925) 753–761. https://doi.org/10.1103/PhysRev.25.753.
[58] A. Hjorth Larsen, J. JØrgen Mortensen, J. Blomqvist, I.E. Castelli, R. Christensen, M. Dułak, J. Friis, M.N. Groves, B. Hammer, C. Hargus, E.D. Hermes, P.C. Jennings, P. Bjerre Jensen, J. Kermode, J.R. Kitchin, E. Leonhard Kolsbjerg, J. Kubal, K. Kaasbjerg, S. Lysgaard, J. Bergmann Maronsson, T. Maxson, T. Olsen, L. Pastewka, A. Peterson, C. Rostgaard, J. SchiØtz, O. Schütt, M. Strange, K.S. Thygesen, T. Vegge, L. Vilhelmsen, M. Walter, Z. Zeng, K.W. Jacobsen, The atomic simulation environment - A Python library for working with atoms, J. Phys. Condens. Matter. 29 (2017). https://doi.org/10.1088/1361-648X/aa680e.
[59] A. Clark, The Chemisorptive Bond, 1st Editio, Oxford : Elsevier Science, 1974. https://doi.org/10.1016/b978-0-12-175440-2.50007-2.
[60] S.J. Carey, W. Zhao, C.T. Campbell, Energetics of adsorbed benzene on Ni(111) and Pt(111) by calorimetry, Surf. Sci. 676 (2018) 9–16. https://doi.org/10.1016/j.susc.2018.02.014.
[61] J.A. Rodriguez, C.T. Campbell, Cyclohexene adsorption and reactions on clean and bismuth-covered Pt(111), J. Catal. 115 (1989) 500–520. https://doi.org/10.1016/0021-9517(89)90053-5.

2.8 Supporting information

2.8.1. Hydrogen adsorption isotherms on Pt/SiO_2 and estimation of Pt particle dispersions.

Pt-particle dispersions ($D = N_H/N_B$, where N_H is the number of H bound by the metal surface and N_B is the number of metal atoms in the bulk) were calculated from H_2 adsorption isotherms measured using a volumetric adsorption apparatus with a Baratron gauge and a turbomolecular pump (Pfeiffer Vacuum, <1 Pa dynamic vacuum), using $H/Pt_s=1$ adsorption stoichiometry. Hydrogen adsorption isotherms (shown in **Figure 2.S1**) were measured at H_2 pressures ranging from 5-105 kPa at 373 K on evacuated catalysts ($<10^{-2}$ mbar, 573 K, 1 h) following treatment in H_2 (573 K, 1 h). The reported dispersion values reflect the H-atom uptake per Pt-atom determined by extrapolating the linear trend observed in the high H_2 pressure regime (50-100 kPa H_2) to zero kPa H_2.

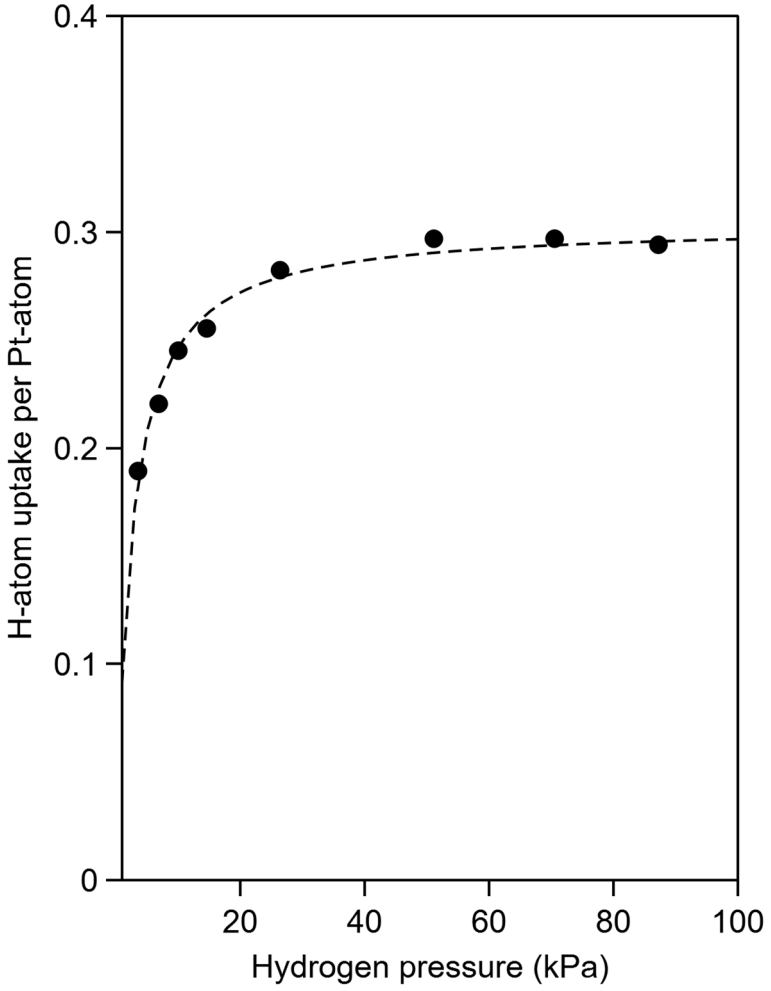

Figure 2.S1: Adsorption isotherms for H_2 on SiO_2-supported Pt nanoparticles (Pt/SiO_2) depicting the number of adsorbed H atoms per bulk Pt site as a function of hydrogen pressure (kPa) with Pt content of 2.1% wt. The hydrogen pressures (kPa) reflect the stable values following catalyst exposure to a set H_2 pressure. The dashed line indicates a Langmuir adsorption isotherm trend.

2.8.2. Depiction of Pt(111) surface and adsorption sites.

Scheme 2.S1 shows the adsorption sites on the Pt(111) surface used in density functional theory (DFT) calculations that bind toluene-derived species relevant during toluene-H_2 reactions.

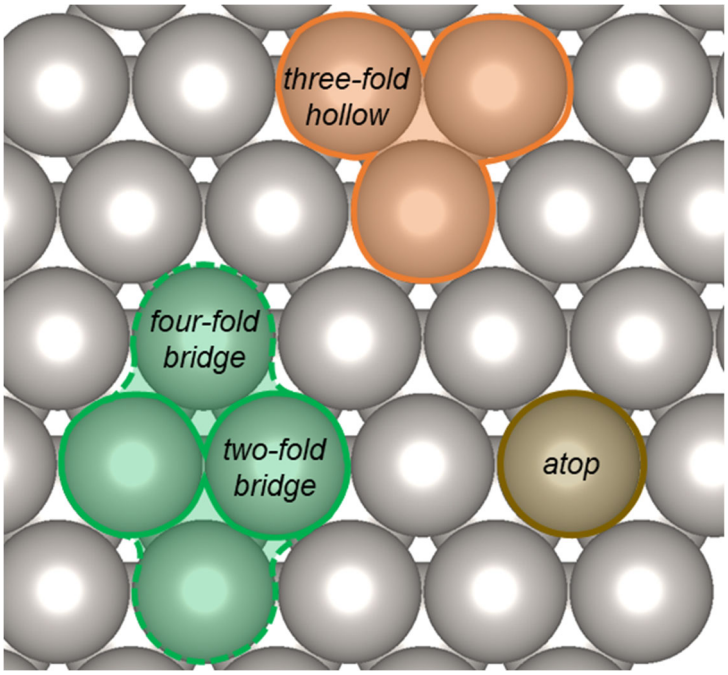

Scheme 2.S1: Top view of the Pt(111) surface used for density function theory calculations for the binding of toluene-derived intermediates during toluene-H_2 reactions. The orange-highlighted group of three atoms depicts the hcp 3-fold hollow site, the brown-highlighted single atom depicts the atop site, the green-highlighted group of four atoms depicts the four-fold bridge site, and the pair of atoms contained within the four-fold bridge site depicts the two-fold bridge site.

2.8.3. Statistical mechanics methods for calculating thermodynamic properties of species formed during toluene-H_2 reactions on Pt/SiO_2 from density functional theory calculations.

Zero-point energies, enthalpies, entropies, and free energies were calculated from density functional theory derived electronic energies and vibrational frequencies using standard statistical thermodynamics methods [39]. These calculations were carried out for isolated gas molecules and for molecules coordinated to Pt surfaces.

The enthalpy (H) is described by the sum of the electronic energy (E_0), zero-point energy (ZPE), and vibrational, translational, and rotational enthalpies (H_{vib}, H_{trans}, and H_{rot}, respectively):

$$H = E_0 + ZPE + H_{vib} + H_{trans} + H_{rot} \tag{2.S67}$$

The entropy (S) is described as the sum of the vibrational, translational, and rotational entropies (S_{vib}, S_{trans}, and S_{rot}, respectively):

$$S = S_{vib} + S_{trans} + S_{rot} \tag{2.S68}$$

The Gibbs free energy (G) at a given temperature (T) is described from the enthalpies and entropies:

$$G = H - TS \tag{2.S69}$$

DFT-derived vibrational frequencies were used to calculate the ZPE, H_{vib}, and S_{vib} with the harmonic oscillator approximation. Vibrational frequencies for adsorbed species were calculated by holding the entire metal surface fixed and allowing displacements of the molecular species only.

$$ZPE = \sum_i \frac{1}{2} h\nu_i \tag{2.S70}$$

$$H_{vib} = \sum_i \left(\frac{h\nu_i e^{-\frac{h\nu_i}{kT}}}{1 - e^{-\frac{h\nu_i}{kT}}} \right) \tag{2.S71}$$

$$S_{vib} = \sum_i \left(\frac{\frac{h\nu_i}{T} e^{-\frac{h\nu_i}{kT}}}{1 - e^{-\frac{h\nu_i}{kT}}} - k \ln\left(1 - e^{-\frac{h\nu_i}{kT}}\right) \right) \tag{2.S72}$$

Where h is Plank's constant, ν is the vibrational frequency, and k is Boltzmann's constant. Vibrational modes below a low frequency cutoff of 100 cm^{-1} were considered as rotational or translational degrees of freedom rather than vibrational. Translational and rotational degrees of freedom aside from the low frequency vibrations were not considered. The values of H_{trans} and H_{rot} are described as follows:

$$H_{trans} = \frac{5}{2} kT \tag{2.S73}$$

$$H_{rot,linear} = kT \tag{2.S74}$$

$$H_{rot,nonlinear} = \frac{3}{2} kT \tag{2.S75}$$

The S_{trans} value is given as:

$$S_{trans} = k \left(\ln\left(\left(\frac{2\pi mkT}{h^2} \right)^{\frac{3}{2}} \frac{kT}{P} \right) + \frac{5}{2} \right) \tag{2.S76}$$

Where m is the molecular mass, P is the total pressure. The S_{rot} value is:

$$S_{rot} = k \left(\ln\left(\frac{\pi^{\frac{1}{2}}}{\sigma} \left(\frac{T^3}{\theta_x \theta_y \theta_z} \right)^{\frac{1}{2}} \right) + \frac{3}{2} \right) \tag{2.S77}$$

$$\theta_i = \frac{h^2}{8\pi^2 I_i k} \tag{2.S78}$$

Where σ is the symmetry number of the molecule; i denotes x, y, and z; and I_i is the moment of inertia about the i axis. Values of σ for gaseous species are shown in **Table 2.S1**. The moments of inertia were calculated using the Atomic Simulation Environment (ASE) package [58].

Table 2.S1: Symmetry numbers (σ) for calculating rotational entropies of gaseous molecules.

Molecule	Symmetry number (σ)
H_2	2
Benzene	12
Toluene	1
1,3-Cyclohexadiene	2
1-Methyl-1,3-cyclohexadiene	1
Cyclohexene	2
1-Methylcyclohexene	1
4-Methylcyclohexene	1

2.8.4. Derivation of the relationship between methylcyclohexene isomer pressures and toluene conversion during toluene-H_2 reactions on Pt surfaces.

The net formation turnover rate (r_{iME}) for each ME isomer (*i*ME) is given from difference between the rates that it is formed from toluene-H_2 reactants and consumed by reaction with H_2:

$$r_{iME} = \alpha_{tol \rightarrow iME}[tol] - \alpha_{iME \rightarrow MA}[iME], \tag{2.S79}$$

where $\alpha_{tol \rightarrow iME}$ is the pseudo-first-order rate constant for *i*ME formation from toluene-H_2 reactants and $\alpha_{iME \rightarrow MA}$ is the pseudo-first-order rate constant for the *i*ME-H_2 reaction. Expanding r_{iME} into the rate of change of the iME concentration gives:

$$\frac{1}{L_{Pt}}\frac{d\dot{n}_{iME}}{dt} = \alpha_{tol \rightarrow iME}[tol] - \alpha_{iME \rightarrow MA}[iME], \tag{2.S80}$$

where L_{Pt} is the number of exposed Pt sites, $\dot{n}_{iME}$ is the molar *i*ME flowrate, where *t* is contact time for the reaction. The rate of change of toluene concentration is given by the sum over the iME formation reactions:

$$\frac{1}{L_{Pt}}\frac{d\dot{n}_{tol}}{dt} = \sum_{i=1,3,4} -\alpha_{tol \rightarrow iME}[tol]. \tag{2.S81}$$

Expressing $\dot{n}_{tol}$ in terms of the toluene concentration ($\dot{n}_{tol} = v[tol]$; where v is the volumetric fluid flowrate) and integrating **equation 2.S81** gives:

$$[tol] = [tol]_0 \exp\left(\frac{L_{Pt}}{v}\sum_{i=1,3,4}(-\alpha_{tol \rightarrow iME})\, t\right), \tag{2.S82}$$

where $[tol]_0$ is the toluene concentration at zero contact time. Rearranging the functional form of **equation 2.S82** gives:

$$X_{tol} = 1 - \exp\left(\frac{L_{Pt}}{v}\sum_{i=1,3,4}(-\alpha_{tol\to iME})\,t\right), \tag{2.S83}$$

with

$$X_{tol} = 1 - \frac{[tol]}{[tol]_0}. \tag{2.S84}$$

Toluene pressures do not change significantly with time under conditions of differential conversion for which catalytic measurements were carried out in this study. As a result, **equation 2.S80** can be integrated while holding $[tol]$ constant to give:

$$\ln\left(1 - \frac{\alpha_{iME\to MA}}{\alpha_{tol\to iME}[tol]}[iME]\right) = -\alpha_{iME\to MA}L_{Pt}t, \tag{2.S85}$$

Substituting the value of *t* with that from the toluene consumption **equation 2.S83** gives the following relation between $[iME]$ and X_{tol}:

$$[iME] = \frac{\alpha_{tol\to iME}[tol]}{\alpha_{iME\to MA}}\left(1 - \exp\left(\frac{\alpha_{iME\to MA}\,ln(1-X_{tol})}{\sum_{i=1,3,4}(-\alpha_{tol\to iME})}\right)\right), \tag{2.S86}$$

which simplifies to:

$$[iME] = [iME]_{PSS} - [iME]_{PSS}\exp\left(\frac{\alpha_{iME\to MA}\,ln(1-X_{tol})}{\sum_{j=1,3,4}(\alpha_{tol\to jME})}\right), \tag{2.S87}$$

with

$$[iME]_{PSS} = \frac{\alpha_{tol\to iME}[tol]}{\alpha_{iME\to MA}}. \tag{2.S88}$$

2.8.5. Multisite Langmuir adsorption model for site occupancy on toluene covered Pt surfaces.

The Nitta et al. [26] reported an equation for localized multi-component adsorption with each adsorbate occupying multiply sites on a homogeneous surface. In the present work, this formalism is utilized to describe the site occupancies of toluene and partially saturated toluene-derived intermediates on Pt surfaces during toluene hydrogenation to account for the multiple C-Pt contacts that characterize their interactions. In what follows, the adsorption isotherm equation is first reproduced from the work of Nitta et al., simplified with forthcoming assumptions pertaining to toluene hydrogenation, then utilized to describe surface coverages of reactive intermediates in kinetic rate equation.

For single-component adsorption, Nitta et al. considers a system of *M* independent binding sites with *N* adsorbed molecules each occupying γ neighboring sites. The chemical potential of an adsorbate on a surface, μ^s, is:

$$\frac{\mu^s}{kT} = -\ln(j_s\zeta) + \ln\left(\frac{N}{M}\right) - \gamma\ln\left(\frac{M-\gamma N}{M}\right) - \frac{\epsilon}{kT} - \frac{\gamma^2 Nu}{MkT} \tag{2.S89}$$

Where k is Boltzmann's constant, T is the absolute temperature in Kelvin, j_s is the internal and vibration partition function of an adsorbed molecule, $-\epsilon$ is the potential energy for interactions between the adsorbate and the surface, and u is a parameter describing the potential energy for interactions between adsorbates. The chemical potential for an ideal gas is given as:

$$\frac{\mu^g}{kT} = \ln\left(\frac{P\Lambda^3}{j_g kT}\right) \tag{2.S90}$$

where P is the total pressure of the single-component gas phase, Λ is the deBroglie wavelength, and j_g is the internal and vibrational partition function of the gaseous molecule.

Equating μ^s and μ^g gives an expression for the surface coverage, defined as $\theta = \frac{\gamma N}{M}$:

$$\ln(\gamma KP) = \ln\theta - \gamma\ln(1-\theta) - \frac{\gamma u\theta}{kT} \tag{2.S91}$$

Where K is the adsorption equilibrium constant defined as:

$$K = \frac{j_s\zeta}{j_g}\cdot\frac{\Lambda^3}{kT}\cdot\exp\left(\frac{\epsilon}{kT}\right) \tag{2.S92}$$

In systems where the interactions between adsorbates are negligible (u is equal to zero), **equation 2.S92** simplifies to:

$$\gamma KP = \frac{\theta}{(1-\theta)^\gamma} \tag{2.S93}$$

The functional form of **equation 2.S93** reproduces the single-component Langmuir adsorption isotherm for γ equal to one.

An analogous expression for the multicomponent adsorption of k molecular components is determined to be:

$$\ln(\gamma_i K_i p_i) = \ln\theta_i - \gamma_i\ln\left(1 - \sum_{j=1}^{k}\theta_j\right) - n_i\sum_{j=1}^{k}\frac{\theta_j u_{ij}}{kT} \tag{2.S94}$$

Where i indexes the k components of the mixture, p_i is the partial pressure of component i. For systems involving non-interacting adsorbates (all u_{ij} values are equal to zero), the following multi-component, multi-site adsorption equation is obtained:

$$\gamma_i K_i p_i = \frac{\theta_i}{\left(1 - \sum_{j=1}^{k}\theta_j\right)^{\gamma_i}} \tag{2.S95}$$

Site occupancies during toluene hydrogenation are expected to depend on steric effects arising from adsorbate stereochemistry (i.e., flat or upright) that determine the packing of adsorbates at high coverages and the number of C-Pt bonds formed depending on the ring saturation and the type of interaction (σ or π depending on rehybridization of the alkene group). Aromatic adsorption on Pt surfaces results in changes in the Pt nanoparticle work function [59] due to electron donation from the metal to the adsorbate molecular orbitals that become more pronounced at high adsorbate with coverage consequences for the strength of adsorbate-surface interactions (ϵ_i). Moreover, high coverages that characterize aromatic adsorption on metal-surfaces necessitates consideration of adsorbate-adsorbate interactions (u_{ij}) due to van der Waals forces. Adsorbate effects on the metal work functions, and therefore the strength of interaction between covalent C-Pt bonds, suggests a functional dependence of ϵ_i on the total adsorbate coverage and adsorbate composition. Spectroscopic [12,16] studies during aromatic

hydrogenations demonstrate the preference for surface saturation by the aromatic reactant in favor of saturated products. Values of ϵ_i are consequently assumed to depend only on toluene coverage (denoted θ_{tol}) during toluene hydrogenation; ϵ_i can thus be approximated as a function of θ_{tol} (denoted $\epsilon_i[\theta_{tol}]$) by a Taylor series expansion about a θ_{tol} value of 1:

$$\epsilon_i[\theta_{tol}] \cong \epsilon_{i,0} + \left.\frac{d\epsilon_i}{d\theta_{tol}}\right|_{\theta_{tol}=1} (\theta_{tol} - 1) + \cdots \tag{2.S96}$$

and

$$\epsilon_{i,0} = \epsilon_i[\theta_{tol} = 1]. \tag{2.S97}$$

Spectroscopic studies [12,16] demonstrate the tendency towards complete monolayer coverages of hydrocarbon species, suggesting deviations from full saturation are small and ϵ_i may be approximated by the zero-order term $\epsilon_{i,0}$. In this small deviation form, K_i is approximated by the adsorbate-surface interactions characterized by full monolayer coverage, given by:

$$K_i = \frac{j_s \zeta}{j_g} \cdot \frac{\Lambda^3}{kT} \cdot \exp\left(\frac{\epsilon_{i,0}}{kT}\right). \tag{2.S98}$$

At low surface coverages, the u_{ij} term can be neglected if adsorbates are randomly distributed and at non-interacting distances on average, in general. Aromatic adsorption and hydrogenation on Pt, however, occurs on surfaces characterized by saturation coverages in which adsorbate-adsorbate interactions cannot be neglected. For instance, micro-calorimetric studies for benzene adsorption report binding enthalpies approaching benzene sublimation enthalpies for monolayer coverages consistent with adsorbate-adsorbate interactions dominating the adsorption process [13,60,61]. The u_{ij} term represents a parameter matrix assigning intermolecular interactions between each component pair. Such complexity can be reduced for the case of toluene hydrogenation occurring on toluene covered surfaces in which adsorbates interact with uniform potential field characteristic of the toluene monolayer. The θ_j terms excluding toluene are therefore negligible and only the interactions arising from the *i*th component and toluene ($u_{i,tol}$) need be considered explicitly to give the following isotherm equation:

$$\ln(\gamma_i K_i p_i) = \ln \theta_i - \gamma_i \ln\left(1 - \sum_{j=1}^{k} \theta_j\right) - \gamma_i \frac{\theta_{tol} u_{i,tol}}{kT}. \tag{2.S99}$$

An effective thermodynamic adsorption constant, K_i', is next defined by grouping the terms involving adsorbate-adsorbate interactions with adsorbate-surface interactions to give the following expression:

$$\ln(\gamma_i K_i' p_i) = \ln \theta_i - \gamma_i \ln\left(1 - \sum_{j=1}^{k} \theta_j\right), \tag{2.S100}$$

where

$$K_i' = \frac{j_s \zeta}{j_g} \cdot \frac{\Lambda^3}{kT} \cdot \exp\left(\frac{\epsilon_{i,0} + \gamma_i \theta_{tol} u_{i,tol}}{kT}\right). \tag{2.S101}$$

In the special case where θ_{tol} is approximated to be 1, a potential energy term for component i adsorption on a toluene monolayer, $\kappa_{i,tol}$, is defined to account for the combined adsorbate-surface and adsorbate-adsorbate interactions:

$$K_i' = \frac{j_s \zeta}{j_g} \cdot \frac{\Lambda^3}{kT} \cdot \exp\left(\frac{\kappa_{i,tol}}{kT}\right). \tag{2.S102}$$

Finally, an expression for θ_i resembling the Langmuir adsorption isotherm is obtained:

$$\gamma_i K_i' p_i = \frac{\theta_i}{\left(1 - \sum_{j=1}^{k} \theta_j\right)^{\gamma}}. \tag{2.S103}$$

CHAPTER THREE

Proximity Effects, Mechanistic Insights, and the Nature of Molecular Shuttles in Catalytic Hydrogenations Involving Bifunctional Cascades

Abstract

Rates of toluene hydrogenation to methylcyclohexane (MA) on SiO_2-supported Pt nanoclusters (per surface Pt-atom) increase when Pt/SiO_2 is mixed physically with Al_2O_3 powders that are themselves inactive for such reactions. These bifunctional synergies have been attributed to hydrogen-spillover mechanisms whereby H atoms migrate from the metal surface, where they form from dissociated H_2, to the oxide and react with unsaturated molecules; however, such routes are unlikely on insulating supports which do not interact favorably with H atoms except at crystallographic defects. Here, two novel bifunctional reaction schemes that are mediated by toluene-derived molecular shuttles, instead of H atoms directly, are investigated to account for the methylcyclohexane formation rate enhancements conferred by γ-Al_2O_3 in Pt/SiO_2+γ-Al_2O_3 physical mixtures. One route involves the formation of TH_n* intermediates from toluene-H_2 reactions on Pt surfaces that can desorb and hydrogenate at nearby γ-Al_2O_3 surfaces, without requiring Pt-γ-Al_2O_3 atomic contact, thus circumventing the kinetic bottlenecks at strictly monofunctional Pt surfaces and increasing methylcyclohexane formation rates. The second route involves the formation of TH_n* species that undergo slow H-addition reactions to form methylcyclohexane, but which compete effectively for binding sites on crowded surfaces with the predominant reactive intermediates involved in monofunctional routes. Their scavenging by advantageous reactions at γ-Al_2O_3 surfaces present within diffusion distances decreases their equilibrium surface coverages and increases the binding spaces available for the competitive reactions of intermediates that mediate monofunctional hydrogenation turnovers at Pt surfaces. MA formation rates on intimate mixtures upon exposure to propanoic acid, a titrant of Lewis acid-base pairs at oxide surfaces, approach those on Al_2O_3-free Pt/SiO_2, consistent with the involvement of such site pairs on γ-Al_2O_3 in mediating these rate enhancements. 1,3-Cyclohexadiene and 4-methylcyclohexene reactions with H_2 are carried out over Pt-free γ-Al_2O_3 surfaces (30-300 Pa hydrocarbon, 0-90 kPa H_2, 393 K) to elucidate reaction pathways that toluene-derived intermediates undergo that may be of catalytic importance for bifunctional Pt/SiO_2+γ-Al_2O_3 catalytic mixtures. These unsaturated molecules hydrogenated predominantly via reaction with molecular H_2 at rates that were catalytically significant in the context of Al_2O_3-catalyzed rates in bifunctional mixtures necessary to account for enhancements for Pt/SiO_2+γ-Al_2O_3 mixtures. Reaction-transport modelling based on the proposed bifunctional mechanisms and measured reactivity trends for independent Pt/SiO_2 and γ-Al_2O_3 functions show that bifunctional synergies are best attributed to γ-Al_2O_3-mediated scavenging of methylcyclohexadiene inhibitors (the second route) at low temperatures (393 K), prevalent only on Pt/SiO_2 catalysts with smallest Pt clusters (0.7 nm mean diameter). At higher temperatures (493-533 K), in which methylcyclohexene hydrogenation becomes rate limiting, an additive methylcyclohexene hydrogenation route at nearby γ-Al_2O_3 is likely to become prevalent. These findings shed light on the mechanistic origins of bifunctional synergies between metal nanoclusters and metal-oxide support and diluent materials that give rise to so-called hydrogen-spillover phenomena. These mechanistic considerations enable future catalytic design that leverages these bifunctional pathways for rate and selectivity gains. These insights may also illuminate the mechanistic origins of metal-support interactions beyond electronic effects or bifunctional reactions at metal-support interfaces.

3.1. Introduction

Aluminum oxides (Al_2O_3) are used in catalytic applications as supports for dispersed metal nanoparticles in reactions such as olefin and monoarene hydrogenations [1,2], hydrodesulfurization [2,3], and Fischer-Tropsch synthesis [2,4], and as substrates for composite catalysts such as those used to control automotive exhaust [5]. Al_2O_3 helps to confer high metal dispersion and favorable structural and physical properties in the practice of such catalytic applications. Beyond the role of Al_2O_3 as a support material, olefin and monoarene hydrogenation reactions often show higher turnover rates (normalized per exposed metal site) for metal nanoclusters supported on Al_2O_3 compared to other oxide supports such as SiO_2 [6,7]. Increased turnover rates are also reported even when supported metal catalysts are physically mixed with Al_2O_3 (e.g. Pt/SiO_2 [8], Pt/Al_2O_3 [9], and Pt/LTA [10]), despite Al_2O_3 being inert for these reactions on its own.

These increased hydrogenation rates have been attributed to an additive hydrogenation route mediated by H atoms that are formed by H_2 dissociation on metal surfaces and which are transported to oxide surfaces, thus rendering them competent in the reduction of unsaturated hydrocarbons [8,11–14]. This invocation of H-atom mediated bifunctional routes, commonly referred to as hydrogen spillover (H-spillover), draws parallels to the mechanism for H-atom migration from metal nanoclusters to conductive, reducible metal oxide supports (such as for WO_3-supported Pt nanoparticles [15,16]). In such systems, metal cations of the oxide are reduced by metal-bound H atoms at the metal-support interface to form stable H^+-e^- pairs that can diffuse across the support surface and even reduce metal cations in some oxides [15–18]. Al_2O_3, however, is an insulating material that lacks the reducible metal cations required to accept electrons and stabilize such H^+-e^- pairs. Al_2O_3 surfaces thus cannot bind H atoms in stable configurations that compensate for the cleaved metal-H bond [14,18].

The theoretical objections and the lack of direct evidence of significant H-atom migration from metals to Al_2O_3 supports [14,18] have led to alternate explanations for the promotional effects of Al_2O_3 in metal-catalyzed hydrogenations. Higher ethylene hydrogenation rates were reported for Pt/SiO_2 diluted with γ-Al_2O_3 compared with SiO_2; these rate differences were attributed to the poisoning of the Pt by carbonaceous impurities present on the SiO_2 diluent, but absent on Al_2O_3 surfaces [19]. These rate differences disappeared upon brief treatment in oxygen at 493 K, a finding attributed to the removal of such impurities by oxidation [19]. Higher rates for benzene hydrogenation [9] on Pt/γ-Al_2O_3 and for toluene hydrogenation on Pt/SiO_2 (this work) when mixed with Al_2O_3 persisted, however, even after such treatments in O_2, suggesting that the effects of any such impurities cannot account for the Al_2O_3-induced rate enhancements in these monoarene hydrogenation reactions. Hydrogen spillover has been shown to occur from Pt particles to carbon supports [20,21], suggesting that carbonaceous deposits consisting of unsaturated organic residues may form on Al_2O_3 surfaces, thus potentially acting as conducting bridges for hydrogen spillover from Pt nanoparticles to unsaturated molecules bound at Al_2O_3 surfaces or at such organic debris [14].

Toluene hydrogenation reactions carried out on SiO_2-supported Pt nanoparticles mixed physically with γ-Al_2O_3 are explored in this work as an illustrative example of Al_2O_3-mediated enhancements for hydrogenation reactions in order to assess the potential mechanistic underpinnings of such bifunctional synergies. Pt/SiO_2 is mixed with γ-Al_2O_3 in intra-pellet mixtures (denoted as "intimate"), prepared by mechanical grinding Pt/SiO_2 and γ-Al_2O_3 powders and pressing into bi-component catalyst pellets; samples are also examined as inter-pellet mixtures

(denoted as "loose") and prepared by dispersing separate Pt/SiO_2 and γ-Al_2O_3 aggregates of varying diameter together within the reactor. These mixtures showed an increase in methylcyclohexane (MA) formation turnover rates (normalized per exposed Pt site) as the γ-Al_2O_3 to Pt/SiO_2 dilution ratio increased for the case of both intimate and loose mixtures; no changes in rates were detected when SiO_2 was used as the diluent. Turnover rates for CO oxidation, a reaction that is insensitive to Pt nanocluster size [22], for intimate $PtSiO_2$+γ-Al_2O_3 and Pt/SiO_2+SiO_2 mixtures were independent of both the extent of dilution and the oxide identity, demonstrating that mechanical mixing protocols do not affect the number of accessible Pt sites that catalyze CO oxidation. These Al_2O_3-mediated hydrogenation turnover rate enhancements cannot be attributed to changes in the spatial Pt nanocluster distribution to form new active sites on Pt/SiO_2+γ-Al_2O_3 mixtures that are not present on the undiluted or SiO_2-diluted Pt/SiO_2. The increased MA formation rate for loose Pt/SiO_2+γ-Al_2O_3 mixtures (relative to Pt/SiO_2 alone), for which γ-Al_2O_3 is not in atomic contact with the Pt/SiO_2 aggregate, rules out any significant role of carbon bridges, which are unlikely to span 10-100 μm distances, as conduits for H-atom spillover in additive toluene hydrogenation routes at the γ-Al_2O_3 surface.

Gaseous methylcyclohexene (ME) isomers were shown to form at pseudo-steady state concentrations during toluene-H_2 reactions on Pt/SiO_2 (**Chapter 2**), indicative of the presence of partially hydrogenated toluene-derived intermediates (denoted TH_n, where *n* is the number of additional C-H bonds relative to toluene) that can desorb before completing the hydrogenation to form MA. Such TH_n species may migrate via diffusion within the porous solids or the fluid phase and react at γ-Al_2O_3 surfaces present within diffusion distances to form MA via pathways that complement those prevalent on Pt surfaces. γ-Al_2O_3 surfaces are able to activate H-H [23,24] and C-H bonds [23] at coordinatively-unsaturated Al^{3+} centers, thus potentially providing active sites for reactions of TH_n at locations beyond atomic distances from the sites that form (and desorb) TH_n. Such active sites can be titrated by propanoic acid (PA), a molecule that binds irreversibly at metal oxide surfaces with exposed Lewis centers [25], but which does influence toluene-H_2 reactions on Pt nanoclusters. Exposure of Pt/SiO_2+γ-Al_2O_3 mixtures to PA is shown to produce rates similar to those on Pt/SiO_2, consistent with the involvement of γ-Al_2O_3 surfaces in kinetically-relevant bifunctional routes. Al_2O_3-catalyzed reactions of H_2 with 1,3-cyclohexadiene (13CHD) (or 4-methylcyclohexene; 4ME) form benzene, cyclohexene, and cyclohexane (or methylcyclohexane and 1-methylcyclohexene) indicating plausible synergistic reactions with toluene-derived intermediates formed by the Pt function.

Here, two bifunctional mechanisms are examined involving Al_2O_3-catalyzed reactions of partially hydrogenated toluene-derived intermediates that may be able to account for the MA formation rate enhancements conferred by γ-Al_2O_3 in Pt/SiO_2+γ-Al_2O_3 physical mixtures. One route (denoted additive/stoichiometric hydrogenation mechanism) involves the formation of TH_n* intermediates from toluene-H_2 reactions on Pt surfaces. These species can desorb and hydrogenate at nearby γ-Al_2O_3 surfaces, without requiring Pt-γ-Al_2O_3 atomic contact, thus circumventing the kinetic bottlenecks at strictly monofunctional Pt surfaces and increasing MA formation rates. Another route involves the formation of TH_n* species that undergo slow H-addition reactions to form MA, but which compete effectively for binding sites on crowded surfaces with the predominant reactive intermediates involved in monofunctional routes. These stranded, less reactive TH_n* species can desorb to give very low equilibrium concentrations of their gaseous analogs; their migration to, and hydrogenation at, Al_2O_3 surfaces present beyond atomic distances leads to their scavenging from the fluid phase, thus decreasing their equilibrium surface coverages

and increasing the binding spaces available for the competing reactions of intermediates that mediate monofunctional hydrogenation turnovers at Pt surfaces.

Both mechanisms are mediated by intermediate species that must migrate between two functions present within diffusion distances, without requiring their atomic contact. In the additive/stoichiometric hydrogenation mechanism, MA is formed in stoichiometric amounts to the number of TH_n molecules that leave the Pt/SiO_2 domain and react at the γ-Al_2O_3 domain. These rates cannot exceed the maximum rates of mass transport for TH_n* leaving the Pt/SiO_2 catalyst aggregates. The maximum driving force for TH_n* diffusion occur when TH_n* reaches its maximum value at the surface of the Pt/SiO_2 aggregate (dictated by thermodynamic equilibrium with toluene and H_2) and is scavenged completely from the fluid phase between the two catalyst domains. Rates of mass transport in this limiting case are calculated using effective mass transfer coefficients based on boundary layer theory for fluid flow around spheres; these rates show that methylcyclohexene (ME) intermediates are the only species with equilibrium concentrations large enough to provide a diffusive driving force sufficient to account for Al_2O_3-induced MA formation rate enhancements on Pt/SiO_2+γ-Al_2O_3 mixtures (at 10-100 kPa H_2, 0.3-2.1 kPa toluene, 393 K). Measured ME pressures measured during toluene-H_2 reactions on Pt/SiO_2 at these same conditions are shown to be a factor of 10^3 smaller than their thermodynamic equilibrium values, indicating that they form irreversibly. Their irreversible formation indicates, moreover, that the elementary steps that limit toluene conversion precede ME formation; thus, ME hydrogenation in parallel routes at the Al_2O_3 do not bypass kinetically relevant steps at the Pt surface and are not catalytically relevant at lower temperatures. Such an additive pathway may be important, however, under conditions where ME formation from toluene-H_2 reactants nears equilibrium and rates become limited by ME+H_2 reactions.

MA formation rates measured on loose mixtures with different Pt/SiO_2 and γ-Al_2O_3 domain sizes but similar diluent ratios (γ-Al_2O_3 surface area to the number of exposed Pt site ratio) show that rate enhancements decrease with concomitant increases in their respective domain size (393 K). Such behavior can be attributed to concentration gradients that arise between the two functions [26] because TH_n* molecules are formed and consumed at the respective Pt/SiO_2 and γ-Al_2O_3 domains rapidly compared to their rates of diffusion between them. Reaction-transport modelling based on the proposed inhibitor-scavenging route and on measured reactivity trends for independent Pt/SiO_2 and γ-Al_2O_3 functions show that bifunctional synergies are accurately accounted for by γ-Al_2O_3-mediated scavenging of methylcyclohexadiene inhibitors. The resulting kinetic and thermodynamic parameters from the reaction-transport model that best describe the measured rates give values that are compared to relevant experimental and theoretical benchmarks. Such comparisons reveal that the proposed inhibitor scavenging route with methylcyclohexadiene inhibitors gives parameters that are in reasonable agreement with relevant benchmarks providing corroborating evidence of their catalytic importance for toluene hydrogenation on Pt/SiO_2+γ-Al_2O_3 mixtures. In doing so, this study presents a novel mechanistic framework for describing bifunctional hydrogenation routes that are mediated by molecular species via gas phase diffusion rather than hydrogen spillover across insulating oxide surfaces.

3.2. Materials and methods

3.2.1. Catalyst synthesis and characterization.

SiO_2 (Cabot Cab-o-sil HS-5) and γ-Al_2O_3 (Sasol SBA200; denoted as Al_2O_3-Sasol) materials were obtained from commercial sources. Another Al_2O_3 sample (denoted as Al_2O_3-solgel)

was prepared from aluminum isopropoxide (AIP; Sigma-Aldrich, 98%) using sol-gel methods [27]. AIP was dissolved in deionized (DI) H_2O (resistivity ≥ 17.6 ohm-cm) (10 cm^3 g^{-1} AIP) by stirring magnetically at 358 K for 1 h to form an AIP sol. HNO_3 (Sigma-Aldrich, 70%) was then added dropwise (0.4 g^{-1}AIP) while stirring and held for 1 h (358 K). The resulting sol was treated in ambient air at 12 h (393 K) to evaporate the H_2O and form a gel. The gel was then treated in flowing dry air at 773 K (0.017 K s^{-1}) for 4 h and in flowing dry air at 923 K (0.017 K s^{-1}) for 2 h to form solid Al_2O_3 particles.

Pt nanoclusters dispersed on SiO_2 (Pt/SiO_2) were prepared using electrostatic adsorption methods [28,29]. SiO_2 (Cabot Cab-o-sil HS-5; washed with DI H_2O, treated in ambient air at 373 K for 12 h, and treated in ambient air at 873 K; 0.017 K s^{-1}; 4 h) was added to a solution of $Pt(NH_3)_4(NO_3)_2$ (Sigma-Aldrich, 99.995%) and DI H_2O (4 cm^3 g^{-1} SiO_2) and then stirred magnetically for 4 h at ambient temperature. NH_4OH (Sigma-Aldrich, 28% NH_3 in H_2O, 99.99%) was added to the SiO_2, DI H_2O, and $Pt(NH_3)_4(NO_3)_2$ suspension to give a pH between 7 and 8. The solids were collected by filtration and rinsed with DI H_2O. They were then treated in (i) flowing dry air (Praxair, ultra-zero purity) at 1.7 cm^3 g^{-1} s^{-1} by increasing the temperature from ambient to the target treatment temperature at 0.017 K s^{-1} and holding for 3 h; (ii) flowing He (Praxair, 99.999%) at 1.7 cm^3 g^{-1} s^{-1} by decreasing the temperature to 373 K at 0.083 K s^{-1}; (iii) flowing H_2 (Praxair, 99.999%) at 1.7 cm^3 g^{-1} s^{-1} by increasing the temperature from 373 to the target treatment temperature at 0.017 K s^{-1} and holding for 2 h then decreasing the temperature at 0.083 K s^{-1} to below 373 K; and (iv) flowing 2% O_2 with He bal. (Praxair) at 1.7 cm^3 g^{-1} s^{-1} for at >1 h. The Pt content was determined by inductively-coupled plasma–atomic emission spectroscopy (ICP-AES) (Galbraith Laboratories). Pt dispersions ($D = \frac{N_s}{N_T}$, where N_s is the total number of surface metal atoms and N_T is the total number of metal atoms) were measured by H_2 chemisorption uptakes as described in **Section 3.8.1**. Treatment temperatures, Pt nanocluster dispersions, and mean Pt nanocluster diameters are reported in **Table 3.1**. Surface areas (m^2 g^{-1}) and pore volumes (cm^3 g^{-1}) of metal oxide powders were determined from N_2 adsorption uptakes at its normal boiling point (Micromeritic 3Flex Surface Analyzer) and summarized in **Table 3.S1** with isotherms shown in **Section 3.8.2**.

3.2.2. Catalytic rate measurements.

The rate of formation of the products of toluene-H_2 and CO-O_2 reactions were measured on Pt/SiO_2 samples (0.001-0.05 g) using a fritted U-shaped quartz tube reactor (1.3 cm internal diameter). Catalyst powders were pressed into wafers then crushed and sieved to retain the target aggregate sizes. These aggregates were mixed with quartz powder (Sigma-Aldrich, 180-250 μm; treated in ambient air at 973 K) to maintain a bed height of 3 cm. Hydrogenation rates were unaffected by changes in volumetric heat release rates (varied by changing the amount of Pt/SiO_2 in the quartz-catalyst mixture), thus confirming the absence of reaction-induced bed temperature gradients. Toluene-H_2 reactions were also carried out on Pt/SiO_2 samples mixed physically with SiO_2 or Al_2O_3. Intra-pellet mixtures (denoted as intimate mixtures) were prepared by grinding Pt/SiO_2 and oxide diluent in a mortar and pestle for 10 minutes and then pressed, crushed, and sieved to retain aggregates with 180-250 μm diameter. Inter-pellet mixtures (denoted as loose mixtures) were prepared by pressing each of the two components into separate wafers, which were then crushed and sieved to retain aggregates with 30-250 μm diameter. The Pt/SiO_2 and oxide aggregates were then interspersed loosely within the reactor (without any quartz added). An Al_2O_3 bed was also prepared before a quartz-diluted Pt/SiO_2 catalyst bed (denoted as Al_2O_3 pre-bed) separated by a 5 mm layer of quartz granules (0.5 g), in some experiments. The products formed

during 1,3-cyclohexadiene and 4-methylcyclohexene reactions with H_2 were also measured on undiluted Al_2O_3 samples (0.03-0.1 g) present as powders with 20-50 μm diameter.

The samples were resistively heated (National Electric furnace), and the temperature was maintained constant using a Watlow controller. The bed temperature was measured by a thermocouple placed in a dimple at the center of the quartz-reactor bed. Catalysts were treated in (i) flowing 10% O_2/He (Praxair) at 100-200 cm^3 g catalyst^{-1} s^{-1} by increasing the temperature from ambient to 573 K at 0.033 K s^{-1} and holding for 1 h; (ii) flowing He (Praxair, 99.999%) at 100-200 cm^3 g Pt/SiO_2^{-1} s^{-1} by holding at 573 K for 0.25 h; and (iii) flowing H_2 (Praxair, 99.999%) at 100-200 cm^3 g Pt/SiO_2^{-1} s^{-1} by holding at 573 K for 1 h before decreasing the temperature to the target temperature for the reaction in flowing H_2 (for hydrogenation reactions) or flowing 10% O_2/He (for CO oxidation reactions). O_2/He, He, and H_2 inlet streams were purified by passing through moisture traps (Agilent BMT).

Gaseous inlet molar rates were set using electronic Parker mass flow controllers. Liquid toluene (Sigma-Aldrich, 99.9%), 1,3-cyclohexadiene (Sigma-Aldrich, 97%), and 4-methylcyclohexene (Sigma-Aldrich, 99%) was introduced into flowing H_2 and He mixtures (100-200 cm^3 g Pt/SiO_2^{-1} s^{-1}) before the reactor using a Parker Hamilton syringe pump. Propanoic acid (Sigma-aldrich, 99.5%) was mixed into the toluene reactants for titration experiments. The effluent stream was analyzed using on-line gas chromatography (GC; Agilent 6890A) with flame ionization detection (FID) after molecular separation using a capillary column (Agilent; HP-1). Methylcyclohexane, 1-methylcyclohexene, 4-methylcyclohexene, cyclohexane, cyclohexene, benzene, and 1,4-cyclohexadiene products were identified in the chromatographs by comparing their retention times to those of chemical standards. Process lines between the liquid injection port and the GC injection system were held at 373-473 K in order to prevent reactant and product condensation; these heated lines did not lead to detectable conversion of any reactants or products and contributed negligibly to measured rates and selectivities. The effluent stream from CO (Praxair; 1% CO, 2% Ar, He bal.) and O_2 reactions was analyzed using on-line GC with thermal conductivity detection (TCD) after molecular separation using a packed column (Agilent; Porapak Q).

Liquid toluene (Sigma-Aldrich, 99.9%), 1,3-cyclohexadiene (Sigma-Aldrich, 97%), and 4-methylcyclohexene (Sigma-Aldrich, 99%) was introduced into flowing H_2 and He mixtures (100-200 cm^3 g Pt/SiO_2^{-1} s^{-1}) before the reactor using a Parker Hamilton syringe pump. Propanoic acid (Sigma-aldrich, 99.5%) was mixed into the toluene reactants for titration experiments. The effluent stream was analyzed using on-line gas chromatography (GC; Agilent 6890A) with flame ionization detection (FID) after molecular separation using a capillary column (HP-1). Methylcyclohexane, 1-methylcyclohexene, 4-methylcyclohexene, cyclohexane, cyclohexene, benzene, and 1,4-cyclohexadiene products were identified in the chromatographs by comparing their retention times to those of chemical standards. Process lines between the liquid injection port and the GC injection system were held at 373-473 K in order to prevent reactant and product condensation; these heated lines did not lead to detectable conversion of any reactants or products and contributed negligibly to measured rates and selectivities.

3.2.3. Calculations of diffusion and mass transfer coefficients.

The pore diffusivities (D_A) of molecular reactants and intermediates through pores of SiO_2 and Al_2O_3 aggregates were estimated from their molecular diffusivities (D_{bA}; from kinetic theory of gases [30]) and Knudsen diffusivities (D_{KA}) combined as resistances in series [31]:

$$D_A = (D_{bA}^{-1} + D_{KA}^{-1})^{-1}. \quad (3.1)$$

The D_{KA} values were calculated using the Knudsen equation [32,33]:

$$D_{KA} = \frac{\langle l_p \rangle}{3}\sqrt{\frac{8RT}{\pi M}}, \quad (3.2)$$

where $\langle l_p \rangle$ is the mean pore diameter determined from N_2 adsorption **Table 3.S1**, R is the ideal gas constant, and M is the molecule's molar mass. The effective diffusivity (D_{eA}) was calculated from the combined pore diffusivity (D_A) and the void fraction (of the catalyst particle), ϵ [31]:

$$D_{eA} = D_A \epsilon^2. \quad (3.3)$$

Overall mass transfer coefficients (k_g) for the transport of partially hydrogenated toluene-derived gaseous intermediates leaving a Pt/SiO_2 aggregate or entering an Al_2O_3 aggregate were calculated from boundary layer theory models developed to describe mass transfer from a sphere into a flowing fluid [34,35]:

$$k_g = \frac{D_{bA}(1-\theta)}{d_p \theta} Sh', \quad (3.4)$$

with

$$Sh' = 1.0(Re')^{\frac{1}{2}}(Sc)^{\frac{1}{3}}, \quad (3.5)$$

$$Re' = \frac{Re}{(1-\theta)}, \quad (3.6)$$

$$Re = \frac{d_p U}{\nu}, \quad (3.7)$$

$$Sc = \frac{\nu}{D_{bA}}, \quad (3.8)$$

where d_p is the aggregate diameter, θ is the void fraction of the catalyst bed, Sh' is the related to the Sherwood number (Sh; $Sh' = Sh\,\epsilon/(1-\epsilon)$), Re is the Reynolds number, U is the superficial velocity, and ν is the kinematic viscosity.

3.2.4. Computational methods.

The thermochemistry of methylcyclohexadiene (MD) and methylcyclohexene (ME) isomers formed from toluene and H_2 were calculated in their gaseous forms using quantum mechanical methods. Structure optimization and electronic energy calculations were performed using the coupled cluster single-double (CCSD) level of theory [36–38] with aug-cc-pvdz basis set [39–43] as implemented in the Gaussian 09 computational package [44]. Vibrational frequencies were calculated using the CBS-QB3 method [45] as implemented in Gaussian 09. Zero-point energies (ZPE), enthalpies (H), entropies (S), and Gibbs free energies (G) were calculated from the computationally-derived electronic energies and vibrational frequencies using standard statistical thermodynamics methods [46], as described in **Chapter 2 Section 2.8.2**.

The free energies (ΔG_i) of formation of MD and ME isomers from toluene and H_2 were determined from the difference in free energy between the gaseous MD or ME (G_i) and their precursors, toluene(g) (G_{tol}) and n/2 H_2 (G_{H_2}) (where n is the number of H atoms added to toluene to form the product):

$$\Delta G_i = G_i - G_{tol} - \frac{n}{2} G_{H_2}. \tag{3.9}$$

The free energy of the gaseous species at a given temperature (T) is related its enthalpy (H) and entropy (S):

$$G = H - TS. \tag{3.10}$$

Equilibrium constants for MD and ME formation are related to the change in the free energy:

$$K_{i,eq} = \exp\left(\frac{-\Delta G_i}{RT}\right). \tag{3.11}$$

The equilibrium partial pressure of the MD and ME ($P_{i,eq}$) is related to the equilibrium constant and to toluene pressure ($P_{tol,eq}$) and H_2 pressure ($P_{H_2,eq}$) at 1 bar:

$$K_{i,eq} = \frac{P_{i,eq}}{P_{tol,eq} P_{H_2,eq}^{\frac{n}{2}}}. \tag{3.12}$$

3.3. Results and discussion

3.3.1. Effects of Pt/SiO_2 dilution with SiO_2 or Al_2O_3 on methylcyclohexane formation rates from toluene-H_2 reactants.

Figure 3.1 shows methylcyclohexane (MA) formation turnover rates (moles MA g-atom Pt_s^{-1} s^{-1}; where Pt_s denotes an exposed Pt-site) during toluene-H_2 reactions on SiO_2-supported Pt nanoclusters (Pt/SiO_2) present as intimate mixtures with SiO_2 and γ-Al_2O_3 (Sasol SBA200; Al_2O_3 refers to Sasol SBA200 henceforth, unless specified otherwise) and loose mixtures with Al_2O_3 (393 K, 90 kPa H_2, 1.4 kPa toluene). MA was the predominant product formed (> 95% selectivity) with 1-methylcyclohexene (1ME) and 4-methylcyclohexene (4ME) as the other detectable products. 3-Methylcyclohexene (3ME) could not be separated from the dominant toluene peak in the chromatographs. MA formation rates increased linearly with the extent of dilution by Al_2O_3 (defined as the ratio between the diluent surface area and Pt_s, denoted as β) present in intimate mixtures. Rates increased monotonically with β for loose mixtures following a sublinear dependence. Al_2O_3 was inert for toluene hydrogenation in the absence of the Pt/SiO_2 component.

Toluene hydrogenation is an exothermic reaction that can lead to temperature gradients within Pt/SiO_2 aggregates. Intra-aggregate volumetric Pt/SiO_2 dilution by SiO_2 would decrease the rate of heat release per aggregate, thus minimizing such artifacts. MA formation rates on Pt/SiO_2 were unaffected by SiO_2 dilution, indicative of the absence of such artifacts even on undiluted Pt/SiO_2. The similar rates on Pt/SiO_2 with or without SiO_2 dilution indicate, moreover, that MA formation rates were not affected by reactant concentration gradients across the Pt/SiO_2 domain due to slow mass transport relative to reaction rates, because such gradients would also be alleviated by volumetric dilution of the active Pt sites by SiO_2. These data demonstrate that dilution did not lead to the removal of any significant heat or mass transfer artifacts that could have led to the MA formation rate differences between Pt/SiO_2 and Pt/SiO_2+Al_2O_3.

Figure 3.2 shows CO oxidation turnover rates (moles CO_2 g-atom Pt_s^{-1} s^{-1}) on intimate Pt/SiO_2+SiO_2 and Pt/SiO_2+Al_2O_3 mixtures. These rates were independent of the extent of dilution and of the identity of the diluent. Pt-catalyzed CO oxidation rates are insensitive to Pt nanocluster diameter [22]; as a result, CO oxidation rates depend solely on the number of exposed Pt sites without any effects of nanocluster size distribution or morphology. The insensitivity of CO oxidation rates to dilution extent and diluent identity indicates that the number of exposed Pt sites that catalyze CO oxidation was unaffected by the mixing protocols used to form these samples. These results indicate, moreover, that the enhanced MA formation rate for Pt/SiO_2+Al_2O_3 mixtures cannot be attributed to an increase in the number of exposed Pt sites or to changes in the Pt nanocluster distribution (which would invariably change the number of exposed sites) to form new types of Pt sites with higher reactivity (such as single Pt-atom sites or Pt nanoclusters of different sizes with lower coordination numbers at the surface).

Table 3.2 shows MA formation turnover rates on Pt/SiO_2 measured on quartz-diluted Pt/SiO_2 (Pt/SiO_2), a loose Pt/SiO_2+Al_2O_3 mixture (40 μm average particle size), and quartz-diluted Pt/SiO_2 with an Al_2O_3 pre-bed (40 μm average particle size). MA formation rates were similar for the Pt/SiO_2 with and without the Al_2O_3 pre-bed (0.12 ± 0.01 and 0.13 moles MA g-atom Pt_s^{-1} s^{-1}, respectively). The MA formation rate for the loose mixture was 0.23 moles MA g-atom Pt_s^{-1} s^{-1}; this loose mixture had an Al_2O_3 to Pt/SiO_2 mass ratio (110 g Al_2O_3 g Pt/SiO_2^{-1}; β=1100 nm^2 Al_2O_3 g-atom Pt_s^{-1}) that was similar to the Al_2O_3 to Pt/SiO_2 mass ratio used for the pre-bed (130 g Al_2O_3 g Pt/SiO_2^{-1}). The lack of a promotional effect for Al_2O_3 present as a pre-bed combined with the two-fold increase in MA formation rate observed for the same amount of Al_2O_3 present as a loose mixture indicates that proximity (at the μm scale) between the Pt/SiO_2 and Al_2O_3 functions is required to affect the measured rate enhancements.

Any impurities present in the reactant stream that bind strongly to Al_2O_3 surfaces would have been trapped by the Al_2O_3 pre-bed, thereby mitigating their poisoning of the Pt surface [9,14]. The observed rates on Pt/SiO_2 were not affected by the presence of the pre-bed, indicating that the higher MA formation rates observed on Al_2O_3-diluted Pt/SiO_2 (compared with Pt/SiO_2) cannot be attributed to the mitigation of Pt-site contamination by poisons in the reactant stream [9,14].

These Pt/SiO_2 and Pt/SiO_2+Al_2O_3 catalysts were exposed to an in-situ pre-treatment in O_2 (10% O_2, He bal.) followed by treatment in H_2 before conducting rate measurements (**Section 3.2.2**). Such an O_2 treatment would have oxidized any carbonaceous debris that adhered to the Pt/SiO_2 or Al_2O_3 surfaces during storage which would have otherwise poisoned Pt sites [9,19]. These data indicate that any effects of Al_2O_3 in trapping such debris during pretreatment and thus mitigating their poisoning of Pt surfaces, as proposed to account for the promotional effect of Al_2O_3 elsewhere [14,19], are negligible.

3.3.2. The effects of propanoic acid on methylcyclohexane formation rates during toluene-H_2 reactions on Pt/SiO_2 and intimate Pt/SiO_2-Al_2O_3 mixtures.

Carboxylic acids bind to Al_2O_3 surfaces as monodentate, bidentate, and chelating bidentate ligands [47–50]. Propanoic acid (PA) has been used as a selective titrant of acid-base pairs on ZrO_2 and TiO_2 surfaces that catalyze ketonization reactions [51,52]. It was used here as a selective titrant of any acid-base pairs that could act as active sites on Al_2O_3 surfaces during toluene-H_2 reactions on Pt/SiO_2+Al_2O_3 mixtures.

Figure 3.3 shows MA formation rates on Pt/SiO_2 during toluene-H_2 reactions as a function of time on stream before and during the introduction of PA into the reactant stream (393 K, 80 kPa

H_2, 1.4 kPa toluene, 3 Pa PA). Similar rates were observed before and during PA introduction; these data indicate that monofunctional toluene hydrogenation routes on Pt nanoclusters were unaffected by such PA titrants. The PA pressure in the effluent was the same as in the inlet stream, indicative of negligible PA adsorption or reaction on Pt nanoclusters or SiO_2 surfaces.

Figure 3.4 shows MA formation rates on an intimate Pt/SiO_2+Al_2O_3 mixture (β=200 nm^2 Al_2O_3 Pt_s^{-1}) during toluene-H_2 reactions as a function of time on stream before and during PA introduction, as well as the effluent PA partial pressures (393 K, 80 kPa H_2, 1.4 kPa toluene, 3 Pa PA). Rates decreased linearly for the first 4 ks that PA was in the reactant feed, then decreased asymptotically towards a value that was similar to that of Al_2O_3-free Pt/SiO_2 (0.12 moles MA g-atom Pt_s^{-1} s^{-1}; **Table 3.2**). PA was not detectable in the effluent during the first 4 ks of PA exposure, after which the pressure increased asymptotically with time to its inlet value (3 Pa). These data show that PA is removed from the inlet stream, either by irreversible titration of Al_2O_3 surfaces or by Al_2O_3-catalyzed reactions. The absence of PA in the effluent stream while rates linearly decreased establishes a link between the loss of the excess component of the MA formation rate and the titration of sites at the Al_2O_3 surface.

3.3.3. 1,3-Cyclohexadiene and 4-methylcyclohexene reactions with H_2 on Pt-free Al_2O_3 surfaces.

Al_2O_3-catalyzed reactions of 1,3-cyclohexadiene (13CHD) and 4ME were carried out to assess the types of reactions that can be mediated by Al_2O_3 surfaces with catalytic relevance for bifunctional MA formation routes during toluene-H_2 reactions on Pt/SiO_2+Al_2O_3 mixtures.

The predominant products formed during 13CHD and H_2 reactions on Al_2O_3 were benzene, cyclohexene (CHE), and cyclohexane (CHA) (393 K, 0-100 kPa H_2; 5-70 Pa 13CHD). **Figure 3.5a** shows benzene, CHE, and CHA formation areal rates as a function of H_2 pressure (extrapolated to zero time on stream, with time-dependent rates show in **Section 3.8.3**) on Al_2O_3-Sasol. CHA formation areal rates increased linearly with H_2 pressure with a y-intercept of zero, benzene showed only a slight positive H_2 dependence with a significant y-intercept, and CHE formation rates increased linearly with H_2 pressure between 0-100 kPa H_2 with a significant y-intercept. Benzene and CHE were formed in the absence of H_2 in stoichiometric amounts, indicating that Al_2O_3-Sasol catalyzed hydrogen-transfer reactions between two 13CHD molecules. The benzene formation areal rate thus reflects the total hydrogen-transfer areal rate because every 13CHD molecule that donates H-H to 13CHD or CHE forms on benzene molecule. CHE and CHA were formed at combined rates that far exceeded benzene formation rates with added H_2 (10-100 kPa), indicating that 13CHD molecules were hydrogenated by reactions with molecular H_2. The total H_2-consumption areal rate corresponds the difference between the number of moles of H_2 consumed to form saturated products and the number of benzene molecules formed.

Figure 3.5b shows hydrogen-transfer and H_2-consumption areal rates as functions of 13CHD pressure on Al_2O_3-Sasol (393 K, 0-100 kPa H_2; 5-70 Pa 13CHD, extrapolated to zero time on stream). These rates increased monotonically with increasing 13CHD pressure in a manner reminiscent of Langmuir-Hinshelwood kinetics, in accordance with the following functional form:

$$r_i = \frac{\alpha_i [HC]}{1 + \delta_i [HC]}, \tag{3.13}$$

where r_i is the areal rate of reaction *i* (denoting hydrogen transfer or H_2 consumption), $[HC]$ is the partial pressure of the hydrocarbon reactant, and $\alpha_{13CHD,i}$ and $\delta_{13CHD,i}$ are lumped reaction parameters. The linear trend at low 13CHD pressures (<10 Pa; corresponding to $\delta_i[HC] \ll 1$) is

consistent with 13CHD consumption reactions occurring on active sites that are essentially uncovered by 13CHD-derived species. The zero-order trend approached at high 13CHD pressures (>60 Pa) suggests that active sites saturated with such species (corresponding to $\delta_i[HC] \gg 1$). The values of the $\alpha_{13CHD,i}$ and $\delta_{13CHD,i}$ constants determined by regressing the measured rate data to the functional form of **equation 3.13** are presented in **Table 3.3**.

The predominant products measured during 4ME-H_2 reactions on Al_2O_3-Sasol and Al_2O_3-solgel were 1-methylcyclohexene (1ME) via isomerization routes and MA via hydrogenation routes. Small amounts of 3ME but no toluene was detected (toluene and 3ME could be separated given the low partial pressures of products during these reactions). **Figure 3.6** shows H_2-consumption areal rates (corresponding to the rates of MA formation) and isomerization areal rates (corresponding to the combined rates of 1ME and 3ME formation) as functions of H_2 (Al_2O_3-solgel) and 4ME (Al_2O_3-Sasol and Al_2O_3-solgel) pressures during 4ME-H_2 reactions (393 K, 0-100 kPa H_2, 10-150 Pa 4ME). H_2 consumption rates on both alumina samples increased monotonically with increasing 4ME pressure with trends that were reminiscent of Langmuir-Hinshelwood kinetics (**eq 3.13**), consistent with 4ME hydrogenation reactions that occurred on sites that were mostly uncovered with 4ME-derived species at low 4ME pressures (< 20 Pa; $\delta_i[HC] \ll 1$) and ultimately became saturated with such species at higher pressures (> 50 Pa; $\delta_i[HC] \gg 1$). Isomerization rates increased linearly with 4ME pressure, with a non-zero y-intercept, on both alumina samples. Both H_2-consumption and isomerization rates on Al_2O_3-solgel increased linearly with H_2 pressure; the H_2-consumption rate showed a zero y-intercept while the 1ME formation rate showed a non-zero intercept. No dehydrogenated products were detected during 4ME-H_2 reactions (toluene, methylcyclohexadiene isomers) indicating that 4ME reactions with molecular H_2, rather than bimolecular hydrogen transfer reactions between 4ME molecules, accounted entirely for the MA formed. The significant y-intercept for the 1ME formation curve indicates that the 4ME isomerization reaction was catalyzed by Al_2O_3-solgel in the absence of H_2. The increase in isomerization rate as a function of H_2 pressure suggests that isomerization routes mediated by bound H_2 at the Al_2O_3 surface [23] may contribute to the rate that 1ME forms.

3.3.4. The role of additive/stochiometric toluene hydrogenation routes via molecular shuttles in Pt/SiO_2 and Al_2O_3 mixtures.

Toluene hydrogenation turnovers that form MA on monofunctional Pt/SiO_2 catalysts are mediated by a sequence of six H-addition elementary steps that form partially hydrogenated toluene-derived species with *n* added H atoms (denoted TH_n*, *n*=1-5). 1ME and 4ME gaseous products were detected during toluene-H_2 reactions on Pt surfaces via the desorption of their respective bound counterparts (**Chapter 2, Section 2.3.1**). The observation that bound 1ME and 4ME intermediates desorb suggests that other partially hydrogenated toluene-derived surface intermediates may too desorb, but at partial pressures that are below the limits of detection (~1 ppm). The data described in the previous section (**Section 3.3.3**) demonstrates, moreover, that Al_2O_3 surfaces catalyze reactions of H_2 with unsaturated cyclic hydrocarbons. These results suggest that partially hydrogenated toluene-derived species that desorb from the Pt nanoparticle surfaces can react at Al_2O_3 surfaces present within diffusion distances. Toluene hydrogenation on Pt/SiO_2 was found to be limited primarily by H addition to TH_1* intermediates (mono-hydrogenated toluene) at 333-393 K (**Chapter 2, Section 2.3.4**) and by H addition to TH_5* (penta-hydrogenated toluene) at significantly higher temperatures (493-533 K; **Chapter 2, Section 2.3.5**); at all temperatures, TH_n* intermediates with fewer added H atoms than the species that reacts in the kinetically-relevant step are present at coverages given by their quasi-equilibrium with toluene-

H_2 reactants. The desorption of these TH_n* intermediates (formed before rate-limiting H-addition steps) from Pt surfaces and their migration to and hydrogenation on Al_2O_3 surfaces (to form MA) would circumvent monofunctional kinetic bottlenecks for MA formation.

A general scheme for such a mechanism, referred to henceforth as the additive/stoichiometric hydrogenation route, is shown in **Scheme 3.1**. These steps are based on the elementary steps proposed to account for measured toluene conversion rates on Pt/SiO_2 (3.6 nm particles) in **Chapter 2** (**Section 2.3.2**), and which are analogous to steps for alkene and other monoarene hydrogenation reactions on transition metal surfaces [53–55]. Two distinct sites are used to bind hydrocarbons (*) and H atoms (*S*) based on the precedent established for reactions on surfaces with high hydrocarbon coverages (i.e., alkane hydrogenolysis [56], alkene hydrogenation [57,58], and monoarene hydrogenation [7,59]). Partial toluene hydrogenation forms cyclic hydrocarbon surface intermediates that differ in their numbers of C atoms that form σ-bonds or π-bonds with surface Pt atoms ([60,61]). Justification for the use of this multisite model for adsorption on Pt surfaces with high hydrocarbon coverage and its implications for kinetics-based reaction modelling are provided in **Chapter 2** (**Sections 2.3.2** and **2.8.5**).

Scheme 3.1, steps 1-3 show quasi-equilibrated H_2 dissociation on an *S*-site pair to form two H adatoms bound at *S*-sites (H-*S*; **Scheme 3.1, step 1**), quasi-equilibrated toluene adsorption at an ensemble of γ_{tol} adjacent *-sites (**Scheme 3.1, step 2**), and a sequence of *m* H additions to bound toluene via reaction with H-*S* in quasi-equilibrated steps to form a bound partially hydrogenated toluene-derived species with *m* additional C-H bonds (TH_m*) bound to γ_{THm} adjacent *-sites (**Scheme 3.1, step 3**). TH_m* reacts further to form MA in two parallel routes shown in **Scheme 3.1, steps 4a-7a** (occurring entirely on Pt surfaces) and **Scheme 3.1, steps 4b-5b** (occurring on both Pt and Al_2O_3 surfaces). **Scheme 3.1, steps 4a-7a** show a sequence of *p-m* H additions to TH_m* via reaction with H-*S* in quasi-equilibrated steps to form a bound partially hydrogenated toluene-derived species with *p* additional C-H bonds (TH_p*) (**Scheme 3.1, step 4a**) bound to γ_{THp} adjacent *-sites, followed by a sequence of 6-*p* H additions to TH_p* via reaction with H-*S* to form MA and γ_{THp} adjacent *-site vacancies, the first of which is irreversible and kinetically relevant (**Scheme 3.1, steps 5a-7a**). **Scheme 3.1, steps 4b-5b** shows reversible desorption of TH_m* to form TH_m(g) and γ_{THm} adjacent *-site vacancies (**Scheme 3.1, steps 4b**) and gaseous MA formation via Al_2O_3-catalyzed TH_m-H_2 reactions (**Scheme 3.1, step 5b**).

Additive/stoichiometric hydrogenation (**Scheme 3.1**) requires that molecular intermediates (TH_m), desorbed from the Pt nanocluster's surface, diffuse across greater than atomic distances to Al_2O_3 surfaces where they are hydrogenated to complete a catalytic turnover. The Pt (or Al_2O_3) sites that catalyze the TH_m's formation (or consumption) in physical Pt/SiO_2+Al_2O_3 mixtures are contained within continuous regions of Pt/SiO_2 (or Al_2O_3) particles with domain boundaries set by the size of either the Pt/SiO_2 (or Al_2O_3) pellets that comprise the loose mixture or the constitutive Pt/SiO_2 (or Al_2O_3) particles that comprise the intimate mixture. The molar TH_m flow leaving a domain of Pt/SiO_2 (W_{PtSiO_2}) is proportional to the difference between the TH_m pressure at the surface of the Pt/SiO_2 aggregate ($[TH_m]^{surf}$) and at the bulk fluid between the catalyst aggregates ($[TH_m]^{bulk}$) [35]:

$$W_{PtSiO_2} = -k_g A_{PtSiO_2}([TH_m]^{bulk} - [TH_m]^{surf}), \tag{3.14}$$

with

$$A_{PtSiO_2} = 4\pi R_{PtSiO_2}^2, \tag{3.15}$$

where k_g is the coefficient for mass transport between a spherical particle and a flowing fluid from boundary layer theory (**Section 3.2.3**), A_{PtSiO_2} is the external surface area of the Pt/SiO_2 aggregate (assuming spherical geometry), and R_{PtSiO_2} is the radius of the Pt/SiO_2 aggregate. The maximum MA formation turnover rate (per exposed surface Pt site) via the additive/stoichiometric hydrogenation route occurs when sufficient Al_2O_3 is present in the mixture to hydrogenate all TH_m molecules that are transported from the Pt/SiO_2 domain to the intervening fluid phase; these rates can be no greater than the maximum rate of TH_m mass transport leaving the Pt/SiO_2 domains. The greatest driving force for TH_m transport from the Pt/SiO_2 domain to the fluid phase occurs when TH_m reaches its maximum allowable concentration at the surface of the Pt/SiO_2 aggregate (which is dictated by the value in gas-phase equilibrium with toluene and $m/2$ H_2 reactants ($[TH_m]^{surf} = [TH_m]_{eq}$)) and is present at negligible pressures in the intervening fluid ($[TH_m]^{bulk} = 0$). The ratio of the maximum mass transfer rate ($W_{PtSiO_2}^{max}$) to the additive hydrogenation rate per Pt/SiO_2 aggregate, denoted ζ, is given by:

$$\zeta = \frac{W_{PtSiO_2}^{max}}{r_{Pt,bi}^{add}\left(\frac{L_{Pt}}{N_{PtSiO2}}\right)}, \tag{3.16}$$

with

$$W_{PtSiO_2}^{max} = k_g A_{PtSiO_2}[TH_m]_{eq}, \tag{3.17}$$

where $r_{Pt,bi}^{add}$ is the MA formation turnover rate (per Pt_s) via the additive hydrogenation route (defined by the difference between the total measured MA formation turnover rate for a Pt/SiO_2+Al_2O_3 mixture and the turnover rate measured for Al_2O_3-free Pt/SiO_2), L_{Pt} is the number of exposed Pt sites, and N_{PtSiO_2} is the number of Pt/SiO_2 pellets.

Upper limits to ζ values were determined by evaluating $W_{PtSiO_2}^{max}$ (**eq 3.17**) using theoretical equilibrium TH_m values determined from their Gibbs free energies of formation from toluene and $m/2$ H_2 reactants calculated using coupled cluster single-double (CCSD) theory and statistical mechanics approaches (**Section 2.2.4**) and using reported experimental values where available. **Table 3.5** shows theoretical equilibrium pressures for the formation of MD and ME isomers from stoichiometric amounts of toluene and H_2 (393 K, 90 kPa H_2, 1.4 kPa toluene) and reported experimental values for 1ME and 4ME, along with ζ values for a loose Pt/SiO_2+Al_2O_3 mixture (R_{PtSiO_2}=70 μm; β=2700 nm^2 Al_2O_3 Pt_s^{-1}). The ζ values for MD isomers were on the order of 10^{-4}-10^{-5}; these values are much less than one indicating that MD isomers formed from the Pt surface cannot diffuse to the Al_2O_3 surface fast enough to account for the increased MA formation rates, even when present at their thermodynamic limits. ME isomers, on the other hand, gave ζ values on the order of 10^4-10^5 (DFT-derived) and 10-10^2 (experimental) which are greater than one, indicating that the maximum rates of ME mass transfer exceeded the observed MA formation rates. Other toluene-derived intermediates contain unpaired electrons making them less stable than MD and ME isomers and are less likely to form at sufficient concentrations necessary for rapid diffusion.

1ME and 4ME intermediates were detected during toluene-H_2 reactions on Pt/SiO_2 at 0.03 and 0.13 Pa, respectively (**Table 3.6**). These values are a factor of 10^3 smaller than the values at

equilibrium with gaseous toluene and two H_2 (from reported experimental values; **Table 3.5**); these large deviations from equilibrium indicate that 1ME and 4ME were formed irreversibly during toluene-H_2 reactions. Kinetically-relevant intermediates in additive hydrogenation routes (**Scheme 3.1**) must form in quasi-equilibrated steps preceding the rate-limiting step for monofunctional Pt-catalyzed MA formation so that their hydrogenation at the Al_2O_3 surface can bypasses the kinetic bottlenecks at the Pt surface. Irreversible 1ME and 4ME formation at the Pt surface, in turn, renders any hydrogenation routes at proximate Al_2O_3 surfaces kinetically irrelevant.

3ME and 4ME both have double bonds at pairs of secondary C atoms; the similar substitution of the C atoms that form the double bond in 3ME and 4ME is reflected in the small free energy change to form 3ME from 4ME (+2 kJ mol^{-1}, 393 K; **Table 3.5**). These similar structural and thermodynamic properties suggest that 3ME and 4ME are formed and consumed in similar elementary steps at the Pt surface; as a result, 3ME is likely to be present at pressures far from its equilibrium limits, as is the case for 4ME, and not expected to contribute significant to MA formation rates through additive Al_2O_3-catalyzed hydrogenation routes.

3.3.5. The role of inhibitor-scavenging routes via molecular shuttles in Pt/SiO_2 and Al_2O_3 mixtures and supporting evidence from reaction-transport models.

Toluene hydrogenates at Pt surfaces via multiple parallel routes that vary in the order of the positions of C atoms that H atoms are added to. These parallel routes form TH_n* species with forty-two distinct numbers and locations of added C-H bonds (**Scheme 3.S1**); such variation in sequences of H-addition steps leads to multiple intermediates with the same H-content but different positions of C-Pt attachments with consequences for adsorbate-surface bond strength and reactivity. Indeed, density functional theory investigations into benzene hydrogenation on Pt(111) surfaces showed that intermediates with the same number of added H atoms but at different relative positions were hydrogenated at different rates [62–65]. Benzene hydrogenation occurred most rapidly through a sequence of H-addition steps in which each H atom was added to a C atom at a position vicinal to a C atom that was hydrogenated in a previous step (denoted the ortho-hydrogenation route) [62,63]. These reports suggest that aromatic rings hydrogenate primarily through a predominant sequence of H-addition steps, and with parallel routes occurring at rates that do not contribute significantly to the overall formation of the saturated product. These parallel routes form stranded surface species with lower reactivities that may cover significant numbers of Pt sites thus inhibiting the formation of transition states that mediate the kinetically-relevant steps of the predominant MA formation route. Their desorption and subsequent hydrogenation at a nearby Al_2O_3 surface within diffusion distances would lower their gaseous concentration and surface coverage, thereby liberating active sites at the Pt surface and increasing rates of the predominant hydrogenation route. A general scheme of a such a mechanism for toluene hydrogenation involving the formation a stranded intermediate at the Pt surface and its scavenging via hydrogenation at an Al_2O_3 function, referred to henceforth as the inhibitor-scavenging route, is shown in **Scheme 3.2**.

Scheme 3.2, steps 1-2 show quasi-equilibrated H_2 dissociation on an *S*-site pair to form two H-*S* species (**Scheme 3.2**, **step 1**) and quasi-equilibrated toluene adsorption at an ensemble of γ_{tol} adjacent *-sites (**Scheme 3.2**, **step 2**). Bound toluene reacts further to form MA via two parallel routes in **Scheme 3.2, steps 3a-6a** (occurring entirely on Pt surfaces) and **Scheme 3.2, steps 3b-10b** (occurring on both Pt and Al_2O_3 surfaces). **Scheme 3.2, steps 3a-6a** show a sequence of *m* H additions to bound toluene via reaction with H-*S* in quasi-equilibrated steps to form a bound

partially hydrogenated toluene-derived species with *m* additional C-H bonds (TH_m-a*) bound to γ_{THm} adjacent *-sites (**Scheme 3.2**, **step 3a**), and a sequence of 6-*m* H addition to TH_m-a* via reaction with H-*S* to form MA and γ_{THm} adjacent *-site vacancies, the first of which is irreversible and kinetically relevant (**Scheme 3.2**, **step 4a-6a**). **Scheme 3.2, steps 3b-10b** show a sequence of *p* quasi-equilibrated H additions to bound toluene via reaction with H-*S* to form TH_p-b* bound to γ_{THp} adjacent *-sites (**Scheme 3.2**, **step 3b**); a sequence of *q*-*m* irreversible H additions to TH_p-b* by reaction with H-*S* to form TH_q-b* bound to γ_{THq} adjacent *-sites (**Scheme 3.2**, **step 4b**); a sequence of *r*-*q* quasi-equilibrated H additions to TH_q-b* via reaction with H-*S* to form TH_r-b* bound to γ_{THr} adjacent *-sites (**Scheme 3.2**, **step 5b**); a sequence of 6-*r* irreversible H additions to TH_r* via reaction with H-*S* to form MA and γ_{THp} vacant, adjacent *-sites, the first of which is irreversible and kinetically relevant (**Scheme 3.2**, **steps 6b-8b**); quasi-equilibrated TH_q-b* desorption to form gaseous TH_q-b (**Scheme 3.2**, **step 9b**); and gaseous MA formation via Al_2O_3-catalyzed TH_q-b and H_2 reactions (**Scheme 3.2**, **step 10b**). In this scheme, TH_q-b* constitutes the most abundant surface intermediate (MASI) at the *-sites and its scavenging via hydrogenation at the Al_2O_3 surface lowers its Pt-surface coverage thus liberating sites that catalyze the kinetically-relevant toluene hydrogenation pathway.

The inhibitor-scavenging route (**Scheme 3.2**), like the additive/stoichiometric hydrogenation route discussed in the previous section (**Section 3.3.4**), requires that TH_q-b molecules diffuse across greater-than-atomic distances from the Pt nanocluster surfaces (where they are formed) to the Al_2O_3 surfaces (where they are hydrogenated) to mediate a catalytic turnover. Geometric segregation of the Pt/SiO_2 and Al_2O_3 domains that catalyze the TH_q-b formation and consumption reactions, respectively, in physical mixtures result in a global maximum TH_q-b concentration at the centers of the Pt/SiO_2 aggregates and a global minimum at the centers of the Al_2O_3 aggregates [26]. Such nonuniform TH_q-b concentration profiles become significant when the intrinsic kinetic rates of TH_q-b formation and consumption become fast relative to the rates of TH_q-b mass transport throughout the pores of the Pt/SiO_2 and Al_2O_3 domains and/or between the Pt/SiO_2 and Al_2O_3 aggregates, and mass transport rates limit overall MA production [26]. Such concentration gradients become more pronounced as aggregate domain sizes increase, along with regions of monofunctional catalytic behaviors [26].

Figure 3.7 shows MA formation turnover rates on loose Pt/SiO_2+Al_2O_3 mixtures as a function of the Pt/SiO_2 aggregate radius (which is equal to the Al_2O_3 aggregate radius) at dilution extents between 2700-3000 nm^2 Al_2O_3 Pt_s^{-1}. These observed MA formation rates decreased monotonically with increasing aggregate radii, asymptotically approaching the rate observed for Al_2O_3-free Pt/SiO_2. Such a decrease in the bifunctional component of the MA formation rate as the aggregate size increased is a strong indication of bifunctional reactions mediated by gaseous intermediates that were limited by their mass transport [26].

A rigorous description of MA formation turnover rates on Pt/SiO_2+Al_2O_3 mixtures that considers TH_q-b concentration gradients across the catalysts' domains is achieved by averaging the MA formation turnover rates over the Pt/SiO_2 volume:

$$\langle r_{MA,Pt} \rangle = \int_0^{v_{PtSiO_2}} r_{MA,Pt}\, dv \Big/ v_{PtSiO_2}, \tag{3.18}$$

where $r_{MA,Pt}$ is the MA formation turnover rate (per exposed Pt site), $\langle r_{MA,Pt} \rangle$ is the volume-averaged $r_{MA,Pt}$ value, dv is a differential volume element, and v_{PtSiO_2} is the volume of a Pt/SiO_2 aggregate. MA formation turnover rates in the inhibitor-scavenging route (**Scheme 3.2**) are limited

by the rate of H addition to TH_m-a* (**Scheme 3.2**, **step 4a**), which is proportional to TH_m-a* ($\theta_{TH_m a*}$) and H-*S* ($\theta_{H,S}$) coverages:

$$r_{MA,Pt} = k_{CH,m+1;a}\theta_{TH_m a*}\theta_{H,S}, \tag{3.19}$$

where $k_{CH,m+1;a}$ is the forward rate constant for the TH_m-a* and H-*S* reaction. The functional form of **equation 3.19** is restated, assuming that TH_m-a* and H-*S* are formed in quasi-equilibrium with gaseous toluene and H_2:

$$r_{MA,Pt} = k_{CH,m+1;a}\prod_{i=1}^{m}\left(K_{CH,i;a}\right)K_{H,S}^{m+1}K_{tol*}[tol][H_2]^{\frac{m+1}{2}}\theta_s\theta_*^{\gamma_{tol}}, \tag{3.20}$$

where K_{tol*} is the equilibrium constant for toluene adsorption at *-sites, $K_{H,S}$ is the equilibrium constant for H_2 dissociation at *S*-site pairs (per H atom), and γ_{tol} is the ensemble of adjacent *-sites that bind toluene. The vacancy coverage term (θ_*) in **equation 3.20** is determined from the balance law describing the conservation of occupied and unoccupied *-sites which, for a Pt surface with *-sites saturated with TH_q-b*, is given by:

$$1 = K_{TH_q b*}\left[TH_q\right]_b\theta_*^{\gamma_{TH_q}}, \tag{3.21}$$

where $K_{TH_q b*}$ is the equilibrium constant for TH_q-b adsorption at *-sites and γ_{TH_q} is the number of adjacent *-sites that bind the TH_q-b molecule. The vacant *S*-site coverage (θ_S) is determined from the balance law describing the conservation of occupied and unoccupied *S*-sites with *S* vacancies and H-*S* as the MASI:

$$1 = \theta_s + K_{H,S}[H_2]^{\frac{1}{2}}\theta_s. \tag{3.22}$$

The MA formation rate (**eq 3.20**) is restated by substituting the *-site vacancy term (θ_*) with the value obtained from the *-site balance (**eq 3.21**), and the *S*-site vacancy term (θ_S) with the value obtained from the *S*-site balance (**eq 3.22**), and assuming that γ_{tol} and γ_{TH_q} are equal ($\gamma_{tol} = \gamma_{TH_q}$):

$$r_{MA,Pt} = \frac{\alpha_{tol\rightarrow TH_{m+1},a}}{\left[TH_q\right]_b}, \tag{3.23}$$

with

$$\alpha_{tol\rightarrow TH_{m+1},a} = \frac{k_{CH,m+1;a}\prod_{i=1}^{m}\left(K_{CH,i;a}\right)K_{H,S}^{m+1}K_{tol*}[tol][H_2]^{\frac{m+1}{2}}}{K_{TH_q b*}\left(1 + K_{H,S}[H_2]^{\frac{1}{2}}\right)}. \tag{3.24}$$

The MA formation rates described by **equation 3.23** are inversely proportional to TH_q-b pressure; as a result, scavenging of TH_q-b species from the fluid phase via hydrogenation at a proximate Al_2O_3 catalyst decreases their pressure and, in turn, increases MA formation rates. The extent to which MA formation rates increase with Al_2O_3 dilution is characterized by an enhancement factor (η) for Pt/SiO_2+Al_2O_3 mixtures defined by the ratio between the volume-averaged MA formation turnover rate for the Pt/SiO_2+Al_2O_3 mixture ($\langle r_{MA,Pt}\rangle$) and the monofunctional MA formation turnover rate ($r_{MA,Pt;mono}$):

$$\eta = \langle r_{MA,Pt} \rangle / r_{MA,Pt;mono}. \tag{3.25}$$

The value of the monofunctional MA formation turnover rate ($r_{MA,Pt;mono}$) in **equation 3.25** is obtained from the $r_{MA,Pt}$ value in **equation 3.23** evaluated for a $\left[TH_q\right]_b$ value that reflects the balance of the TH_q-b formation and consumption rates on the Pt function at pseudo-steady state (denoted as $\left[TH_q\right]_{b,PSS}^{mono}$):

$$r_{MA,Pt;mono} = \frac{\alpha_{tol \rightarrow TH_{m+1},a}}{\left[TH_q\right]_{b,PSS}^{mono}}, \tag{3.26}$$

Substituting the volume-averaged rate with its value from **equation 3.18** and the monofunctional rate with its value from **equation 3.23** gives the following restated form of the enhancement factor (**eq 3.25**):

$$\eta = \frac{\left[TH_q\right]_{b,PSS}^{mono}}{v_{PtSiO_2}} \int_0^{v_{PtSiO_2}} \frac{1}{\left[TH_q\right]_b} \, dv. \tag{3.27}$$

The TH_q-b concentration profile across the dimensions of the Pt/SiO_2 aggregates must be determined in order to evaluate the integral in **equation 3.27** and determine the η value. The TH_q-b concentrations across the radial coordinate of the Pt/SiO_2 aggregates (assuming spherical symmetry) are determined by solving the coupled ordinary differential equations (ODE) that describe the reaction and diffusion of TH_q-b across the Pt/SiO_2 and Al_2O_3 domains. The TH_q-b pressure within the Pt/SiO_2 domain is derived from a balance on the moles of TH_q-b, given in its dimensionless form (with the corresponding derivation in **Section 3.8.6**):

$$\frac{1}{\tilde{l}^2} \frac{\partial}{\partial \tilde{l}} \tilde{l}^2 \frac{\partial}{\partial \tilde{r}} \left[\widetilde{TH}_q\right]_b + \phi_{Pt}^2 \left(\frac{1}{\left[\widetilde{TH}_q\right]_b} - 1 \right) = 0, \tag{3.28}$$

with

$$\phi_{Pt} = R_{Pt} \sqrt{\frac{\rho_{Pt} \alpha_{TH_q b \rightarrow MA,Pt}}{D_{e,TH_q b;Pt} \left[TH_q\right]_{b,PSS}^{mono}}} \tag{3.29}$$

and

$$\left[\widetilde{TH}_q\right]_b = \frac{\left[TH_q\right]_b}{\left[TH_q\right]_{b,PSS}^{mono}}, \tag{3.30}$$

where $\tilde{l}$ is the radial coordinate of the Pt/SiO_2 aggregate divided by the total aggregate radius ($\tilde{l} = l/R_{PtSiO_2}$), ρ_{Pt} is the density of Pt sites in the Pt/SiO_2 aggregate, and $D_{e,TH_q b;Pt}$ is the effective TH_q-b diffusivity throughout the pores of the Pt/SiO_2 aggregate (**Section 3.2.3**). The $\alpha_{TH_q b \rightarrow MA,Pt}$ term denotes a grouping of parameters that describes the rate of TH_q-b hydrogenation at the Pt surface (**Scheme 3.2; steps 5b-8b**, described in detail in **Section 3.8.6**), given as:

$$\alpha_{TH_qb\rightarrow MA,Pt} = \frac{k_{CH,r+1;b}K_{H,S}^{r-q+1}\prod_{i=q}^{r}\left(K_{CH,i;b}\right)[H_2]^{\frac{r-q+1}{2}}}{\left(1+K_{H,S}[H_2]^{\frac{1}{2}}\right)}. \quad (3.31)$$

The term enclosed in the parentheses of **equation 3.28** is derived from the net rate of TH_q-b formation at the Pt surface ($r_{TH_qb,Pt}$; **eq 3.S60**) reflecting the difference between TH_q-b formation from toluene and H_2 (**Scheme 3.2, steps 1-4b**) and its consumption by H_2 addition (**Scheme 3.2, steps 5b-8b**) (**Section 3.8.6**). The $\left[TH_q\right]_{b,PSS}^{mono}$ value reflects the TH_q-b pressure at pseudo-steady state at the Pt/SiO_2 function in which the net TH_q-b formation rate is zero, given (with the corresponding derivation provided in **Section 3.8.6**) by:

$$\left[TH_q\right]_{b,PSS}^{mono} = \frac{\alpha_{tol\rightarrow TH_qb,Pt}}{\alpha_{TH_qb\rightarrow MA,Pt}}. \quad (3.32)$$

The $\alpha_{tol\rightarrow TH_qb,Pt}$ term is a grouping of parameters related to the rate of TH_q-b formation from toluene and H_2 on the Pt surface (**Scheme 3.2, steps 1-4b**, described in detail in **Section 3.8.6**), given by:

$$\alpha_{tol\rightarrow TH_qb,Pt} = \frac{k_{CH,p+1;b}K_{H,S}^{p+1}\prod_{i=1}^{p}\left(K_{CH,i;b}\right)[tol][H_2]^{\frac{p+1}{2}}}{K_{TH_qb*}\left(1+K_{H,S}[H_2]^{\frac{1}{2}}\right)}. \quad (3.33)$$

The TH_q-b pressure within the Al_2O_3 domain is derived from a balance on the moles of TH_q-b, given in its dimensionless form (with the corresponding derivation in **Section 3.8.6**):

$$\frac{1}{\tilde{s}^2}\frac{\partial}{\partial\tilde{s}}\tilde{s}^2\frac{\partial}{\partial\tilde{s}}\left[\widetilde{TH}_q\right]_b - \phi_{Al}^2\left[\widetilde{TH}_q\right]_b = 0, \quad (3.34)$$

with

$$\phi_{Al} = R_{Al}\sqrt{\frac{\sigma_{Al}\alpha_{TH_qb\rightarrow MA,Al}}{D_{e,TH_qb;Al}}}, \quad (3.35)$$

where $\tilde{s}$ is the radial coordinate of the Al_2O_3 aggregate divided by the total aggregate radius ($\tilde{s} = s/R_{Al}$, where R_{Al} is the Al_2O_3 aggregate radius), σ_{Al} is the ratio of the internal Al_2O_3 surface area to the Al_2O_3 aggregate volume, $\alpha_{TH_qb\rightarrow MA,Al}$ is the pseudo-first order rate constant for TH_q-b hydrogenation at the Al_2O_3 surface (from **equation 3.S74** with details described in **Section 3.8.6**), and $D_{e,TH_qb;Al}$ is the TH_q-b diffusivity throughout the voids of the Al_2O_3 aggregate (**Section 3.2.3**).

The TH_q-b pressure distribution across the radial dimensions of the Pt/SiO_2 and Al_2O_3 aggregates was determined for given ϕ_{Pt} and ϕ_{Al} values by solving the coupled ODEs (**eq 3.28** and **eq 3.34**) subject to boundary conditions enumerated in **Section 3.8.6**. The values of the $\alpha_{TH_qb\rightarrow MA,Pt}$ to $\left[TH_q\right]_{b,PSS}$ ratio and $\alpha_{TH_qb\rightarrow MA,Al}$ that constitute ϕ_{Pt} and ϕ_{Al}, respectively, were estimated by regressing the observed enhancement factors to the those determined from the reaction-transport model for loose mixtures with dilution extents ranging from 1000-3000 nm^2 Al_2O_3 Pt_s^{-1} and aggregate diameters ranging from 30-250 μm (393 K, 90 kPa H_2, 1.4 kPa toluene). These estimated parameter values and uncertainties are reported in **Table 3.4**.

Figure 3.8 shows a plot of parity for measured and predicted enhancement factors at the same conditions. The excellent agreement between the mechanism-based kinetic model and measured MA formation enhancement factors demonstrates that the proposed Al_2O_3-mediated hydrogenation of TH_q-b inhibitors from the fluid phase can accurately account for the promotional effect of Al_2O_3-dilution on Pt/SiO_2-catalyzed MA formation turnover rates. These results indicate, moreover, that the decreasing magnitude of the promotional effect as Pt/SiO_2 and Al_2O_3 aggregate domain sizes was increased can be attributed to kinetically-relevant diffusion of molecular intermediates between the two phases that mediate catalytic turnovers.

3.3.6. The relevance of methylcyclohexene isomers as reactive intermediates in prevalent inhibitor-scavenging routes.

The reactions of toluene, H_2, and 1ME or 4ME were carried out on Pt/SiO_2 to investigate whether bound ME isomers occupy significant coverages on Pt surfaces during toluene-H_2 reactions to assess their role as intermediates in inhibitor-scavenging routes. **Table 3.6** shows the MA formation turnover rate, 1ME or 4ME conversion, 1ME or 4ME conversion turnover rate (per exposed Pt site), and initial and final 1ME and 4ME pressures for mixtures of toluene, H_2, and 1ME or 4ME (393 K, 80 kPa H_2, 1.4 kPa toluene, 10-30 Pa ME). The MA formation turnover rate was 0.17 and 0.22 moles MA g-atom Pt_s^{-1} s^{-1} for toluene-H_2 reactions with added 1ME and 4ME, respectively, which exceeded the MA formation turnover rate measured during toluene-H_2 reactions without a ME co-reactant (0.12 mole MA g-atom Pt_s^{-1} s^{-1}, **Table 3.2**) by 0.05 and 0.1 moles MA g-atom Pt_s^{-1} s^{-1}, respectively. These excess MA formation turnover rates were similar to the respective 1ME and 4ME conversion turnover rates (0.050 and 0.094 moles ME g-atom Pt_s^{-1} s^{-1}, respectively); these similar rates indicate that all of the converted ME reactants were accounted for by the increased MA production, demonstrating that ME isomers reacted predominantly via hydrogenation to form MA rather than dehydrogenation to form toluene.

Mixtures of toluene, H_2, and 1ME or 4ME showed inlet and outlet 1ME and 4ME pressures that exceeded their pseudo-steady state values (**Table 3.6**), indicating that the ME pressures were higher throughout the length of the catalyst bed when a ME isomer was introduced as a co-reactant. MA formation turnover rates for inhibitor-scavenging routes (**Scheme 3.2**) are inversely proportional to the pressure of the inhibitor species (**eq 3.23**); as a result, if bound ME isomers inhibited toluene conversion on the Pt surface, then the increased ME pressure prevalent during toluene-H_2-ME reactions (compared with toluene-H_2 reactions) would have lowered the observed toluene conversion turnover rates compared with ME-free toluene-H_2 reactant mixtures. The sum of the MA formation turnover rates for ME-free toluene-H_2 reactant mixtures and the respective ME conversion turnover rate for toluene-H_2-ME mixtures were in close agreement with the observed MA formation turnover rates for toluene-H_2-ME mixtures. Such agreement indicates that the toluene conversion turnover rate must be the same for reactant mixtures with and without added ME to account for observed MA formation rates, thus ruling out any inhibition of toluene conversion on Pt surfaces by 1ME or 4ME co-reactants.

3ME and 4ME both have double bonds at pairs of secondary C atoms; the similar substitution of the C atoms that form the double bond in 3ME and 4ME is reflected in the small free energy change to form 3ME from 4ME (+2 kJ mol^{-1}, 393 K; **Table 3.5**). These similar structural and thermodynamic properties suggest that 3ME and 4ME have similar reactivities for H-addition and H-abstraction reaction steps and bind to the Pt surface with similar strength. As a result, it is unlikely that only 3ME, but not 4ME, constitutes the sole MASI during toluene-H_2 reactions, and moreover, that 3ME would remain the MASI in the presence of 4ME pressures that

exceed their pseudo-steady state values by the 30-100 fold factor achieved by 4ME cofeeding. These data thus indicate that surface-bound counterparts of ME isomers are unlikely to constitute the inhibitor species in inhibitor-scavenging routes.

3.3.7. The relevance of methylcyclohexadiene isomers as reactive intermediates in prevalent inhibitor-scavenging routes.

Comparisons between MA formation turnover rates measured on toluene-H_2-ME and ME-free toluene-H_2 reactant mixtures ruled out the role of ME isomers as inhibitors for toluene hydrogenation on Pt surfaces (at 393 K; **Section 3.3.7**), leaving MD isomers (the only other partially hydrogenated toluene-derived species with closed shell molecular structures) as the best remaining candidate intermediate for inhibitor-scavenging routes (**Scheme 3.2**). Comparisons between the observed kinetic trends for MA formation turnover rates on intimate Pt/SiO_2+Al_2O_3 mixtures as a function of H_2 and toluene pressure and the expected trends from kinetics-based models are drawn in this section to investigate such a role of MD isomers in inhibitor-scavenger routes.

Figure 3.9 shows MA formation turnover rates as a function of H_2 (a) and toluene (b) pressure for Pt/SiO_2 catalysts with 0.7 and 3.6 nm mean Pt-nanocluster diameters (denoted as Pt/SiO_2-0.7 and Pt/SiO_2-3.6, respectively) and an intimate Pt/SiO_2+Al_2O_3 mixture (composed of Pt/SiO_2-0.7). Rates showed a zero-order dependence on toluene pressure for Pt/SiO_2-0.7, Pt/SiO_2-3.6, and the intimate Pt/SiO_2+Al_2O_3 mixture. Rates on both Pt/SiO_2-0.7 and Pt/SiO_2-3.6 showed between a one-half- and first-order dependence on H_2 pressure while rates on the intimate Pt/SiO_2+Al_2O_3 mixture showed a stronger H_2 dependence between first and three-halves order.

The similarity between the dependences of MA formation turnover rates for Pt/SiO_2-0.7 and Pt/SiO_2-3.6 on toluene and H_2 pressures suggests that these rates were limited by the same elementary step, despite their difference in mean Pt-nanocluster diameter. MA formation turnover rates were found to be limited by the reaction between TH_1* (mono-hydrogenated toluene) and H-*S* intermediates on Pt/SiO_2-3.6 at 393 K (**Chapter 2**, **Section 2.3.4**); the MA formation turnover rates on Pt/SiO_2-0.7 are thus assumed to be limited by the rate of this same step, given by **equations 3.23** and **3.24** (**Scheme 3.2, steps 1-4a**, with m=1 and q=2):

$$r_{MA,Pt} = \frac{k_{tol\rightarrow TH_2a}[tol][H_2]}{[TH_2]_b\left(1 + K_{H,S}[H_2]^{\frac{1}{2}}\right)}, \tag{3.36}$$

with

$$k_{tol\rightarrow TH_2a} = \frac{k_{CH,2;a}K_{CH,1;a}K_{H,S}^2K_{tol*}}{K_{TH_2b*}}, \tag{3.37}$$

where $[TH_2]_b$ is the pressure of the kinetically relevant MD intermediate(s) (that constitute the inhibitor, TH_2-b; **Scheme 3.2**) and $K_{TH_2,b*}$ is the equilibrium constant for TH_2-b adsorption to an ensemble of γ_{TH_2} adjacent *-sites (where $\gamma_{TH_2} = \gamma_{tol}$). The functional form of **equation 3.36** is inversely proportional to TH_2-b pressure, which is governed by the balance of the rate that TH_2-b is formed from toluene-H_2 reactants (**Scheme 3.2, steps 1-4b**) and consumed by reactions with H-*S* (**Scheme 3.2, steps 5b-8b**) at the Pt surface at pseudo-steady state. The monofunctional MA formation turnover rate on Pt/SiO_2-0.7 (in the absence of Al_2O_3; $r_{MA,Pt;mono}$) is, in turn,

determined by substituting the $[TH_2]_b$ term in **equation 3.36** with the pseudo-steady state value ($[TH_2]_{b,PSS}^{mono}$) described previously by **equations 3.31**, **3.32**, and **3.33** (for q=2):

$$r_{MA,Pt;mono} = \frac{k_{tol\rightarrow TH_2a} k_{TH_2b\rightarrow MA,Pt} [H_2]^{\left(\frac{r-p}{2}\right)}}{k_{tol\rightarrow TH_2b,Pt}\left(1 + K_{H,S}[H_2]^{\frac{1}{2}}\right)}, \quad (3.38)$$

with

$$k_{tol\rightarrow TH_2b,Pt} = \frac{k_{CH,p+1;b} K_{H,S}^{p+1} \prod_{i=1}^{p}\left(K_{CH,i;b}\right)}{K_{TH_2b*}}, \quad (3.39)$$

and

$$k_{TH_2b\rightarrow MA,Pt} = k_{CH,r+1;b} K_{H,S}^{r-1} \prod_{i=q}^{r}\left(K_{CH,i;b}\right). \quad (3.40)$$

The form of **equation 3.38** is independent of toluene pressure, which is consistent with the observed toluene-independent MA formation turnover rates from toluene-H_2 reactants on Pt/SiO_2-0.7 (**Figure 3.9**). The functional form of **equation 3.38** is proportional to H_2 pressure raised to the power of one-half *r-p* in the numerator ($(r-p)/2$), and inversely proportional to H_2 pressure arising from the summation term enclosed in the parentheses in the denominator ($1 + K_{H,S}[H_2]^{\frac{1}{2}}$). Observed MA formation turnover rates on Pt/SiO_2-0.7 showed a sublinear dependence on H_2 pressure (**Figure 3.9**); this trend is best described by the functional form of **equation 3.38** with an r value that is two greater than p ($r = p + 2$), which results in a linear [H_2] dependence in the numerator of **equation 3.38** that is canceled in part by the term enclosed in the parentheses in the denominator. This relationship between r and p indicates that TH_r-b* (the kinetically relevant intermediate for TH_q-b* hydrogenation; **Scheme 3.2**, **steps 5b-8b**) contains two H atoms more than TH_p-b* (the kinetically relevant intermediate for TH_q-b* formation from toluene and H_2; **Scheme 3.2**, s**teps 3b-4b**). The estimated $K_{H,S}$ value that best describes the Pt/SiO_2-catalyzed MA formation turnover rates (**Figure 3.9**) is shown in **Table 3.4**.

Pseudo-steady state TH_2-b pressures during toluene-H_2 reactions on Pt/SiO_2+Al_2O_3 mixtures depend not only on the rate that TH_2-b is formed and consumed at the Pt surface but also on the rate that TH_2-b is scavenged by the Al_2O_3. Al_2O_3-catalyzed TH_2-b conversion rates are most likely to depend linearly on TH_2-b pressures because H_2 consumption areal rates during 13CHD-H_2 and 4ME-H_2 reactions on Al_2O_3 increased linearly with the respective unsaturated hydrocarbon species at <10 Pa (**Figure 3.5**). This 10 Pa threshold is well above the expected pseudo-steady-state pressures of prevalent TH_2-b species that must fall below their thermodynamic equilibrium with toluene and H_2 (~10^{-6}-10^{-4} Pa, **Table 3.5**). These H_2 consumption areal rates also increased linearly with H_2 pressure (**Figure 3.5**), suggesting that TH_2-b hydrogenation followed a linear dependence on H_2 pressure as well. The TH_2-b hydrogenation rate at the Al_2O_3 surface in a Pt/SiO_2+Al_2O_3 mixture (normalized per exposed Pt site), assuming first-order dependence on TH_2-b and H_2 pressures, is:

$$r_{TH_2b,Al} = \alpha_{TH_2b\rightarrow MA,Al} [TH_2]_b [H_2] [tol]^{\omega_{tol}} \beta, \quad (3.41)$$

where $\alpha_{TH_2b\rightarrow MA,Al}$ is the pseudo-first-order rate constant for TH_2-b consumption, ω_{tol} is the apparent reaction order for TH_2-b hydrogenation on Al_2O_3 with respect to toluene pressure, and β is the ratio between the Al_2O_3 surface area and the number of exposed surface Pt sites. The pseudo-steady state TH_2-b values for Pt/SiO_2+Al_2O_3 mixtures are obtained by equating the TH_2-b formation rate at the Pt surface (**equation 3.S61**; **Scheme 3.2**, s**teps 1-4b**) to the rates of TH_2-b consumption at the Pt (**equation 3.S63**; **Scheme 3.2, steps 5b-8b**) and Al_2O_3 surface (**equation 3.41**; **Scheme 3.2, steps 9b-10b**), described in detail in **Section 3.8.7**, to give:

$$[TH_2]_{b,PSS}^{bi} = \frac{[TH_2]_{b,PSS}^{mono}}{2}\left(\sqrt{\left(\frac{\sigma}{\beta}\right)^2 + 4\frac{\sigma}{\beta}} - \frac{\sigma}{\beta}\right). \tag{3.42}$$

with

$$\sigma = \frac{k_{TH_2b\rightarrow MA,Pt}}{\alpha_{TH_2b\rightarrow MA,Al}[tol]^{\omega_{tol}}[TH_2]_{b,PSS}^{mono}}\left(\frac{[H_2]^{\frac{r-3}{2}}}{1 + K_{H,S}[H_2]^{\frac{1}{2}}}\right). \tag{3.43}$$

The enhancement factor (η; **eq 3.25**) for an intimate Pt/SiO_2+Al_2O_3 mixture (assuming that these mixtures are unaffected by concentration gradients) is given by substituting the $[TH_2]_b$ value in **equation 3.36** with the $[TH_2]_{b,PSS}^{bi}$ value from **equation 3.42** and rearranging:

$$\eta = \frac{1}{2}\left(\sqrt{1 + 4\frac{\beta}{\sigma}} + 1\right). \tag{3.44}$$

Figure 3.9 shows the MA formation rate ratio (η_{inh}) between an intimate Pt/SiO_2+Al_2O_3 mixture and Pt/SiO_2 as a function of H_2 pressure (393 K, 20-90 kPa H_2, 1.4 kPa toluene, 600 nm^2 Al_2O_3 Pt_s^{-1}). The measured η values showed a monotonic increase with H_2 pressure; this measured trend is compared to two predicted trends from **equations 3.44** and **3.43** with *r* values of two (corresponding to TH_q-b* hydrogenation limited by TH_2-b and H-*S* reaction, **Scheme 3.2, steps 5b-8b**) and three (corresponding to TH_q-b* hydrogenation limited by TH_3-b and H-*S* reaction, **Scheme 3.2, steps 5b-8b**). The trend predicted with an *r* value of two shows excellent agreement with the observed values, which indicates that TH_2-b consumption at the Pt surface (**Scheme 3.2, steps 5b-8b**) is limited by an irreversible TH_2-b* reaction with H-*S*. This *r* value of two requires, moreover, that the *p* value is equal to zero (because $r = p + 2$), indicating that TH_2-b formation is limited by the reaction between bound toluene and H-*S* (**Scheme 3.2, steps 1-4b**).

Agreement between the kinetic model and the observed kinetic trends for Pt/SiO_2 and Pt/SiO_2+Al_2O_3 mixtures demonstrates that the increased MA formation turnover rates for Al_2O_3-diluted Pt/SiO_2 catalysts is consistent with the inhibitor-scavenging route (**Scheme 3.2**) involving MD species (TH_2-b) as Pt-site inhibitors. The identification of the kinetically-relevant steps that govern TH_2-b formation and consumption at the Pt surface, moreover, enables rigorous comparisons of the values of the kinetic and thermodynamic parameters determined from reaction-transport modeling in this section and **Sections 3.3.5** with relevant experimental and theoretical benchmarks in the next section.

3.3.8. Chemical significance of kinetic parameters that govern reactivity in methylcyclohexadiene-mediated inhibitor-scavenging routes.

The TH_q-b concentration profiles throughout the pores and channels of Pt/SiO_2 and Al_2O_3 aggregates in loose Pt/SiO_2+Al_2O_3 mixtures, derived from reaction-transport models (**Section 3.3.5**), depended on the Thiele moduli for the respective domains (ϕ_{Pt} (**eq 3.29**) and ϕ_{Al} (**eq 3.35**)). These Thiele moduli depended on the values of two unknown parameters consisting of the $\alpha_{TH_qb\rightarrow MA,Pt}$ to $\left[TH_q\right]_{b,PSS}^{mono}$ ratio and $\alpha_{TH_qb\rightarrow MA,Al}$; their values were estimated by regressing the observed rate enhancements for loose Pt/SiO_2+Al_2O_3 mixtures to values predicted from reaction transport models (**Table 3.4**). The chemical significance of these regressed parameters is investigated in this section for enhanced MA formation rates mediated by the scavenging of TH_2-b inhibitors (**Scheme 3.2**) with the kinetically-relevant steps as identified in **Section 3.3.7** (p=0, q=2, and r=2).

Dividing both sides of **equation 3.31** (evaluated for q=2 and r=2) by $[TH_2]_{b,PSS}^{mono}$ gives the following description of the $\alpha_{TH_2b\rightarrow MA,Pt}$ to $[TH_2]_{b,PSS}^{mono}$ ratio:

$$\frac{\alpha_{TH_2b\rightarrow MA,Pt}}{[TH_2]_{b,PSS}^{mono}} = \frac{k_{CH,3;b}K_{H,S}[H_2]^{\frac{1}{2}}}{[TH_2]_{b,PSS}^{mono}\left(1+K_{H,S}[H_2]^{\frac{1}{2}}\right)}. \tag{3.45}$$

Rearranging **equation 3.45** and solving for $k_{CH,3;b}$ gives:

$$k_{CH,3;b} = \frac{[TH_2]_{b,PSS}^{mono}\left(1+K_{H,S}[H_2]^{\frac{1}{2}}\right)}{K_{H,S}[H_2]^{\frac{1}{2}}}\left(\frac{\alpha_{TH_2b\rightarrow MA,Pt}}{[TH_2]_{b,PSS}^{mono}}\right). \tag{3.46}$$

The $[TH_2]_{b,PSS}^{mono}$ values on that appear on the right-hand side of **equation 3.46** cannot exceed the equilibrium limit for MD formation from gaseous toluene and H_2 which falls below the limits of detection (~1 ppm) thus precluding their observation. An upper limit for the $k_{CH,3;b}$ value is obtained instead by substituting the $[TH_2]_{b,PSS}^{mono}$ value in **equation 3.46** with the pressure of 1-methyl-1,4-cyclohexadiene (1M14CHD) formed in equilibrium with gaseous toluene and H_2 ($1.75x10^{-4}$ Pa; 393 K, 1.4 kPa toluene, and 90 kPa H_2; **Table 3.5**), which constitutes the most abundant among MD isomers at equilibrium. Evaluating the right-hand side of **equation 3.46** with $[TH_2]_{b,PSS}^{mono}$ given by the 1M14CHD equilibrium value, the regressed value of the $\alpha_{TH_2b\rightarrow MA,Pt}$ to $[TH_2]_{b,PSS}^{mono}$ ratio from reaction-transport modeling (**Table 3.4**), and the regressed $K_{H,S}$ value (**Table 3.4**), gives a measured $k_{CH,3;b}$ value of $4(\pm1)x10^{-6}$ moles MA g-atom Pt_s^{-1} s^{-1} bar $H_2^{-1/2}$ (393 K, 90 kPa H_2, 1.4 kPa toluene).

The $k_{CH,3;b}$ term depends exponentially on the difference in free energy between the transition state for the TH_2-b* and H-*S* reaction ($G_{CH,3;b}^{\ddagger}$) and the reactant state consisting of TH_2-b* (G_{TH_2b*}) and H-*S* ($G_{H,S}$), according to transition state theory formalisms [66,67]:

$$k_{CH,3;b} = \frac{k_BT}{h}\exp\left(-\frac{\Delta G_{CH,3;b}^{\ddagger}}{RT}\right) \tag{3.47}$$

with

$$\Delta G^{\ddagger}_{CH,3;b} = G^{\ddagger}_{CH,3;b} - G_{TH_2,b*} - G_{H,S}. \quad (3.48)$$

The measured $k_{CH,3;b}$ value (4(±1)x10^{-6} moles MA g-atom Pt$_s^{-1}$ s^{-1} bar $H_2^{-1/2}$) corresponds to a positive change in Gibbs free energy ($\Delta G^{\ddagger}_{CH,3;b}$) of 135±2 kJ mol^{-1}. Larger free energy values reflect lower rates (because of the negative sign in the exponential; **eq 3.47**) thus indicating that this measured $\Delta G^{\ddagger}_{CH,3;b}$ value (which was evaluated using the $k_{CH,3;b}$ maximum) corresponds to the lower limit of the free energy barrier. The free energy barrier to form the transition state for the reaction between bound 1-methyl-1,3-cyclohexadiene (1M13CHD) and bound H on an Al_2O_3-supported 13 Pt-atom cluster (which is similar in size to the Pt nanoclusters expected to cover the SiO_2 surface on the Pt/SiO_2-0.7 catalyst) has been reported to be 108 kJ mol^{-1} (393 K, 1 bar) based on DFT studies [68]. Their reported free energy barrier differs from the $\Delta G^{\ddagger}_{CH,3;b}$ value measured here by only 27±2 kJ mol^{-1} (in magnitude); these values are in reasonable agreement given that other plausible methylcyclohexadiene isomers and binding orientations (for which the barriers were not calculated) with different reactivities may constitute the inhibitor species in relevant bifunctional routes. Such comparison suggesting, moreover, that the measured $k_{CH,3;b}$ and corresponding $\Delta G^{\ddagger}_{CH,3;b}$ values based on reaction-transport modeling are reasonably similar to appropriate theoretical benchmarks providing supporting evidence for catalytically-relevant inhibitor-scavenging routes mediated by MD species.

TH_2-b scavenging at Al_2O_3 surfaces can only increase MA formation turnover rates catalyzed by Pt surfaces if pseudo-steady state TH_2-b* coverages are affected by the Al_2O_3-catalyzed TH_2-b consumption. The maximum effect of the Al_2O_3 scavenger is achieved in the limit where TH_2-b is depleted completely from the fluid phase and TH_2-b* desorption becomes irreversible (because the TH_2-b re-adsorption rate is zero when TH_2-b is absent from the fluid phase). The net rate that TH_2-b is formed ($r_{TH_2b,Pt}$) reflects the difference between the forward TH_2-b formation rate from toluene and H_2 ($r_{tol\rightarrow TH_2b,Pt}$) and the consumption rates by reaction with H-*S* ($r_{TH_2b\rightarrow MA,Pt}$) and by irreversible desorption ($r_{-TH_2b,Pt}$):

$$r_{TH_2b,Pt} = r_{tol\rightarrow TH_2b,Pt} - r_{TH_2b\rightarrow MA,Pt} - r_{-TH_2b*}, \quad (3.49)$$

with

$$r_{-TH_2b*} = k_{TH_2*}\theta_{TH_2b}, \quad (3.50)$$

where k_{TH_2*} is the forward rate constant for TH_2-b desorption from γ_{TH_2} adjacent *-sites and θ_{TH_2b} is the TH_2-b coverage at *-sites. Substituting $r_{tol\rightarrow TH_2b,Pt}$ with its value from **equation 3.39** (with p=0), $r_{TH_2b\rightarrow MA,Pt}$ with its value from **equation 3.S63**, and r_{-TH_2b*} with its value from **equation 3.50** for a TH_2-b covered surface ($\theta_{TH_2b} = 1$) gives the following restated form of **equation 3.49**:

$$r_{TH_2b,Pt} = k_{CH,1;b}K_{H,S}K_{tol*}[tol][H_2]^{\frac{1}{2}}\theta_s\theta_*^{\gamma_{tol}} - k_{CH,3;b}K_{H,S}[H_2]^{\frac{1}{2}}\theta_s - k_{TH_2b*}. \quad (3.51)$$

The net TH_2-b formation rate is zero at pseudo-steady state ($r_{TH_2b,Pt} = 0$); as a result, an expression for the *-site vacancy term is obtained by rearranging **equation 3.51 (**evaluated with $r_{TH_2b,Pt} = 0$):

$$\theta_*^{\gamma_{tol}} = \frac{k_{CH,3;b}K_{H,S}[H_2]^{\frac{1}{2}}\theta_s + k_{TH_2b*}}{k_{CH,1;b}K_{H,S}K_{tol*}[tol][H_2]^{\frac{1}{2}}\theta_s}. \quad (3.52)$$

Substituting the $\theta_*^{\gamma_{tol}}$ value in the MA formation rate (**eq 3.20**; m=1) with its value from **equation 3.52** gives the maximum MA formation turnover rate for irreversible TH_2-b desorption:

$$r_{MA,Pt} = k_{CH,1;a}K_{CH,2;a}K_{H,S}^2K_{tol*}[tol][H_2]\theta_s\left(\frac{k_{CH,3;b}K_{H,S}[H_2]^{\frac{1}{2}}\theta_s + k_{TH_2b*}}{k_{CH,1;b}K_{H,S}K_{tol*}[tol][H_2]^{\frac{1}{2}}\theta_s}\right). \quad (3.53)$$

Equation 3.53 reveals that the TH_2-b desorption (and subsequent scavenging) only contributes to the MA formation turnover rate if the value of k_{TH_2b*} is comparable to or greater than the rate that TH_2-b* reacts with H-*S* ($k_{CH,3;b}K_{H,S}[H_2]^{\frac{1}{2}}\theta_s$) at the Pt surface. The measured value for the rate of TH_2-b* reaction with H-*S* ($k_{CH,3;b}K_{H,S}[H_2]^{\frac{1}{2}}\theta_s$) was 1.1(±0.3)x$10^{-6}$ (at 393 K, 1.4 kPa toluene, 90 kPa H_2; based on measured $k_{CH,3;b}$ and $K_{H,S}$ values (**Table 3.4**) and θ_s from **equation 3.22**). The TH_2-b desorption rate constant (k_{TH_2b*}) was calculated to be 5.3x10^{-7} moles TH_2-b g-atom Pt_s^{-1} s^{-1} (393 K, 1.4 kPa toluene, 90 kPa H_2) from the DFT-derived change in free energy to form gaseous 1M14CHD from its bound counterparts at bridge sites on a Pt(111) surface (144 kJ mol^{-1} (**Table 3.S2**); 393 K, 1.4 kPa toluene, 90 kPa H_2), assuming that the energy of the transition state for desorption differs negligibly from the energy of the gaseous product. The TH_2-b* desorption rate (k_{TH_2b*}) and rate of TH_2-b* reaction with H-*S* ($k_{CH,3;b}K_{H,S}[H_2]^{\frac{1}{2}}\theta_s$) differed by only a factor of 2; this similarity suggests that TH_2-b* desorption rate is competitive with the rate of TH_2-b* and H-*S* reaction and consistent with the role of TH_2-b species as relevant intermediates in inhibitor-scavenging routes.

The measured pseudo-first-order rate constant for TH_2-b hydrogenation at the Al_2O_3 surface ($\alpha_{TH_2b\rightarrow MA,Al}$; defined as in **equation 3.35** with q=2) was determined to be 5.1(±1.9)x10^{-5} molec. MA nm^{-2} Al_2O_3 s^{-1} Pa^{-1} (393 K, 90 kPa H_2, 1.4 kPa toluene; **Table 3.4**) from reaction-transport modeling. This measured $\alpha_{TH_2b\rightarrow MA,Al}$ value is within a factor of 10 of the first-order rate constant observed for 1,3-CHD hydrogenation on Al_2O_3 surfaces (5.6x10^{-6}; **Table 3.3**, linearly extrapolated from the value measured at 20 kPa to 90 kPa H_2). The similarity between these values indicates that the rates of TH_2-b hydrogenation necessary to account for increased MA formation turnover rates on Pt/SiO_2+Al_2O_3 mixtures are reasonably similar to the measured 1,3-CHD hydrogenation rates (a reaction that resembles the hydrogenation of MD isomers proposed to comprise TH_2-b) on Pt-free Al_2O_3 surfaces. These data suggest that Al_2O_3 surfaces can hydrogenate MD isomers on Pt/SiO_2+Al_2O_3 mixtures, thereby lowering their partial pressures, at rates sufficient to account for enhanced MA formation rates by removing Pt-site inhibitors.

3.3.9. The effects of Pt nanoparticle size on the prevalence of Al_2O_3-dilution induced methylcyclohexane formation rate enhancements on Pt/SiO_2.

Increased MA formation turnover rates on Pt/SiO_2 when mixed physically with Al_2O_3 showed kinetic trends with reactant pressures and with sizes of Pt/SiO_2 and Al_2O_3 domains that were consistent with the formation of stranded MD isomers at the Pt surface that were scavenged by Al_2O_3 surfaces within diffusion distances. Such a mechanistic proposal seemingly disagrees with the conclusion that Pt/SiO_2-3.6 surfaces are covered by toluene (reached in **Chapter 2**) at

similar conditions to those in which bifunctional synergies were observed for Pt/SiO2-0.7+Al_2O_3 mixtures. This apparent contradiction suggests that the nature of the MASI during toluene-H_2 reactions on Pt/SiO_2 depends on Pt nanocluster size.

Figure 3.11 shows the rate enhancement factor (η; **eq 3.25**) for loose (a) and intimate (b) Pt/SiO_2+Al_2O_3 mixtures with different mean Pt nanocluster diameters (Pt/SiO_2-0.7, Pt/SiO_2-0.8, Pt/SiO_2-1.0, and Pt/SiO_2-3.6; **Table 3.1**) as a function of the Al_2O_3 surface area to exposed Pt site ratio (β). For the loose mixtures, η values increased linearly with β for Pt/SiO_2-0.7 up to a value of 2.5 (for β=2700 $nm^2\ Pt_s^{-1}$), showed a value of 1.5 that was insensitive to β for Pt/SiO_2-0.8, and showed a value close to one for Pt/SiO_2-1.0. For the intimate mixtures, η values increased linearly with β for Pt/SiO_2-0.7 up to a value of 2.5 (for β=600 $nm^2\ Pt_s^{-1}$) but did not exceed a value of 1.3 for the other Pt/SiO_2 catalysts. These data indicate that dilution with Al_2O_3 increased MA formation turnover rates on Pt/SiO_2-0.7 most significantly; showed a relatively small rate enhancement for Pt/SiO_2-0.8 that was more evident on loose mixtures than on the intimate mixture; and did not affect the rates on the other Pt/SiO_2 catalysts.

The prevalent increases in MA formation rates due to Al_2O_3-dilution for Pt/SiO_2 catalysts with smaller mean-Pt nanocluster diameters and the absence of such effects for Pt/SiO_2 with larger Pt nanoclusters suggests that smaller Pt nanoclusters are more susceptible to the inhibitor-scavenger routes that mediate Pt/SiO_2+Al_2O_3 bifunctional synergies (at 393 K). Two plausible explanations are consistent with such a particle-size effect: (i) MD inhibitors cover Pt nanocluster surfaces irrespective of the particle size, but do not desorb from the surfaces of large Pt nanoparticles to be scavenged by proximate Al_2O_3 sites at rates sufficient to lower their coverages; and (ii) toluene, as opposed to MD inhibitors, constitutes the MASI on the surfaces of larger Pt nanoclusters (as concluded in **Chapter 2** for Pt/SiO_2-3.6) such that the scavenging of MD intermediates at proximate Al_2O_3 surfaces does not affect the coverage vacant *-sites that mediate the transition states for kinetically-relevant elementary steps for toluene hydrogenation.

Surfaces of small Pt nanoclusters contain exposed metal atoms with fewer Pt neighbors and have lower coordination numbers than larger clusters; such low coordination makes them interact more strongly with molecular adsorbates [56,69]. Such properties of small nanoclusters suggests that MD molecules would bind more strongly (with a more negative free energy of adsorption) to small Pt nanoclusters than their larger counterparts; consequently, it is unlikely that large, but not small, Pt nanoclusters bind MD molecules at strengths that preclude their desorption to account for the effect of particle size on MA formation rates for Pt/SiO_2+Al_2O_3 mixtures.

A greater fraction of the surface of large metal nanoclusters exposes low index planes compared with their smaller counterparts [56,69]. Toluene binds with a more negative enthalpy of adsorption (relative to gaseous toluene) on Pt(111) to bridge sites (-134 kJ mol^{-1} (DFT-derived); 393 K; 0.11 monolayer (ML) coverage (**Table 3.7**)) compared with three-fold hollow sites (-86.4 kJ mol^{-1} (DFT-derived); 393 K; 0.11 monolayer (ML) coverage (**Table 3.7**)). The toluene bound at bridge sites form C-Pt bonds with four adjacent Pt-atoms (**Scheme 3.3**); the curvature on the surface of small Pt nanoclusters precludes interactions between toluene and bridge sites without significant molecular strain. MD isomers also bind most favorably to Pt(111) surfaces at bridge sites [61], but only forms C-Pt bonds with two adjacent Pt-atoms (**Scheme 3.3**). Such a binding geometry is hypothesized to form easily even on curved surfaces without significant molecular strain. These proposed effects of binding orientation on the relative coverages of toluene and MD adsorbates on Pt nanoclusters could be confirmed through a systematic investigation of the

adsorbate structures and binding energies of toluene and MD isomers using density functional theory on model Pt nanoclusters with different sizes and exposed index planes.

3.4. Conclusions

Methylcyclohexane formation turnover rates from toluene-H_2 reactants on Pt/SiO_2 were shown to increase when mixed physically with γ-Al_2O_3 (0.7 and 0.8 nm mean Pt nanocluster diameter;10-100 kPa H_2, 0.3-2.1 kPa toluene, 393 K). These rates increased less significantly for the same γ-Al_2O_3 to Pt/SiO_2 site ratio when the size of each catalyst domain increased (by varying the size of the Pt/SiO_2 and γ-Al_2O_3 aggregates that comprise the physical mixtures), and no effect of γ-Al_2O_3 was observed when used as a pre-bed. These trends with domain size followed the expected behaviors for a bifunctional reaction mechanism involving sequential reaction steps that occur on geometrically separated catalytic sites facilitated by gaseous molecular intermediates. MA formation rates measured on Pt/SiO_2+γ-Al_2O_3 mixtures following exposure to propanoic acid, a selective titrant for acid-base pairs on oxide surfaces, resembled rates on γ-Al_2O_3-free Pt/SiO_2, demonstrating the catalytic significance of acid, base, or acid-base pair active sites on the γ-Al_2O_3 surface in MA formation. These observations informed two novel bifunctional reaction mechanisms for increased MA formation during toluene hydrogenation. In the first mechanism, a reactive intermediate is generated by toluene-H_2 reactions at the Pt surface that desorbs from the Pt then diffuses to and reacts at the Al_2O_3 surface in an additive hydrogenation route that bypasses the kinetic bottlenecks at the Pt surface. In the second mechanism, stranded surface intermediates are formed by unproductive toluene-H_2 reactions at the Pt surface that block surface sites and inhibit toluene conversion rates. Inhibitors desorb from the Pt surface at low, kinetically limited gaseous pressures, and are subsequently scavenged at the Al_2O_3 surface thereby liberating active Pt sites. The first mechanism was ruled out (at 393 K) because none of the candidate toluene-derived species can form at pressures sufficient to diffuse between the domains at the requisite rates. The second mechanism with methylcyclohexadiene intermediates as inhibitors was best able to account for the effects of domain size, dilution extent, and toluene and H_2 kinetic dependences. γ-Al_2O_3 surface, in the absence of a P/SiO_2 co-catalyst, catalyzed the hydrogenation of 1,3-cyclohexadiene and 4-methylcyclohexene; these reactions occurred at rates that were catalytically significant in the context of Al_2O_3-catalyzed rates in bifunctional mixtures necessary to account for enhancements for Pt/SiO_2+γ-Al_2O_3 mixtures. Reaction-transport modelling based on the proposed bifunctional mechanisms and measured reactivity trends for independent Pt/SiO_2 and γ-Al_2O_3 functions showed that bifunctional synergies are best attributed to γ-Al_2O_3-mediated scavenging of methylcyclohexadiene inhibitors at low temperatures (393 K), prevalent only on Pt/SiO_2 catalysts with small Pt clusters (0.7 nm mean diameter). At higher temperatures (493-533 K), in which methylcyclohexene hydrogenation becomes rate limiting, an additive methylcyclohexene hydrogenation route at nearby γ-Al_2O_3 is likely to become more prevalent.

3.5. Acknowledgements

I would like to acknowledge financial support from the Chevron Corporation, Chevron UC-Berkeley Graduate Research Fellowship, and the National Science Foundation Graduate Research Fellowship, and computational resources provided by the Extreme Science and Engineering Discovery Environment (XSEDE) of the National Science Foundation and the National Energy Research Scientific Computing Center (NERSC) of the Department of Energy. I also acknowledge Dr. Prashant Deshlahra and Dr. Zhijie Wu for performing the coupled cluster calculations reported in this chapter. I would also like to acknowledge Dr. Xueyi Zhang and Dr. Edwin Yik for helpful insights and establishing much of the groundwork for this study.

3.6. Figures, tables, and schemes

Figure 3.1: Methylcyclohexane formation turnover rates (per exposed surface Pt-atom (Pt_s)) for toluene-H_2 reactions on Pt/SiO_2 (0.7 nm mean nanocluster diameter) mixed physically with Al_2O_3-Sasol in loose (■) or intimate mixtures (●), with Al_2O_3-solgel in an intimate mixture (◆), and with SiO_2 in intimate mixtures (▲) as a function of diluent surface area to Pt_s ratios (β) (393 K, 90 kPa H_2, 1.4 kPa toluene). Dashed lines indicate linear trends.

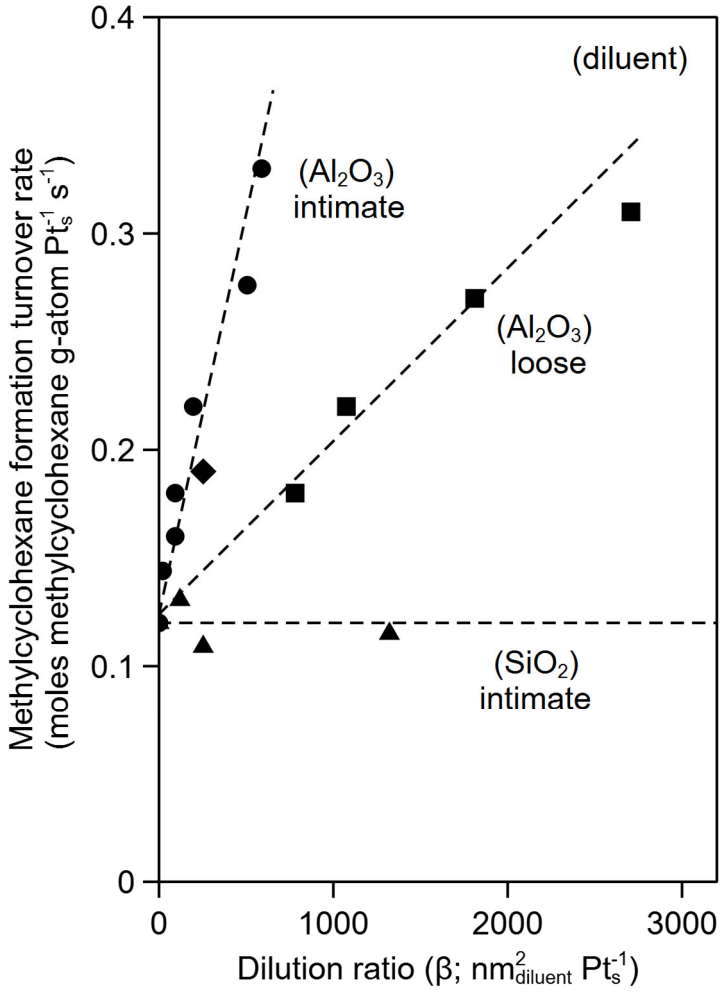

Figure 3.2: CO oxidation turnover rates (per exposed surface Pt-atom (Pt_s)) during CO-O_2 reactions on Pt/SiO_2 (0.7 nm mean nanocluster diameter) mixed with SiO_2 in intimate mixtures (●) and with Al_2O_3-Sasol in intimate mixtures (■) as a function of diluent surface area to Pt_s ratios (β) (473 K, 0.5 kPa CO, 5 kPa O_2). The dashed line indicates a horizontal trend.

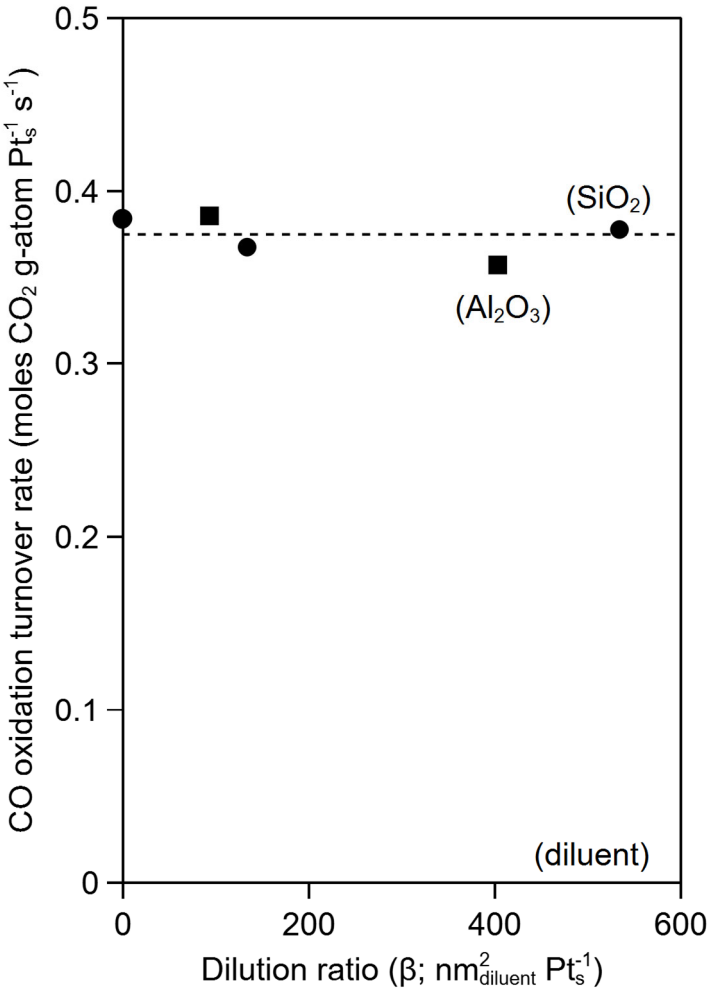

Figure 3.3: Methylcyclohexane formation turnover rates (per exposed surface Pt-atom (Pt_s); ●) and PA pressure (■) in the effluent as a function of time on stream during toluene-H_2 reactions with propanoic acid (PA) on Pt/SiO_2 (0.7 nm mean particle diameter; 393 K, 80 kPa H_2, 1.4 kPa toluene, 3 Pa PA).[a]

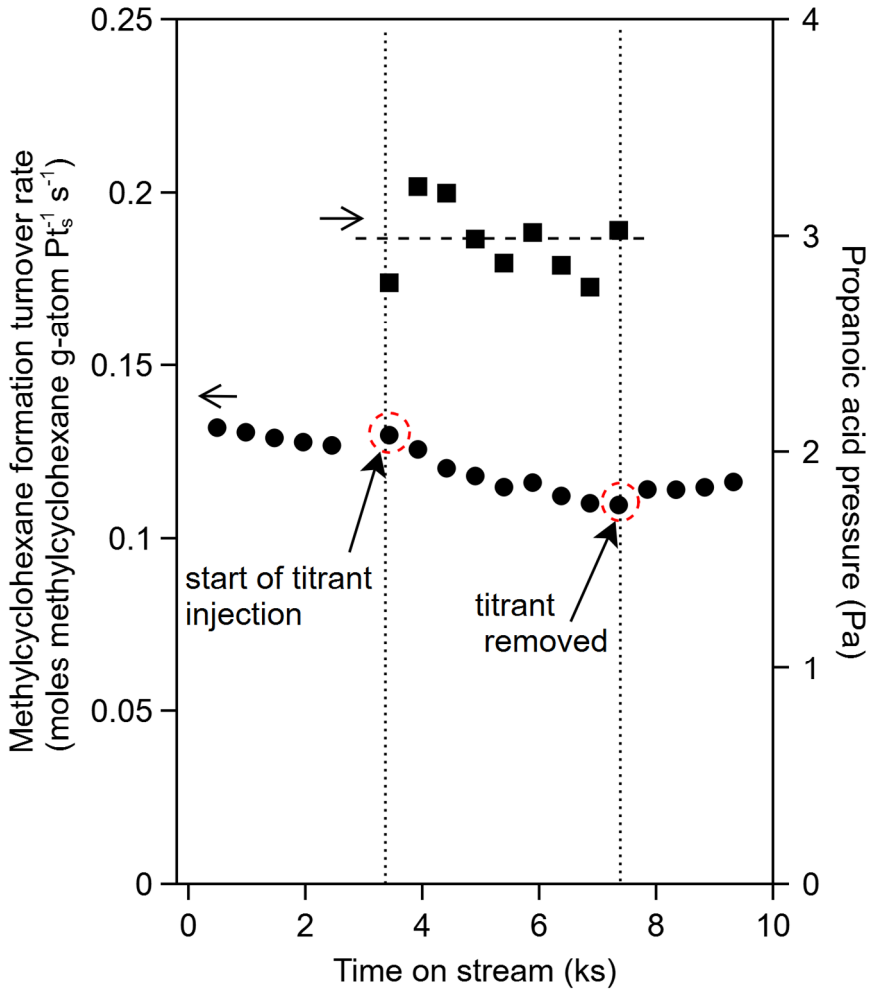

[a]The dashed line represents a horizontal trend, and the dotted vertical lines represent the start and stop of titrant injection.

Figure 3.4: Methylcyclohexane formation turnover rates (per exposed surface Pt-atom (Pt_s); ●) and propanoic acid (PA) pressure (■) in the effluent as a function of time on stream during toluene-H_2 reactions with PA on Pt/SiO_2 (0.7 nm mean particle diameter) present as an intimate mixture with Al_2O_3-Sasol (393 K, 80 kPa H_2, 1.4 kPa toluene, 3 Pa PA, 200 nm^2 Al_2O_3 diluent Pt_s^{-1}).[a]

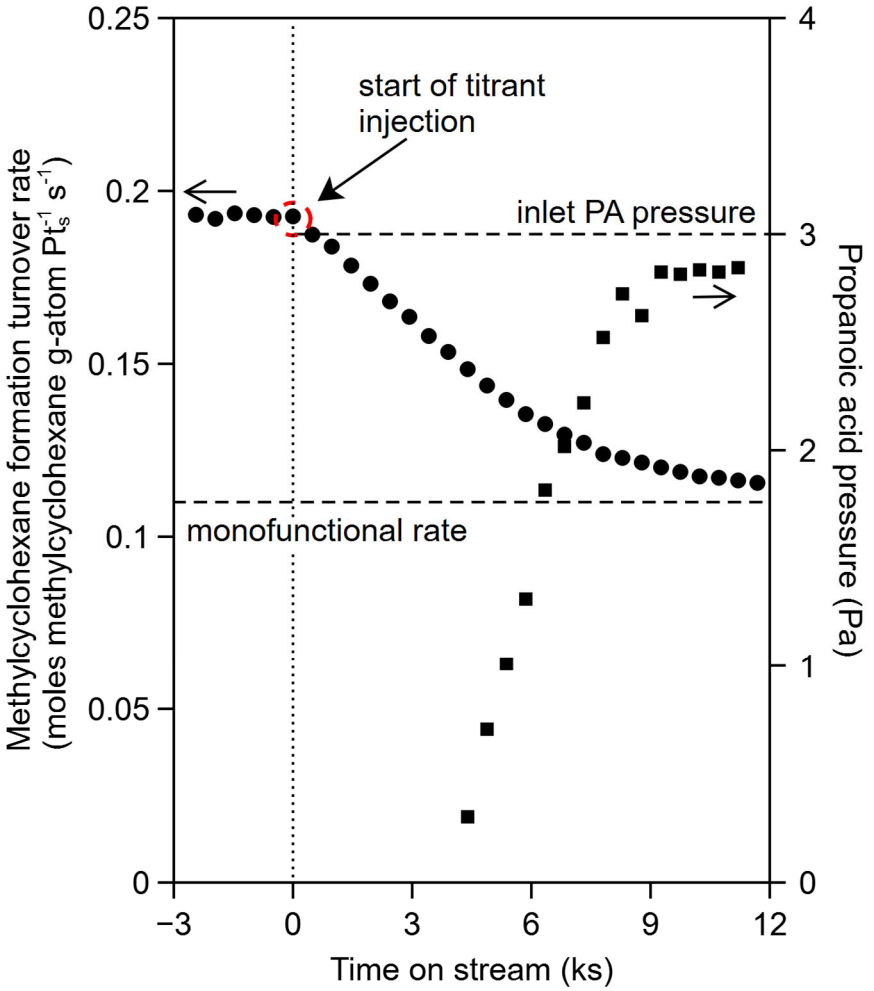

[a]The dotted vertical line indicates the start of the titrant injection, the top dashed line indicates the inlet PA pressure, and the bottom dashed line indicates the monofunctional MA formation turnover rate (on Al_2O_3-free Pt/SiO_2).

Figure 3.5: (a) 1,3-Cyclohexadiene (13CHD) conversion areal rates (molec. 13CHD nm^{-2} Al_2O_3 s^{-1}) to form cyclohexane (CHA; ◆) cyclohexene (CHE; ●) and benzene (■), and H_2 consumption areal rates (molec. H_2 nm^{-2} Al_2O_3 s^{-1}; ▲) as a function of H_2 pressure on Al_2O_3-Sasol (393 K, 12 kPa 13CHD). (b) H_2 consumption (▲) and H-transfer areal rates (■; molec. H_2 nm^{-2} Al_2O_3 s^{-1}) as a function of 13CHD pressure on Al_2O_3-Sasol (393 K, 20 kPa H_2). Dashed lines indicate trends.

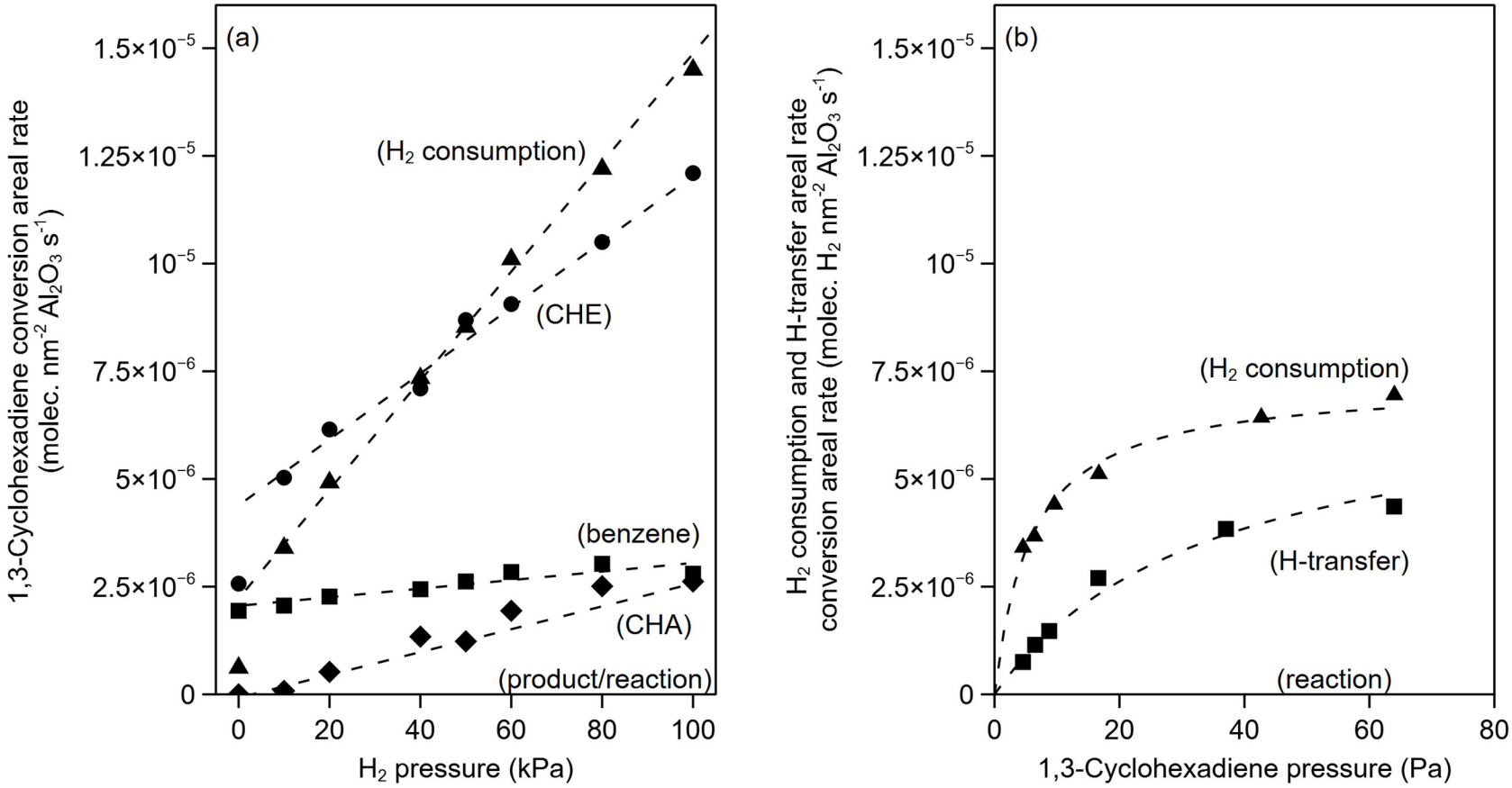

Figure 3.6: (a) H_2 consumption (to form methylcyclohexane (MA); ▲) and isomerization (to form 1-methylcyclohexene (1ME) and 3-methylcyclohexene (3ME); ■) areal rates (molec. 4-methylcyclohexene nm^{-2} Al_2O_3 s^{-1}) during 4-methylcyclohexene (4ME)-H_2 reactions on Al_2O_3-solgel as a function of H_2 pressure (393 K, 30 Pa 4ME). (b) H_2 consumption and isomerization areal rates (molec. 4ME nm^{-2} Al_2O_3 s^{-1}) on Al_2O_3-solgel (▲ and ■, respectively) and Al_2O_3-Sasol (● and ◆, respectively) as a function of 4ME pressure (393 K, 90 kPa H_2). Dashed lines indicate trends.

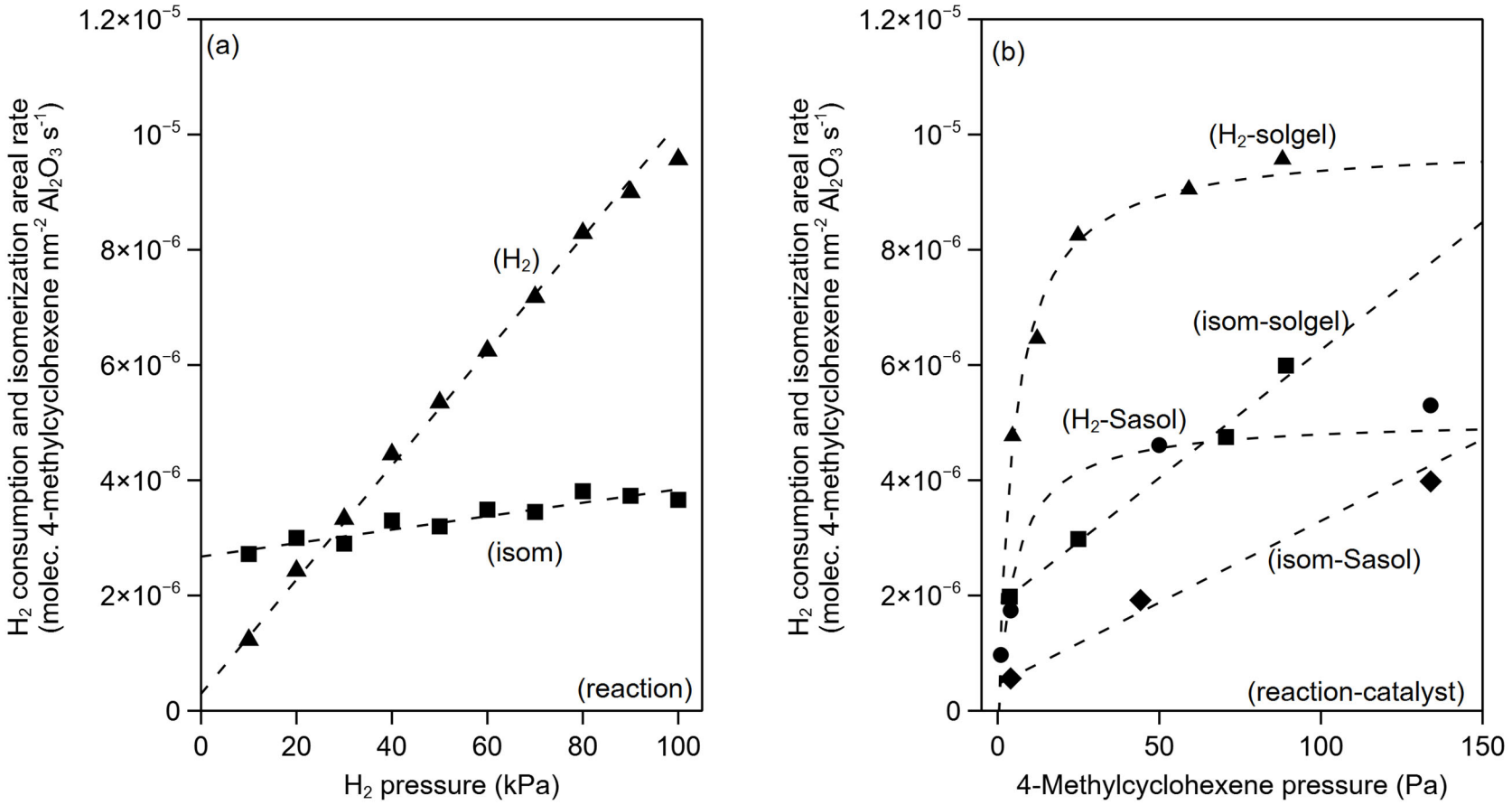

Figure 3.7*:* Methylcyclohexane formation turnover rates (per exposed surface Pt-atom (Pt_s)) during toluene-H_2 reactions on Pt/SiO_2 (0.7 nm mean nanocluster diameter) mixed with Al_2O_3-Sasol in loose mixtures as a function of the Pt/SiO_2 aggregate dimension (393 K, 90 kPa H_2, 1.4 kPa toluene). The solid line indicates the trend, and the dashed line indicates the monofunctional rate measured on Al_2O_3-free Pt/SiO_2.

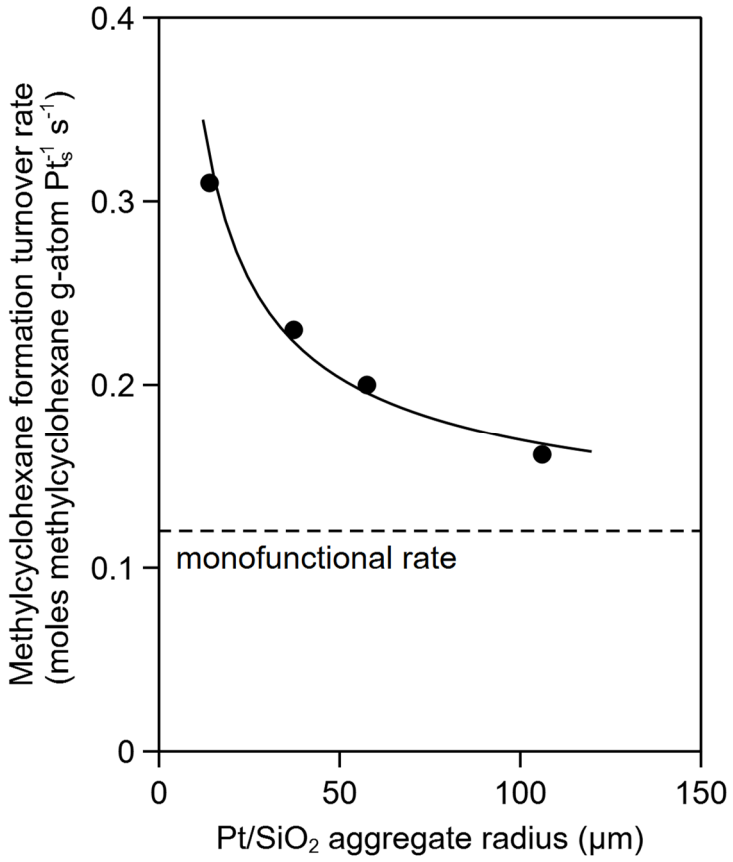

Figure 3.8: Plot of parity for measured and predicted MA formation enhancement factors (η; MA formation turnover rate ratio between $Pt/SiO_2+Al_2O_3$ and SiO_2) for the scavenger-inhibitor model (**Scheme 3.2**) based on the solution to **equations 3.27, 3.28**, and **3.34** with parameter values reported in **Table 3.4**. The enhancement factors were measured on loose mixtures with dilution extents ranging from 1000-3000 nm^2 Al_2O_3 Pt_s^{-1} and aggregate diameters ranging from 40-200 μm (393 K, 90 kPa H_2, 1.4 kPa toluene). The dashed line indicates parity.

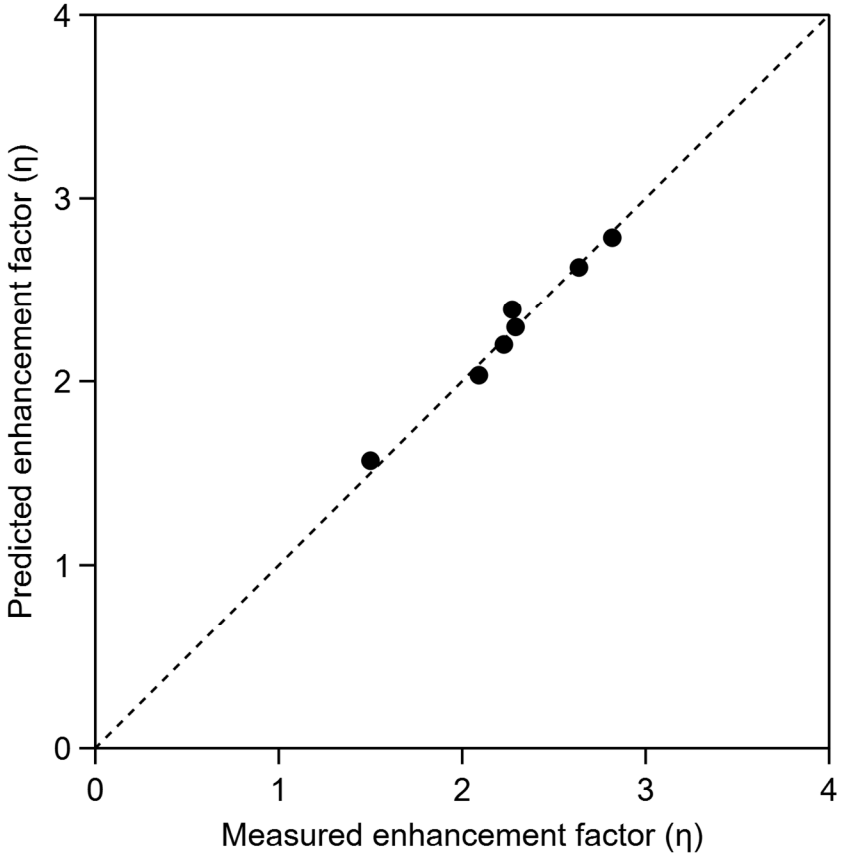

Figure 3.9: Methylcyclohexane formation turnover rates (per exposed surface Pt-atom (Pt_s)) from toluene-H_2 reactants on Pt/SiO_2-0.7 (0.7 nm mean nanocluster diameter) undiluted (●), Pt/SiO_2-3.6 (3.6 nm mean nanocluster diameter) undiluted (■), and on an intimate Pt/SiO_2-0.7 mixture with Al_2O_3-Sasol (○ ; 500 nm^2 Al_2O_3 Pt_s^{-1}) as a function of H_2 pressure (393 K, 1.4 kPa toluene; a) and toluene pressure (393 K, 90 kPa H_2; b).[a]

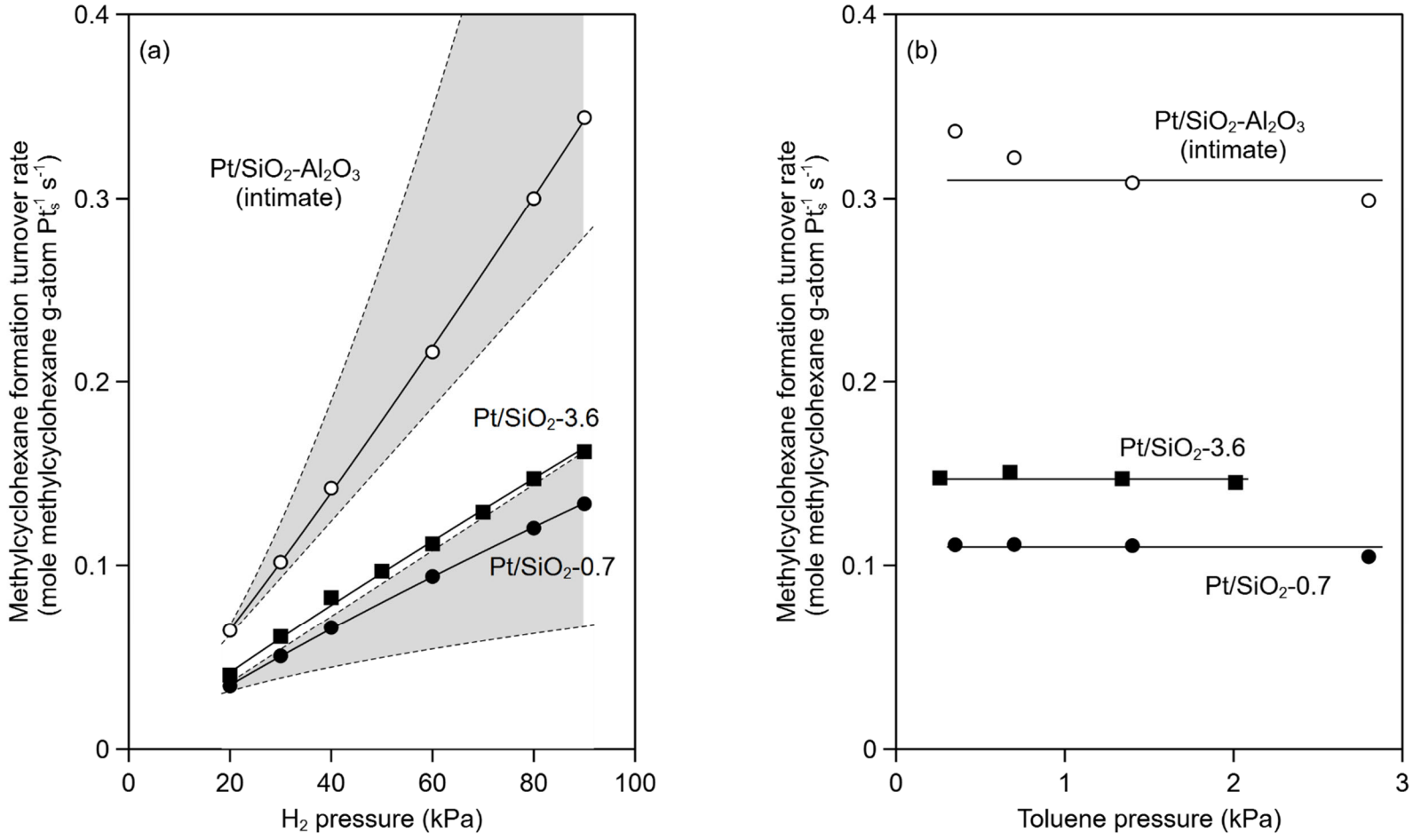

[a] The solid lines indicate trends (a) and (b), the dashed lines at the upper and lower edges of the shaded region enclosing the (●) data (a) indicate first-order and one-half order power law trends, respectively, and the dashed lines at the upper and lower edges of the shaded region enclosing the (○) data (a) indicate three-halves-order and first order power law trends, respectively.

Figure 3.10: MA formation enhancement factors (η; MA formation turnover rate ratio between $Pt/SiO_2+Al_2O_3$ and SiO_2) for the scavenger-inhibitor model (**Scheme 3.2**) as a function of H_2 pressure for an intimate $Pt/SiO_2+Al_2O_3$ mixture (Pt/SiO_2-0.7 and Al_2O_3-Sasol; 393 K, 1.4 kPa toluene).[a]

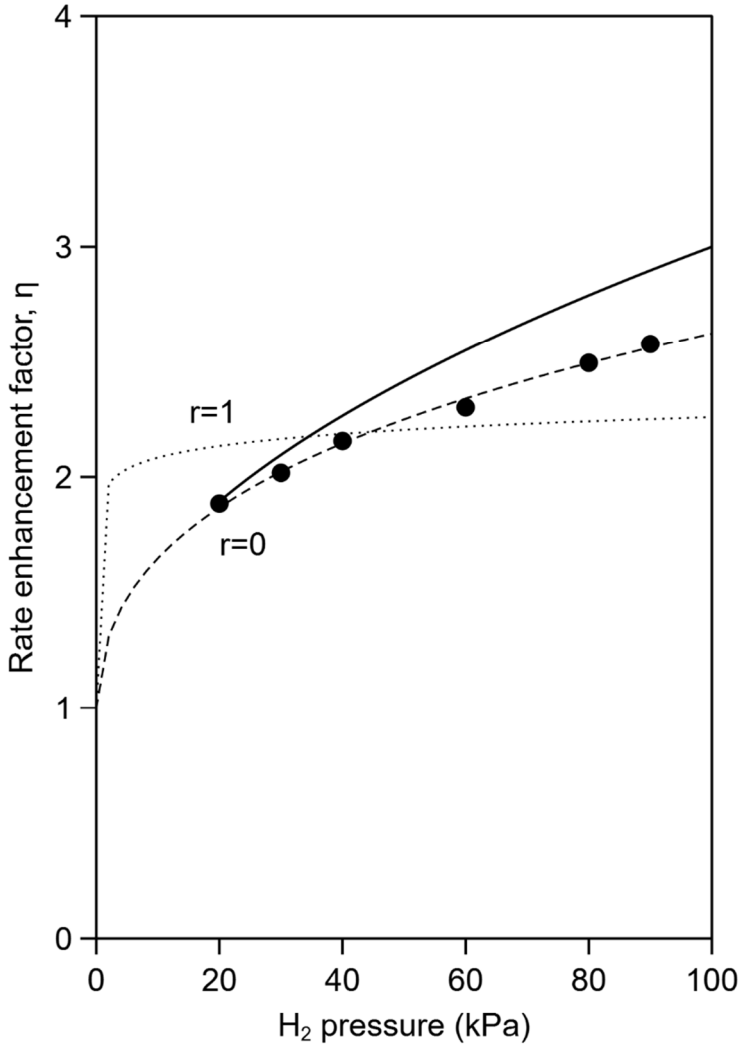

[a]The dashed line indicates the trend of the functional form of **equation 3.44** with an r value of zero and the dotted line indicates the trend with an r value of 1. The solid line indicates a one-half-order power-law trend.

Figure 3.11: Methylcyclohexane formation turnover rate (per exposed surface Pt-atom (Pt_s)) ratio (η) between physical Pt/SiO_2+Al_2O_3-Sasol mixtures and Al_2O_3-free Pt/SiO_2 for toluene-H_2 reactions on Pt/SiO_2 catalysts with mean Pt nanocluster diameters (derived from H_2 adsorption uptakes; **Table 3.1**) of 0.7 (Pt/SiO_2-0.7; ●), 0.8 (Pt/SiO_2-0.8; ◆), 1.0 (Pt/SiO_2-1.0; ■), and 3.6 (Pt/SiO_2-3.6; ▲) nm for loose (a) and intimate (b) mixtures as a function of diluent surface area to Pt_s ratios (β) (393 K, 90 kPa H_2, 1.4 kPa toluene). The dashed line indicates trends.

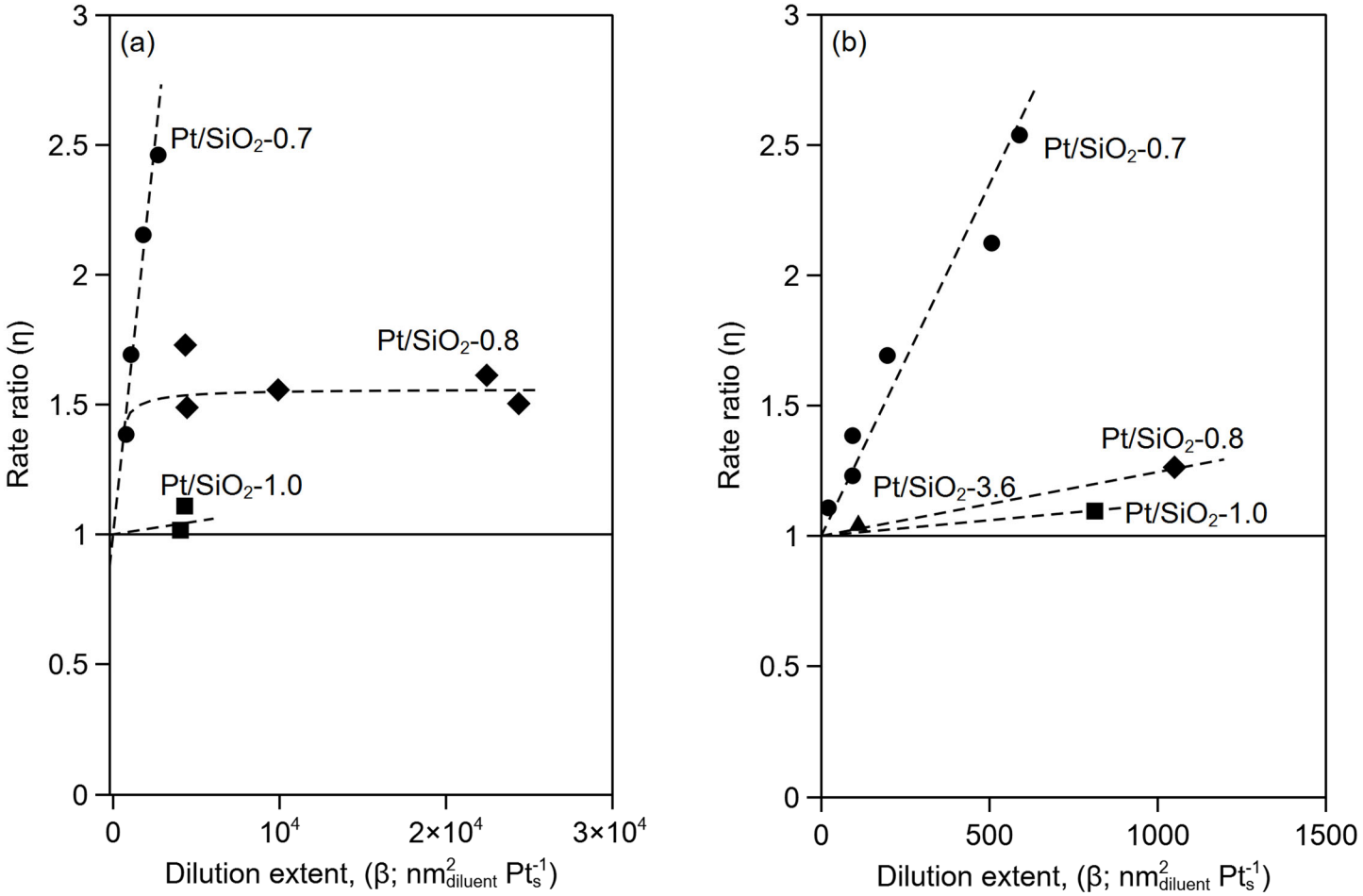

Table 3.1: Pt loading, Pt fractional dispersion (D), mean Pt nanocluster diameter (d_{Pt}), and temperatures for air and H_2 treatments during Pt/SiO_2 catalyst synthesis.

Catalyst-(mean Pt nanoparticle diameter)	Pt loading (wt.%)[a]	Pt fractional dispersion (D)[b]	Mean Pt nanoparticle diameter, d_{Pt}[c] (nm)	Treatment temperature (K): air, [H_2]
Pt/SiO_2-0.7	0.47	1.6	0.7	573, [623]
Pt/SiO_2-3.6	2.1	0.30	3.6	873, [773]
Pt/SiO_2-0.8	0.10	1.4	0.8	673, [623]
Pt/SiO_2-1.0	0.17	1.1	1.0	573, [623]

[a] From inductively coupled plasma – atomic emission spectroscopy.

[b] Metal dispersion (D) from H_2 uptake data, defined as $D = N_H/N_B$, where N_H is the number of H bound by the Pt surface and N_B is the number of metal atoms in the bulk.

[c] Mean Pt cluster diameter from the Pt dispersion with the following relation: $d_{Pt} = 6\,v_{Pt}/(D\,a_{Pt})$ [70], where v_{Pt} is the atomic volume of a Pt-atom in metal (15.10×10^{-3} nm^3) and a_{Pt} is the occupied area of a Pt-atom on a bulk Pt(111) surface for an FCC lattice (6.7×10^{-2} nm^{-2} [71]), the lowest energy crystal facet.

Table 3.2: Methylcyclohexane (MA) formation turnover rates (per exposed surface Pt-atom (Pt_s)) during toluene-H_2 reactions on undiluted Pt/SiO_2 (0.7 nm mean nanocluster diameter), Pt/SiO_2 with an Al_2O_3-Sasol pre-bed,[a] and a loose Pt/SiO_2+Al_2O_3-Sasol mixture (393 K, 90 kPa H_2, 1.4 kPa toluene).

Catalyst mixture	MA formation turnover rate (mole MA g-atom Pt_s^{-1} s^{-1})	Al_2O_3 to Pt ratio (nm^2 Al_2O_3 g-atom Pt_s^{-1})
Pt/SiO_2	0.12 ± 0.01[c]	0
Pt/SiO_2-Al_2O_3 (pre-bed)[a]	0.13	1300
Pt/SiO_2-Al_2O_3 (loose mixture)[b]	0.23	1100

[a] Consists of a layer of Al_2O_3 pellets (40 μm average diameter), a 5mm thick quartz layer (200 μm average diameter), and layer of quartz-diluted Pt/SiO_2 (200 μm average diameter).

[b] 40 μm average diameter for both Pt/SiO_2 and Al_2O_3 aggregates.

[c] Error reflects the standard deviation of measurements from multiple charges of the same catalyst

Table 3.3: Lumped parameters (α_i and δ_i) for 1,3-cyclohexadiene-H_2 (13CHD-H_2) and 4-methylcyclohexene-H_2 (4ME-H_2) reactions on Al_2O_3-Sasol that best fit the rate data in **Figure 3.5** and **Figure 3.6**, respectively, for a rate model following Langmuir-Hinshelwood-type kinetics (**eq 3.13**; 393 K). Errors indicate 95% confidence intervals for parameter estimates.

Reactants	Reaction	α_i (molec. nm^2 Al_2O_3 s^{-1} Pa^{-1})	δ_i (Pa^{-1})
13CHD-H_2[a]	H_2 consumption	1.2(±0.1)x10^{-6}	0.17±0.02
	H-transfer	2.0(±0.1)x10^{-7}	2.1(±0.3)x10^{-3}
4ME-H_2[b]	H_2 consumption	9.1(±0.6)x10^{-7}	0.18±0.02

[a] measured at 20 kPa H_2.
[b] measured at 90 kPa H_2.

Table 3.4: Regressed values of the $\alpha_{TH_q b \rightarrow MA,Pt}$ to $\left[TH_q\right]_{b,PSS}^{mono}$ ratio ($\alpha_{TH_q b \rightarrow MA,Pt}/\left[TH_q\right]_{b,PSS}^{mono}$) and $\alpha_{TH_q b \rightarrow MA,Al}$ parameters for methylcyclohexane (MA) formation from toluene-H_2 reactants on Pt/SiO_2+Al_2O_3 mixtures via the inhibitor-scavenging route (**Scheme 3.2**),[a] and the $K_{H,S}$ value for MA formation from toluene-H_2 reactants on Pt/SiO_2 (0.7 nm mean nanocluster diameter).[b] Errors indicate 95% confidence intervals for parameter estimates.

Parameter	Values
$\alpha_{TH_q b \rightarrow MA,Pt}/\left[TH_q\right]_{b,PSS}^{mono}$ (moles MA g-atom Pt_s^{-1} s^{-1} Pa^{-1})	6.1(±2.0)x10^{-3}
$\alpha_{TH_q b \rightarrow MA,Al}$ (molec. MA nm^{-2} s^{-1} Pa^{-1})	5.1(±1.9)x10^{-5}
$K_{H,S}$ ($bar^{-1/2}$)	0.37±0.04
$k_{CH,3;b}$	4(±1)x10^6

[a] determined by regressing observed MA formation enhancement factors to the reaction transport model described in **Section 3.3.5** for loose Pt/SiO_2+Al_2O_3 mixtures.

[b] determined from regressing the rate data in **Figure 3.9a** to the functional form of **equation 3.38** (with *r*-*p*=2).

Table 3.5: Changes in enthalpy (ΔH), entropy (ΔS), and Gibbs free energy (ΔG) to form gaseous methylcyclohexadiene and methylcyclohexene isomers from stoichiometric amounts of gaseous toluene and H_2 (determined from quantum mechanics calculations evaluated at 393 K and 1 bar (**Section 3.2.3**)), equilibrium pressures (393 K, 1.4 kPa toluene, and 90 kPa H_2), and external mass transfer to additive hydrogenation rate ratio (ζ, **eq 3.38**) evaluated for a loose Pt/SiO_2-Al_2O_3 mixture with a 2700 nm^2 Pt_s^{-1} dilution extent and a 70 μm aggregate diameter. The values for 1-methylcyclohexene and 4-methylcyclohexene enclosed in the square brackets reflect those derived from reported experimental ΔH values.

Molecular species		ΔH (kJ mol^{-1})	ΔS (J mol^{-1} K^{-1})	ΔG (kJ mol^{-1})	Equilibrium pressure (Pa)	ζ
Cyclohexa-1,3-diene	1-methyl	-0.0814	-155	60.7	1.1×10^{-5}	1.6×10^{-5}
	2-methyl	-3.15	-144	53.3	1.1×10^{-4}	1.6×10^{-4}
	5-methyl	4.88	-146	62.2	6.7×10^{-6}	1.0×10^{-5}
Cyclohexa-1,4-diene	1-methyl	-3.61	-140	51.6	1.8×10^{-4}	2.6×10^{-4}
	6-methyl	5.50	-143	61.6	8.2×10^{-6}	1.2×10^{-5}
Cyclohexene	1-methyl	-124 [-102[a]]	-279	-13.6 [8[a]]	7.4×10^{4} [98[a]]	1.1×10^{5} [140[a]]
	3-methyl	-118 [-94[a]]	-281	-8.70 [17[a]]	1.6×10^{4} [6.2[a]]	2.5×10^{4} [9.4[a]]
	4-methyl	-122 [-95.7[a]]	-281	-11.3 [15[a]]	3.6×10^{4} [12[a]]	5.5×10^{4} [17[a]]

[a] reported experimental ΔH values for 1-methylcyclohexene [72], 3-methylcyclohexene [73], and 4-methylcyclohexene [74] (STP) and corresponding ΔG, equilibrium pressure, and ζ values calculated using DFT-derived ΔS values.

Table 3.6: 1-methylcyclohexene (1ME) or 4-methylcyclohexene (4ME) pressures at the reactor inlet and outlet, fractional ME conversion (ME conv.), observed MA formation turnover rates (MA TOR; moles MA g-atom surface Pt $(Pt_s)^{-1}$ s^{-1}), ME conversion turnover rate (ME TOR; moles MA g-atom Pt_s^{-1} s^{-1}), and the sum of the ME and toluene conversion turnover rates (ME+toluene TOR; moles MA g-atom Pt_s^{-1} s^{-1}) from toluene-H_2 and toluene-H_2-ME reactions on Pt/SiO_2 (0.7 nm mean nanocluster diameter; 393 K, 80 kPa H_2, 1.4 kPa toluene).

Hydrocarbon reactants	1ME pressure (Pa) inlet [outlet]	4ME pressure (Pa) inlet [outlet]	ME conv.	MA TOR (moles MA g-atom Pt_s^{-1} s^{-1})	ME TOR (moles MA g-atom Pt_s^{-1} s^{-1})	ME+toluene TOR (moles MA g-atom Pt_s^{-1} s^{-1})[a]
Toluene	0 [0.13]	0 [0.03]	-	0.12	-	0.12
Toluene+1ME	4.5 [2.9]	0 [0.17]	0.36	0.17	0.050	0.17
Toluene+4ME	-	3.3 [0.96]	0.71	0.22	0.094	0.22

[a] Calculated from the sum of the MA formation turnover rate during toluene-H_2 reactions (with no ME co-reactant, at the same conditions) and the ME conversion turnover rate for the toluene-H_2-ME mixture.

Table 3.7: DFT-derived electronic energies at 0 K (ΔE), enthalpies (ΔH), entropies (ΔS), and Gibbs free energies (ΔG) to form surface-bound toluene and 1-methyl-1,4-cyclohexadiene from the gaseous precursor and bare Pt at 0.11 ML coverage on Pt (111).

Hydrocarbon moiety	Binding site	ΔE (kJ mol^{-1})	ΔH[a] (kJ mol^{-1})	ΔS[a] (J mol^{-1} K^{-1})	ΔG[b] (kJ mol^{-1})
Toluene	four-fold bridge	-146	-134	-194	-57.6
	hcp hollow	-98.7	-86.4	-194	-10.0
1-Methyl-1,4-cyclohexadiene	two-fold bridge	-234	-219	-190.	-144

[a] ΔH and ΔS values were evaluated at 393 K and 1 bar, and computed using methods reported in **Chapter 2**, **Section 2.8.2.**

[b] ΔG values from ΔH and ΔS (**eq 3.10**) (393 K, 1 bar).

Scheme 3.1: Proposed sequence of steps (**Section 3.3.4**) describing toluene hydrogenation to form methylcyclohexane via a monofunctional, Pt-catalyzed route (steps 1-3 and 4a-7a) and a bifunctional, Pt and Al_2O_3 coupled route (steps 1-3 and 4b-5b). All steps occur at the Pt surface except for step 5b which occurs at the Al_2O_3 surface.[a,b,c]

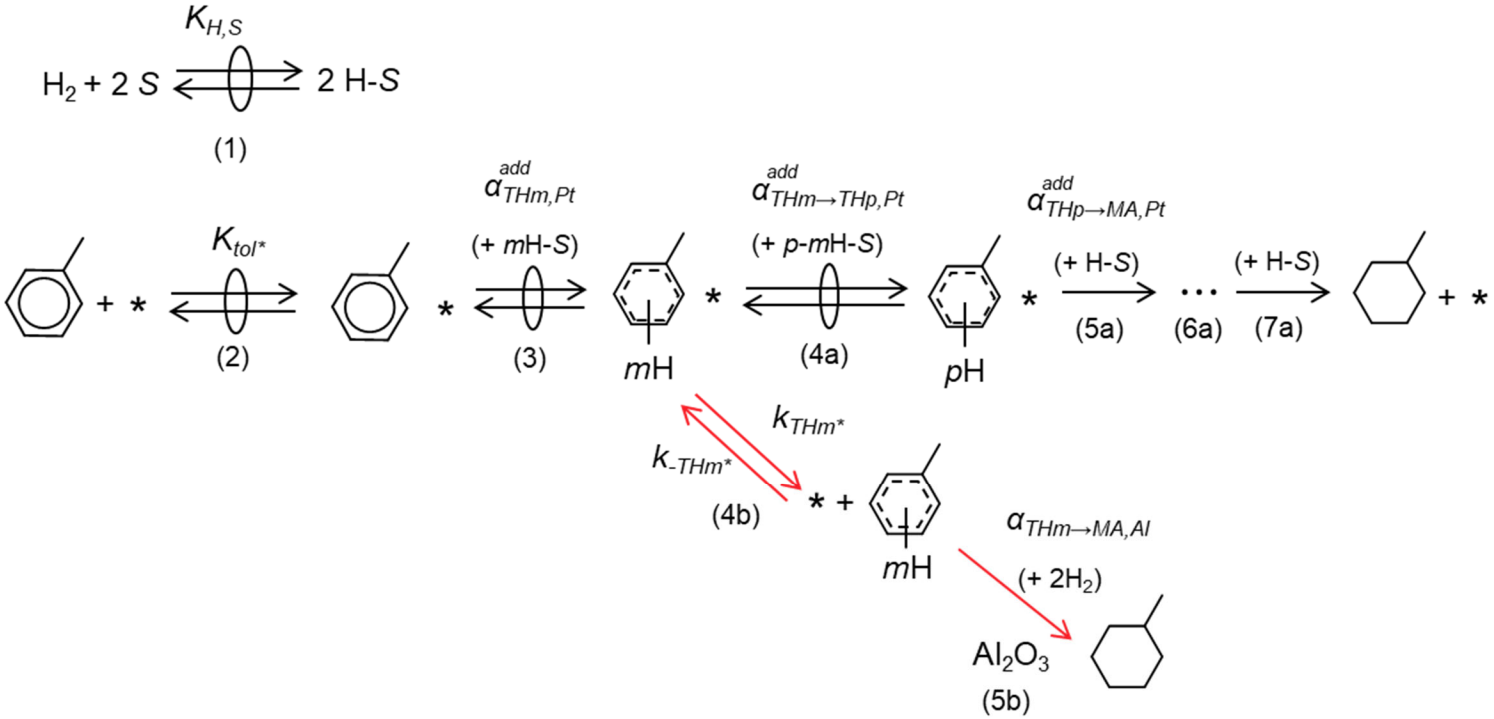

[a] The * term denotes an ensemble of adjacent *-sites that bind the respective hydrocarbon intermediate. The number of adjacent sites (γ_i) is omitted for clarity.
[b] The *S* term denotes an *S*-site that binds H-adatoms.
[c] K_x denotes equilibrium adsorption constants and k_x and k_{-x} denote the forward and reverse kinetic constants for the elementary steps with single forward arrow denote irreversible step, steps with forward and backward arrow denote reversible step, and steps with circled forwards and backward arrows denotes a quasi-equilibrated step. α_x denotes groupings of parameters.

Scheme 3.2: Proposed sequence of steps (**Section 3.3.4**) describing toluene hydrogenation to form methylcyclohexane on Pt surfaces via a predominant route (steps 1-2 and 3a-6a) and secondary route (steps 1-2 and 3b-8b) that forms TH_q-b* as a most abundant surface intermediate (MASI). All steps occur at the Pt surface except for step 10b which occurs at the Al_2O_3 surface.[a,b,c]

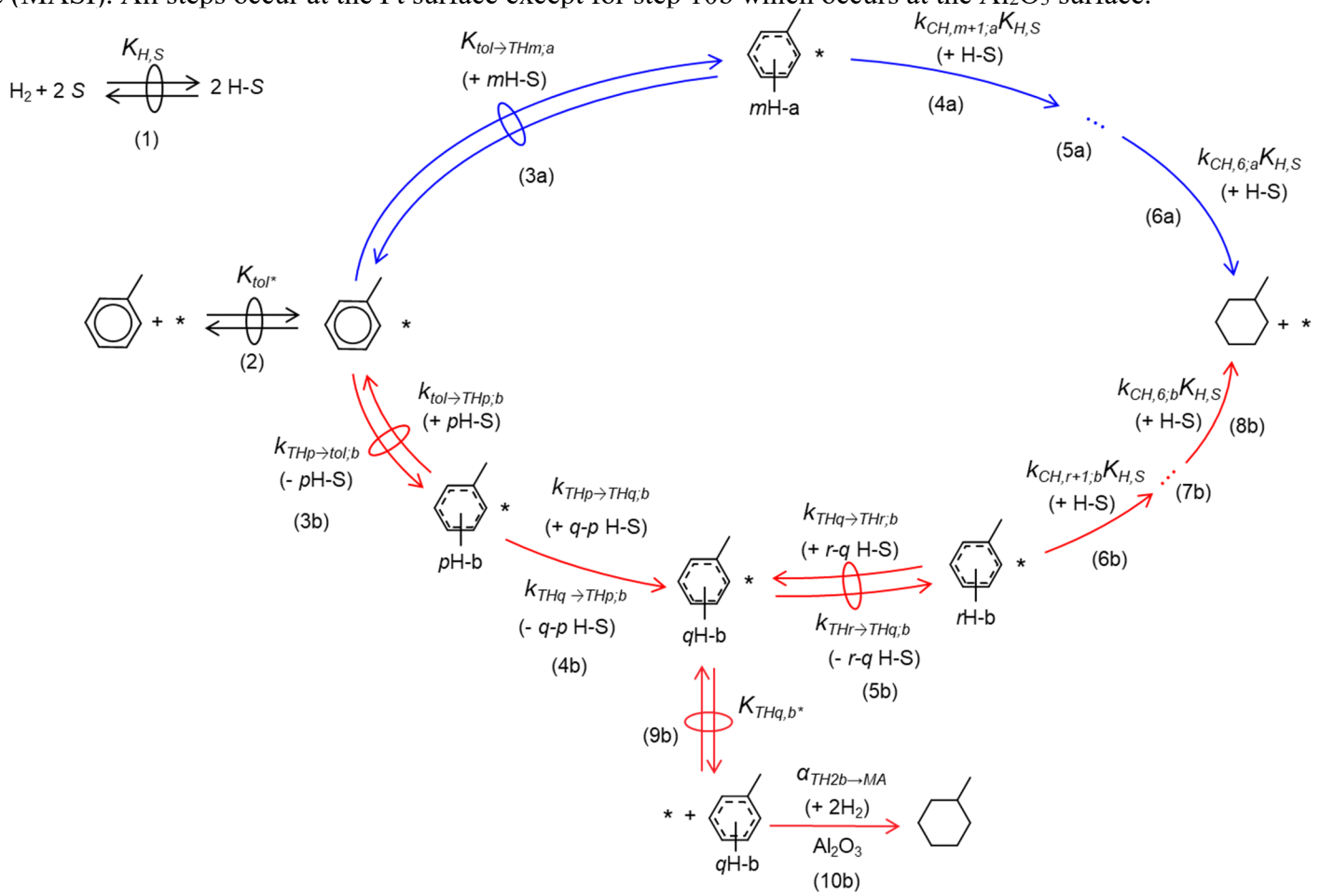

[a] The * term denotes an ensemble of adjacent *-sites that bind the respective hydrocarbon intermediate. The number of adjacent sites (γ_i) is omitted for clarity.
[b] The *S* term denotes an *S*-site that binds H-adatoms.
[c] K_x denotes equilibrium adsorption constants and k_x and k_{-x} denote the forward and reverse kinetic constants for the elementary steps with single forward arrow denote irreversible step, steps with forward and backward arrow denote reversible step, and steps with circled forwards and backward arrows denotes a quasi-equilibrated step. α_x denotes groupings of parameters.

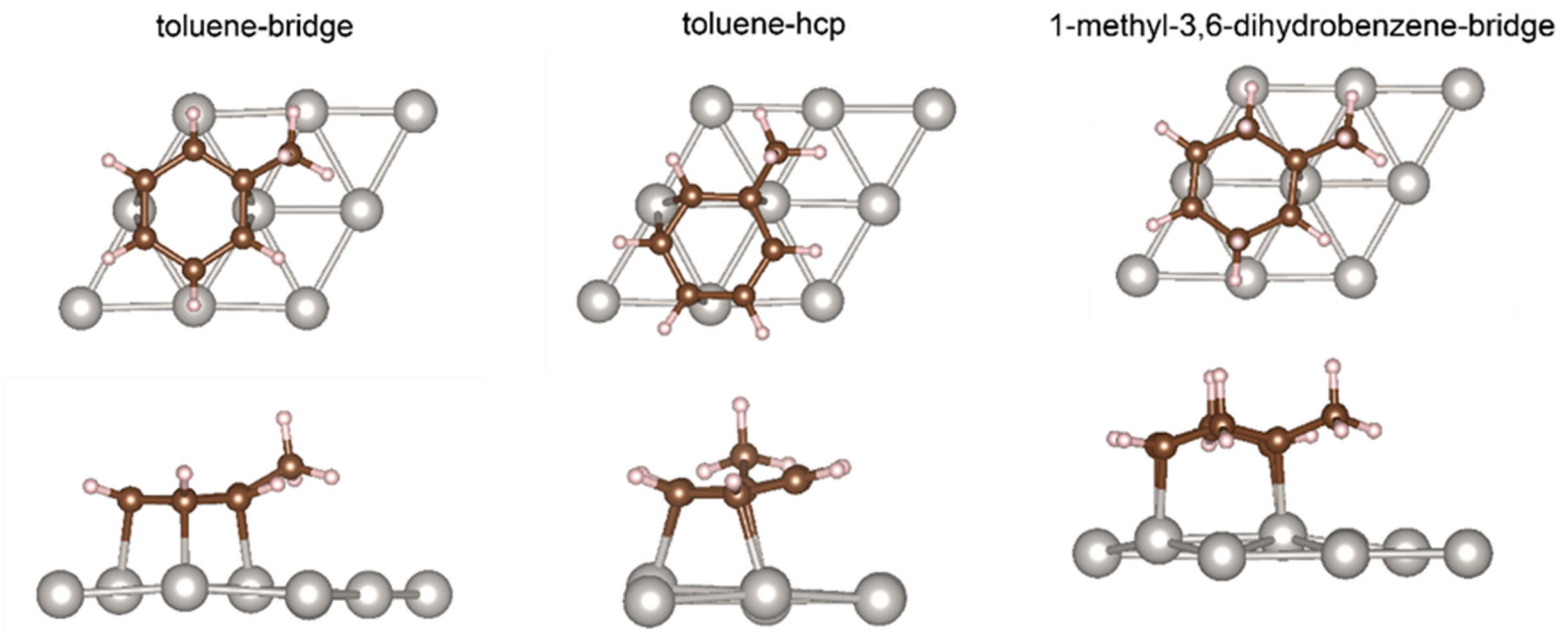

Scheme 3.3: Top and side view of DFT-derived optimized molecular structures of toluene bound at the four-fold bridge site (left; toluene-bridge), toluene bound at the hcp three-fold hcp hollow site (center; toluene-hcp), and 1-methyl-1,4-cyclohexadiene at the two-fold bridge site (right; 1-methyl-3,6-dihydrobenzene-bridge) on the Pt(111) surface of a 4-layer period Pt slab (with only the top layer shown for clarity) computed using methods reported in **Chapter 2**, **Section 2.2.3** (reproduced from **Chapter 2, Scheme 2.2**).

3.7. References

[1] R.S. Haizmann, L.H. Rice, M.S. Turowicz, US patent 5453552 to UOP, 5453552, 1995.

[2] G. Busca, Structural, surface, and catalytic properties of aluminas, in: Adv. Catal., 1st ed., Elsevier Inc., 2014: pp. 319–404. https://doi.org/10.1016/B978-0-12-800127-1.00003-5.

[3] J. Hancsók, G. Marsi, T. Kasza, D. Kalló, Hydrogenation of the aromatics and olefins in FCC gasoline during deep desulphurisation, Top. Catal. 54 (2011) 1102. https://doi.org/10.1007/s11244-011-9731-9.

[4] F. Diehl, A.Y. Khodakov, Promotion of cobalt Fischer-Tropsch catalysts with noble metals : a review, 64 (2009) 11–24. https://doi.org/10.2516/ogst.

[5] M. V Twigg, Catalytic control of emissions from cars, Catal. Today. 163 (2011) 33–41. https://doi.org/https://doi.org/10.1016/j.cattod.2010.12.044.

[6] S.D. Lin, M.A. Vannice, Hydrogenation of aromatic hydrocarbons over supported Pt catalysts: I. Benzene hydrogenation, J. Catal. 143 (1993) 539–553. https://doi.org/10.1006/jcat.1993.1297.

[7] S.D. Lin, M.A. Vannice, Hydrogenation of aromatic hydrocarbons over supported Pt catalysts: III. Reaction models for metal surfaces and acidic sites on oxide supports, J. Catal. 143 (1993) 563–572. https://doi.org/10.1006/jcat.1993.1299.

[8] J.H. Sinfelt, P.J. Lucchesi, Kinetic evidence for the migration of reactive intermediates in surface catalysis, J. Am. Chem. Soc. 85 (1963) 3365–3367. https://doi.org/10.1021/ja00904a012.

[9] S. Cęckiewicz, B. Delmon, Cooperative action of Pt/γ-Al2O3 catalyst and γ-Al2O3 diluent in the hydrogenation of benzene, J. Catal. 108 (1987) 294–303. https://doi.org/10.1016/0021-9517(87)90179-5.

[10] M. Choi, S. Yook, H. Kim, Hydrogen spillover in encapsulated metal catalysts: New opportunities for designing advanced hydroprocessing catalysts, ChemCatChem. 7 (2015) 1048–1057. https://doi.org/10.1002/cctc.201500032.

[11] H. Shin, M. Choi, H. Kim, A mechanistic model for hydrogen activation, spillover, and its chemical reaction in a zeolite-encapsulated Pt catalyst, Phys. Chem. Chem. Phys. 18 (2016) 7035–7041. https://doi.org/10.1039/c5cp05536a.

[12] P. Antonucci, N. van Truong, N. Giordano, R. Maggiore, Hydrogen spillover effects in the hydrogenation of benzene over Pt γ-Al_2O_3 catalysts, J. Catal. 75 (1982) 140–150. https://doi.org/10.1016/0021-9517(82)90129-4.

[13] S.S.M. Konda, S. Caratzoulas, D.G. Vlachos, Computational insights into the role of metal and acid sites in bifunctional metal/zeolite catalysts: A case study of acetone hydrogenation to 2-propanol and subsequent dehydration to propene, ACS Catal. 6 (2016) 123–133. https://doi.org/10.1021/acscatal.5b01686.

[14] R. Prins, Hydrogen spillover. Facts and fiction, Chem. Rev. 112 (2012) 2714–2738. https://doi.org/10.1021/cr200346z.

[15] J.E. Benson, H.W. Kohn, M. Boudart, On the reduction of tungsten trioxide accelerated by platinum and water, 5 (1966) 307–313.

[16] R.B. Levy, M. Boudart, The kinetics and mechanism of spillover, J. Catal. 32 (1974) 304–314.

[17] Spreafico, C.; Karim, W.; Ekinci, Y.; Van Bokhoven, J. A.; Van De Vondele, J. Hydrogen Adsorption on Nanosized Platinum and Dynamics of Apillover onto Alumina and Titania. *J. Phys. Chem. C* **2017**, *121* (33), 17862–17872. https://doi.org/10.1021/acs.jpcc.7b03733.

[18] R. Prins, V.K. Palfi, M. Reiher, Hydrogen spillover to nonreducible supports, J. Phys. Chem.

C. 116 (2012) 14274–14283. https://doi.org/10.1021/jp212274y.
[19] J.C. Schlatter, M. Boudart, Hydrogenation of ethylene on supported platinum, J. Catal. 24 (1972) 482–492. https://doi.org/10.1039/tf9625801761.
[20] M. Boudart, A.W. Aldag, M.A. Vannice, On the slow uptake of hydrogen by platinized carbon, J. Catal. 18 (1970) 46–51. https://doi.org/10.1016/0021-9517(70)90310-6.
[21] A.J. Robell, E. V Ballou, M. Boudart, Surface diffusion of hydrogen carbon, J. Phys. Chem. 68 (1964) 2748–2753.
[22] A.D. Allian, K. Takanabe, K.L. Fujdala, X. Hao, T.J. Truex, J. Cai, C. Buda, M. Neurock, E. Iglesia, Chemisorption of CO and mechanism of CO oxidation on supported platinum nanoclusters, J. Am. Chem. Soc. 133 (2011) 4498–4517. https://doi.org/10.1021/ja110073u.
[23] R. Wischert, P. Laurent, C. Coperet, F. Delbecq, P. Sautet, γ-Alumina: The essential and unexpected role of water for the structure, stability, and reactivity of "defect" sites, J. Am. Chem. Soc. 134 (2012) 14430–14449. https://doi.org/10.1021/ja3042383.
[24] Y. Amenomiya, Adsorption of hydrogen and H2-D2 exchange reaction on alumina, J. Catal. 22 (1971) 109–122. https://doi.org/10.1016/0021-9517(71)90271-5.
[25] S. Wang, K. Goulas, E. Iglesia, Condensation and esterification reactions of alkanals, alkanones, and alkanols on TiO2: Elementary steps, site requirements, and synergistic effects of bifunctional strategies, J. Catal. 340 (2016) 302–320. https://doi.org/10.1016/j.jcat.2016.05.026.
[26] P.B. Weisz, Polyfunctional Heterogeneous Catalysis, in: Adv. Catal., 1962: pp. 137–190. https://doi.org/10.1016/S0360-0564(08)60287-4.
[27] I.H. Cho, S. Bin Park, S.J. Cho, R. Ryoo, Investigation of Pt/γ-Al2O3 catalysts prepared by sol-gel method, J. Catal. 173 (1998) 295–303.
[28] S. Soled, W. Wachter, H. Wo, Use of zeta potential measurements in catalyst preparation, Stud. Surf. Sci. Catal. 175 (2010) 101–107. https://doi.org/10.1016/S0167-2991(10)75013-8.
[29] J.P. Brunelle, Preparation of catalysts by metallic complex adsorption on mineral oxides, Pure Appl. Chem. 50 (1978) 1211–1229. https://doi.org/10.1351/pac197850091211.
[30] F.W. Sears, G.L. Salinger, Thermodynamics, kinetic theory, and statistical thermodynamics, 3rd ed, Addison-Wesley Pub. Co., Reading, Mass, 1975.
[31] N. Wakao, J.M. Smith, Diffusion in catalyst pellets, Chem. Eng. Sci. 17 (1962) 825–834. https://doi.org/10.1016/0009-2509(62)87015-8.
[32] M. Knudsen, Die Gesetze der Molekularströmung und der inneren Reibungsströmung der Gase durch Röhren, Ann. Phys. 333 (1909) 75–130. https://doi.org/https://doi.org/10.1002/andp.19093330106.
[33] G.F. Froment, K.B. Bischoff, J. De Wilde, Chemical reactor analysis and design, 3rd ed, Wiley, Hoboken, NJ, 2010.
[34] D. Thoenes, H. Kramers, Mass transfer from spheres in various regular packings to a flowing fluid, Chem. Eng. Sci. 8 (1958) 271–283. https://doi.org/10.1016/0009-2509(58)85034-4.
[35] H.S. Fogler, Elements of chemical reaction engineering, 5th ed, Pearson, 2016.
[36] G.D. Purvis, R.J. Bartlett, A full coupled-cluster singles and doubles model: The inclusion of disconnected triples inclusion of disconnected triples, J. Chem. Phys. 76 (1982) 1910.
[37] G.E. Scuseria, C.L. Janssen, H.F. Schaefer, An efficient reformulation of the closed-shell coupled cluster single and double excitation (CCSD) equations, J. Chem. Phys. 89 (1988) 7382.

[38] G.E. Scuseria, H.F.I. Schaefer, Is coupled cluster singles and doubles (CCSD) more computationally intensive than quadratic configuration interaction (QCISD)?, J. Chem. Phys. 90 (1989) 3700.
[39] T.H.J. Dunning, Gaussian basis sets for use in correlated molecular calculations. I. The atoms boron through neon and hydrogen, J. Chem. Phys. 90 (1989) 1007.
[40] R.A. Kendall, T.H. Dunning, R.J. Harrison, Electron affinities of the first-row atoms revisited. Systematic basis sets and wave functions and wave functions, J. Chem. Phys. 96 (1992) 6796.
[41] D.E. Woon, T.H. Dunning, Gaussian basis sets for use in correlated molecular calculations. III . The atoms aluminum through argon, J. Chem. Phys. 98 (1993) 1358.
[42] K.A. Peterson, D.E. Woon, T.H. Dunning, Benchmark calculations with correlated molecular wave functions. IV . The classical barrier height of the H+H2→H2+H reaction, J. Chem. Phys. 100 (1994) 7410.
[43] A.K. Wilson, T. van Mourik, T.H.J. Dunning, Gaussian basis sets for use in correlated molecular calculations. VI. Sextuple zeta correlation consistent basis sets for boron through neon, J. Mol. Struct. 388 (1996) 339–349.
[44] M.J. Frisch, E. Al., Gaussian 09, Revision D.01, (2009).
[45] J.A.J. Montgomery, M.J. Frisch, J.W. Ochtersk, G.A. Petersson, A complete basis set model chemistry. VII. Use of the minimum population localization method, J. Chem. Phys. 112 (2000) 6532.
[46] D. McQuarrie, J. Simon, Molecular Thermodynamics, 5th ed, University Science Books, 1999.
[47] M. Tang, W.A. Larish, Y. Fang, A. Gankanda, V.H. Grassian, Heterogeneous Reactions of Acetic Acid with Oxide Surfaces : E ff ects of Mineralogy and Relative Humidity, (2016) 0–7. https://doi.org/10.1021/acs.jpca.6b05395.
[48] M.A. Hasan, M.I. Zaki, L. Pasupulety, Oxide-catalyzed conversion of acetic acid into acetone : an FTIR spectroscopic investigation, 243 (2003) 81–92.
[49] A.R. Barron, The interaction of carboxylic acids with aluminium oxides: journeying from a basic understanding of industrial and humanitarian applications, (2014) 8127–8143. https://doi.org/10.1039/c4dt00504j.
[50] S.R. Tong, L.Y. Wu, M.F. Ge, W.G. Wang, Z.F. Pu, and Physics Heterogeneous chemistry of monocarboxylic acids on α -Al 2 O 3 at different relative humidities, (2010) 7561–7574. https://doi.org/10.5194/acp-10-7561-2010.
[51] S. Wang, E. Iglesia, Experimental and theoretical assessment of the mechanism and site requirements for ketonization of carboxylic acids on oxides, J. Catal. 345 (2017) 183–206. https://doi.org/10.1016/j.jcat.2016.11.006.
[52] S. Wang, E. Iglesia, Experimental and Theoretical Evidence for the Reactivity of Bound Intermediates in Ketonization of Carboxylic Acids and Consequences of Acid-Base Properties of Oxide Catalysts, J. Phys. Chem. C. 121 (2017) 18030–18046. https://doi.org/10.1021/acs.jpcc.7b05987.
[53] F. Zaera, The Surface Chemistry of Metal-Based Hydrogenation Catalysis, ACS Catal. 7 (2017) 4947–4967. https://doi.org/10.1021/acscatal.7b01368.
[54] G.C. Bond, P.B. Wells, The mechanism of the hydrogenation of unsaturated hydrocarbons on transition metal catalysts, in: Adv. Catal., 1965: pp. 91–226. https://doi.org/10.1016/S0360-0564(08)60554-4.
[55] A. Stanislaus, H.C. Barry, Aromatic hydrogenation catalysis: A review, Catal. Rev. Eng. 36

(1994) 75–123. https://doi.org/10.1080/01614949408013921.
[56] M. Boudart, G. Djega-Mariadassou, Kinetics of Heterogeneous Catalytic Reactions., Princeton University Press, 1984.
[57] J.E. Rekoske, R.D. Cortright, S.A. Goddard, S.B. Sharma, J.A. Dumesic, Microkinetic analysis of diverse experimental data for ethylene hydrogenation on platinum, J. Phys. Chem. 96 (1992) 1880–1888. https://doi.org/10.1021/j100183a067.
[58] R.D. Cortright, S.A. Goddard, J.E. Rekoske, J.A. Dumesic, Kinetic study of ethylene hydrogenation, J. Catal. 127 (1991) 342–353. https://doi.org/10.1016/0021-9517(91)90230-2.
[59] L.P. Lindfors, T. Salmi, S. Smeds, Kinetics of toluene hydrogenation on a supported Ni catalyst, Chem. Eng. Sci. 48 (1993) 3813–3828. https://doi.org/10.1016/0009-2509(93)80224-E.
[60] M. Yang, K.C. Chou, G.A. Somorjai, The structures and reactions of linear and cyclic C6 hydrocarbons adsorbed on the Pt(111) crystal surface studied by sum frequency generation vibrational spectroscopy: Pressure, temperature, and H2 coadsorption effects, J. Phys. Chem. B. 108 (2004) 14766–14779. https://doi.org/10.1021/jp048238n.
[61] C. Morin, D. Simon, P. Sautet, Intermediates in the hydrogenation of benzene to cyclohexene on Pt(111) and Pd(111): A comparison from DFT calculations, Surf. Sci. 600 (2006) 1339–1350. https://doi.org/10.1016/j.susc.2006.01.033.
[62] M.K. Sabbe, G. Canduela-Rodriguez, M.F. Reyniers, G.B. Marin, DFT-based modeling of benzene hydrogenation on Pt at industrially relevant coverage, J. Catal. 330 (2015) 406–422. https://doi.org/10.1016/j.jcat.2015.08.003.
[63] T. Bera, J.W. Thybaut, G.B. Marin, Single-Event microkinetics of aromatics hydrogenation on Pt/H-ZSM22, Ind. Eng. Chem. Res. 50 (2011) 12933–12945. https://doi.org/10.1021/ie200541q.
[64] M. Saeys, M. Neurock, G.B. Marin, T. Hall, V. Charlottes, Density functional theory analysis of benzene (de)hydrogenation on Pt(111): Addition and removal of the first two H-atoms, J. Phys. Chem. B. 107 (2003) 3844–3855.
[65] M. Saeys, M. Reyniers, J.W. Thybaut, First-principles based kinetic model for the hydrogenation of toluene, 236 (2005) 129–138. https://doi.org/10.1016/j.jcat.2005.09.019.
[66] H. Eyring, The activated complex in chemical reactions, J. Chem. Phys. 3 (1935) 63–71. https://doi.org/10.1063/1.1749604.
[67] W.F.K. Wynne-Jones, H. Eyeing, The absolute rate of reactions in condensed phases, J. Chem. Phys. 3 (1935) 492–502. https://doi.org/10.1063/1.1749713.
[68] W. Zhao, C. Chizallet, P. Sautet, P. Raybaud, Dehydrogenation mechanisms of methyl-cyclohexane on Γ-Al2O3 supported Pt13: Impact of cluster ductility, J. Catal. 370 (2019) 118–129. https://doi.org/10.1016/j.jcat.2018.12.004.
[69] T. Bligaard, J.K. Nørskov, B.I. Lundqvist, Understanding heterogeneous catalysis from the fundamentals, in: Handb. Surf. Sci., 2008: pp. 269–340. https://doi.org/10.1016/S1573-4331(08)00008-5.
[70] G. Ertl, K. Helmut, F. Schüth, J. Weitkamp, Handbook of Heterogeneous Catalysis, 2nd ed, Wiley-VCH, 2008.
[71] W.P. Davey, Precision Measurements of the Lattice Constants of Twelve Common Metals, Phys. Rev. 25 (1925) 753–761. https://doi.org/10.1103/PhysRev.25.753.
[72] M. Peereboom, B. van de Graaf, J.M.A. Baas, Experimental and calculated thermodynamic data for the isomeric methylcyclohexenes and methylenecyclohexane, Recl. Des Trav.

Chim. Des Pays-Bas. 101 (1982) 336–338. https://doi.org/10.1002/recl.19821011003.
[73] I.A. Yursha, G.Y. Kabo, D.N. Andreevskii, Equilibriums and thermodynamics of the isomerization of methylcyclohexenes, Neftekhimiya. 14 (1974) 688–693.
[74] A. Labbauf, F.D. Rossini, Heats of Combustion, Formation, and Hydrogenation of 14 Selected Cyclomonoolefin Hydrocarbons, J. Phys. Chem. 65 (1961) 476–480.
[75] S. Brunauer, P.H. Emmett, E. Teller, Adsorption of Gases in Multimolecular Layers, J. Am.Chem.Soc. 60 (1938) 309–319.
[76] E.P. Barrett, L.G. Joyner, P.P. Halenda, The Determination of Pore Volume and Area Distribution in Porous Substances. I. Computations from Nitrogen Isotherms, J. Am. Chem. Soc. 73 (1951) 373–380.

3.8. Supporting information

3.8.1. Hydrogen chemisorption isotherms and estimation of Pt particle dispersions

Pt-particle dispersions ($D = N_H/N_B$, where N_H is the number of H bound by the metal surface and N_B is the number of metal atoms in the bulk) were calculated from H_2 adsorption isotherms measured using a volumetric adsorption apparatus with a Baratron gauge and a turbomolecular pump (Pfeiffer Vacuum, <1 Pa dynamic vacuum), using $H/Pt_s=1$ adsorption stoichiometry. Hydrogen adsorption isotherms (shown in **Figure 3.S1**) were measured at H_2 pressures ranging from 5-105 kPa at 373 K on evacuated catalysts ($<10^{-2}$ mbar, 573 K, 1 h) following treatment in H_2 (573 K, 1 h). The reported dispersion values reflect the H atom uptake per Pt-atom determined by extrapolating the linear trend observed in the high H_2 pressure regime (50-100 kPa H_2) to zero kPa H_2.

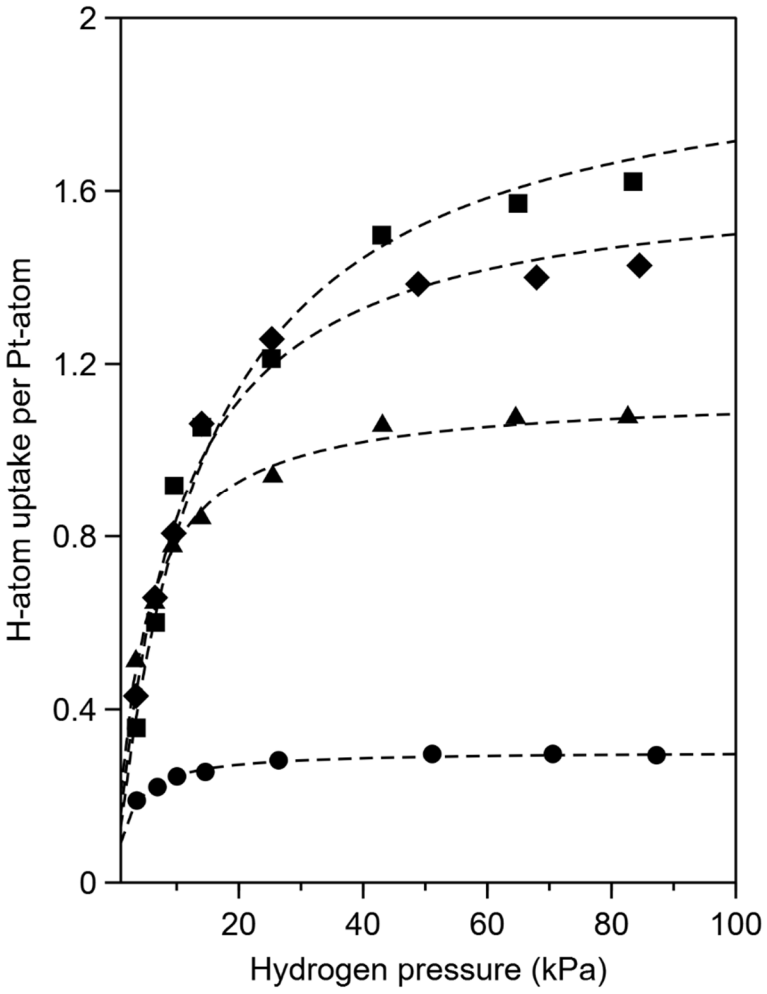

Figure 3.S1: Adsorption isotherms for H_2 on SiO_2-supported Pt nanoparticles (Pt/SiO_2) depicting the number of adsorbed H atoms per bulk Pt-site as a function of hydrogen pressure (kPa) with Pt contents of 2.1% (●) 0.47% (■), 0.17% (▲), and 0.10% (◆) wt. The hydrogen pressures (kPa) reflect the stable values following catalyst exposure to a set H_2 pressure. Dashed lines indicate a Langmuir adsorption isotherm trend.

3.8.2. N_2 adsorption isotherms, surface areas, and pore volumes for SiO_2 and Al_2O_3.

Figure 3.S2, **Figure 3.S3**, and **Figure 3.S4** show N_2 adsorption and desorption isotherms (77 K) on SiO_2, Al_2O_3 (Sasol), and Al_2O_3 (sol-gel) powders, respectively. **Table 3.S1** shows the surface areas (BET method [75]), mean pore volume (BJH method [76]), and mean pore radius (BJH method [76]).

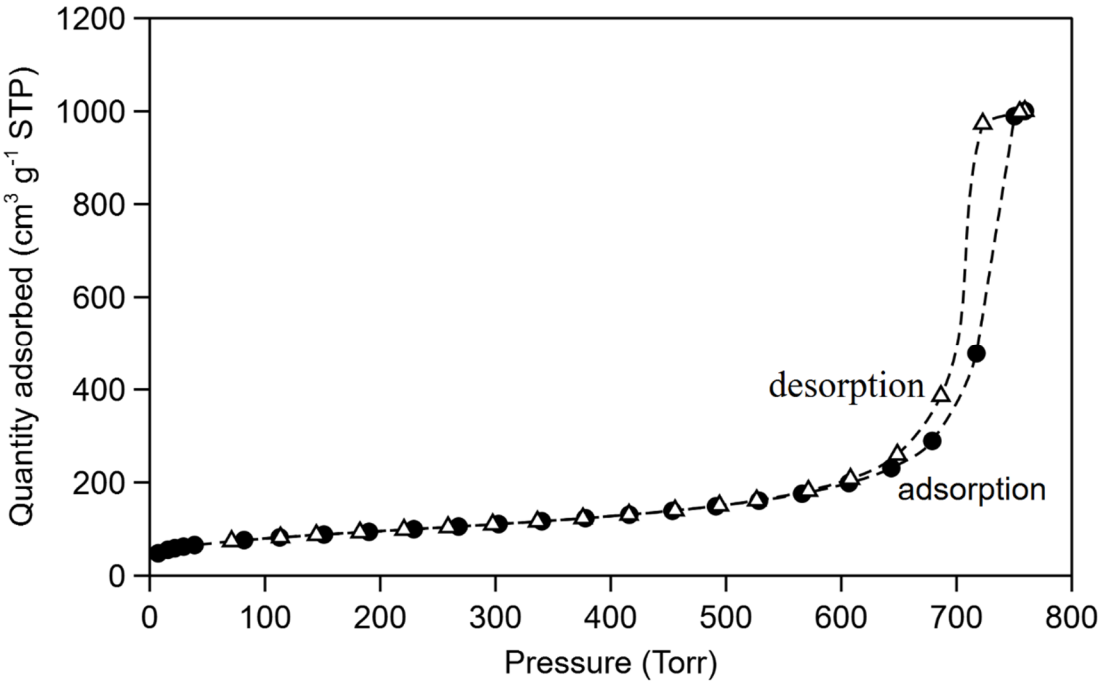

Figure 3.S2: N_2 adsorption (●) and desorption (△) isotherms (77 K) on SiO_2 (Cab-o-sil HS-5) powders.

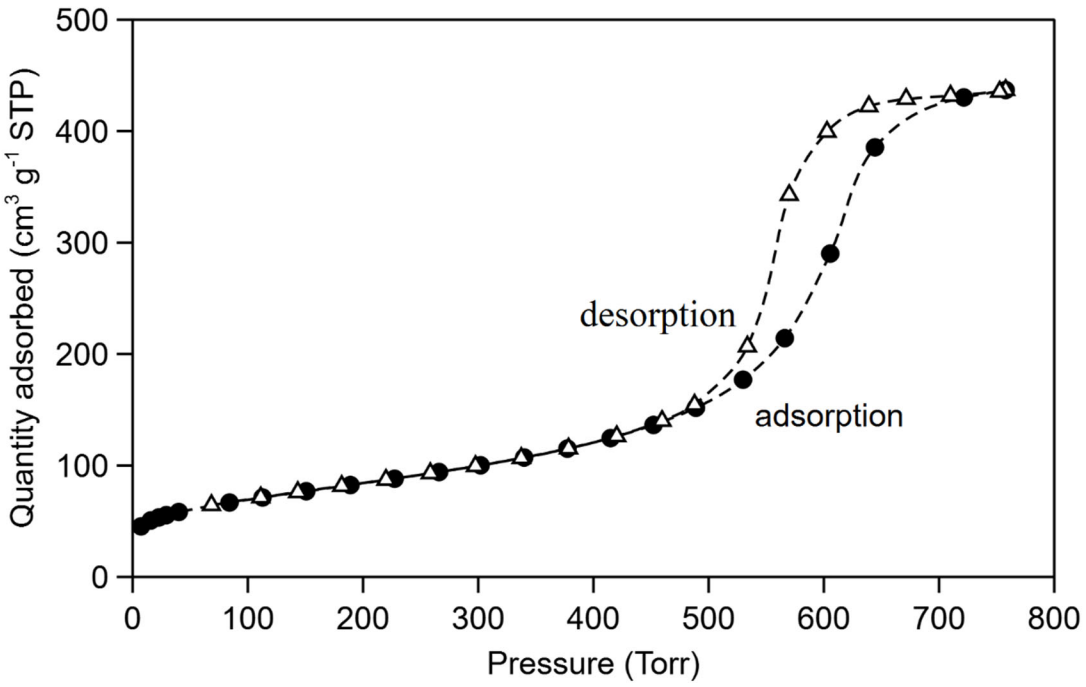

Figure 3.S3: N_2 adsorption (●) and desorption (△) isotherms (77 K) on Al_2O_3 (Sasol) powders.

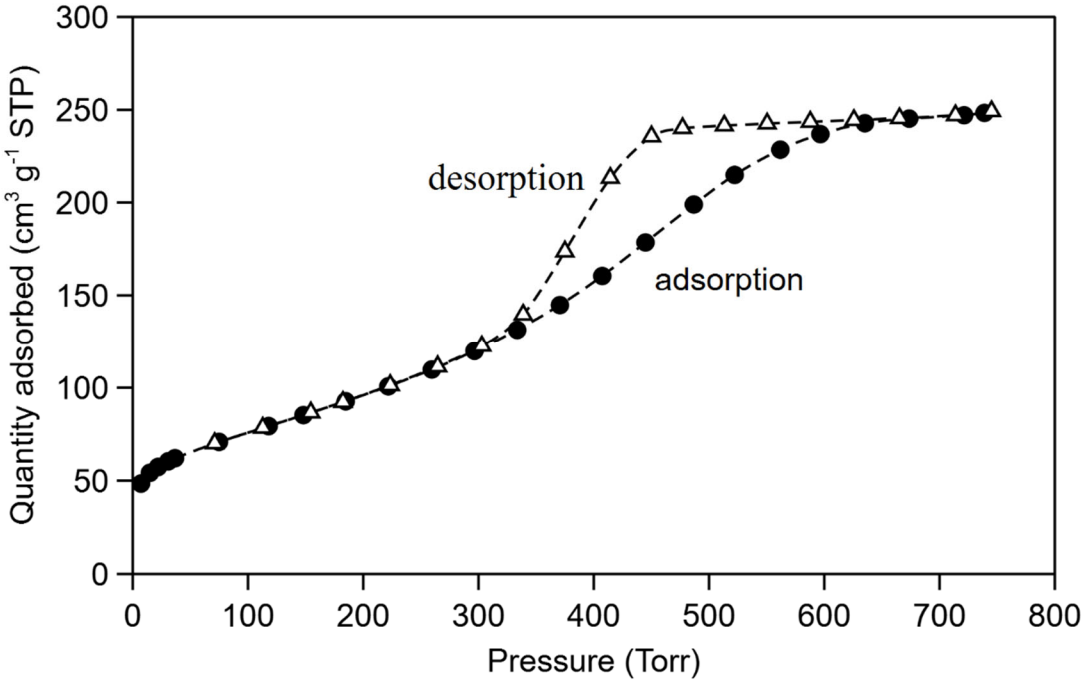

Figure 3.S4: N_2 adsorption (●) and desorption (△) isotherms (77 K) on Al_2O_3 (sol-gel) powders.

Table 3.S1: Pore volume, surface area, and mean pore radius from N_2 adsorption isotherms (77 K) measured on SiO_2 (**Figure 3.S2**), Al_2O_3-Sasol (**Figure 3.S3**), and Al_2O_3-solgel (**Figure 3.S4**) powders.

Metal oxide	Surface area[a] (m^2 g^{-1})	Pore volume[b] (cm^3 g^{-1})	Mean pore radius[c] (nm)
SiO_2	320	1.5	11
Al_2O_3-Sasol	270	0.68	4.5
Al_2O_3-solgel	320	0.40	2.2

[a] Internal surface area using BET method [75].
[b] Cumulative volume of pores between 0.85-150 nm radius from adsorption isotherm using BJH method [76].
[c] Mean pore radius from BJH method (2V/A, where V is the pore volume and A is the surface area) from adsorption isotherm using BJH method [76].

3.8.3. Time on stream data for 1,3-cyclohexadiene and 4-methylcyclohexene reactions with H_2 on Al_2O_3.

Figure 3.S5 shows 1,3-cyclohexadiene conversion areal rates during reaction with H_2 to form cyclohexene (CHE), cyclohexane (CHA), 1,4-cyclohexadiene (14CHD), and benzene as a function of time on stream on Al_2O_3 surfaces. **Figure 3.S6** shows 4-methylcyclohexene conversion areal rates during reaction with H_2 to form methylcyclohexane (MA) and 1-methylcyclohexene (1ME) as a function of time on stream on Al_2O_3 surfaces.

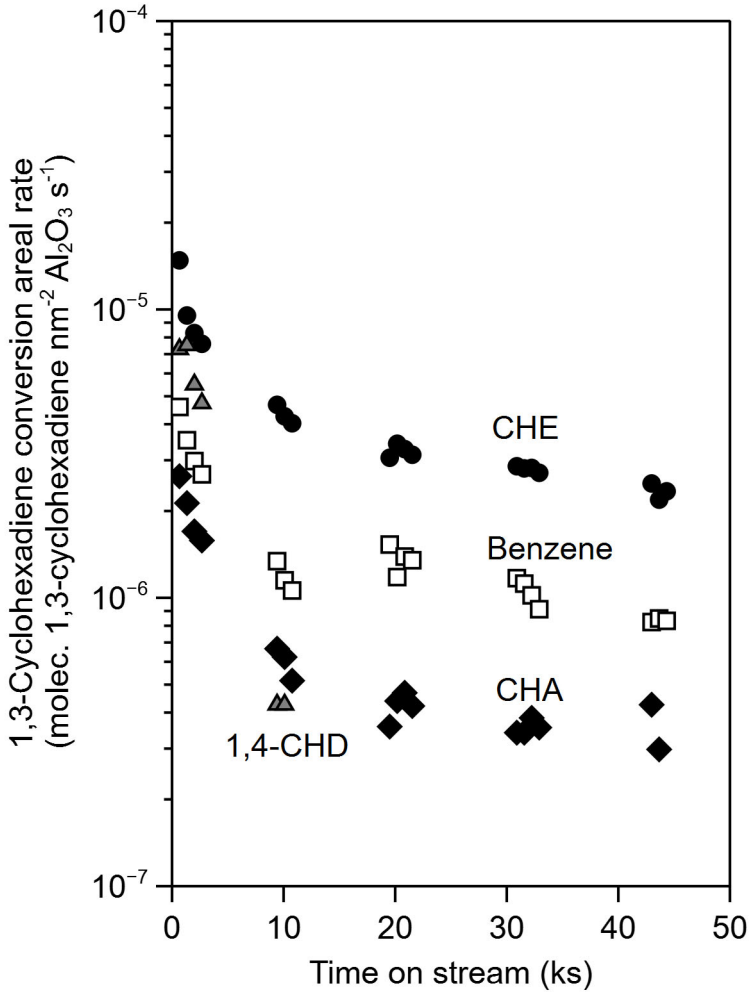

Figure 3.S5: 1,3-Cyclohexadiene conversion areal rates (molec. 1,3-cyclohexadiene nm^{-2} Al2O3 s^{-1}) on Al2O3 (Sasol SBA200) to form benzene (□), 1,4-cyclohexadiene (1,4-CHD, ▲), cyclohexene (CHE, ●), and cyclohexane (CHA, ◆) as a function of time on stream (393 K, 12 Pa 1,3-cyclohexadiene, 100 kPa H_2).

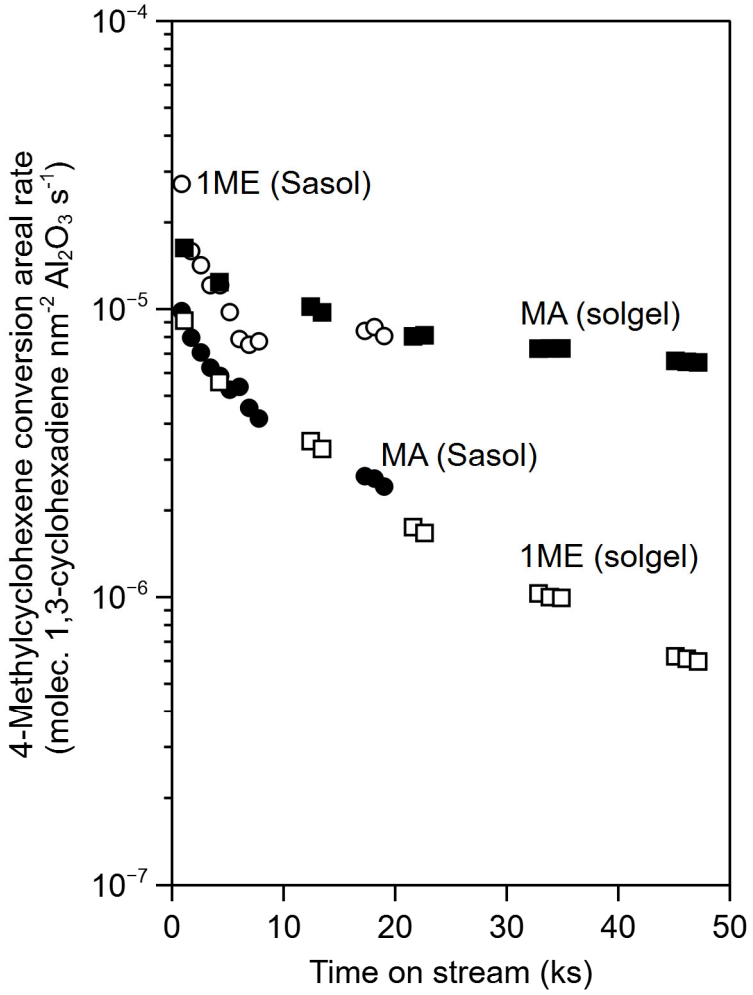

Figure 3.S6: 4-Methylcyclohexene conversion areal rates (molec. 4-methylcyclohexene nm^{-2} Al_2O_3 s^{-1}) on Al_2O_3 to form 1-methylcyclohexene (1ME; □, Al_2O_3-solgel and ○, Al_2O_3-Sasol) and methylcyclohexane (MA; ■, Al_2O_3-solgel and ●, Al_2O_3-Sasol) as a function of time on stream (393 K, 24 Pa (Al2O3-solgel) and 200 Pa (Al_2O_3-Sasol) 4-methylcyclohexene, 90 kPa H_2).

3.8.4. Complete set of toluene-derived intermediates.

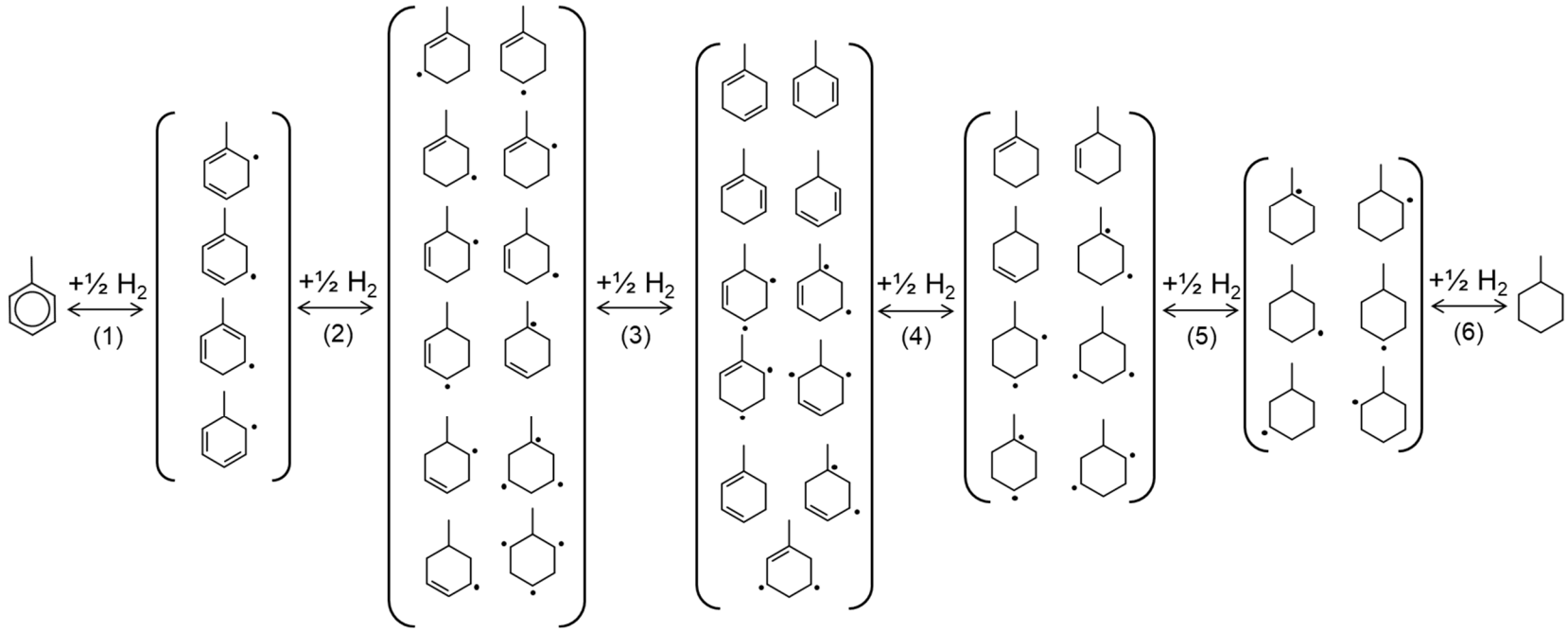

Scheme 3.S1: Intermediates formed from gas phase toluene+H_2 reactions grouped together by their molecular compositions.

3.8.5. Expanded reaction-transport model describing methylcyclohexane formation via inhibitor-scavenging routes.

This section provides further details to supplement the derivation of the reaction-transport model that describes MA formation via the inhibitor-scavenging route (**Scheme 3.2**), introduced in **Section 3.3.5**.

A balance on the moles of TH_q-b (for the reactive intermediate in inhibitor-scavenging route **Scheme 3.2**) in a spherical shell with a differential thickness (dl) within a spherical Pt/SiO_2 aggregate of a Pt/SiO_2+Al_2O_3 mixture is:

$$4\pi l^2 N_{TH_qb}|_l - 4\pi r^2 N_{TH_qb}|_{l+dl} + \rho_{Pt} r_{TH_qb,Pt} 4\pi l^2 dl = 0, \tag{3.S54}$$

with N_{TH_qb}, the molar flux, given by Fick's law:

$$N_{TH_qb} = -D_{e,N_{TH_qb};Pt} \frac{d[TH_q]_b}{dl}, \tag{3.S55}$$

where l is the radial coordinate of the sphere, ρ_{Pt} is the volumetric density of Pt-sites, $r_{TH_qb,Pt}$ is the net turnover rate of TH_q-b formation (per exposed Pt site) at the Pt surface, $D_{e,TH_qb;Pt}$ is the effective diffusivity of TH_q-b throughout the pores of the Pt/SiO_2 aggregate (**Section 3.2.3**), and $[TH_q]_b$ is the TH_q-b concentration. Dividing both sides of **equation 3.S54** by the volume of the spherical shell ($4\pi l^2 dl$) and taking the limit as $dl \to 0$ gives:

$$\frac{D_{e,TH_qb;Pt}}{l^2} \frac{d}{dl}\left(l^2 \frac{d[TH_q]_b}{dl} \right) + \rho_{Pt} r_{TH_qb,Pt} = 0. \tag{3.S56}$$

The following non-dimensional groups are defined:

$$\tilde{l} = \frac{l}{R_{Pt}}, \tag{3.S57}$$

and

$$[\widetilde{TH}_q]_b = \frac{[TH_q]_b}{[TH_q]_{b,PSS;Pt}}, \tag{3.S58}$$

where R_{Pt} is the radius of the Pt/SiO_2 aggregate and $[TH_q]_{b,PSS;Pt}$ is the concentration of TH_q-b at pseudo-steady state on Al_2O_3-free Pt/SiO_2. The dimensionless form of **equation 3.S56** is obtained by substituting l and $[TH_q]_b$ values with those from **equations 3.S57** and **3.S58**, respectively:

$$\frac{1}{\tilde{l}^2} \frac{d}{d\tilde{l}}\left(\tilde{l}^2 \frac{d[\widetilde{TH}_q]_b}{d\tilde{l}} \right) + \frac{R_{Pt}^2 \rho_{Pt}}{D_{e,N_{TH_qb};Pt}[TH_q]_{b,PSS;Pt}} r_{TH_qb,Pt} = 0, \tag{3.S59}$$

The net TH_q-b formation rate ($r_{TH_qb,Pt}$) reflects the difference between the rate that TH_q-b is formed via toluene-H_2 reactions ($r_{tol \to TH_qb,Pt}$) and consumed via subsequent H-addition reactions ($r_{TH_qb \to MA,Pt}$) at the Pt surface:

$$r_{TH_qb,Pt} = r_{tol\rightarrow TH_qb,Pt} - r_{TH_qb\rightarrow MA,Pt}. \quad (3.S60)$$

The TH_q-b formation rate ($r_{tol\rightarrow TH_qb,Pt}$) reflects the toluene conversion rate via the secondary route, which is limited by H-addition to TH_p-b* (**Scheme 3.2, step 1-4b**) and is proportional to TH_p-b* and H-*S* coverages. The $r_{tol\rightarrow TH_qb,Pt}$ value is given by assuming that TH_p-b* and H-*S* are formed in quasi-equilibrium with gaseous toluene and H_2 (**Scheme 3.2, step 1-3b**) and that TH_q-b* desorption is quasi-equilibrated (**Scheme 3.2, step 9b**):

$$r_{tol\rightarrow TH_qb,Pt} = \frac{\alpha_{tol\rightarrow TH_qb,Pt}}{\left[TH_q\right]_b}, \quad (3.S61)$$

with

$$\alpha_{tol\rightarrow TH_qb,Pt} = \frac{k_{CH,p+1;a}K_{H,S}^{p+1}\prod_{i=1}^{p}\left(K_{CH,i;b}\right)[tol][H_2]^{\frac{p+1}{2}}}{K_{TH_qb*}\left(1+K_{H,S}[H_2]^{\frac{1}{2}}\right)}, \quad (3.S62)$$

The TH_q-b consumption rate ($r_{TH_qb\rightarrow MA,Pt}$) is limited by H addition to TH_r-b* (**Scheme 3.2, step 6b**) and is proportional to TH_r-b* and H-*S* coverages. This rate is given assuming that TH_r-b* and H-*S* are formed in quasi-equilibrium with TH_q-b* and H_2(g) (**Scheme 3.2, step 1,5b**) and that TH_q-b* desorption is quasi-equilibrated (**Scheme 3.2, step 9b**):

$$r_{TH_qb\rightarrow MA,Pt} = \alpha_{TH_qb\rightarrow MA,Pt}, \quad (3.S63)$$

with

$$\alpha_{TH_qb\rightarrow MA,Pt} = \frac{k_{CH,r+1;a}K_{H,S}^{r-q+1}\prod_{i=q}^{r}\left(K_{CH,i;b}\right)[H_2]^{\frac{r-q+1}{2}}}{\left(1+K_{H,S}[H_2]^{\frac{1}{2}}\right)} \quad (3.S64)$$

The net rate of TH_q-b formation is necessarily zero ($r_{TH_qb,Pt} = 0$), in the absence of a scavenger function, to maintain pseudo-steady state. Equating the TH_q-b formation rate (**eq 3.S61**) and consumption (**eq 3.S62**) rates and rearranging gives the pseudo-steady state TH_q-b value:

$$\left[TH_q\right]_{b,PSS;Pt} = \frac{\alpha_{tol\rightarrow TH_qb,Pt}}{\alpha_{TH_qb\rightarrow MA,Pt}}. \quad (3.S65)$$

The net TH_q-b formation rate (**eq 3.S60**) is then restated by substituting the TH_q-b formation ($r_{tol\rightarrow TH_qb,Pt}$) and consumption ($r_{TH_qb\rightarrow MA,Pt}$) rates with their values from **equations 3.S61** and **3.S62**, respectively:

$$r_{TH_qb,Pt} = \alpha_{TH_qb\rightarrow MA,Pt}\left(\frac{\left[TH_q\right]_{b,PSS}}{\left[TH_q\right]_b} - 1\right), \quad (3.S66)$$

The diffusion equation describing TH_q-b pressures across the Pt domain (**eq 3.S59**) is next restated in its dimensionless form by substituting $r_{TH_qb,Pt}$ with its value from **equation 3.S66**:

$$\frac{1}{\tilde{r}^2}\frac{\partial}{\partial \tilde{r}}\tilde{r}^2\frac{\partial}{\partial \tilde{r}}[\widetilde{I_H}] + \phi_{Pt}^2\left(\frac{1}{[\widetilde{I_H}]} - 1\right) = 0, \tag{3.S67}$$

with

$$\phi_{Pt} = R_{Pt}\sqrt{\frac{\rho_{Pt}\alpha_{TH_qb\rightarrow MA,Pt}}{D_{e,N_{TH_qb};Pt}\left[TH_q\right]_{b,PSS}}}. \tag{3.S68}$$

A balance on the moles of TH_q-b (the reactive intermediate in inhibitor-scavenging route) in a spherical shell with a differential thickness (ds) within a spherical Al_2O_3 aggregate of a Pt/SiO_2+Al_2O_3 mixture is:

$$4\pi s^2 N_{TH_qb}|_s - 4\pi r^2 N_{TH_qb}|_{s+ds} - \sigma_{Al} r_{-TH_qb,Al} 4\pi l^2 ds = 0, \tag{3.S69}$$

with N_{TH_qb}, the molar flux, is given by Fick's law:

$$N_{TH_qb} = -D_{e,TH_qb;Al}\frac{d\left[TH_q\right]_b}{ds}, \tag{3.S70}$$

where s is the radial coordinate, σ_{Al} is the Al_2O_3 internal surface area to volume ratio, $r_{-TH_qb,Al}$ is the TH_q-b consumption areal rate at the Al_2O_3 surface, and $D_{e,TH_qb;Al}$ is the effective diffusivity of TH_q-b throughout the pores of the Al_2O_3 aggregate (**Section 3.2.3**). Dividing both sides of **equation 3.S69** by the volume of the spherical shell ($4\pi s^2 ds$) and taking the limit as $ds \rightarrow 0$ gives:

$$\frac{D_{e,TH_qb;Al}}{s^2}\frac{d}{ds}\left(s^2\frac{d\left[TH_q\right]_b}{ds}\right) - \sigma_{Al} r_{-TH_qb,Al} = 0, \tag{3.S71}$$

The following non-dimensional Al_2O_3 radial dimension ($\tilde{s}$) is defined as:

$$\tilde{s} = \frac{s}{R_{Al}}, \tag{3.S72}$$

Where R_{Al} is the radius of the Al_2O_3 aggregate. The dimensionless form of **equation 3.S71** is obtained by substituting the values of s and $\left[TH_q\right]_b$ with their values from **equations 3.S72** and **3.S65**, respectively:

$$\frac{1}{\tilde{s}^2}\frac{d}{d\tilde{s}}\left(\tilde{s}^2\frac{d\left[\widetilde{TH}_q\right]_b}{d\tilde{s}}\right) - \frac{R_{Al}^2\sigma_{Al}}{D_{e,TH_qb;Al}\left[TH_q\right]_{b,PSS}} r_{-TH_qb,Al} = 0. \tag{3.S73}$$

The observation that Al_2O_3-catalyzes hydrogenation reactions of 4ME and 13CHD reactants (**Section 3.3.3**) suggests that hydrogenation of TH_q-b intermediates may be relevant in these bifunctional routes. 4ME and 13CHD hydrogenation rates were first order in the respective hydrocarbon pressures at values below 10 Pa (**Figure 3.5**), which is significantly higher than the pressures that TH_q-b intermediates would be present during toluene-H_2 reactions on Pt/SiO_2+Al_2O_3 mixtures, suggesting that the areal TH_q-b consumption rates ($r_{TH_q,Al}$) are proportional to TH_q-b pressure:

$$r_{-TH_qb,Al} = \alpha_{TH_qb\rightarrow MA,Al}\left[TH_q\right]_b, \tag{3.S74}$$

where $\alpha_{TH_qb\rightarrow MA,Al}$ is a pseudo-first order rate constant for TH_q-b hydrogenation at the Al_2O_3 surface. Substituting the $r_{-TH_qb,Al}$ value **equation 3.S73** with the value from **equation 3.S74** gives:

$$\frac{1}{\tilde{s}^2}\frac{\partial}{\partial \tilde{s}}\tilde{s}^2\frac{\partial}{\partial \tilde{s}}\left[\widetilde{TH}_q\right]_b - \phi_{Al}^2\left[\widetilde{TH}_q\right]_b = 0, \tag{3.S75}$$

with

$$\phi_{Al} = R_{Al}\sqrt{\frac{\sigma_{Al}\alpha_{TH_qb\rightarrow MA,Al}}{D_{TH_qb,Al}}}, \tag{3.S76}$$

The TH_q-b pressure distribution across the radial dimensions of the Pt/SiO_2 and Al_2O_3 aggregates can be determined for given ϕ_{Pt} and ϕ_{Al} values by solving the coupled differential equations (**eq 3.S67** and **3.S75**) subject to the following boundary conditions: (i and ii) the first derivative of the TH_q-b pressure is zero at the center of each aggregate ($\tilde{r} = 0$ and $\tilde{s} = 0$) due to spherical symmetry, (iii) the TH_q-b pressure in the intervening fluid between the Pt/SiO_2 and Al_2O_3 aggregates in between the two functions are equal, and (iv) the rate of external TH_q-b mass transfer leaving the Pt/SiO_2 aggregates is equal to the rate of Pt/SiO_2 mass transfer into the Al_2O_3 aggregates. The rate of external TH_q-b mass transfer between each catalyst domain and the bulk fluid (W_i, where i denotes the Pt/SiO_2 or Al_2O_3 domain) is related to the overall mass transfer coefficient, k_g (**Section 3.2.3**), and the change in TH_q-b concentration between the bulk fluid ($\left[TH_q\right]_b^{bulk}$) and the surface of the catalyst aggregate ($\left[TH_q\right]_b^{surf}$; at $\tilde{l} = 1$ or $\tilde{s} = 1$):

$$W_i = -k_g A_i\left(\left[TH_q\right]_b^{bulk} - \left[TH_q\right]_b^{surf}\right), \tag{3.S77}$$

with

$$A_i = 4\pi R_i^2, \tag{3.S78}$$

where A_i is the external surface area of the catalyst aggregate and R_i is the aggregate radius.

3.8.6. Derivation of enhancement factors for intimate Pt/SiO_2 and Al_2O_3 mixtures for inhibitor-scavenging routes at pseudo-steady state.

The net rate that TH_2-b intermediates are formed from toluene-H_2 reactants on Pt/SiO_2+Al_2O_3 mixtures reflects the difference between the TH_2-b formation rate at the Pt surface ($r_{tol\rightarrow TH_2b,Pt}$; **Scheme 3.2, steps 1-4b**) and the rates of TH_2-b consumption at the Pt ($r_{TH_2b\rightarrow MA,Pt}$; **Scheme 3.2, steps 5b-8b**) and Al_2O_3 surface ($r_{TH_2b,Al}$; **Scheme 3.2, steps 9b-10b**):

$$r_{TH_2b,Pt} = r_{tol\rightarrow TH_2b,Pt} - r_{TH_2b\rightarrow MA,Pt} - r_{-TH_2b,Al}. \tag{3.S79}$$

Substituting the values of $r_{tol\rightarrow TH_qb,Pt}$, $r_{TH_qb\rightarrow MA,Pt}$, and $r_{-TH_2b,Al}$ in **equation 3.S79** with their respective values from **equations 3.S61**, **3.S63**, and **3.41** (for q=2) gives:

$$r_{TH_2b,Pt} = \frac{\alpha_{tol\rightarrow TH_2b,Pt}}{[TH_2]_b} - \alpha_{TH_2b\rightarrow MA,Pt} - \alpha_{TH_2b\rightarrow MA,Al}[TH_2]_b[H_2][tol]^{\omega_{tol}}\beta. \tag{3.S80}$$

where $\alpha_{tol\rightarrow TH_2b,Pt}$ is a grouping of parameters defined in **equation 3.S62**, $\alpha_{TH_2b\rightarrow MA,Pt}$ is a grouping of parameters defined in **equation 3.S64**, $\alpha_{TH_2b\rightarrow MA,Al}$ is the pseudo-first order rate constant for Al_2O_3-catalyzed TH_2-b consumption, ω_{tol} is the apparent reaction order for TH_2-b

hydrogenation on Al_2O_3 with respect to toluene pressure, and β is the ratio between the Al_2O_3 surface area and the number of exposed surface Pt sites. Under conditions in which TH_2-b forms at pseudo-steady state pressures, the net TH_2-b formation rate becomes zero ($r_{TH_2b,Pt} = 0$) and **equation 3.S80** simplifies to the following second-order polynomial:

$$0 = \alpha_{tol\rightarrow TH_2b,Pt} - \alpha_{TH_2b\rightarrow MA,Pt}[TH_2]^{bi}_{b,PSS} - \alpha_{TH_2b\rightarrow MA,Al}[H_2][tol]^{\omega_{tol}}\beta\left([TH_2]^{bi}_{b,PSS}\right)^2. \quad (3.S81)$$

where $[TH_2]^{bi}_{b,PSS}$ is the pseudo-steady state TH_2-b concentration for a bifunctional Pt/SiO_2+Al_2O_3 mixture in the absence of concentration gradients. The functional form of **equation 3.S81** is restated in the following form by substituting $\alpha_{tol\rightarrow TH_2b,Pt}$ with its value from **equation 3.S65** and rearranging terms:

$$0 = \left(\frac{[TH_2]^{bi}_{b,PSS}}{[TH_2]^{mono}_{b,PSS}}\right)^2 - \frac{\alpha_{TH_2b\rightarrow MA,Pt}}{\alpha_{TH_2b\rightarrow MA,Al}[H_2][tol]^{\omega_{tol}}[TH_2]^{mono}_{b,PSS}\beta}\left(1 - \frac{[TH_2]^{bi}_{b,PSS}}{[TH_2]^{mono}_{b,PSS}}\right). \quad (3.S82)$$

where $[TH_2]^{mono}_{b,PSS}$ is the pseudo-steady state TH_2-b concentration for an Al_2O_3-free (monofunctional) Pt/SiO_2 catalyst. An expression for $[TH_2]^{bi}_{b,PSS}$ is obtained by solving **equation 3.S82**:

$$[TH_2]^{bi}_{b,PSS} = \frac{[TH_2]^{mono}_{b,PSS}}{2}\left(\sqrt{\left(\frac{\sigma}{\beta}\right)^2 + 4\frac{\sigma}{\beta}} - \frac{\sigma}{\beta}\right), \quad (3.S83)$$

where

$$\sigma = \frac{\alpha_{TH_2b\rightarrow MA,Pt}}{\alpha_{TH_2b\rightarrow MA,Al}[H_2][tol]^{\omega_{tol}}[TH_2]^{mono}_{b,PSS}}. \quad (3.S84)$$

Substituting the $\alpha_{TH_2b\rightarrow MA,Pt}$ value with the value from **equation 3.S64** (with q=2) gives the following definition of the σ term:

$$\sigma = \frac{k_{TH_2b\rightarrow MA,Pt}[H_2]^{\frac{r-3}{2}} \Big/ \left(1 + K_{H,S}[H_2]^{\frac{1}{2}}\right)}{\alpha_{TH_2b\rightarrow MA,Al}[tol]^{\omega_{tol}}[TH_2]^{mono}_{b,PSS}}. \quad (3.S85)$$

The enhancement factor for the inhibitor scavenging route (η) can thus be obtained by taking the ratio between **equation 3.23** ($r_{MA,Pt} = \alpha_{tol\rightarrow TH_{m+1},a}/\left[TH_q\right]_b$) evaluated for $\left[TH_q\right]_b$ values of $[TH_2]^{bi}_{b,PSS}$ and $[TH_2]^{mono}_{b,PSS}$, then simplifying:

$$\eta = \frac{1}{2}\left(\sqrt{1 + 4\frac{\beta}{\sigma}} + 1\right). \quad (3.S86)$$

APPENDICES

A.1. Density functional theory-derived optimized geometries of molecules bound to Pt(111) surfaces.

Density functional theory (DFT) was used to determine optimized geometries of toluene-derived hydrocarbons bound to the surface of a Pt(111) slab (3x3 unit cell, 0.11 monolayer coverage; four Pt layers; with computational details described **Chapter 2, Section 2.2.3**). The lattice vectors (v_i) for the 3x3 unit cell are:

Lattice vectors	x_1 (Å)	x_2 (Å)	x_3 (Å)
v_1	8.456	0.0	0.0
v_2	4.228	7.322	0.0
v_3	0.0	0.0	26.904

The bottom two layers of the four-layer Pt slab were fixed to their bulk coordinates (with a 3.986 Å lattice constant):

Methylbenzene; four-fold bridge; -234.47174 eV			
Atom	x_1	x_2	x_3
Pt	0.225	0.217	0.543
Pt	0.557	0.221	0.543
Pt	0.889	0.221	0.543
Pt	0.224	0.554	0.542
Pt	0.556	0.555	0.544
Pt	0.888	0.555	0.543
Pt	0.225	0.886	0.544
Pt	0.556	0.886	0.545
Pt	0.89	0.888	0.542
Pt	0.005	0.331	0.629
Pt	0.332	0.331	0.629
Pt	0.669	0.329	0.631
Pt	0.325	0.668	0.631
Pt	0.675	0.668	0.632
Pt	0	0.667	0.629
Pt	0.997	0	0.629
Pt	0.33	0.006	0.636
Pt	0.67	0	0.629

The following tables show the atomic positions (x_i) in fractional coordinates (relative to the unit cell) for the atoms that comprise the top two Pt layers and the adsorbate. The adsorbate, binding mode (as depicted in **Scheme 2.S1**), and absolute electronic energy (eV) are included in the heading.

Methylbenzene; four-fold bridge; -234.47174 eV			
Atom	x_1	x_2	x_3
Pt	0.225	0.217	0.543
Pt	0.557	0.221	0.543

Toluene; four-fold bridge, -238.56904 eV			
Atom	x_1	x_2	x_3
Pt	0.225	0.215	0.543
Pt	0.558	0.221	0.543

Toluene; hcp hollow; -238.07309 eV			
Atom	x_1	x_2	x_3
Pt	0.221	0.232	0.543
Pt	0.553	0.233	0.544

Pt	0.889	0.221	0.543
Pt	0.224	0.554	0.542
Pt	0.556	0.555	0.544
Pt	0.888	0.555	0.543
Pt	0.225	0.886	0.544
Pt	0.556	0.886	0.545
Pt	0.89	0.888	0.542
Pt	0.005	0.331	0.629
Pt	0.332	0.331	0.629
Pt	0.669	0.329	0.631
Pt	0.325	0.668	0.631
Pt	0.675	0.668	0.632
Pt	0	0.667	0.629
Pt	0.997	0	0.629
Pt	0.33	0.006	0.636
Pt	0.67	0	0.629
C	0.441	0.494	0.715
C	0.637	0.394	0.713
C	0.339	0.689	0.713
C	0.73	0.499	0.716
C	0.433	0.793	0.715
C	0.632	0.693	0.714
C	0.333	0.99	0.716
H	0.368	0.42	0.723
H	0.708	0.255	0.727
H	0.196	0.759	0.725
H	0.876	0.428	0.724
H	0.701	0.767	0.726
H	0.406	0.057	0.73
H	0.191	0.053	0.728

Pt	0.887	0.222	0.543
Pt	0.225	0.554	0.543
Pt	0.556	0.555	0.544
Pt	0.888	0.553	0.543
Pt	0.224	0.885	0.544
Pt	0.557	0.885	0.544
Pt	0.89	0.887	0.542
Pt	0.009	0.324	0.629
Pt	0.334	0.323	0.627
Pt	0.665	0.336	0.634
Pt	0.322	0.663	0.633
Pt	0.679	0.665	0.632
Pt	0.001	0.663	0.628
Pt	0.995	0.002	0.629
Pt	0.336	0.993	0.634
Pt	0.67	0.002	0.629
C	0.404	0.563	0.713
C	0.605	0.456	0.709
C	0.308	0.759	0.71
C	0.698	0.564	0.709
C	0.399	0.869	0.708
C	0.601	0.76	0.709
H	0.669	0.332	0.732
H	0.166	0.83	0.722
H	0.841	0.493	0.721
H	0.337	0.992	0.732
H	0.674	0.83	0.721
C	0.31	0.472	0.738
H	0.371	0.327	0.727
H	0.164	0.541	0.729
H	0.324	0.478	0.779

Pt	0.882	0.233	0.544
Pt	0.225	0.561	0.545
Pt	0.554	0.561	0.544
Pt	0.889	0.562	0.542
Pt	0.221	0.894	0.543
Pt	0.554	0.897	0.541
Pt	0.889	0.896	0.542
Pt	0.996	0.348	0.63
Pt	0.329	0.34	0.634
Pt	0.659	0.351	0.637
Pt	0.329	0.694	0.633
Pt	0.669	0.684	0.627
Pt	0.997	0.682	0.629
Pt	0.994	0.019	0.63
Pt	0.328	0.018	0.628
Pt	0.668	0.009	0.628
C	0.394	0.326	0.716
C	0.573	0.318	0.714
C	0.234	0.503	0.724
C	0.583	0.481	0.713
C	0.243	0.664	0.722
C	0.413	0.659	0.712
H	0.691	0.192	0.727
H	0.106	0.509	0.733
H	0.706	0.48	0.726
H	0.122	0.795	0.731
H	0.424	0.778	0.722
C	0.392	0.167	0.742
H	0.507	0.035	0.73
H	0.264	0.167	0.735
H	0.404	0.182	0.782

1-methyl-6-hydrobenzene; hcp hollow; -242.05782 eV

Atom	x_1	x_2	x_3
Pt	0.221	0.223	0.545
Pt	0.553	0.226	0.543
Pt	0.889	0.225	0.543
Pt	0.225	0.554	0.544
Pt	0.555	0.559	0.542
Pt	0.892	0.557	0.542
Pt	0.224	0.894	0.545
Pt	0.553	0.895	0.543
Pt	0.896	0.893	0.543
Pt	0.988	0.35	0.631
Pt	0.329	0.334	0.635
Pt	0.662	0.34	0.628
Pt	0.336	0.664	0.629
Pt	0.671	0.67	0.627
Pt	0.002	0.678	0.629

2-methyl-6-hydrobenzene; four-fold bridge; -241.80224 eV

Atom	x_1	x_2	x_3
Pt	0.221	0.223	0.545
Pt	0.553	0.226	0.543
Pt	0.889	0.225	0.543
Pt	0.225	0.554	0.544
Pt	0.555	0.559	0.542
Pt	0.892	0.557	0.542
Pt	0.224	0.894	0.545
Pt	0.553	0.895	0.543
Pt	0.896	0.893	0.543
Pt	0.988	0.35	0.631
Pt	0.329	0.334	0.635
Pt	0.662	0.34	0.628
Pt	0.336	0.664	0.629
Pt	0.671	0.67	0.627
Pt	0.002	0.678	0.629

1-methyl-5,6-dihydrobenzene; four-fold bridge; -245.41347 eV

Atom	x_1	x_2	x_3
Pt	0.222	0.224	0.546
Pt	0.555	0.226	0.541
Pt	0.89	0.226	0.543
Pt	0.222	0.56	0.541
Pt	0.556	0.561	0.541
Pt	0.893	0.556	0.543
Pt	0.223	0.896	0.545
Pt	0.553	0.895	0.544
Pt	0.892	0.894	0.543
Pt	0.994	0.343	0.635
Pt	0.333	0.344	0.627
Pt	0.663	0.342	0.627
Pt	0.335	0.669	0.627
Pt	0.671	0.672	0.628
Pt	0.001	0.674	0.629

Pt	0.351	0	0
Pt	0.68	0.004	0.626
Pt	0.004	0.017	0.638
C	0.121	0.368	0.732
C	0.315	0.264	0.711
C	0.387	0.063	0.713
C	0.995	0.307	0.708
C	0.264	0.991	0.712
C	0.064	0.106	0.709
H	0.062	0.517	0.728
H	0.408	0.3	0.73
H	0.854	0.386	0.723
H	0.317	0.851	0.725
H	0.987	0.059	0.732
H	0.129	0.341	0.773
C	0.569	0.947	0.739
H	0.669	0.987	0.729
H	0.627	0.801	0.731
H	0.544	0.969	0.78

		-	
Pt	0.351	0.009	0.635
Pt	0.68	0.004	0.626
Pt	0.004	0.017	0.638
C	0.121	0.368	0.732
C	0.315	0.264	0.711
C	0.387	0.063	0.713
C	0.995	0.307	0.708
C	0.264	0.991	0.712
C	0.064	0.106	0.709
H	0.062	0.517	0.728
H	0.408	0.3	0.73
H	0.854	0.386	0.723
H	0.317	0.851	0.725
H	0.987	0.059	0.732
H	0.129	0.341	0.773
C	0.569	0.947	0.739
H	0.669	0.987	0.729
H	0.627	0.801	0.731
H	0.544	0.969	0.78

Pt	0.344	0.004	0.638
Pt	0.673	0.007	0.628
Pt	0.001	0.011	0.634
C	0.073	0.337	0.745
C	0.281	0.236	0.738
C	0.364	0.038	0.722
C	0.973	0.277	0.71
C	0.248	0.963	0.713
C	0.048	0.074	0.708
H	0.017	0.486	0.743
H	0.042	0.31	0.783
H	0.347	0.238	0.774
H	0.321	0.311	0.712
H	0.826	0.35	0.718
H	0.305	0.816	0.719
H	0.971	0.022	0.729
C	0.555	0.913	0.742
H	0.648	0.962	0.731
H	0.612	0.772	0.728
H	0.55	0.914	0.783

1-Methyl-5,6-dihydrobenzene; hcp hollow; -245.96758 eV			
Atom	x_1	x_2	x_3
Pt	0.224	0.219	0.545
Pt	0.554	0.225	0.542
Pt	0.888	0.226	0.542
Pt	0.223	0.556	0.542
Pt	0.553	0.561	0.545
Pt	0.884	0.558	0.543
Pt	0.224	0.891	0.544
Pt	0.553	0.89	0.545
Pt	0.888	0.89	0.541
Pt	0.999	0.336	0.629
Pt	0.332	0.335	0.629
Pt	0.665	0.337	0.628
Pt	0.326	0.669	0.633
Pt	0.67	0.667	0.637
Pt	0.999	0.667	0.627
Pt	0.992	0.007	0.626
Pt	0.337	0.995	0.638
Pt	0.667	0.006	0.627
C	0.611	0.563	0.741
C	0.629	0.718	0.715
C	0.418	0.583	0.741
C	0.458	0.899	0.715
C	0.277	0.739	0.709
C	0.284	0.911	0.713
H	0.71	0.431	0.724
H	0.656	0.556	0.78
H	0.424	0.455	0.73
H	0.365	0.612	0.78
H	0.467	0.015	0.73
H	0.139	0.764	0.716
H	0.163	0.034	0.726
C	0.789	0.728	0.739
H	0.806	0.837	0.722
H	0.918	0.598	0.735
H	0.762	0.757	0.779

1-Methyl-3,6-dihydrobenzene; two-fold bridge; -246.35577 eV			
Atom	x_1	x_2	x_3
Pt	0.228	0.214	0.543
Pt	0.566	0.215	0.546
Pt	0.892	0.215	0.546
Pt	0.231	0.549	0.547
Pt	0.56	0.546	0.547
Pt	0.896	0.547	0.543
Pt	0.23	0.877	0.546
Pt	0.561	0.881	0.543
Pt	0.896	0.88	0.544
Pt	0.014	0.313	0.632
Pt	0.341	0.31	0.63
Pt	0.681	0.311	0.643
Pt	0.343	0.643	0.646
Pt	0.678	0.65	0.63
Pt	0.007	0.649	0.633
Pt	0.344	0.981	0.631
Pt	0.678	0.978	0.632
Pt	0.012	0.979	0.633
C	0.318	0.556	0.723
C	0.434	0.353	0.737
C	0.399	0.672	0.727
C	0.635	0.264	0.722
C	0.719	0.377	0.722
C	0.605	0.577	0.739
H	0.722	0.115	0.728
H	0.432	0.346	0.779
H	0.371	0.272	0.723
H	0.869	0.313	0.727
H	0.666	0.661	0.726
H	0.615	0.574	0.78
H	0.17	0.619	0.731
C	0.286	0.867	0.747
H	0.14	0.932	0.735
H	0.341	0.956	0.735
H	0.29	0.86	0.788

2-Methyl-4,5,6-trihydrobenzene; hcp hollow; -249.71302 eV			
Atom	x_1	x_2	x_3
Pt	0.22	0.225	0.542
Pt	0.553	0.226	0.544
Pt	0.885	0.225	0.543
Pt	0.221	0.555	0.543
Pt	0.556	0.554	0.544
Pt	0.886	0.558	0.542
Pt	0.22	0.89	0.541
Pt	0.555	0.892	0.543
Pt	0.883	0.893	0.543
Pt	0.994	0.338	0.628
Pt	0.324	0.338	0.632
Pt	0.666	0.338	0.636
Pt	0.328	0.673	0.627
Pt	0.663	0.673	0.629
Pt	0.993	0.674	0.629
Pt	0.998	0.002	0.628
Pt	0.328	0.001	0.627
Pt	0.657	0.013	0.634
C	0.378	0.259	0.708
C	0.582	0.146	0.707
C	0.291	0.426	0.743
C	0.679	0.253	0.711
C	0.392	0.534	0.745
C	0.6	0.409	0.749
H	0.315	0.174	0.715
H	0.643	0.016	0.728
H	0.147	0.516	0.732
H	0.826	0.163	0.718
H	0.34	0.632	0.776
H	0.668	0.491	0.744
H	0.29	0.374	0.78
H	0.362	0.618	0.71
C	0.648	0.322	0.802
H	0.587	0.235	0.808
H	0.595	0.429	0.831
H	0.797	0.236	0.807

5-methyl-4,5,6-trihydrobenzene; hcp hollow; -249.72500 eV			
Atom	x_1	x_2	x_3
Pt	0.221	0.224	0.542
Pt	0.553	0.225	0.544
Pt	0.884	0.225	0.542
Pt	0.221	0.553	0.543
Pt	0.556	0.552	0.544
Pt	0.886	0.557	0.542
Pt	0.222	0.888	0.541
Pt	0.556	0.891	0.543
Pt	0.883	0.891	0.543
Pt	0.996	0.336	0.628
Pt	0.326	0.337	0.633
Pt	0.671	0.332	0.637
Pt	0.331	0.669	0.627
Pt	0.663	0.67	0.629
Pt	0.994	0.67	0.628
Pt	0.001	0.998	0.626
Pt	0.329	0.999	0.627
Pt	0.657	0.011	0.635
C	0.38	0.259	0.709
C	0.585	0.145	0.708
C	0.294	0.424	0.744
C	0.688	0.246	0.714
C	0.389	0.537	0.744
C	0.596	0.416	0.748
H	0.319	0.173	0.715
H	0.643	0.014	0.729
H	0.148	0.509	0.736
H	0.339	0.635	0.775
H	0.666	0.495	0.744
H	0.303	0.367	0.782
H	0.628	0.36	0.787
H	0.354	0.621	0.71
C	0.885	0.125	0.732
H	0.958	0.995	0.711
H	0.884	0.088	0.771
H	0.964	0.196	0.729

1-Methylcyclohexene; two-fold bridge; -253.45018 eV			
Atom	x_1	x_2	x_3
Pt	0.217	0.227	0.542
Pt	0.551	0.228	0.544
Pt	0.881	0.229	0.543
Pt	0.217	0.562	0.542
Pt	0.552	0.558	0.544
Pt	0.883	0.562	0.543
Pt	0.218	0.894	0.542
Pt	0.552	0.896	0.544
Pt	0.881	0.896	0.543
Pt	0.991	0.345	0.627
Pt	0.322	0.346	0.627
Pt	0.658	0.342	0.637
Pt	0.325	0.677	0.628
Pt	0.657	0.678	0.629
Pt	0.989	0.679	0.628
Pt	0.995	0.008	0.627
Pt	0.325	0.01	0.628
Pt	0.655	0.017	0.638
C	0.508	0.176	0.796
C	0.503	0.108	0.743
C	0.662	0.095	0.713
C	0.674	0.269	0.715
C	0.512	0.425	0.742
C	0.497	0.365	0.796
H	0.392	0.184	0.818
H	0.633	0.073	0.815
H	0.509	0.975	0.744
H	0.371	0.205	0.726
H	0.793	0.976	0.724
H	0.383	0.466	0.723
H	0.528	0.547	0.743
H	0.606	0.361	0.819
H	0.367	0.471	0.812
C	0.855	0.239	0.737
H	0.857	0.209	0.777
H	0.974	0.121	0.72
H	0.869	0.361	0.732

4-Methylcyclohexene; two-fold bridge; -253.48939 eV			
Atom	x_1	x_2	x_3
Pt	0.218	0.221	0.541
Pt	0.554	0.224	0.543
Pt	0.882	0.223	0.544
Pt	0.22	0.557	0.543
Pt	0.551	0.555	0.544
Pt	0.886	0.555	0.542
Pt	0.22	0.885	0.544
Pt	0.551	0.889	0.542
Pt	0.886	0.889	0.542
Pt	0.992	0.332	0.629
Pt	0.323	0.329	0.627
Pt	0.657	0.336	0.636
Pt	0.327	0.661	0.636
Pt	0.66	0.667	0.628
Pt	0.991	0.666	0.628
Pt	0.992	0.999	0.63
Pt	0.325	0.998	0.629
Pt	0.659	0.999	0.628
C	0.317	0.485	0.792
C	0.25	0.547	0.738
C	0.392	0.577	0.712
C	0.581	0.412	0.713
C	0.596	0.249	0.742
C	0.503	0.303	0.794
H	0.212	0.469	0.812
H	0.327	0.594	0.811
H	0.115	0.673	0.738
H	0.231	0.442	0.72
H	0.392	0.699	0.726
H	0.685	0.447	0.723
H	0.531	0.184	0.721
H	0.741	0.144	0.746
H	0.595	0.321	0.819
C	0.479	0.145	0.813
H	0.611	0.017	0.816
H	0.416	0.176	0.85
H	0.39	0.122	0.788

1-methylcyclohexyl; atop; -257.21462 eV				4-methylcyclohexyl; atop; -257.2742487 eV			
Atom	x_1	x_2	x_3	Atom	x_1	x_2	x_3
Pt	0.217	0.228	0.542	Pt	0.224	0.225	0.543
Pt	0.552	0.23	0.544	Pt	0.56	0.224	0.542
Pt	0.881	0.23	0.544	Pt	0.894	0.226	0.544
Pt	0.217	0.562	0.542	Pt	0.226	0.557	0.543
Pt	0.552	0.559	0.544	Pt	0.56	0.557	0.543
Pt	0.884	0.562	0.542	Pt	0.894	0.555	0.544
Pt	0.216	0.896	0.542	Pt	0.226	0.89	0.543
Pt	0.55	0.896	0.542	Pt	0.56	0.891	0.542
Pt	0.884	0.896	0.542	Pt	0.892	0.891	0.542
Pt	0.99	0.346	0.629	Pt	0.01	0.338	0.637
Pt	0.322	0.346	0.628	Pt	0.344	0.337	0.629
Pt	0.655	0.35	0.64	Pt	0.676	0.337	0.63
Pt	0.321	0.683	0.628	Pt	0.342	0.67	0.629
Pt	0.656	0.681	0.629	Pt	0.675	0.671	0.629
Pt	0.989	0.681	0.629	Pt	0.008	0.671	0.629
Pt	0.989	0.015	0.629	Pt	0.007	0.004	0.629
Pt	0.323	0.014	0.629	Pt	0.342	0.003	0.629
Pt	0.656	0.014	0.629	Pt	0.675	0.004	0.63
C	0.445	0.312	0.808	C	0.968	0.297	0.82
C	0.387	0.505	0.79	C	0.902	0.486	0.797
C	0.43	0.501	0.734	C	0.868	0.485	0.741
C	0.631	0.371	0.721	C	0.043	0.341	0.715
C	0.694	0.178	0.741	C	0.113	0.151	0.737
C	0.649	0.181	0.797	C	0.143	0.155	0.794
H	0.457	0.563	0.811	H	0.007	0.527	0.803
H	0.239	0.597	0.795	H	0.776	0.591	0.815
H	0.387	0.641	0.72	H	0.824	0.622	0.725
H	0.625	0.117	0.721	H	0.149	0.379	0.718
H	0.842	0.089	0.735	H	0.014	0.104	0.731
H	0.732	0.221	0.82	H	0.243	0.051	0.72
H	0.688	0.041	0.809	H	0.252	0.189	0.8
H	0.344	0.455	0.714	H	0.192	0.018	0.809
H	0.363	0.262	0.788	H	0.756	0.456	0.735
H	0.417	0.313	0.848	C	0.995	0.297	0.877
C	0.753	0.445	0.739	H	0.861	0.261	0.813
H	0.751	0.453	0.78	H	0.1	0.333	0.886
H	0.705	0.585	0.725	H	0.037	0.162	0.892
H	0.896	0.357	0.727	H	0.867	0.397	0.895

A.2. Density functional theory-derived vibrational frequencies of molecules bound to Pt(111) surfaces.

The following tables show the vibrational frequencies calculated for toluene-derived hydrocarbons bound to the surface of a Pt(111) slab (3x3 unit cell, 0.11 monolayer coverage; 4 Pt-layers; unit cell in **Appendix A1**) calculated as described in **Chapter 2, Section 2.2.3**. The adsorbate and binding mode (as depicted in **Scheme 2.S1**) are reported in the headings.

Toluene; four-fold bridge		1-Methyl-5,6-dihydrobenzene; hcp hollow		1-Methyl-3,6-dihydrobenzene; two-fold bridge		1-Methylcyclohexene; two-fold bridge	
Mode	Frequency (cm^{-1})	Mode	Frequency (cm^{-1})	Mode	Frequency (cm^{-1})	Mode	Frequency (cm^{-1})
1	3071	1	3020	1	3052	1	2997
2	3066	2	2989	2	3044	2	2990
3	3057	3	2977	3	3041	3	2987
4	3044	4	2969	4	3004	4	2971
5	3016	5	2963	5	2975	5	2968
6	3010	6	2956	6	2931	6	2946
7	2987	7	2944	7	2920	7	2938
8	2870	8	2884	8	2833	8	2932
9	1463	9	2853	9	2824	9	2917
10	1458	10	2726	10	2808	10	2904
11	1431	11	1459	11	1471	11	2858
12	1395	12	1452	12	1446	12	2808
13	1377	13	1445	13	1444	13	1489
14	1368	14	1433	14	1425	14	1472
15	1353	15	1408	15	1421	15	1466
16	1303	16	1373	16	1414	16	1447
17	1266	17	1349	17	1373	17	1443
18	1153	18	1342	18	1351	18	1436
19	1152	19	1318	19	1333	19	1369
20	1096	20	1297	20	1298	20	1340
21	1045	21	1276	21	1274	21	1333
22	1035	22	1217	22	1200	22	1321
23	994	23	1196	23	1190	23	1310
24	959	24	1131	24	1158	24	1301
25	931	25	1104	25	1134	25	1258
26	923	26	1084	26	1057	26	1246
27	906	27	1048	27	1048	27	1224
28	885	28	1020	28	1009	28	1184
29	862	29	1011	29	982	29	1141
30	830	30	990	30	970	30	1121
31	731	31	950	31	955	31	1058
32	642	32	911	32	912	32	1023
33	573	33	905	33	876	33	1019
34	534	34	865	34	854	34	999
35	517	35	822	35	828	35	980
36	474	36	784	36	813	36	971
37	414	37	693	37	703	37	939

38	377	38	605	38	583	38	903
39	341	39	557	39	512	39	858
40	339	40	496	40	496	40	825
41	297	41	471	41	474	41	787
42	254	42	444	42	396	42	719
43	211	43	414	43	372	43	694
44	175	44	400	44	365	44	566
45	131	45	331	45	329	45	551
		46	300	46	298	46	494
		47	257	47	253	47	452
		48	203	48	229	48	424
		49	187	49	170	49	388
		50	153	50	143	50	310
		51	121	51	108	51	273
						52	262
						53	226
						54	213
						55	158
						56	119
						57	75

4-Methylcyclohexene; two-fold bridge		1-methyl-6-hydrobenzene; hcp hollow		5-methyl-4,5,6-trihydrobenzene		1-methylcyclohexyl; atop	
Mode	Frequency (cm^{-1})	Mode	Frequency (cm^{-1})	Mode	Frequency (cm^{-1})	Mode	Frequency (cm^{-1})
1	3022	1	3047	1	2997	1	2981
2	3001	2	3009	2	2990	2	2975
3	2981	3	2982	3	2987	3	2970
4	2979	4	2976	4	2971	4	2965
5	2969	5	2967	5	2968	5	2955
6	2965	6	2963	6	2946	6	2935
7	2953	7	2957	7	2938	7	2918
8	2924	8	2879	8	2932	8	2913
9	2897	9	2793	9	2917	9	2900
10	2894	10	1457	10	2904	10	2881
11	2882	11	1450	11	2858	11	2833
12	2870	12	1441	12	2808	12	2821
13	1486	13	1421	13	1489	13	2806
14	1483	14	1376	14	1472	14	1481
15	1473	15	1344	15	1466	15	1470
16	1464	16	1334	16	1447	16	1463
17	1445	17	1313	17	1443	17	1450
18	1390	18	1293	18	1436	18	1443
19	1343	19	1227	19	1369	19	1430
20	1338	20	1199	20	1340	20	1421
21	1334	21	1138	21	1333	21	1365
22	1323	22	1107	22	1321	22	1348
23	1310	23	1062	23	1310	23	1347
24	1299	24	1038	24	1301	24	1331

25	1279	25	1027	25	1258	25	1315
26	1249	26	1019	26	1246	26	1293
27	1225	27	1002	27	1224	27	1282
28	1157	28	974	28	1184	28	1278
29	1130	29	948	29	1141	29	1245
30	1124	30	907	30	1121	30	1212
31	1084	31	876	31	1058	31	1151
32	1037	32	823	32	1023	32	1146
33	1026	33	808	33	1019	33	1111
34	1003	34	709	34	999	34	1051
35	973	35	628	35	980	35	1031
36	960	36	573	36	971	36	1010
37	948	37	557	37	939	37	985
38	918	38	501	38	903	38	968
39	875	39	468	39	858	39	955
40	868	40	436	40	825	40	942
41	806	41	419	41	787	41	875
42	736	42	366	42	719	42	843
43	681	43	347	43	694	43	824
44	570	44	327	44	566	44	805
45	552	45	234	45	551	45	713
46	530	46	217	46	494	46	654
47	452	47	172	47	452	47	537
48	404	48	143	48	424	48	486
49	401			49	388	49	450
50	390			50	310	50	446
51	261			51	273	51	412
52	230			52	262	52	376
53	202			53	226	53	294
54	174			54	213	54	284
55	108					55	240
56	76					56	220
						57	158
						58	132
						59	98
						60	50

A.3. Density functional theory-derived optimized geometries of gas-phase molecules.

Density functional theory (DFT) was used to determine optimized geometries of gaseous reactants and intermediates during toluene hydrogenation (computational details in **Chapter 2, Section 2.2.3**). The lattice vectors (v_i) of the unit cell are:

Lattice vectors	x_1 (Å)	x_2 (Å)	x_3 (Å)
v_1	11.087	0.0	0.0
v_2	5.544	9.602	0.0
v_3	0.0	0.0	26.789

The following tables show the atomic positions (x_i) in fractional coordinates (relative to the unit cell) for toluene, H_2, 1-methyl-1,3-cyclohexadiene, 1-methylcyclohexene, and 4-methylcyclohexene molecules in vacuum. The molecule's name and absolute electronic energy (eV) are denoted in the heading.

Toluene; -92.849765 eV			
Atom	x_1	x_2	x_3
C	0.277	0.512	0.629
C	0.186	0.463	0.626
C	0.418	0.422	0.628
C	0.234	0.322	0.622
C	0.467	0.281	0.624
C	0.376	0.232	0.621
H	0.237	0.622	0.632
H	0.075	0.534	0.627
H	0.489	0.461	0.63
H	0.577	0.21	0.623
H	0.415	0.122	0.618
C	0.134	0.269	0.619
H	0.188	0.157	0.617
H	0.07	0.31	0.586
H	0.066	0.302	0.651

1-Methyl-1,3-cyclohexadiene; -99.71414 eV			
Atom	x_1	x_2	x_3
C	0.219	0.477	0.752
C	0.372	0.401	0.738
C	0.432	0.247	0.736
C	0.142	0.423	0.723
C	0.349	0.198	0.722
C	0.205	0.29	0.71
C	0.583	0.158	0.745
H	0.175	0.588	0.747
H	0.209	0.462	0.793
H	0.431	0.428	0.764
H	0.385	0.435	0.701
H	0.033	0.491	0.715
H	0.391	0.087	0.718
H	0.149	0.248	0.69
H	0.64	0.19	0.72
H	0.618	0.05	0.738
H	0.61	0.169	0.783

H_2; -7.0256449 eV			
Atom	x_1	x_2	x_3
H	0.354	0.513	0.888
H	0.354	0.513	0.860

1-Methylcyclohexene; -107.9829 eV			
Atom	x_1	x_2	x_3
C	0.378	0.308	0.629
C	0.508	0.316	0.636
C	0.318	0.353	0.577
C	0.618	0.226	0.597
C	0.426	0.294	0.537
C	0.561	0.236	0.545
C	0.666	0.175	0.504

4-Methylcyclohexene; -107.91056 eV			
Atom	x_1	x_2	x_3
C	0.379	0.307	0.629
C	0.506	0.322	0.635
C	0.317	0.349	0.576
C	0.616	0.233	0.597
C	0.425	0.295	0.536
C	0.559	0.242	0.545
C	0.563	0.287	0.688

H	0.301	0.371	0.657	H	0.301	0.369	0.657
H	0.402	0.201	0.635	H	0.408	0.199	0.636
H	0.55	0.285	0.673	H	0.256	0.462	0.573
H	0.483	0.424	0.631	H	0.243	0.313	0.569
H	0.262	0.466	0.574	H	0.67	0.125	0.609
H	0.24	0.322	0.569	H	0.696	0.263	0.595
H	0.67	0.117	0.609	H	0.39	0.3	0.498
H	0.699	0.253	0.596	H	0.632	0.203	0.514
H	0.391	0.3	0.498	H	0.475	0.43	0.627
H	0.618	0.186	0.468	H	0.595	0.18	0.697
H	0.737	0.065	0.511	H	0.485	0.353	0.716
H	0.73	0.224	0.502	H	0.652	0.301	0.692

A.4. Density functional theory-derived vibrational frequencies of gas-phase molecules.

The following tables show the vibrational frequencies calculated for the optimized structures of toluene, H_2, 1-methyl-1,3-cyclohexadiene, 1-methylcyclohexene, and 4-methylcyclohexene molecules in vacuum from **Appendix A.3** (with computational details in **Chapter 2, Section 2.2.3**).

Toluene		1-Methyl-1,3-cyclohexadiene		1-Methylcyclohexane		4-Methylcyclohexane	
Mode	Frequency (cm^{-1})	Mode	Frequency (cm^{-1})	Mode	Frequency (cm^{-1})	Mode	Frequency (cm^{-1})
1	3120	1	3090	1	3037	1	3075
2	3096	2	3083	2	3018	2	3054
3	3088	3	3070	3	2969	3	3004
4	3069	4	3023	4	2965	4	2997
5	3060	5	2984	5	2959	5	2963
6	3044	6	2965	6	2930	6	2944
7	3028	7	2956	7	2929	7	2934
8	2952	8	2903	8	2919	8	2926
9	1676	9	2872	9	2916	9	2918
10	1581	10	2855	10	2896	10	2906
11	1489	11	1645	11	2894	11	2889
12	1475	12	1584	12	2885	12	2878
13	1469	13	1470	13	1673	13	1657
14	1437	14	1458	14	1475	14	1486
15	1385	15	1450	15	1472	15	1480
16	1335	16	1437	16	1462	16	1467
17	1321	17	1394	17	1459	17	1458
18	1224	18	1381	18	1456	18	1452
19	1195	19	1359	19	1446	19	1396
20	1188	20	1332	20	1384	20	1385
21	1092	21	1311	21	1368	21	1361
22	1044	22	1245	22	1352	22	1342
23	1034	23	1185	23	1342	23	1338
24	1006	24	1177	24	1338	24	1308
25	995	25	1155	25	1320	25	1300
26	988	26	1072	26	1281	26	1267
27	972	27	1054	27	1257	27	1243
28	912	28	1037	28	1189	28	1215
29	859	29	1002	29	1162	29	1163
30	795	30	987	30	1150	30	1123
31	739	31	963	31	1090	31	1096
32	698	32	942	32	1084	32	1064
33	632	33	874	33	1043	33	1036
34	551	34	862	34	1038	34	986
35	475	35	762	35	1007	35	981
36	421	36	748	36	958	36	959
37	366	37	703	37	932	37	944
38	237	38	540	38	882	38	900
39	181	39	516	39	852	39	881
		40	496	40	827	40	861

41	416
42	363
43	325
44	259
45	177

41	812
42	749
43	634
44	504
45	459
46	432
47	348
48	336
49	310
50	259
51	154
52	95
	71
53	
54	46

41	788
42	726
43	673
44	513
45	457
46	443
47	417
48	346
49	327
50	237.9765
51	167
52	77.13923
	66
53	
54	5

H_2

Mode	Frequency (cm^{-1})
1	4243

A.5. Molecular geometries of gas-phase molecules optimized using coupled cluster singles and doubles (CCSD) theory.

The following tables show the atomic coordinates (in Å) for the optimized geometries determined using coupled clusters singles and doubles (CCSD) theory (with computational details in **Chapter 3, Section 3.2.4**) for toluene, H_2, methylcyclohexadiene isomers, and methylcyclohexene isomers in vacuum. The molecule's name and absolute electronic energy (eV) are listed in the heading.

Toluene; -7368.297934 eV			
Atom	x_1	x_2	x_3
C	-0.194	1.2	-0.009
C	1.199	1.203	0.002
C	1.902	0	0.008
C	1.199	-1.203	0.002
C	-0.194	-1.2	-0.009
C	-0.912	0	-0.012
H	-0.732	2.143	-0.018
H	1.735	-2.146	0.002
H	-0.732	-2.143	-0.018
C	-2.422	0	0.009
H	-2.801	-0.008	1.038
H	-2.828	0.888	-0.48
H	1.736	2.145	0.002
H	2.986	0	0.014
H	-2.828	-0.88	-0.495

1-Methyl-1,3-cyclohexadiene; -7400.263786 eV			
Atom	x_1	x_2	x_3
C	2.469	0.009	-0.083
C	0.963	0.088	0.013
C	-1.219	-1.184	-0.279
C	0.204	-1.2	0.311
C	-1.922	0.13	0.02
C	0.271	1.252	-0.065
C	-1.202	1.276	0.098
H	2.776	-0.643	-0.921
H	2.892	-0.431	0.84
H	2.916	1.006	-0.232
H	-1.801	-2.036	0.115
H	-1.164	-1.315	-1.379
H	0.764	-2.069	-0.078
H	0.152	-1.323	1.414
H	-3.014	0.148	0.111
H	0.799	2.199	-0.23
H	-1.698	2.237	0.271

2-Methyl-1,3-cyclohexadiene; -7400.237377 eV			
Atom	x_1	x_2	x_3
C	-0.278	1.232	-0.206
C	1.065	1.318	-0.047
C	1.866	0.086	0.346
C	1.234	-1.189	-0.247
C	-0.271	-1.211	-0.026
C	-0.99	-0.061	-0.021
H	-0.868	2.122	-0.455
H	1.439	-1.229	-1.337
H	-0.779	-2.178	0.074
C	-2.495	-0.023	0.142
H	-2.78	0.574	1.028
H	-2.971	0.448	-0.737
H	1.578	2.281	-0.148
H	2.913	0.182	0.013
H	-2.909	-1.039	0.259
H	1.883	0.013	1.453
H	1.702	-2.083	0.199

5-Methyl-1,3-cyclohexadiene; -7400.180133 eV			
Atom	x_1	x_2	x_3
C	-2.47	-0.099	0
C	-0.957	-0.083	0
C	-0.313	1.292	0.001
C	-0.225	-1.219	0
C	1.201	1.258	0
C	1.29	-1.261	0.001
H	1.918	0.116	-0.001
H	-2.867	0.426	-0.89
H	-2.863	-1.13	-0.001
C	-2.868	0.424	0.889
H	-0.676	1.863	-0.879
H	-0.674	1.861	0.882
H	-0.745	-2.186	-0.001
H	1.721	2.224	-0.001
H	1.646	-1.832	0.882
H	1.647	-1.833	-0.879
H	3.014	0.166	-0.001

1-Methyl-1,4-cyclohexadiene; -7400.264064 eV			
Atom	x_1	x_2	x_3
C	-2.47	-0.099	0
C	-0.957	-0.083	0
C	-0.313	1.292	0.001
C	-0.225	-1.219	0
C	1.201	1.258	0
C	1.29	-1.261	0.001
C	1.918	0.116	-0.001
H	-2.867	0.426	-0.89
H	-2.863	-1.13	-0.001
H	-2.868	0.424	0.889
H	-0.676	1.863	-0.879
H	-0.674	1.861	0.882
H	-0.745	-2.186	-0.001
H	1.721	2.224	-0.001
H	1.646	-1.832	0.882
H	1.647	-1.833	-0.879
H	3.014	0.166	-0.001

6-Methyl-1,4-cyclohexadiene; -7400.176149 eV			
Atom	x_1	x_2	x_3
C	-1.095	-1.259	0.039
C	0.215	-1.256	-0.285
C	1.049	0	-0.46
C	0.215	1.256	-0.285
C	-1.095	1.259	0.039
C	-1.909	0	0.249
C	2.247	0	0.519
H	-1.617	-2.217	0.158
H	0.737	-2.212	-0.422
H	0.737	2.212	-0.422
H	-1.617	2.217	0.158
H	-2.779	0	-0.437
H	-2.341	0	1.269
H	2.878	-0.894	0.368
H	2.878	0.894	0.368
H	1.887	0	1.562
H	1.465	0	-1.488

1-Methylcyclohexene; -7433.434324 eV			
Atom	x_1	x_2	x_3
C	-2.526	0.072	0.055
C	-1.012	0.084	0.003
C	-0.331	-1.275	0.079
C	-0.304	1.233	-0.095
C	1.156	-1.217	-0.319
C	1.213	1.299	-0.107
C	1.846	-0.024	0.363
H	-2.88	-0.425	0.978
H	-2.94	1.093	0.03
H	-2.942	-0.496	-0.798
H	-0.434	-1.67	1.11
H	-0.874	-1.985	-0.574
H	-0.848	2.185	-0.166
H	1.656	-2.165	-0.054
H	1.236	-1.101	-1.417
H	1.565	1.541	-1.13
H	1.549	2.132	0.537
H	1.728	-0.117	1.46
H	2.93	-0.025	0.151

3-Methylcyclohexene; -7433.474187 eV			
Atom	x_1	x_2	x_3
C	-2.424	0.006	0.263
C	-1.032	-0.067	-0.392
C	-0.199	-1.229	0.183
C	-0.29	1.252	-0.232
C	1.268	-1.143	-0.273
C	1.021	1.348	0.082
C	1.925	0.142	0.268
H	-2.33	0.213	1.344
H	-3.035	0.808	-0.187
H	-2.967	-0.948	0.139
H	-1.178	-0.248	-1.478
H	-0.24	-1.183	1.29
H	-0.648	-2.194	-0.118
H	-0.875	2.171	-0.374
H	1.834	-2.03	0.063
H	1.303	-1.134	-1.379
H	1.47	2.341	0.209
H	2.161	0.023	1.344
H	2.89	0.323	-0.24

4-Methylcyclohexene; -7433.493186 eV			
Atom	x_1	x_2	x_3
C	-2.436	-0.069	-0.028
C	-0.932	-0.031	-0.335
C	-0.182	-1.201	0.329
C	-0.304	1.305	0.113
C	1.293	-1.241	-0.115

C	1.214	1.277	0.056
C	1.929	0.137	-0.061
H	-2.61	-0.025	1.063
H	-2.961	0.787	-0.489
H	-2.898	-0.997	-0.409
H	-0.793	-0.119	-1.432
H	-0.232	-1.074	1.429
H	-0.678	-2.159	0.09
H	-0.683	2.128	-0.521
H	-0.632	1.538	1.146
H	1.866	-1.937	0.525
H	1.366	-1.64	-1.146
H	1.74	2.238	0.112
H	3.024	0.193	-0.119

H_2; -31.69854353 eV			
Atom	x_1	x_2	x_3
H	-0.483	0.473	0
H	-1.227	0.473	0

A.6. Vibrational frequencies of gas-phase molecules using the complete basis set (CBS-QB3) method.

The following tables show the vibrational frequencies for toluene, H_2, methylcyclohexadiene isomers, and methylcyclohexene isomers using the optimized structures reported in **Appendix A.5** and using the complete basis set (CBS-QB3) method with computational details in **Chapter 3, Section 3.2.4**.

Toluene		1-Methyl-1,3-cyclohexadiene		2-Methyl-1,3-cyclohexadiene		5-Methyl-1,3-cyclohexadiene	
Mode	Frequency (cm^{-1})	Mode	Frequency (cm^{-1})	Mode	Frequency (cm^{-1})	Mode	Frequency (cm^{-1})
1	3187	1	3172	1	3159	1	3176
2	3174	2	3153	2	3136	2	3165
3	3166	3	3143	3	3135	3	3150
4	3153	4	3095	4	3099	4	3140
5	3151	5	3056	5	3050	5	3085
6	3100	6	3049	6	3029	6	3082
7	3074	7	3038	7	3012	7	3053
8	3020	8	2999	8	3008	8	3018
9	1649	9	2970	9	3001	9	2955
10	1627	10	2958	10	2995	10	2934
11	1530	11	1711	11	1738	11	1701
12	1504	12	1650	12	1676	12	1634
13	1491	13	1489	13	1499	13	1502
14	1470	14	1481	14	1495	14	1499
15	1414	15	1477	15	1481	15	1472
16	1356	16	1469	16	1476	16	1438
17	1328	17	1422	17	1434	17	1411
18	1229	18	1412	18	1414	18	1395
19	1203	19	1391	19	1380	19	1366
20	1181	20	1358	20	1358	20	1341
21	1111	21	1333	21	1325	21	1308
22	1062	22	1269	22	1290	22	1237
23	1052	23	1202	23	1227	23	1200
24	1018	24	1187	24	1206	24	1187
25	1000	25	1173	25	1186	25	1143
26	999	26	1079	26	1117	26	1108
27	975	27	1073	27	1066	27	1073
28	910	28	1046	28	1035	28	1019
29	854	29	1013	29	1031	29	988
30	799	30	994	30	986	30	981
31	744	31	979	31	948	31	965
32	713	32	949	32	924	32	952
33	638	33	886	33	853	33	916
34	529	34	874	34	850	34	879
35	476	35	766	35	798	35	775
36	415	36	755	36	736	36	762
37	343	37	705	37	716	37	694
38	209	38	526	38	588	38	580

39	27	39	515	39	538	39	550
		40	496	40	469	40	456
		41	389	41	329	41	420
		42	332	42	304	42	312
		43	226	43	219	43	282
		44	182	44	172	44	231
		45	150	45	150	45	126

1-Methyl-1,4-cyclohexadiene		6-Methyl-1,4-cyclohexadiene		1-Methylcyclohexene		3-Methylcyclohexene	
Mode	Frequency (cm^{-1})	Mode	Frequency (cm^{-1})	Mode	Frequency (cm^{-1})	Mode	Frequency (cm^{-1})
1	3155	1	3151	1	3122	1	3143
2	3131	2	3148	2	3094	2	3117
3	3128	3	3125	3	3059	3	3083
4	3097	4	3124	4	3055	4	3082
5	3044	5	3094	5	3043	5	3058
6	3004	6	3084	6	3028	6	3050
7	2974	7	3020	7	3024	7	3030
8	2972	8	2980	8	3010	8	3017
9	2970	9	2976	9	3006	9	3012
10	2966	10	2952	10	3003	10	3002
11	1758	11	1746	11	2982	11	2987
12	1715	12	1700	12	2981	12	2961
13	1493	13	1501	13	1731	13	1711
14	1480	14	1496	14	1503	14	1502
15	1473	15	1469	15	1494	15	1501
16	1469	16	1440	16	1491	16	1498
17	1422	17	1400	17	1483	17	1491
18	1414	18	1399	18	1481	18	1478
19	1399	19	1377	19	1475	19	1425
20	1375	20	1356	20	1413	20	1406
21	1332	21	1315	21	1394	21	1379
22	1229	22	1227	22	1381	22	1372
23	1219	23	1219	23	1373	23	1370
24	1202	24	1189	24	1368	24	1343
25	1170	25	1129	25	1337	25	1326
26	1084	26	1087	26	1298	26	1282
27	1069	27	1042	27	1270	27	1251
28	1019	28	1014	28	1201	28	1232
29	1011	29	1010	29	1169	29	1169
30	986	30	1003	30	1167	30	1131
31	963	31	976	31	1105	31	1117
32	962	32	944	32	1102	32	1079
33	910	33	921	33	1062	33	1069
34	894	34	881	34	1049	34	1004
35	822	35	797	35	1015	35	996
36	747	36	738	36	974	36	988
37	671	37	706	37	938	37	967
38	571	38	582	38	898	38	902

39	483	39	554	39	863	39	877
40	444	40	486	40	834	40	862
41	398	41	442	41	814	41	784
42	334	42	282	42	766	42	731
43	252	43	279	43	625	43	678
44	177	44	237	44	505	44	542
45	99	45	81	45	441	45	468
				46	431	46	445
				47	332	47	339
				48	302	48	292
				49	251	49	270
				50	183	50	235
				51	128	51	113

4-Methylcyclohexene	
Mode	Frequency (cm^{-1})
1	3149
2	3125
3	3080
4	3074
5	3049
6	3029
7	3023
8	3014
9	3004
10	2988
11	2987
12	2974
13	1717
14	1501
15	1500
16	1495
17	1480
18	1475
19	1418
20	1410
21	1398
22	1376
23	1368
24	1333
25	1326
26	1283
27	1254
28	1226
29	1167
30	1140
31	1115
32	1097
33	1051

H_2	
Mode	Frequency (cm^{-1})
1	3155

34	1003
35	1000
36	968
37	957
38	908
39	896
40	875
41	795
42	735
43	668
44	512
45	447
46	417
47	391
48	308
49	235
50	197
51	140